

DISSERTATION

submitted to the

Combined Faculty for the Natural Sciences and Mathematics

of

Heidelberg University, Germany

for the degree of

Doctor of Natural Sciences

put forward by

Dipl.-Ing. Khai-Long Ho Hoang

born in Ulm, Germany

Oral examination

.....

Model-Based Optimization
for the Analysis of Human Movement
and the Design of Rehabilitation Devices

Advisor

PROF. DR. KATJA MOMBAUR

PD DR. SEBASTIAN I. WOLF

"It's quite easy if you don't know how."

Arthur Dent, *Hitchhiker's Guide to the Galaxy*

ZUSAMMENFASSUNG

Bewegungen des Menschen sind das Ergebnis komplexer und fein abgestimmter Interaktionen zwischen den Körpersegmenten. Das Gehen sowie das Aufstehen aus der Sitzhaltung gehören dabei, aufgrund der hohen Anforderungen an die Koordination und den starken Belastungen, zu den anspruchsvollsten solcher Bewegungen. In dieser Arbeit stellen wir die modellbasierte nichtlineare Optimalsteuerung als Methode vor, um diese Art von Bewegungen unter Berücksichtigung der Bewegungsdynamik über den gesamten betrachteten Zeitraum zu *rekonstruieren* und zu *generieren*. Aufgrund der Redundanz und dem hohen Grad an Nichtlinearität der untersuchten Bewegungen bietet es sich an, das Mehrzielverfahren anzuwenden, um das Optimierungsproblem zu diskretisieren. Das Ziel ist es, dadurch Grundprinzipien zu identifizieren, die es uns ermöglichen die Muster dieser Bewegungen zu beschreiben.

Wir betrachten die *menschliche Gehbewegung* aus der Sicht von unbeeinträchtigten Personen sowie einer unilateral mit Oberschenkelprothesen versorgten Person. Dazu *rekonstruieren* wir deren Gehbewegungen aus Bewegungsaufnahmen aus dem Ganglabor. Dazu werden probandenspezifische dreidimensionale Mehrkörpermodelle erstellt und in mehrphasigen Optimalsteuerungsproblemen mit der Methode der kleinsten Fehlerquadrate an die gemessenen Bewegungen eines ganzen Doppelschritts approximiert. Eine Auswertung der rekonstruierten Bewegungen nach der individuellen Positionierung des Fußes der Probanden legt nahe, dass diese dem Konzept der *Capturability* gerecht wird. Es werden solche Positionen angestrebt, die den inhärent widersprüchlichen Zielen zwischen einer Fortbewegung mit geringem Aufwand und einer schnellen Anpassung an äußere Störeinflüsse ausgleicht. Zusätzlich spielt die Anpassung der Auftrittskräfte bei Fersenauftritt eine große Rolle in der schrittweisen Stabilitätsstrategie. Aufbauend auf diesen Erkenntnissen regen wir das Konzept der *Capturability* als ein ergänzendes Kriterium zu etablierten klinischen Methoden zur Stabilitätseinschätzung an.

Die Aufstehbewegung aus der Sitzposition ist, aufgrund der hohen Gelenkbelastungen, die notwendig sind, um den Körper in die stehende Position zu heben, insbesondere herausfordernd für Menschen mit eingeschränkter Mobilität. Wir *generieren* optimale Aufstehbewegungen mithilfe zweiphasiger Optimalsteuerungsprobleme. Wir setzen voraus, dass die Aufstehbewegung wesentlich durch eine Vorbereitungsphase vor dem eigentlichen Aufstehen charakterisiert wird. Die dazu aufgestellten Ganzkörpermodelle enthalten Modellparameter, die eigens die dynamischen Segmenteigenschaften älterer Menschen aus unterschiedlichen Mobilitätsklassen repräsentieren. Für Menschen mit eingeschränkter Mobilität wird angenommen, dass eine generelle Art von Mobilitätsassistenz geleistet wird. Aus den Optimalitätsrechnungen resultieren unterschiedliche Bewegungsmuster, die signifikante Armbewegungen in beiden Phasen enthalten. Dadurch bestärken die Ergebnisse unseren Ansatz, den Menschen für die Aufstehbewegung durch ein Ganzkörpermodell zu repräsentieren, sowie ein zweiphasiges Optimalsteuerungsproblem zu betrachten.

Durch die Berechnung optimaler unterstützter Aufstehbewegungen mobil eingeschränkter Menschen, bietet es sich an, *optimale Konstruktionsparameter* für Mobilitätsassistenzsysteme zu bestimmen, die entsprechende Unterstützung bieten. Auf der Grundlage der unterstützenden Maßnahmen für die Aufstehbewegungen, die für zwei unterschiedliche Klassen der Mobilitätseinschränkung optimiert wurden, berechnen wir die optimalen Konstruktionsparameter für zwei unterschiedliche Assistenzgeräte. Durch unseren Ansatz, die Mensch-Maschine Interaktion an ihrer Schnittstelle zu trennen, kann sichergestellt werden, dass die optimale Unterstützung am Menschen nicht durch dynamische Kopplung mit dem Assistenzgerät beeinträchtigt wird. Durch Lösung umfangreicher mehrphasiger nichtlinearer Optimalsteuerungsprobleme erhalten wir Konstruktionsparameter, welche die Optimalitätsbedingungen hinsichtlich des abzudeckenden Arbeitsraums sowie des aufzubringenden mechanischen Aufwands erfüllen.

ABSTRACT

Human motions result from a complex and well-coordinated interaction between the body segments. Walking and the sit-to-stand transfer are amongst the most challenging human motion in terms of coordination and internal loads, respectively. We propose model-based nonlinear optimal control methods to *reconstruct* and *synthesize* these motions while considering the dynamics of the motion over the whole time horizon. The redundant and highly nonlinear character of the computed motions encourages to discretize the optimization problem according to direct multiple-shooting methods. The goal is to identify principles which enable us to describe the patterns of these motions.

We approach *human walking* from the perspective of unimpaired subjects and subjects walking with unilateral transfemoral prostheses. Their walking motion is *reconstructed* from motion capture data using subject-specific threedimensional multibody models. The motion of the models is fitted to the recorded data for a whole stride in a least-squares sense in multi-stage optimal control problems. Analyzing the reconstructed motion for the individual foot placement of the subjects suggests that it relates with the *Capturability* concept: foot locations are chosen by the subjects which enable a balance between the inherently conflicting goals of effortless progression and quick response to perturbations. In addition, the modulation of the ground collision impact forces at heel strike is found to play a major role in the step-by-step stability strategy. Based on these findings, we propose *Capturability* as a complementary criterion to the established clinical stability assessment methods.

The *sit-to-stand* motion is particularly demanding for humans with mobility impairments, due to the high joint loads required to lift the body into the standing pose. We *synthesize* optimal sit-to-stand by solving two-stage optimal control problems. We presume that the sit-to-stand motion is substantially characterized by a preparation phase prior to the actual lift-off. Full body models are established with dynamic model parameters which specifically represent elderly humans from different levels of mobility. For impaired subjects, mobility support is assumed to be provided by generic support actions. The optimization computations result in different patterns which include significant arm motion in both phases. Therefore, the results support our approach to choose a full body representation of the human as well as to consider two stages in the optimal control problem.

The computation of optimal assisted sit-to-stand motions of impaired humans offers the opportunity to *optimize design parameters* for mobility assistance devices providing adequate support. Based on the support actions for the sit-to-stand motions computed for two different levels of impairment, optimal mechanical design parameters for two different sit-to-stand assistance devices are generated. Our approach to separate the human-device interaction at their interface ensures that the optimal support provided to the human by the device is not compromised by any dynamic coupling between them. Solving large-scale nonlinear optimal control problems with multiple stages, we obtain design parameters for the devices which are optimal in terms of the workspace and the mechanical effort required.

ACKNOWLEDGEMENTS

The present thesis has been created at the research group *Optimization in Robotics and Biomechanics (ORB)* at the *Interdisciplinary Center for Scientific Computing (IWR)* and the *Faculty of Mathematics and Computer Science, University Heidelberg*. I would sincerely like to thank my supervisors *Prof. Dr. Katja Mombaur* and *PD Dr. Sebastian I. Wolf* for their strong interest in my work as well as substantial support for my PhD project and their encouragement to pursue my own research interests. They substantially contributed to the success of the project with their trust and valuable advice and never hesitated to share their extensive expertise.

The colorful blend of great personalities within the *ORB*-group boosted my motivation to strive for great work and provided me with great inspiration. In particular, I would like to address *Dr. Martin Felis, Alexander Schubert, Manuel Kudruss, Benjamin Reh, Dr. Kai Henning Koch, Dr. Kathrin Hatz, Dr. Manish Sreenivasa, Dr. Matt Millard* and *Paul Manns* for the great discussions as well as *Davide Corradi* and *Sascha Tebben* for their contribution to this research. I am also deeply thankful to *Julia Block* and *Daniel Heitzmann* from the *Heidelberg MotionLab* for sharing their clinical expertise and supporting me in gathering and analyzing the experimental data. Furthermore, I like to thank *Phoebe Ullrich* and *Christian Werner* from the research department of the *Agaplesion Bethanien-Hospital, Heidelberg University* as well as *Milad Geravand* from the *Robotics and Automation Systems* group at *Fraunhofer IPA* for the close cooperation within the *MOBOT* project. I am particularly grateful to those of my colleagues who could find the time and patience to proof-read parts of my thesis. This thesis would not have been possible without the previous hard work from *Dr. Martin Felis* who developed and maintained the extremely useful and well-designed *Rigid Body Dynamics Library (RBDL)* as well as the software tools *Meshup* and *Puppeteer* which have become a foundation of the lab and which I used to compute most of my results. I would also like to thank *Julia Feuerer, Ina Scheid, Pamela Schmidts,* and *Sarah Otto* for their assistance in administrative tasks.

I would like to thank the research group *Simulation and Optimization* led by *Prof. Dr. Dr. h.c. mult. Hans Georg Bock* for providing and maintaining the software package *MUSCOD-II*. Furthermore, I am very grateful to *Dr. Johannes P. Schlöder* for offering me valuable advice and mentoring throughout the project. I am indebted to *Dr. Jerry E. Pratt* from the *Institute for Human & Machine Cognition (IHMC)* in Pensacola, Florida for generously inviting me to join his lab for a research visit and providing me with an exciting and insightful environment during my stay. The collaboration and great discussions with him, *Twan Koolen* and other brilliant lab mates pointed at my research questions from a different fascinating perspective.

I wish to gratefully acknowledge the financial support for this project which I generously received from *Heidelberg Graduate School of Mathematical and Computational Methods for the Sciences (HGS MathComp)* funded by the *Deutsche Forschungsgemeinschaft (DFG)*, from the *Heidelberg University Graduate Academy*, as well as from the *MOBOT* project funded by the European Union within the FP7 program under grant agreement no. 600796.

I am deeply indebted to my parents *Hieu Kieu* and *Kiet Ho Hoang* for their love and trust and for passing me a curious mind. I am greatly thankful to my brother *Nam-Long* for giving me his trust and encouragement. Finally, I express my deepest gratitude to my wife, *Susana*, for her constant love, encouragement and patience. Her great dedication and support sustained me during the years of research for this thesis.

CONTENTS

0	Introduction	1
1	Preliminaries in Human Motion Analysis	5
1.1	Anatomical Terms in Biomechanics of Humans	5
1.2	Fundamentals of Human Gait	5
1.3	Camera-Based Motion Capturing	8
1.4	Modeling Dynamic Human Locomotion	10
1.5	Challenges in Dynamic Human Locomotion	12
1.6	Human Walking with Transfemoral Protheses	14
1.7	Assisted and unassisted Sit-to-Stand	15
I	Theoretical Principles for Human Motion Generation and Analysis	21
2	Modeling of Human Motions	22
2.1	Basics of Multibody systems	22
2.2	Equations of Motion for Multibody Systems	26
2.3	Multibody Model of a Human	28
2.4	Dynamic Model Parameters for Adults and Elderly Humans	31
3	Optimal Control for Human Motions	40
3.1	Multi-Phase Optimal Control Problems	40
3.2	Direct Multiple-Shooting Method	41
4	Stability Criteria for Human Locomotion	47
4.1	Basic Definitions for Stability Analysis	47
4.2	Stability of Dynamic Systems	48
4.3	Ground reference points in bipedal locomotion	50
4.4	Implications for Human Motions	59
II	Application and Results	61
5	Model-based Optimization of Human Walking	62
5.1	Dynamic Human Model for Gait Reconstruction	62
5.2	Least-Squares Reconstruction of Human Walking Motions	62
5.3	Numerical Results for Reconstructed Human Walking Motion	71
5.4	Discussion	91
6	Optimal Sit-to-Stand Motions	93
6.1	Modeling of Sit-to-Stand Motions	93
6.2	Optimal Control Problem for Sit-to-Stand Motions	94
6.3	Optimal Unassisted Sit-to-Stand Motions	96
6.4	Optimal Assisted Sit-to-Stand Motion	97
6.5	Discussion	102

7	Optimal Design of Sit-to-Stand Assistance Devices	103
7.1	Human-Centered Approach for Severely Impaired Subjects	103
7.2	Optimal Design Parameters for Nurse-Type Device	107
7.3	Human-Centered Approach for Moderately Impaired Subjects	107
7.4	Optimal Design Parameters for Rollator-Type Device	113
7.5	Discussion	114
III	Conclusion and Outlook	117
IV	Appendices	123
A	Anthropometric Parameters for the Human Body	124
B	Path Constraints for Human Walking	128
	Bibliography	133

0. INTRODUCTION

Self-reliance in everyday tasks is essential for human beings in order to maintain their quality of life and self-confidence. Being able to independently locomote in public environments is one of the skills which strongly facilitate participation in social life. While it may seem trivial for unimpaired adult humans, locomotion often poses a major challenge to humans affected by mobility impairment, such as elderly humans or humans with lower-limb amputations. Elderly subjects are often provided with mobility assistance by caregivers and/or assistive devices. For amputee subjects, a range of sophisticated prosthetic devices has been developed during the last decades to replace the functions of physiological human legs. However, the questions still arise: *How is stable motion defined? Are the prosthetic devices able to adequately replace the human limbs? Is the provided mobility assistance appropriate for the elderly human? How can mobility assistance devices be designed to provide suitable support?*

In terms of physical mobility, elderly humans and humans walking with transfemoral prostheses are faced with two fundamental challenges:

On the one hand, the limited abilities in responding to sudden perturbations require to adapt the strategies to maintain gait stability. The postural stability of transfemoral amputee subjects, i.e. their ability to maintain standing balance, has greatly improved with the recent development towards microprocessor-controlled prostheses [77]. Yet, it is still significantly reduced compared to unimpaired subjects [87]. Unimpaired humans are able to instantly react on sudden perturbations by actively shifting their intended foot location or applying appropriate counter-torques on the joints of the lower limbs. Subjects walking with transfemoral prostheses, however, usually have no access to actuation in the artificial limb and need to rely on other strategies to respond to perturbations. Such strategies could be based on compensatory motions of other limbs or integrated in a prosthetic design which preventively induces stable gait. The exact stability strategies underlying human gait, however, are still to be identified. Thoroughly understanding them is crucial for any advances in the design of transfemoral prostheses and facilitates the choice of appropriate prosthetic components towards a safer and more efficient gait.

On the other hand, rising from the sitting position represents one of the most demanding human motions. Lifting the major part of the body weight into the standing position imposes high demands on muscular strength and endurance. In elderly sit-to-stand (STS) motions, age-related deficits in muscle strength and joint functions often lead to compensatory motion patterns adapting to the abilities of the impaired part of the body [136]. In case additional assistance is required for the elderly human to successfully perform the STS-motion, several techniques are applied by caregivers to provide support to the subject and ensure a safe transfer. STS assistance can also be externally provided by technical equipment such as exoskeletons or mobility assistance devices. Simulating the STS-motion of elderly humans using optimization methods can help to identify optimal motion sequences and support the design of suitable assistive devices: Considering local impairments in the formulation of the optimization problem results in motion sequences which potentially prevent stress on the affected body parts and might find their application in physical therapy. Additionally incorporating external assistance into the simulation allows for the computation of optimal support actions and might, eventually, lead to design recommendations for an STS assistance device which provides support suitable for the individual needs of the impaired elderly subject.

Similar questions are approached in related work, however with different methods and outcomes. Several studies investigate the stability strategies in human walking based on common criteria borrowed from the research field of humanoid robotics. Most of these criteria do not prove meaningful for human walking since, according to their context, humans tend to walk unstable.

Questions related to optimal STS motions are frequently approached by simulating the motion and focusing on detailed musculoskeletal models of the lower body. However, the influence of the upper body on the whole body dynamics is most often entirely neglected.

Several projects also address the design of STS assistance devices. While optimal support of the STS motion is often strived for, these projects rely only on heuristics and simple assumptions for the supported motions.

In addition to simulation, human motions are commonly analyzed using recorded data obtained in motion laboratories. Usually, the motions are reconstructed using inverse dynamics. This way, however, the reconstructed motion does not satisfy the dynamics of the model throughout the entire time horizon but only on discrete time steps. Furthermore, the skeletal structure of the human is often reconstructed based on joint locations estimated from bony landmarks by linear regression. This method often leads to non-consistent geometrical properties of the body segments.

Scope of this Thesis

In this thesis, we develop scientific computation methods to approach challenging clinical questions from three different angles:

- (i) optimization-based motion reconstruction,
- (ii) optimization-based motion prediction, as well as
- (iii) human-centered design optimization.

We *reconstruct human walking* motions of unimpaired subjects and subjects walking with prostheses from motion capture data using subject-specific three-dimensional multibody models and optimal control. The motion of the models is fitted to the recorded data for a whole stride in a least-squares sense in large-scale multi-phase nonlinear optimal control problems. This approach allows us to identify gait parameters which potentially describe the strategies underlying unimpaired human walking and evaluate them on the gait of the subject walking with prostheses.

In order to *predict* sit-to-stand motions which protect the joints and require less effort, we synthesize optimal sit-to-stand by solving multi-phase optimal control problems. The cost-functions are formulated using terms which have been heuristically determined in consultation with clinical experts. Full body models are established with dynamic model parameters which specifically represent elderly humans. For impaired subjects, mobility assistance is assumed to be provided by a generic source of support actions.

Based on optimal sets of generic support forces assisting the sit-to-stand motions of impaired subjects we *optimize design parameters* for mobility assistance devices providing suitable support. We compute optimal mechanical design parameters for two different assistance devices providing the sit-to-stand support actions for subjects representing two different levels of impairment. The human-device interaction is separated at their interface to ensure that the optimal support provided to the human by the device is not compromised by any dynamic coupling between them.

In all three cases, the dynamics of human motions are modeled as multi-phase nonlinear optimal control problems of an underactuated hybrid differential algebraic system. Due to this approach, we ensure that the dynamics of the system are fulfilled for the entire motion. We model the human body in terms of a multibody system and derive the system's equations of motion considering subject-specific model parameters. The resulting highly nonlinear optimal control problems are solved using the *direct multiple-shooting* method [17].

Contributions of this Thesis

During the research for this thesis, scientific contribution has been made in several topics:

Regression Equations for Dynamic Model Parameters of Elderly Humans:

We develop regression equations which improve the formulation of mathematical models. These equations provide the dynamic model parameters for elderly humans which are difficult to obtain on living humans. The regression equations facilitate the creation of parameterized multibody models since they are based on the full body mass and length, respectively. Generic models of the body of an elderly human can be established with realistic dynamic parameters using the equations and values presented in this thesis.

Stability Strategies in Human Walking:

In this thesis, we propose an optimal control based method for providing physiologically sound reconstruction of unimpaired and prosthetic gait to analyze subject-specific walking motions in a clinical context. Using such methods we ensure that the dynamics of the system are satisfied throughout the entire motion. Along with the reconstructed motions, we propose a non-standard stability criterion - the Capture Point - as an intuitive and comprehensive reference to evaluate stability strategies in human gait based on the coordination of the gait velocity, step length, step timing and ground collision impact. We encourage the application of Capturability as a complementary criterion to the established clinical stability assessment methods.

Optimal Assisted and Unassisted Sit-to-Stand Motions:

We propose optimal control formulations to synthesize STS motions assuming different mobility levels for elderly subject. Recommendations for motion sequences can be derived from the results that take into account the full amount of body dynamics available to an unimpaired elderly human. For severely impaired elderly subjects, we compute assistive force profiles and trajectories which can be used as requirements for an assistance device providing suitable STS support. In addition, the results support our approach to consider a full body model of the human as well as a multi-stage optimal control problem.

Optimal Design Parameters for a Sit-to-Stand Assistance Device:

Optimal control methods are applied to obtain sets of mechanical design parameters for two different kinds of STS assistance devices. The parameters are computed to provide support for the 20th to the 80th body height percentile of both male and female elderly subjects. Prototypes of the sit-to-stand assistance devices have been manufactured based on the results presented in this thesis.

Thesis Overview

This thesis is organized in four major parts preceded by a preliminary chapter:

Chapter 1 provides a brief introduction into the fundamental concepts and approaches in the research field of biomechanics and, in particular, human gait. It discusses the challenges in dynamic human locomotion with a particular focus on balance and stability.

Part I describes the theoretical and computational principles underlying our applications. Chapter 2 explains the methods to model the human body in terms of a multibody system and deriving the system's equations of motion considering subject-specific model parameters. In Chapter 3 we elaborate on the optimal control framework used in this thesis along with direct multiple shooting methods to optimize human motions. Chapter 4 summarizes common stability criteria used for bipedal walking and compares them with mathematical criteria. We discuss their implications for human motions with a particular focus on the Capturability concept.

Part II is dedicated to the application of the described methods on challenging clinical questions. In Chapter 5 we reconstruct human walking from the perspective of subjects walking with unilateral transfemoral prostheses. We describe the dynamic human model used for this task and establish the optimal control problem which fits the motion of the model to the recorded data. The resulting gait parameters are discussed for their relevance to describe the individual gait motion and, in particular, the stability strategy of each subject. In Chapter 6, we present how optimal STS motions are synthesized by solving multi-stage optimal control problems. The model formulation as well as the formulation of the optimal control problem are described for assisted and unassisted STS motions. Chapter 7 describes our approach to perform human-centered optimization of mechanical design parameters for mobility assistance devices. We present the established models and the large-scale optimal control problems for two different devices based on two levels of desired mobility assistance.

Part III concludes the thesis and provides a brief outlook.

Part IV contains supplementary material provided in the Appendices A and B.

1. PRELIMINARIES IN HUMAN MOTION ANALYSIS

During the course of evolution, the anatomy of the human body has evolved to enable efficient locomotion in upright posture on two legs. Walking and running, i.e. different modes of locomotion which a human chooses depending on the desired gait speed, are made possible through a sophisticated interplay between muscles, elastic tendons and the skeletal structure. Different shapes of the joints such as ball and socket joints, e.g. in the hip, or hinge joints, e.g. in the knee, allow for complex motions that combine both rotational and translational degrees of freedom. Elastic articular discs located in the joint spaces between the bones absorb shocks and reduce friction. A system of redundant muscles, some of them spanning over multiple joints, is responsible for both actuating and stabilizing the skeletal system.

This chapter provides a brief introduction into the common terminology in the research field of biomechanics in Section 1.1 as well as into the fundamentals of human gait in Section 1.2. Section 1.3 introduces the methods applied to record and analyze the human motions used in this thesis. Section 1.4 describes our approaches to obtain subject-specific parameters for the multibody models of the human body. We elaborate on the challenges in dynamic human locomotion in Sections 1.5 with a particular focus on balance and stability in human gait. Section 1.6 and 1.7 summarize the most important systems to assist and restore impaired human walking.

1.1. Anatomical Terms in Biomechanics of Humans

According to clinical standards, motions of body segments can be described with respect to a set of planes and main axes [141]. Based on an upright posture, the human body can be divided along the *sagittal*, *horizontal* and *frontal plane*. As shown in Figure 1.1, the sagittal plane divides the human body into right and left parts, the frontal plane cuts the body into front and back parts and the horizontal plane is parallel to the ground. Rotations can be specified with respect to the sagittal, transversal, and longitudinal axes.

Locations and directions within the human body can be specified in both absolute and relative terms with respect to specific landmarks or, if not further specified, relative to the center of the body, see Table 1.1 for a compilation of the most important of such expressions.

1.2. Fundamentals of Human Gait

Walking is a repetitive sequence of coordinated motions of the lower limbs. In a reciprocal manner, motions are performed with the right and left leg segments that alternately carry the human body into the gait direction and swing the foot forward again resulting in a step [125].

Considering the periodicity of this repetitive motion, a complete *gait cycle* (or: *stride*) comprises of two *steps*, see also Figure 1.2. A step can be subdivided into the *stance* and the *swing phase* denoting the periods in which the foot is in contact with the ground or being swung forward. These phases are separated by the gait events *heel strike* (or: *initial contact*) and *toe off*. The heel strike denotes the instance in which the heel touches the ground after the swing phase and initiates the stance phase whereas the toe off denotes the event in which the toes leave the ground and initiates the swing phase. In physiological walking the stance phase typically

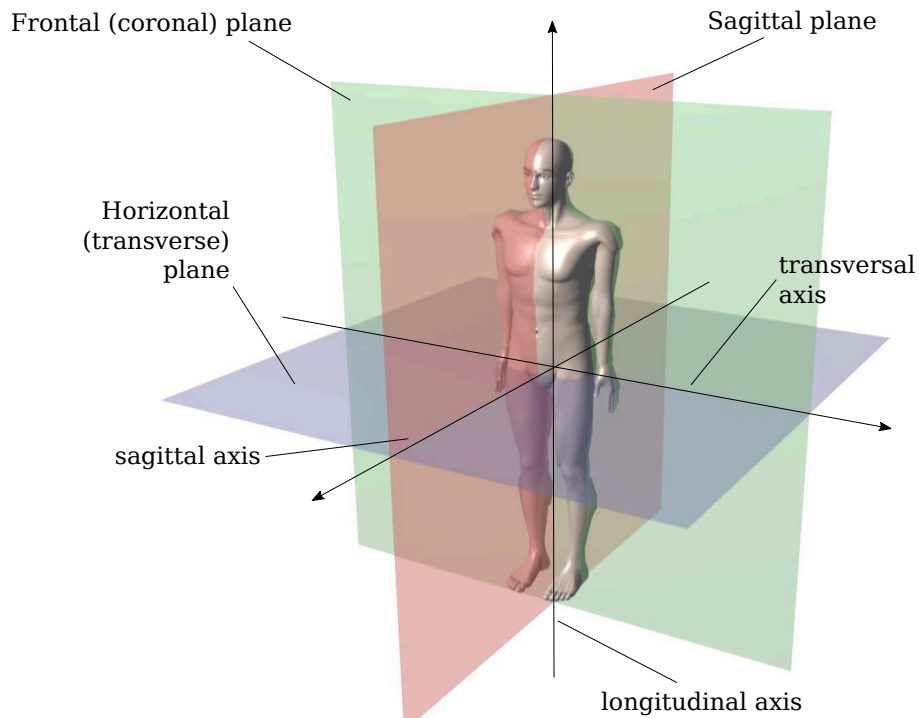


Figure 1.1: Anatomical planes and axes of the human body. Base image from [36].

Table 1.1: Anatomical terms for locations and directions in the human body.

Frontal planes	planes parallel to the front of the body. Divides the body into a front and a back section. The <i>coronal plane</i> is the frontal plane that contains the body center of mass.
Sagittal planes	planes orthogonal to the frontal planes which divide the body into a left and a right section. The <i>median plane</i> is the sagittal plane that contains the body center of mass.
Horizontal planes	planes orthogonal to the <i>longitudinal axis</i> of the body. Divides the body into an upper and a lower section. The <i>transversal plane</i> is the horizontal plane that contains the body center of mass.
Sagittal axis	intersection line of the median and the transversal plane.
Transverse axis	intersection line of the coronal and transversal plane.
Longitudinal axis	intersection line of the coronal and median plane.
medial	towards the center
lateral	towards the side
proximal	towards the trunk
distal	away from the trunk
anterior	(also: ventral) situated at the front
posterior	(also: dorsal) situated at the back

lasts for approximately 60% of a gait cycle leaving 40% of the stride for the swing phase [125]. The stance phase can further be separated into the phases *loading response*, *mid stance*, *terminal stance*, and its last phase the *pre-swing* which initiates the transition into the swing phase

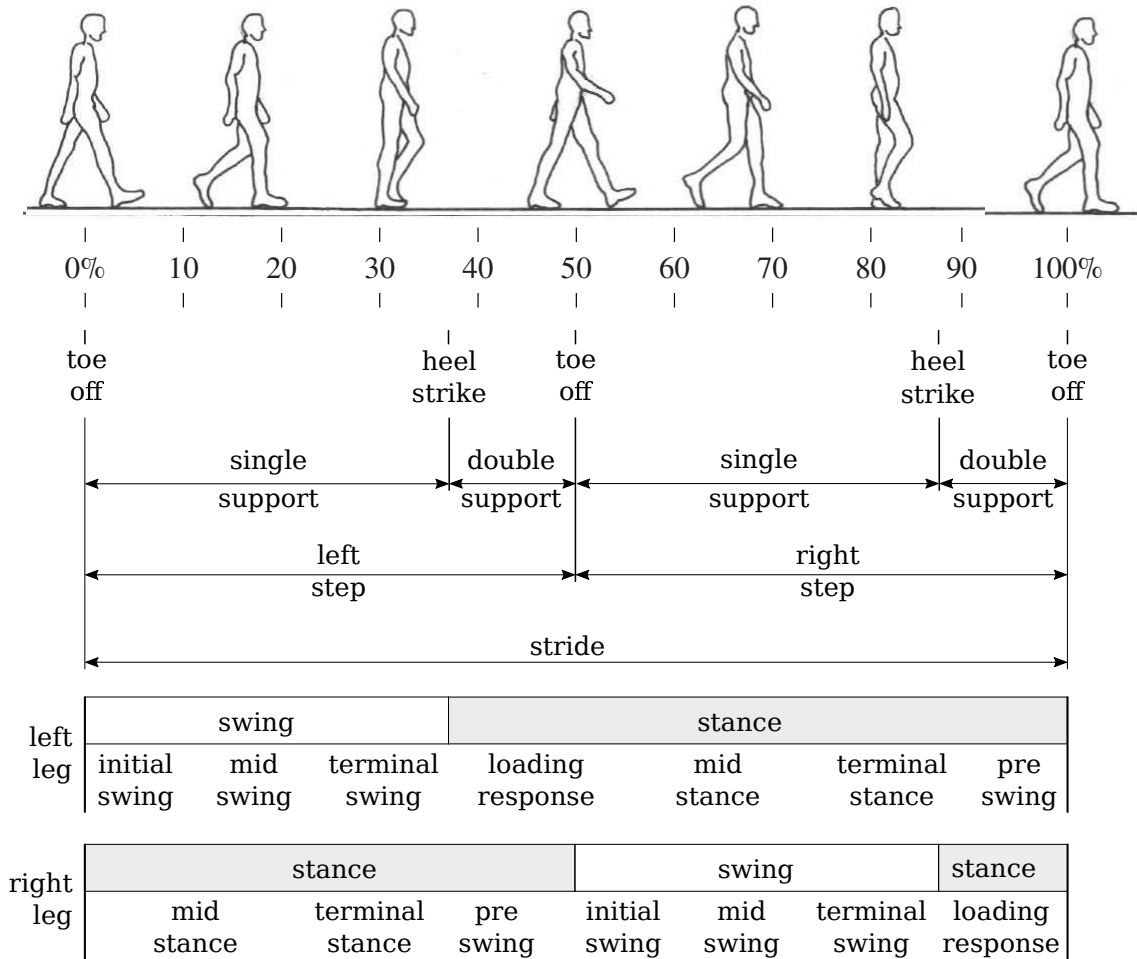


Figure 1.2: Gait phases and events during gait cycle in healthy walking. The figure shows two consecutive *steps* forming one *stride* beginning and ending with the *toe off* of the right foot. Base image from [2].

separated into the *initial swing*, *mid swing* and, finally, the *terminal swing* phases. The biomechanics community has agreed on using the heel strike as the delimiting event to define a gait cycle [125]. However, since the focus of this research work is rather directed towards swing phase phenomena, throughout this thesis, a gait cycle is defined to begin with a swing phase and, thus, initiated by a toe off.

Walking is characterized by the existence of the gait phase *double support* in which both feet are in contact with the ground versus the *single support* when only one leg is in contact with the ground. In contrast, running can be distinguished from walking by the existence of a *flight phase* in which no ground contact occurs at all.

1.2.1. Basic Gait Parameters

Gait performance is often assessed using *temporal-spatial* parameters such as the *gait velocity*, *step length*, *step width*, and *step duration*. Other common parameters are the *ratio between the durations of the single support and the double support phases* as well as the *cadence* measured in steps per minute [1, 47, 68, 70, 146]. In this work, we define the step length as the distance

of one heel strike location to the location of the same event in the previous step in anterior-posterior direction (1.1) and the step width as the distance of the same events in medio-lateral direction (1.2).

$$l_{\text{step},x} = r_{\text{heel,front},x} - r_{\text{heel,rear},x} \quad (1.1)$$

$$l_{\text{step},y} = r_{\text{heel,front},y} - r_{\text{heel,rear},y} \quad (1.2)$$

The step duration is the time Δt_{step} between two consecutive heel strikes. The gait velocity is defined as the velocity of the center of mass location $\mathbf{v}_{\text{com}} = \dot{\mathbf{r}}_{\text{com}}$ and will be further defined in Chapter 2.

Further meaningful conclusions about human gait can be drawn by sub-dividing the step length into two components reflecting the COM-heel distances in gait direction at heel strike. Considering the heel position $\mathbf{r}_{\text{heel, rear},x}$ of the rear leg in terminal stance and position $\mathbf{r}_{\text{heel, front},x}$ of the front leg at initial contact we introduce the gait parameters

$$\text{Rear foot outreach: } RFO = \mathbf{r}_{\text{com},x} - \mathbf{r}_{\text{heel, rear},x} \quad (1.3)$$

$$\text{Front foot outreach: } FFO = \mathbf{r}_{\text{heel, front},x} - \mathbf{r}_{\text{com},x} \quad (1.4)$$

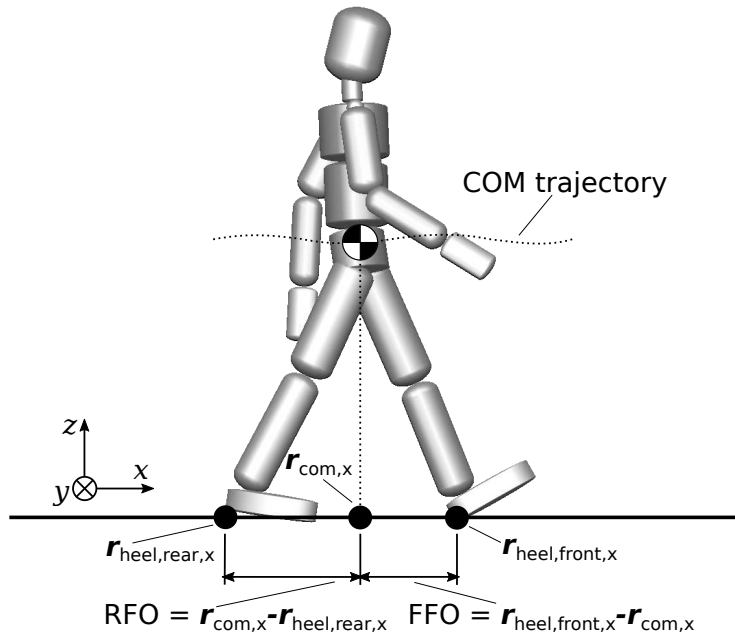


Figure 1.3: The step length can be subdivided into the two components *rear foot outreach (RFO)* and the *front foot outreach (FFO)*.

1.3. Camera-Based Motion Capturing

One of the major interests in understanding the fundamentals of human motion and in particular human gait lies in quantifying the complex interaction between the body segments of a human on a musculoskeletal level. For the kinematic part of this, camera-based *Motion Capture Recordings (MoCap)* using passive reflective markers are a reliable tool, combining good precision with an acceptable effort required for set-up and maintenance.

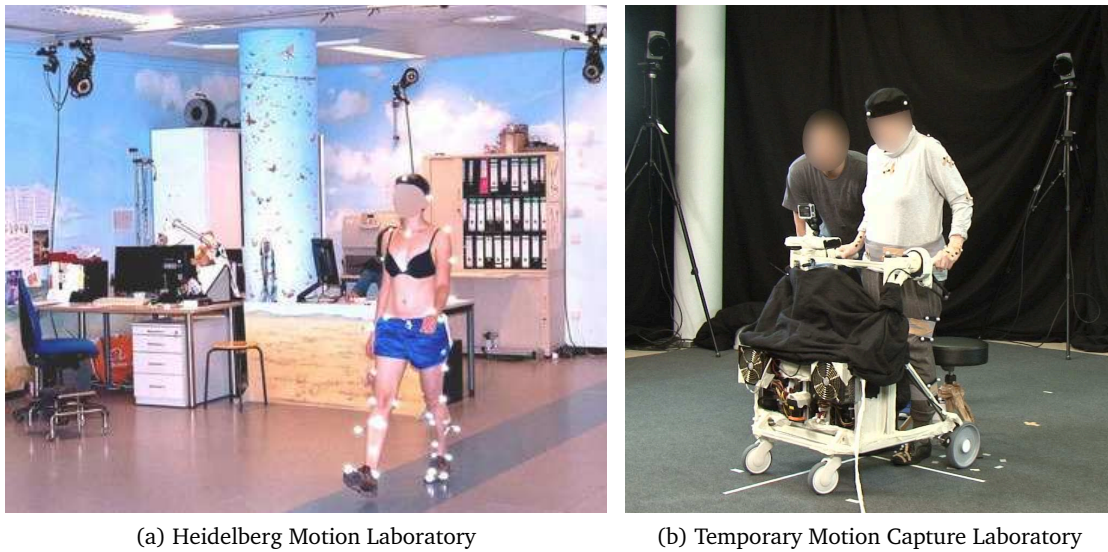


Figure 1.4: (a) Heidelberg Motion Laboratory equipped with infrared cameras and force plates. A marked subject is participating at motion capture recordings. Picture with courtesy of *Heidelberg MotionLab*. (b) Temporary motion capture laboratory set-up at the geriatric hospital equipped with infrared cameras. A marked subject performs motion capture experiments with a rollator prototype.

For this thesis, MoCap recordings are used which were obtained from two different labs:

- Walking of healthy subjects and prosthetic walkers have been recorded in the *Heidelberg Motion Laboratory*¹ located in the *Heidelberg University Orthopedic Hospital* equipped with a Vicon MoCap system [152] and three Kistler [78] force plates (Figure 1.4a)
- Sit-to-stand motions as well as assisted and unassisted gait of elderly humans were recorded in a temporary gait lab set-up at the *Clinic for Geriatric Rehabilitation*² equipped with a Qualisys MoCap system [134] (Figure 1.4b).

The motion capture systems in both laboratories record the position of passive-reflective markers using infrared cameras. Three dimensional spatial trajectories of each marker are reconstructed by the post-processing software from the calibrated camera signals and provided as output.

1.3.1. Marker Sets and Spatial Reconstruction

The spatial position and orientation of body segments can be obtained from the threedimensional positions of markers attached to them. In case of a passive-reflective MoCap system, the markers have a spheric shape and a retroreflective surface which enables them to reflect light into the same direction of its source. By attaching infrared light sources to cameras capable of recording in the infrared spectrum the markers can be separated from their surroundings in the captured images. In a calibrated Motion Capture Laboratory, the threedimensional position of each marker can then be reconstructed using triangulation and the synchronized frames of at least two cameras.

¹Heidelberg MotionLab, www.heidel-motionlab.de

²Agaplesion Bethanien Hospital Heidelberg, www.bethanien-heidelberg.de

During human motions, recording artefacts may occur, amongst other reasons, due to markers being occluded by body segments, poor placement of the markers on the body surface, or markers being placed too close to each other. Different measures can be taken to avoid such artefacts [24], e.g.

- providing redundancy by increasing the number of cameras: although only two perspectives are necessary to perform triangulation, between 6 and 12 cameras are often used in Motion Capture laboratories to maximize visibility of all markers from various perspectives.
- providing redundancy by increasing the number of markers per body segment: the positions of only three markers are necessary to uniquely define a segment's spatial orientation. Since single markers are often occluded by body segments, e.g. markers attached to the pelvis being hidden behind the arm during arm swing, the segment orientation can still be reconstructed if at least one additional marker is attached to the segment and visible during that time.
- minimizing relative movement of markers: to ensure repeatability of the experiments and to minimize soft tissue movement between the bones and the skin, the markers are attached to bony landmarks of the subjects' body.

Recommendations for specific marker sets to satisfy the requirements in different recording scenarios are provided from various sources. One example is the *PlugIn-Gait (PiG)* marker set, proposed by Vicon [153], which establishes a model of the human body by reconstructing joint centers from the measured marker positions. This method, however, does not rely on rigid bodies and the lengths of the body segments, which are defined as the distances between the joints, are variable.

Less than three markers can be used per segment by relying on a multibody model and computing joint angles from the marker trajectories in case of an *Inverse Kinematic* fit. This method exploits the fact that the position and rotation of a rigid body in a kinematic chain is fully determined by the position and rotation of its neighboring segments and the coupling constraints between them. In this thesis, motion resulting from recordings which involved walking are reconstructed based on whole body *Inverse Kinematics* implemented in PUPPETEER [38].

1.4. Modeling Dynamic Human Locomotion

Dynamic modeling of the human body is an important part of describing the fundamentals of the biomechanics of human movement. In human movement science, the human body is commonly modeled in terms of a multibody system where the major body parts are represented by rigid bodies connected by simple joints. This is possible since the range of the regarded motions can be considered as larger scale phenomena which render most of the complex combinations of translational and rotational degrees of freedom and minor elasticities negligible. Depending on the research question at hand, the multibody model can be refined and enhanced e.g. by equations to describe the muscle dynamics or by detailed foot models. There has been a variety of research into human walking, e.g. the emotional aspects of human walking have been described in [36] using a 3D model of the human body in which the actuating torques are applied directly on the joints. A 2D musculoskeletal model has been proposed by [5] to evaluate different fatigue and energy-related cost functions for optimal control problems that are potentially involved in human walking. Human walking has also been simulated using a 3D neuromusculoskeletal model in [10] while it has been verified that metabolic energy per

unit distance traveled is a valid measure for gait performance. A review of common concepts to model human motions with various levels of complexity is provided by [164].

1.4.1. *Dynamic Model Parameters*

The inertial and geometric properties of body segments are reflected in the rigid bodies as segment lengths, segment masses, center of mass positions, and inertia matrices. To establish individual models it would be most desirable to have access to subject-specific parameters. However, such *anthropometric parameters* are extremely difficult to obtain on living humans making it practically impossible to gather them on an individual basis.

Regression data provided by de Leva [29] and Dumas [32] have proven to be helpful in determining anthropometric parameters in a sufficient approximation for young adults. While both sources are useful for the modeling task, the widely used *de Leva* data provides a more meaningful segmentation of the human body. Another common, however incomplete, set of dynamic data has been compiled from various sources by Winter [161]. The mass distribution of the segments of the elderly human body, although lacking the geometric properties of the body segments, has been addressed by Jensen and Fletcher [71].

The *de Leva* data has been used in many different biomechanical applications involving the dynamics of human motions and modeling in terms of rigid body systems, e.g. to perform inverse dynamic analysis and estimate the energy expenditure in human motions [3], to examine causes for injury during sudden motions [95], to study emotional body expressions in human walking [39], or to investigate foot placement during human locomotion after perturbations [99]. It has also been used in computer graphics to ensure generated animations of human characters obey the laws of physics [130] and in orthopedics medicine to describe the effect of foot orthoses on the kinematics and dynamics of human gait [113]. Because of its versatility and comprehensiveness the *de Leva* data provides a solid foundation for deriving a comprehensive set of anthropometric parameters for elderly humans.

Age related pathologies such as intervertebral disc degeneration, arthrosis, or osteoporosis cause the human body to decrease in height and change the overall body proportions. Large studies aimed on gathering the weight, height and body dimensions of male and female humans from various ages and social backgrounds have been summarized in Panero et al. [123], Stoudt et al. [145], Pheasant [126] and NASA [111]. The body dimensions obtained in these studies are specified with respect to reference points which are not commonly used for creating dynamic models. Furthermore, these ergonomic tables focus on workspace problems and do not necessarily contain meaningful body parameters which could be directly used for establishing dynamic models of a human. However, they can provide insights into the amount of age-related changes in body parameters if the data for younger people is compared with those for elderly humans. In addition, the mass distribution over the whole body changes due to degeneration of muscular mass, fat deposition, water retention and changes in tissue composition.

1.4.2. *Adjusted Anthropometric Parameters for Elderly Humans*

In Section 2.4, we provide *regression equations* for the geriatric dynamic parameters by combining existing sources for dynamic parameters of young and healthy humans with others about the age-related changes in body proportions. These equations are formulated to facili-

tate the creation of parameterized multibody models by relating all parameters to the full body mass and length, respectively. Furthermore, the reference points in each segment are chosen according to a tree-structured modeling approach where the tree originates from the *Pelvis* segment. Applying the regression equations on body dimensions which were gathered from subjects in recent studies [57] yields absolute values that represent the anthropometric data of the average elderly population living in the early 21st century.

The equations and values presented in Section 2.4 are useful to establish generic models of the body of an elderly human using parameters which otherwise would be difficult to obtain on living humans. The equations provide an estimation for the body parameters of an average elderly human. The methods presented here are designed in such a way that the model can be individualized by replacing the parameters of a given body segment by measured parameters. Adjustment coefficients in the regression equations allows for tuning the anthropometric parameters to mass and length proportions that differ from the proportions of a young and healthy population. Although different coefficients are presented for the adjustment of each segment's mass properties, in this thesis we apply only three different coefficients to adjust for changes in segment lengths in the upper and lower body and the arms. This simplification is justified by the assumption that a similar bone structure within these body parts stressed by the usual loads lead to a similar decrease in segment length.

1.5. Challenges in Dynamic Human Locomotion

Human locomotion results from a sequence of well-coordinated motions of a complex articulated system of limbs and joints which enable an energy-efficient and versatile way to travel short distances. The articulated system is redundant, i.e. its number of available degrees of freedom (DoF) is greater than necessary to perform the locomotion task [110, 165]. At the same time, the system is also underactuated since the number of actuators is lower than the system's number of DoFs [34]. Due to the underactuation, the entire system's motion can only be manipulated through the contacts with the environment [86].

The dynamics in human locomotion has been of major interest in the field of biomechanics with some early work on the biomechanics of human gait [92, 156], on generally understanding the interaction between motion and reaction forces [108], on the balancing behavior and risk of fall in the elderly population [120] and on modeling the dynamics in human locomotion [42, 94, 143] often also proposing first approaches to recording human motions [22, 41, 109, 162]. With the rise of high-performance computing technologies starting from the second half of the 20th century, simulation of the human locomotion became increasingly prevalent mostly focusing on model-based optimal control methods to obtain physically consistent results [5, 9, 12, 23, 25, 121]. Since then and due to increased computational power and improved algorithms, research questions have advanced from the general understanding of human locomotion towards addressing increasingly complex problems through modeling and simulation. Some of these problems are related to the metabolic cost of human locomotion [2, 14, 138, 151], the muscle force distribution during human walking [4, 164] and the neuromuscular control of human locomotion [21, 76] which has been disputed whether it exploits muscle synergies [8, 30, 150]. The insights gathered from these fields are increasingly merging with research on humanoid robots performing human-like tasks [86, 105], on assistive robots supporting human motions [15, 61, 67, 81, 91] and on microprocessor controlled prostheses replacing human limbs [60, 62, 148, 163].

1.5.1. *Stability in Human Walking*

During walking, one leg serves as a body support while the opposite leg is moved towards the next support location. The legs alternate their roles repeatedly with reciprocal timing until the subject stops [125]. While performing this repetitive sequence, one of the major objectives in human locomotion is to maintain stability not only on flat ground but also on rough surfaces and inclinations. With an elevated center of mass balancing over a small contact surface, the human body is an inherently unstable system if it weren't for a continuously acting control system [160]. Stability and balance control in human walking have been approached from different perspectives. This includes describing the human body as a hybrid dynamic system and examining its properties in terms of Lyapunov stability [19, 58, 104]. Although, this approach has led to meaningful insights into the self-stabilization properties of the human locomotion, modeling the human response to unpredictable changes in the environment in terms of a hybrid dynamic system has so far been an unsolved task [20]. Fundamental knowledge about the feedback loops which are active during human locomotion has not yet been gathered in sufficient accuracy.

Other approaches which have been proven useful to clinical applications and the humanoid robotics community seek to explain foot placement during walking and fall prevention as a response to pushes based on *ground reference points* which require only little computational effort to be obtained and can be evaluated in real-time. The most common ground reference points are summarized in Chapter 4. The present thesis, however, focuses on describing the foot placement strategy of human subjects in terms of the velocity-based *Capture Point (CaP)* [83, 132] (also known as the *Extrapolated Center of Mass (xCoM)* [69]) since it is able to describe gait phenomena *in the future* and, therefore, provides a versatile method to predict and evaluate the gait of individual subjects. The Capture Point concept has been successfully implemented in the gait control of humanoid robots [33, 84, 85]. It has also been described as a recovery strategy applied by humans as a response to unexpected perturbations in everyday situation [6]. Furthermore, based on the Capture Point, strategies to adapt temporal-spatial gait parameters to varying environmental conditions [53, 54] and asymmetric step lengths in transtibial prosthetic gait [55] have been associated with functional compensation strategies in order to reduce the risk of falling backwards. Unfortunately, these studies suffer from a misconception of the Capturability concept and, in case of [55], from the unjustified assumption that transtibial gait is asymmetric.

1.5.2. *Foot Placement in Unimpaired Walking and Walking with Prostheses*

In Chapter 5, we elaborate on the foot placement strategies of unimpaired subjects and a subject walking with transfemoral prostheses. The walking motion is reconstructed from recorded motion data obtained in a gait laboratory. The motion of multibody models with subject-specific model parameters is fitted to recorded motions in a least squares sense. The fitting problem is approached using nonlinear optimal control with multiple stages and multiple-shooting discretization. This approach leads to physiologically consistent simulation results in which the individual gait patterns are preserved. The reconstructed walking motions are analyzed for general full-body gait patterns as well as the foot placement behavior with respect to the Capture Point.

1.6. Human Walking with Transfemoral Prostheses

During the recent decades, highly versatile exo-prostheses, i.e. prostheses which are externally attached to a human, have emerged enabling a transfemoral amputee patient to master various difficult gait situations, e.g. walking at different gait speeds, ascending and descending slopes, and walking on uneven terrain. Sophisticated prosthetic design has strongly improved since the 1960s when the first fluid-controlled above-knee prostheses became available enhancing gait security by enabling a well-timed swing phase at various walking velocities [90, 107]. Since the beginning of the 1990s, microprocessor controlled hydraulic knees like the Össur Rheo Knee [116], the Otto Bock C-Leg [118] and the Otto Bock Genium [119] (Figure 1.5) have been made commercially available and are nowadays commonly fitted to amputee subjects. The prosthetic walking motion of the amputee subject participating in the motion capture recordings for this thesis has been recorded walking with both the C-Leg and the Genium.

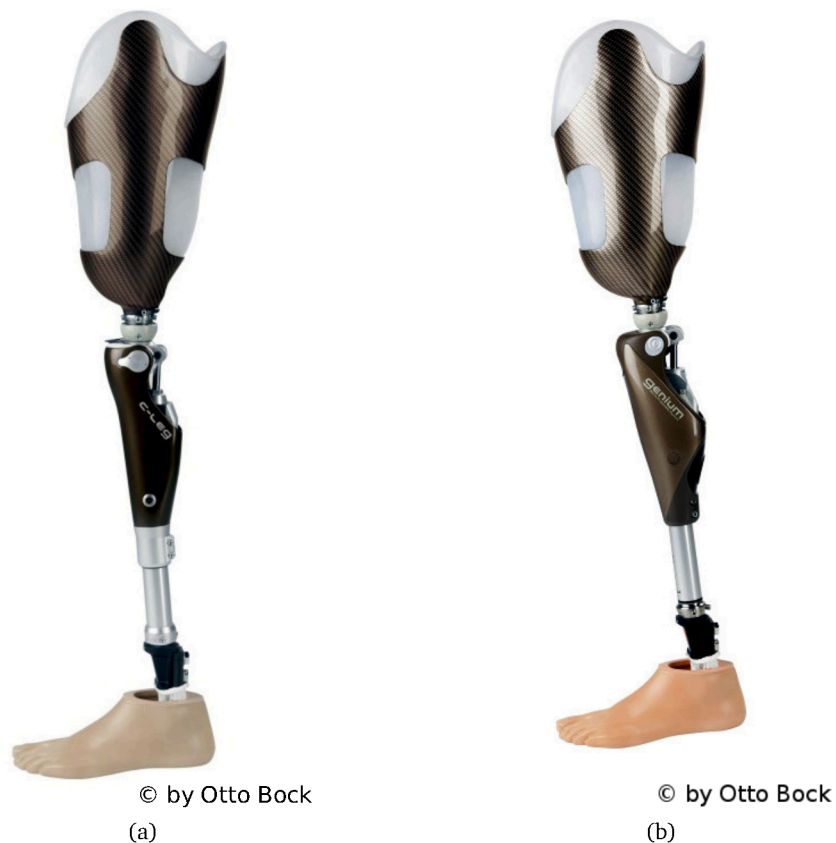


Figure 1.5: Prosthetic walking motion is analyzed in this thesis on a subject walking with the Otto Bock (a) C-Leg and (b) Genium, shown here with a socket, a prosthetic foot and standard adapters. Images are taken from the Otto Bock company website.

Since the beginning of the 21st century, many research projects have been working on fully actuated lower limb prostheses [159]. Seamlessly integrating such active devices into a subject's life is a major challenge since it requires highly sophisticated control strategies that reliably recognize and comply with the subject's intent. Furthermore, long-endurance, high-power, small size and low weight are conflicting goals in the mechanical design which are difficult to reconcile. To date, only the Össur Power Knee [115] is available to the end user.

With micro-processor assisted passive prosthetic devices that make use of sensoric information and passive-adaptive mechanical elements highly dynamic locomotion became possible for the patient. Nevertheless, stable walking is still challenging for above-knee amputee patients due to the lack of active control of the knee and ankle motion of the prosthetic devices. Understanding the strategy of unimpaired humans in maintaining balance while walking is the key task for developing more versatile and safe prosthetic components.

In previous studies, dynamic stability of prosthetic walking has been investigated in a biomechanical analysis for common microprocessor-controlled knee joints [13]. The risk of falling with transfemoral prostheses has been investigated in everyday situations such as abruptly stopping and side-stepping, stepping on an obstacle and stumbling. However, a measure to quantify stability has not been formulated. Stability in terms of variability and symmetry of prosthetic gait has been studied in [31, 87] where unstable walking was connected to deviation from symmetric motion patterns. In the present thesis, however, it is shown that asymmetric gait might play a role in achieving stability.

1.7. Assisted and unassisted Sit-to-Stand

Rising from sitting into the standing position, commonly referred to as the *Sit-to-Stand transfer (STS)*, belongs to the most demanding motions in everyday life of a human [103]. Several studies have simulated this type of motion using optimization methods [7] while seeking to generally describe the STS motion [122] and focusing on optimal strategies to reduce the mechanical demand [16] for simplified musculoskeletal models of the human body. None of them, however, considered full body models during the STS-task or a preparation phase in which specific motions are executed to initiate the STS transfer.

In Chapter 6 of this thesis, STS motions are optimized using full body models. It is shown that arm swing is intentionally applied in the preparation phase of the STS task right before the subject actually lifts off the chair and can be exploited to reduce the load on the joints of the lower limbs. Therefore, it is crucial to consider a full body model for analyzing the STS-transfer and to treat the STS-motion as a multi-phase problem. Furthermore, based on the assumptions of how to provide external support to two different levels of impairments in the elderly population, optimal assisted STS-motions are obtained which are used as an input for the computations in Chapter 7 in which optimal mechanical design parameters are computed for an STS-assistance device.

1.7.1. Mobility assistance devices

Recent technological progress brings robots not only into industrial buildings and research labs but also into our homes, e.g. as assistance robots. The medical sector, in particular, allows for an effective application of robots which may assist both patients and medical staff during the therapy and in the clinical routine. In the long term, as soon as direct human-robot interaction has become a common scenario, assistance robotics is supposed to grow out of the protected clinical environment and extend into the private setting.

The group of subjects potentially benefiting the most from medical assistance robots are humans which are physically limited to an extent where they are unable to independently perform everyday tasks. Also, there is a huge benefit to subjects which are given the chance to enhance or recover important physical and cognitive functions by the additional support provided by

an assistance robot. Hence, medical robots find their way into important fields of application which enable almost autonomous mobility for impaired people as well as adopt essential tasks in therapy, training, clinical diagnostics and medical monitoring during rehabilitation. Assistive tasks in clinical care are usually carried out by specially trained staff. However, the demographic shift in the industrialized countries leads to a dramatic disequilibrium between a low amount of manpower and a great number of subjects in need of care. This discrepancy could be reduced by the employment of assistive robots in clinical care. In addition to that, a close interaction between medical staff and adaptive assistive systems leads to an ergonomic work environment which reduces the risk of physical stress.

Within the field of *rehabilitation robotics* one can generally distinguish between *assistance* and *therapy robots* [142]. Therapy robots are operated by at least two persons: on the one hand the patient, on the other hand the therapist who supervises the process of the therapy and adjusts the robots behavior to the individual needs of the patient. Movement therapy for upper and lower extremities following a stroke or communication therapy for autistics are potential fields of application. In contrast, assistance robots are supposed to be included into daily life rather than only used during therapy. Their tasks are related to situations in which a subject, due to limited cognitive or motor capabilities, needs support in order to independently perform everyday tasks. In this context, assistance robots can be grouped into *cognition*, *manipulation*, and *mobility assistance robots*, respectively. Cognition assistance robots provide support to subjects with limited cognitive functions which might be caused by dementia, autism or multiple strokes in perception of and communication with their environment. This kind of support can be provided by navigation robots such as the cane robot *GuideCane* [18] or by systems which transform an individualized form of input into speech output such as the speech synthesizer used by the Stephen Hawking [59].

According to the type of platform, manipulation assistance robots can be categorized into *stationary* and *portable*. Work spaces in which a subject is supported by a robot to accomplish complex physical tasks are typical environments for stationary manipulation robots. Portable manipulation robots solve very similar tasks, however, they can be relocated, e.g. by mounting them to a wheelchair. A special case of portable manipulation assistance robots are *exoskeletons* which are worn by the user and used as an direct amplification of his own strength. Famous examples are the *ReWalk* [144], *Cyberdyne HAL5* [155], *ekso Bionics* [82], and the *IHMC Mina v2* [50] shown in Figure 1.6, which can be used to assist paraplegic subjects ascending and descending stairs and slopes or walking over uneven terrain.



Figure 1.6: Subject operating IHMC Mina v2 exoskeleton (Image: ETH Zürich/Nicola Pitaro).

Mobility assistance robots are mobile systems which provide passive or actuated mobility support to subjects with limited mobility to enable them to locomote stably and reduce the risk of fall. Oftentimes, additional systems for manipulation and cognition assistance are integrated on the same platform. An example for a passive system is the *RT Walker* [64], shown in Figure 1.7a, which uses laser range sensors to scan its environment and is able to steer the user into predefined trajectories and avoid obstacles by appropriate braking of the right or the left wheels, respectively. Actuated mobility assistance robots are able to change their location independently without any active control by the user. This ability can be used to additionally support the user's mobility or provide manipulation and cognition assistance from a distance. While in its first version the mobile platform *Care-O-Bot* was designed to perform interactive social communication with the user [140] its second evolution was enhanced by an adaptive gait assistance as well as a gripper arm to pick up and transport smaller items [48], see Figure 1.7b. Subsequent generations of the platform omitted the mobility assistance and focused on home assistance tasks [49, 79, 93].



(a) RT Walker



(b) Care-O-Bot 2

Figure 1.7: The mobility assistance devices RT Walker [64] and Care-O-Bot 2 [40] providing walking support to subjects.

To date, two projects have addressed walking assistance combined with STS-assistance. The *Monimad* device mainly consists of a mobile platform and an STS-mechanism, made of two robotic arms with two degrees of freedom [96, 97, 98]. Although it is claimed that the mechanical design parameters were optimized, no objective function has been specified in the literature. The support trajectories during STS-transfer are predetermined and were created based on experimental data gathered in a clinical environment involving physiotherapists helping the patients standing up using handles attached to force-sensors. Because of the non-repeatability of the experiments and since only a small number of patients was included in these studies, the measured support trajectories show a huge variety and have no statistical relevance. However, in [124] a method for the *Monimad* device is proposed to select and adjust predefined assistance trajectories to minimize the user effort. The *Chugo* device provides both walking and STS assistance, while support is not only provided at the hands, but also at the forearms and the trunk [26]. The STS-transfer motion supported by this device is based on typical motions performed by physiotherapists during STS-assistance [75].



Figure 1.8: Prototype of the Chugo device providing STS support to a subject [26].

1.7.2. Optimal mobility assistance devices

Although a lot of practical and theoretical experience leads to the support motions applied by clinical staff during STS-support, these actions are mainly determined by the anatomical structure and ergonomic requirements of the human body of both patient and caregiver and are not necessarily optimally adjusted to the patient's needs. During the task of developing an assistive device, however, the limits imposed by the supporting part can be omitted and an optimal set of support actions can be identified and applied which serves to entirely comply with the subject's ergonomic needs. This approach has been applied with the optimization computation for the mechanical design parameters of the *MOBOT* device in Chapter 7. The mobility assistance devices, which the design of the STS support has been optimized in this thesis for, has been developed within the scope of the EU-project *MOBOT* [100]. The main functionalities of the *MOBOT* devices are the adaptive walking assistance as well as the sit-to-stand (STS) transfer assistance which supports the patient during the STS-transfer motion using optimal support patterns. The elderly humans in the subject group of the project are suffering from mobility disabilities e.g. due to Parkinson's disease, dementia or strokes. For the use of these specific devices it is assumed that the subjects are able to walk with assistance once they have risen from the sitting position. Prototypes of both devices have been manufactured by a project partner based on the optimized design which resulted from this thesis (Figure 1.9).



(a) First *MOBOT* prototype



(b) Second *MOBOT* prototype

Figure 1.9: Elderly subjects walking assisted by prototypes of the *MOBOT* device during the motion capture recordings and validation studies, respectively.

In this work, we propose methods to support the mechanical design process by applying optimal control methods, which lead to optimal assistive actions performed by the device as well as optimal design parameters that satisfy the requirements in terms of desired work-space and applied torques. In order to perform this design optimization, it is sufficient to focus on the class of STS motions since in terms of loads and work-space they are more challenging than walking. Therefore, we choose to direct our attention towards the optimization of the STS-mechanism design since we consider that part of the design the most crucial.

Part I

Theoretical Principles for Human Motion Generation and Analysis

2. MODELING OF HUMAN MOTIONS

Modeling human motions for optimization and simulation purposes is faced with the challenge to reproduce the structure the human musculoskeletal system as realistically as possible while, at the same time, keep the computational complexity as simple as possible. Considering that human gait results mostly from redundant and nonlinear larger scale motions [125], assumptions can be made that allow phenomena of smaller scale e.g. elasticities in the skeletal structure or non-trivial joint kinematics to be neglected. Therefore, the human body can be considered as a mechanical system which can be represented using *multibody systems* (MBS).

We introduce the basic concept of multibody systems in Section 2.1 and derive the *equations of motion* of multibody systems in the context of human motion modeling in Section 2.2. The models of the human body used in this thesis are described in Section 2.3. In Section 2.4, we derive regression equations which provide *geometrical and inertial model parameters* for elderly humans.

2.1. Basics of Multibody systems

According to the methods of multibody modeling [139], a mathematical model of a mechanical system can be established using a finite number of rigid bodies, mass-less linking and coupling elements as well as ideal joints. Figure 2.1 illustrates the most common elements used in multibody modeling and the symbols commonly used to visualize them. A rigid body includes the mass and inertia properties of the modeled system specified as the position of its *Center of Mass* (COM) and the *radii of inertia* with respect to a body-specific local coordinate system (COS).

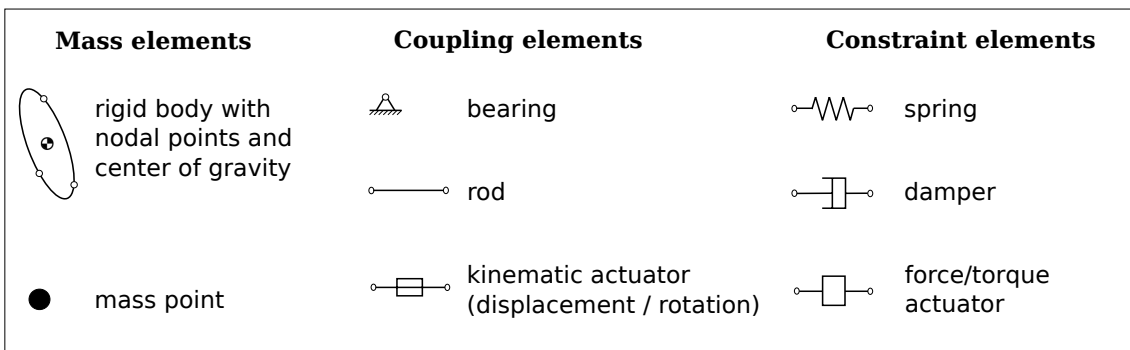


Figure 2.1: Elements of a multibody model

A model of a mechanical system can be established by connecting rigid bodies with ideal, i.e. friction-less, joints as well as constraint elements and coupling elements to a multibody system. The rigid bodies B_0, B_1, \dots, B_{n_B} (n_B : no. of rigid bodies) can be connected by the joints J_1, J_2, \dots, J_{n_J} (n_J : no. of joints) to a system with a *chain topology*, a *tree topology* or a *closed-loop topology*, refer to Figure 2.2. Systems with closed loop topology can be considered as tree topology systems with additional *loop constraints*.

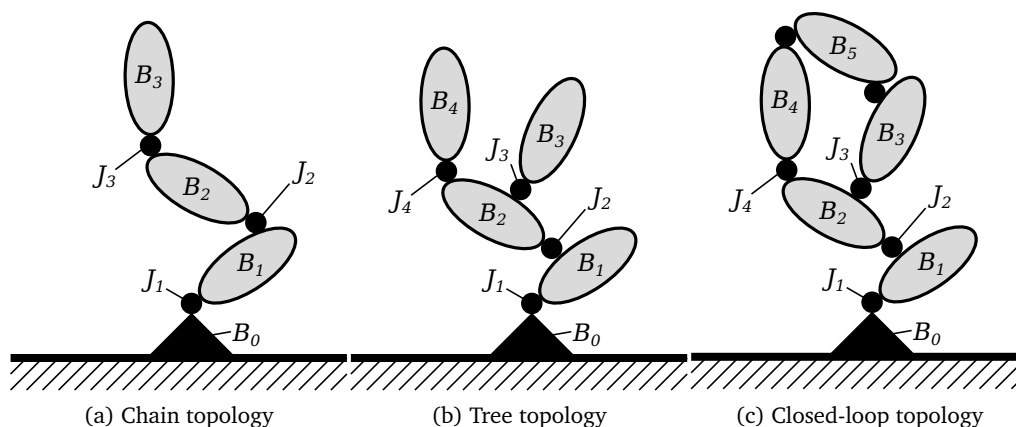


Figure 2.2: Rigid bodies can be connected to multibody systems with (a) *chain topology*, (b) *tree topology* or (c) *closed-loop topology*.

2.1.1. Generalized Coordinates

The position and orientation of a single rigid body in a multibody system can be described by three translational and three rotational variables, the so-called *Cartesian coordinates*. The state of the whole multibody system can then be described by a total of $6n_B$ variables. This formulation suffers from the drawback that it has redundant coordinates and allows for states that are infeasible due to constraints imposed by the coupling and constraint elements in the system. Using *generalized coordinates*, the state of the system can be described using a number of coordinates equal to the number of system's degrees of freedom. Disregarding possible constraints on the joint angles or to prevent collision of the segments any vector in $\mathbb{R}^{n_{\text{dof}}}$ characterizes a valid state of the model.

2.1.2. Kinematics

A holonomic multibody system consisting of p ($p \in \mathbb{N}$) rigid bodies and subject to n_c ($n_c \in \mathbb{N}$) holonomic constraints has $n_{\text{dof}} = 6p - n_c$ ($n_{\text{dof}} \geq 0$) degrees of freedom (DoF) and the same number of generalized coordinates

$$\mathbf{y} = [y_1 \ y_2 \ \dots \ y_{n_{\text{dof}}}]^T \quad (2.1)$$

The rotation and translation of the i -th rigid body in the inertial system Θ is described by the rotation matrix

$$\mathbf{S}_i = \mathbf{S}_i(\mathbf{y}, t) \in \mathbb{R}^{3 \times 3} \quad (2.2)$$

of the body-fixed local COS and by the translation vector

$$\mathbf{r}_i = \mathbf{r}_i(\mathbf{y}, t) \in \mathbb{R}^3 \quad (2.3)$$

with respect to the origin of the same COS, respectively. The time derivative of (2.3) yields the

translational velocity of the rigid body

$$\begin{aligned}\mathbf{v}_i &= \dot{\mathbf{r}}_i = \frac{\partial \mathbf{r}_i}{\partial \mathbf{y}^T} \dot{\mathbf{y}} + \frac{\partial \mathbf{r}_i}{\partial t} \\ &= \mathbf{J}_{Ti}(\mathbf{y}, t) \dot{\mathbf{y}} + \bar{\mathbf{v}}_i(\mathbf{y}, t).\end{aligned}\quad (2.4)$$

where $\mathbf{J}_{Ti} \in \mathbb{R}^{3 \times n_{\text{dof}}}$ denotes the Jacobian of translation and $\bar{\mathbf{v}}_i \in \mathbb{R}^3$ the vector of the local translational velocity.

Similarly, the angular velocity can be derived from the time derivative of (2.2)

$$\boldsymbol{\omega}_i = \dot{\mathbf{S}}_i = \mathbf{J}_{Ri}(\mathbf{y}, t) \dot{\mathbf{y}} + \bar{\boldsymbol{\omega}}_i(\mathbf{y}, t) \quad (2.5)$$

with the Jacobian of rotation $\mathbf{J}_{Ri} \in \mathbb{R}^{3 \times n_{\text{dof}}}$ and the vector for the local angular velocity $\bar{\boldsymbol{\omega}}_i \in \mathbb{R}^3$. Both the local translational velocity $\bar{\mathbf{v}}_i$ and local rotational velocity $\bar{\boldsymbol{\omega}}_i$ vanish for skleronomic systems. The angular velocity vector $\boldsymbol{\omega}_i = [\omega_1 \ \omega_2 \ \omega_3]^T$ results from the corresponding skew-symmetric rotation tensor [137]

$$\tilde{\boldsymbol{\omega}}_i = \begin{pmatrix} 0 & -\omega_3 & \omega_2 \\ \omega_3 & 0 & -\omega_1 \\ -\omega_2 & \omega_1 & 0 \end{pmatrix} = \mathbf{S}_i \mathbf{S}_i^T. \quad (2.6)$$

The translational and rotational accelerations \mathbf{a}_i and $\boldsymbol{\alpha}_i$ are obtained by the time derivative of (2.4) and (2.5), respectively, as well as introducing the local translational and rotational accelerations $\bar{\mathbf{a}}_i$ and $\bar{\boldsymbol{\alpha}}_i$

$$\mathbf{a}_i = \dot{\mathbf{v}}_i = \frac{\partial \mathbf{r}_i}{\partial \mathbf{y}^T} \ddot{\mathbf{y}} + \frac{\partial \mathbf{v}_i}{\partial \mathbf{y}^T} \dot{\mathbf{y}} + \frac{\partial \mathbf{v}_i}{\partial t} = \mathbf{J}_{Ti}(\mathbf{y}, t) \ddot{\mathbf{y}} + \bar{\mathbf{a}}_i(\dot{\mathbf{y}}, \mathbf{y}, t) \quad (2.7a)$$

$$\boldsymbol{\alpha}_i = \dot{\boldsymbol{\omega}}_i = \frac{\partial \mathbf{S}_i}{\partial \mathbf{y}^T} \dot{\mathbf{y}} + \frac{\partial \boldsymbol{\omega}_i}{\partial \mathbf{y}^T} \dot{\mathbf{y}} + \frac{\partial \boldsymbol{\omega}_i}{\partial t} = \mathbf{J}_{Ri}(\mathbf{y}, t) \dot{\mathbf{y}} + \bar{\boldsymbol{\alpha}}_i(\dot{\mathbf{y}}, \mathbf{y}, t) \quad (2.7b)$$

2.1.3. Kinetics

The motion of a rigid body results from the forces and moments acting on it while considering its inertial properties. The relationship between the motion of the i -th rigid body K_i of a multibody system and the forces and moments applied on it is described by the *Newton-Euler equations* [139]

$$m_i \mathbf{a}_i = \mathbf{f}_i^r + \mathbf{f}_i^e \quad (2.8a)$$

$$\boldsymbol{\Theta}_i \boldsymbol{\alpha}_i + \tilde{\boldsymbol{\omega}}_i \boldsymbol{\Theta}_i \boldsymbol{\omega}_i = \mathbf{l}_i^r + \mathbf{l}_i^e \quad (2.8b)$$

where (2.8a) describes Newton's *law of conservation of linear momentum* and (2.8b) describes Euler's *law of conservation of rotational momentum*. The mass m_i and the inertia tensor $\boldsymbol{\Theta}_i \in \mathbb{R}^{3 \times 3}$ with respect to its center of mass indicate the inertial properties of the rigid body. The forces and moments acting on the body with respect to the center of mass can be distinguished between the vectors for the resultant reaction (or constraint) forces $\mathbf{f}_i^r \in \mathbb{R}^3$ and resultant applied forces $\mathbf{f}_i^e \in \mathbb{R}^3$ as well as the resultant reaction (or constraint) moments $\mathbf{l}_i^r \in \mathbb{R}^3$ and resultant applied moments $\mathbf{l}_i^e \in \mathbb{R}^3$. Applied forces and moments are determined by equations relating them to the motion of the multibody system imposed by weight, actuation, and elements such as springs and dampers. In contrast, reaction forces and moments are due to

contacts and elements such as joints which impose kinematic constraints on the system.

With (2.7a) in (2.8a) and (2.7b) in (2.8b), respectively, we receive

$$m_i J_{Ti} \dot{\mathbf{y}} + m_i \underbrace{\bar{\mathbf{a}}_i}_{\bar{\mathbf{c}}_{Ti}} = \mathbf{f}_i^e + \mathbf{f}_i^r \quad (2.9a)$$

$$\Theta_i J_{Ri} \dot{\mathbf{y}} + \underbrace{\Theta_i \bar{\mathbf{a}}_i + \tilde{\boldsymbol{\omega}}_i \Theta_i \boldsymbol{\omega}_i}_{\bar{\mathbf{c}}_{Ri}} = \mathbf{l}_i^e + \mathbf{l}_i^r \quad (2.9b)$$

The $6p$ scalar equations of the p rigid bodies of the multibody system can be summarized in the $6p$ -Newton Euler equations of the entire system

$$\bar{\mathbf{M}} \bar{\mathbf{J}} \dot{\mathbf{y}} + \bar{\mathbf{c}} = \bar{\boldsymbol{\tau}}^i + \bar{\boldsymbol{\tau}}^r \quad (2.10)$$

with the block diagonal matrix of mass and inertia tensors

$$\bar{\mathbf{M}}(\mathbf{y}, t) = \begin{pmatrix} m_1 \mathbf{I} & & & & & 0 \\ & \ddots & & & & \\ & & m_p \mathbf{I} & & & \\ & & & \Theta_1 & & \\ & & & & \ddots & \\ 0 & & & & & \Theta_p \end{pmatrix} \in \mathbb{R}^{6p \times 6p} \quad (2.11)$$

the global Jacobian

$$\bar{\mathbf{J}}(\mathbf{x}, t) = \begin{pmatrix} \mathbf{J}_{T1} \\ \vdots \\ \mathbf{J}_{Tp} \\ \mathbf{J}_{R1} \\ \vdots \\ \mathbf{J}_{Rp} \end{pmatrix} \in \mathbb{R}^{6p \times n_{\text{dof}}} \quad (2.12)$$

and the vector $\bar{\mathbf{c}}$ as the generalized bias force term which includes the nonlinear effects, such as the Coriolis, centrifugal and gyroscopic forces, $\bar{\boldsymbol{\tau}}^e$ for the applied forces and moments as well as $\bar{\boldsymbol{\tau}}^r$ for the reaction forces and moments

$$\bar{\mathbf{c}} = \begin{pmatrix} \bar{\mathbf{c}}_{T1} \\ \vdots \\ \bar{\mathbf{c}}_{Tp} \\ \bar{\mathbf{c}}_{R1} \\ \vdots \\ \bar{\mathbf{c}}_{Rp} \end{pmatrix} \in \mathbb{R}^{6p}, \quad \bar{\boldsymbol{\tau}}^e = \begin{pmatrix} \mathbf{f}_1^e \\ \vdots \\ \mathbf{f}_p^e \\ \mathbf{l}_1^e \\ \vdots \\ \mathbf{l}_p^e \end{pmatrix} \in \mathbb{R}^{6p}, \quad \bar{\boldsymbol{\tau}}^r = \begin{pmatrix} \mathbf{f}_1^r \\ \vdots \\ \mathbf{f}_p^r \\ \mathbf{l}_1^r \\ \vdots \\ \mathbf{l}_p^r \end{pmatrix} \in \mathbb{R}^{6p} \quad (2.13)$$

2.2. Equations of Motion for Multibody Systems

The global Newton-Euler equations (2.10) describe the motion of a multibody system with $6p$ equations for n_{dof} degrees of freedom and n_c constraints using the full number of equations which also include the reaction forces and moments occurring in constraint systems. Applying the *Principle of d'Alembert*, the reaction forces and moments can be eliminated and the equations (2.10) can be written in their *minimal form* using the system's *generalized coordinates* and only as many as n_{dof} equations. This reduction exploits the *generalized orthogonality* between the direction of motion and reaction, respectively, which causes the reaction to be ineffective towards the motion. According to the *Principle of Virtual Work* [139] we obtain $\bar{\mathbf{J}}^T \bar{\boldsymbol{\tau}} = 0$.

The state of mechanical systems is uniquely defined by its positions $\mathbf{q} \in \mathbb{R}^{n_{\text{dof}}}$ and its corresponding velocities $\dot{\mathbf{q}} \in \mathbb{R}^{n_{\text{dof}}}$ indicated by the vector of state variables $\mathbf{x} \in \mathbb{R}^{2n_{\text{dof}}}$

$$\mathbf{x} = \begin{pmatrix} \mathbf{q} \\ \dot{\mathbf{q}} \end{pmatrix} \quad (2.14)$$

Hence, (2.10) can be transformed into an explicit first-order system of *ordinary differential equations (ODE)* in \mathbf{x}

$$\dot{\mathbf{q}} = \mathbf{v} \quad (2.15)$$

$$\dot{\mathbf{v}} = \mathbf{a} = \mathbf{H}(\mathbf{q})^{-1}(\boldsymbol{\tau}(\mathbf{q}, \mathbf{v}) - \mathbf{C}(\mathbf{q}, \mathbf{v})) \quad (2.16)$$

with the symmetric and positive-definite mass matrix $\mathbf{H} = \bar{\mathbf{J}}^T \bar{\mathbf{M}} \bar{\mathbf{J}} \in \mathbb{R}^{n_{\text{dof}} \times n_{\text{dof}}}$, the generalized nonlinear effects $\mathbf{C} \in \mathbb{R}^{n_{\text{dof}}}$ and the generalized internal forces $\boldsymbol{\tau} \in \mathbb{R}^{n_{\text{dof}}}$.

According to the specific kind of problem to be solved, the connection between the forces and moments acting on a multibody system and the resulting motions can be used to investigate the dynamics of a multibody system in two fundamental ways.

For *Forward Dynamics* problems, (2.16) provides the accelerations \mathbf{a} for given \mathbf{q} , \mathbf{v} and $\boldsymbol{\tau}$:

$$\mathbf{a} = \mathbf{H}(\mathbf{q})^{-1}(\boldsymbol{\tau}(\mathbf{q}, \mathbf{v}) - \mathbf{C}(\mathbf{q}, \mathbf{v})) \quad (2.17)$$

For *Inverse Dynamics* problems, the generalized forces $\boldsymbol{\tau}$ can be computed for given generalized coordinates, velocities and accelerations \mathbf{q} , \mathbf{v} and \mathbf{a} as

$$\boldsymbol{\tau}(\mathbf{q}, \mathbf{v}) = \mathbf{H}(\mathbf{q})\mathbf{a} + \mathbf{C}(\mathbf{q}, \mathbf{v}) \quad (2.18)$$

2.2.1. Modeling of Contacts

Mechanical systems such as a walking human are in perpetually changing contact with the environment, in this case the ground, which additionally constrains the motion of the system and causes external forces acting on the system. The ground contacts occurring during human walking can be described as holonomic skleronomic constraints

$$\mathbf{g}(\mathbf{q}) = \mathbf{0} \quad (2.19)$$

For point constraints which restrict a given body point to a specific location $\mathbf{g}(\mathbf{q}) \in \mathbb{R}^3$ where the entries correspond to the x , y and z -coordinate, respectively, and $\mathbf{g}(\mathbf{q})$ represents the distance of the point from its desired position.

Introducing the vector of Lagrange multipliers $\boldsymbol{\lambda}$ and the *contact Jacobian* $\mathbf{G}(\mathbf{q}) = \frac{\partial}{\partial \mathbf{q}} \mathbf{g}(\mathbf{q})$, the equations of motion for a rigid body model subject to an external contact can be described by the *differential algebraic equation* (DAE) of differential index 3 in descriptor form

$$\mathbf{H}(\mathbf{q})\mathbf{a} + \mathbf{C}(\mathbf{q}, \mathbf{v}) = \boldsymbol{\tau}(\mathbf{q}, \mathbf{v}) + \mathbf{G}(\mathbf{q})^T \boldsymbol{\lambda} \quad (2.20a)$$

$$\mathbf{g}(\mathbf{q}) = \mathbf{0} \quad (2.20b)$$

Here, the Lagrange multipliers $\boldsymbol{\lambda}$ can be interpreted as the contact forces.

Differentiating (2.20b) twice provides the index 1 system which can be easily transformed into a first order ODE:

$$\dot{\mathbf{q}} = \mathbf{v} \quad (2.21a)$$

$$\dot{\mathbf{v}} = \mathbf{a} \quad (2.21b)$$

$$\mathbf{H}(\mathbf{q})\mathbf{a} + \mathbf{C}(\mathbf{q}, \mathbf{v}) = \boldsymbol{\tau}(\mathbf{q}, \mathbf{v}) + \mathbf{G}(\mathbf{q})^T \boldsymbol{\lambda} \quad (2.21c)$$

$$\mathbf{G}(\mathbf{q})\mathbf{a} + \dot{\mathbf{G}}(\mathbf{q})\mathbf{v} = \mathbf{0} \quad (2.21d)$$

or written as a linear system

$$\begin{pmatrix} \mathbf{H}(\mathbf{q}) & \mathbf{G}(\mathbf{q})^T \\ \mathbf{G}(\mathbf{q}) & \mathbf{0} \end{pmatrix} \begin{pmatrix} \mathbf{a} \\ -\boldsymbol{\lambda} \end{pmatrix} = \begin{pmatrix} -\mathbf{C}(\mathbf{q}, \mathbf{v}) + \boldsymbol{\tau}(\mathbf{q}, \mathbf{v}) \\ \boldsymbol{\gamma}(\mathbf{q}, \mathbf{v}) \end{pmatrix} \quad (2.22)$$

with the differential variables \mathbf{q} and \mathbf{v} , the algebraic variables \mathbf{a} and $\boldsymbol{\lambda}$ and the *contact Hessian*

$$\boldsymbol{\gamma}(\mathbf{q}, \mathbf{v}) = -\dot{\mathbf{G}}(\mathbf{q})\mathbf{v} = -\mathbf{v}^T \frac{d\mathbf{G}(\mathbf{q})}{d\mathbf{q}} \mathbf{v}. \quad (2.23)$$

For non-redundant constraints $\mathbf{g}(\mathbf{q})$ the contact Jacobian $\mathbf{G}(\mathbf{q})$ has full rank and (2.22) can be uniquely solved. In addition, the invariants of the constraints on position and velocity level have to be satisfied to ensure equivalence of (2.20) and (2.22):

$$\mathbf{g}(\mathbf{q}) = \mathbf{0} \quad (2.24)$$

$$\mathbf{G}(\mathbf{q})\dot{\mathbf{q}} = \mathbf{0} \quad (2.25)$$

These conditions are only required at the beginning of the contact since (2.21d) ensures on acceleration level that the conditions are satisfied for the rest of the contact. With numerical integration, (2.21d) can not be solved exactly leading to a drift due to accumulating errors. This drawback, which occurs particularly for large step sizes and long time horizons, can be treated using Baumgarte stabilization [11].

Different contact configurations of mechanical systems require corresponding sets of equations of motion (2.22). In an optimal control context, if the contact sequence is known, these configurations can be implemented in dedicated phases. These phases are separated by implicitly defined switching points where a switching function equals zero

$$s(t, \mathbf{q}, \mathbf{v}) = 0 \quad (2.26)$$

and discontinuities of the velocities $\Delta \mathbf{v}(t, \mathbf{q}, \mathbf{v})$ and the accelerations $\Delta \mathbf{a}(t, \mathbf{q}, \mathbf{v})$ can occur.

2.2.2. Modeling of Collision Impacts

A multibody system gaining a contact with the environment is exposed to high forces acting in a short amount of time. Due to the high forces, a physical body would compress and, depending on its physical properties, remain in contact or bounce off. The first case is called the *perfect inelastic collision* while the latter case represents the *perfect elastic collision*. For multibody systems these elasticities are often neglected and the contact gain is treated as an instantaneous collision. A restitution parameter $e \in [0, 1]$ is introduced where $e = 0$ denotes the perfect inelastic collision and $e = 1$ the perfect elastic case.

The contact gain causes a discontinuous transition from the generalized velocity \mathbf{v}^- before the collision to the generalized velocity \mathbf{v}^+ after the collision. The transition is determined by

$$\begin{pmatrix} \mathbf{H}(\mathbf{q}) & \mathbf{G}(\mathbf{q})^T \\ \mathbf{G}(\mathbf{q}) & \mathbf{0} \end{pmatrix} \begin{pmatrix} \mathbf{v}^+ \\ -\Lambda \end{pmatrix} = \begin{pmatrix} \mathbf{H}(\mathbf{q})\mathbf{v}^- \\ -e\mathbf{G}(\mathbf{q})\mathbf{v}^- \end{pmatrix} \quad (2.27)$$

where Λ denotes the contact impulse. The first line of (2.27)

$$\mathbf{H}(\mathbf{q})\mathbf{v}^+ - \mathbf{H}(\mathbf{q})\mathbf{v}^- = \mathbf{G}(\mathbf{q})^T \Lambda \quad (2.28)$$

is the change of the system's momentum caused by the collision, while the second line

$$\mathbf{G}(\mathbf{q})\mathbf{v}^+ = -e\mathbf{G}(\mathbf{q})\mathbf{v}^- \quad (2.29)$$

determines the contact velocity after the collision.

2.2.3. Efficient Computation of Equations of Motion

For modeling and efficient computation of the equations of motion for a rigid-body model we use the code library *Rigid Body Dynamics Library (RBDL)* [37] which has been developed and implemented based on the *Spatial Algebra* notation [35]. Instead of the traditional notation for rigid body dynamics using two sets of 3D vectors Spatial Algebra follows a 6D vector notation and allows for a efficient expression of rigid-body motions. The *Recursive Newton-Euler Algorithm (RNEA)* is used for the inverse dynamics, the *Composite Rigid Body Algorithm (CRBA)* for the joint space inertia matrix, and the *Articulated Body Algorithm (ABA)* for the forward dynamics computations.

2.3. Multibody Model of a Human

As mentioned before, neglecting small-scale phenomena in the course of motion during human gait, the human body can be modeled as a multibody system consisting of rigid bodies which represent the major body segments of a human connected by ideal joints.

2.3.1. Segmentation and Model Complexity

In the context of modeling human walking by means of a multibody system, it is apparent to represent the human body according to the structure of the human skeletal system. The lower body of a human can then be represented by the rigid body segments *pelvis*, *left* and *right thighs*, *left* and *right shanks* as well as *left* and *right feet* and the upper body by the segments

mid and upper trunk, left and right upper arms, left and right lower arms, left and right hands and head. These segments are connected by the joints *left and right hips, left and right knees, left and right ankles, Lumbo-Sacral joint, Xiphoid, Cervicale, left and right shoulders, left and right elbows* as well as *left and right wrists*. Figure 2.3 provides an overview over the body segments and the joints chosen in this thesis for the multibody model of the human body. According to this segmentation a multibody system is established. The 34 degrees of freedom of the model including their ranges are listed in Appendix B.

Since, during walking, the back bends only in minor ranges the complex behavior of the 24 articulating vertebrae of the spine can be reduced to four parts. Each of these parts is considered rigid and represents the anatomical regions of the spine: the *cervical, thoracic, lumbar and sacral curves*. In the multibody model, these curves are included into the body segments *head, upper trunk, mid trunk and pelvis*, respectively. The multibody model of the human body can then be build in the tree topology shown in Figure 2.3.

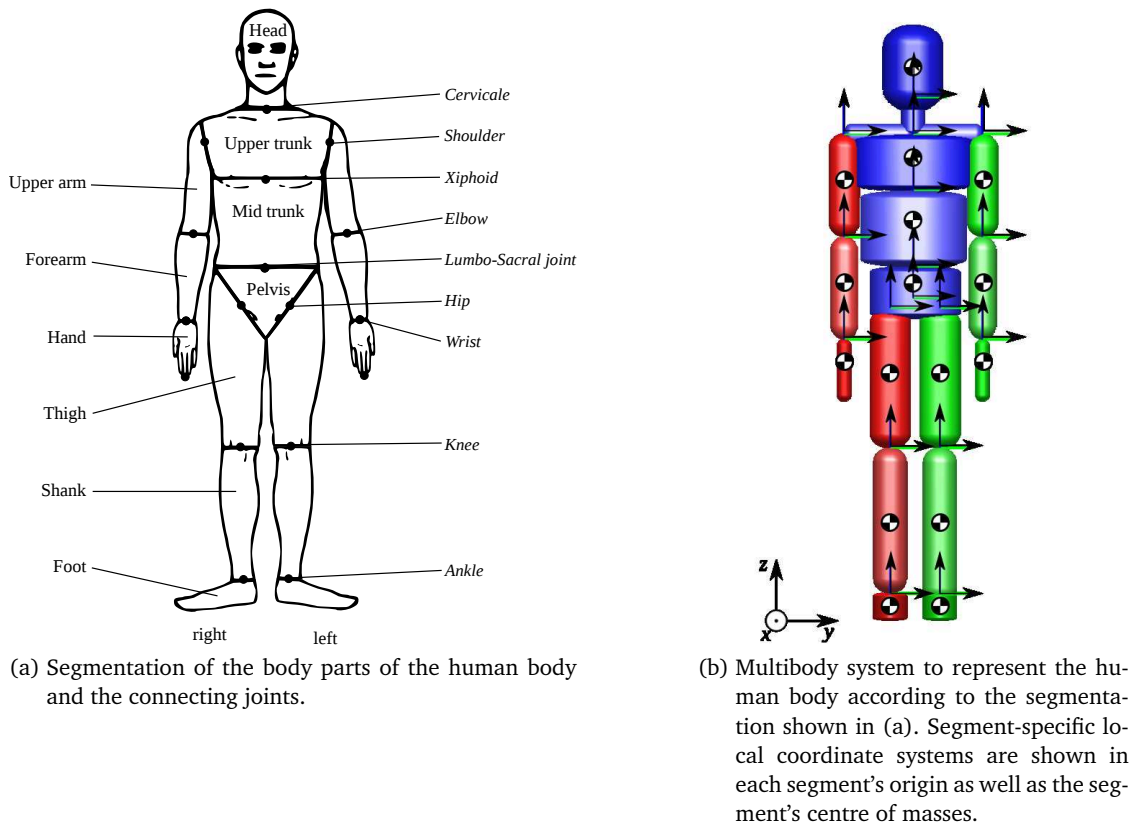


Figure 2.3: Segmentation of the human body for the modeling in terms of multibody systems.

The absolute position of the model in Euclidean space is defined by the position

$$\mathbf{r}_{0,1} = (x_{0,1}, y_{0,1}, z_{0,1})^T \quad (2.30)$$

of the root segment 1 with respect to the origin O of the global coordinate system. The absolute rotation $S_{0,1}$ of the model is then described by the elemental rotations of the three Cardan

angles θ, φ, ψ .

$$S_{O,1} = \theta_{O,1} \cdot \varphi_{O,1} \cdot \psi_{O,1} \quad (2.31)$$

where $\theta_{O,1}$, $\varphi_{O,1}$, and $\psi_{O,1}$ denote the rotations in the sagittal, frontal, and transversal plane, respectively. In order to consistently describe all kinds of human motion and exploiting the skeletal structure of the human body it is common in human motion analysis to choose the pelvis as the root segment and treat the other segments as branches in the tree topology. Subsequently, the position and rotation of the other body segments can be uniquely expressed in terms of the generalized coordinates, in this case the relative rotations of the next distal body segment with respect to its next proximal neighbor. Typical human locomotive tasks such as walking and sit-to-stand transitions consist of combinations of intersegmental rotations that mainly occur in the sagittal plane, followed by the frontal and the transversal plane. In order to prevent singularities in the definition and expression of the Cardan angles and the occurrence of the *Gimbal Lock* rotation sequences should be avoided for which the first and the third rotations are likely to be driven into a parallel configuration by the second rotation. Considering this, in case the largest motions are expected to occur in the sagittal plane, it is common to choose the rotation sequence

$$S_{i,j} = \theta_{i,i} \cdot \varphi_{i,j} \cdot \psi_{i,j} \quad (2.32)$$

to represent the rotation of the j -th body segment with respect to the i -th segment in the sagittal, frontal and transversal plane, respectively [24]. For lower limb motions these planes represent the *flexion-extension*, *abduction-adduction*, and *internal-external rotation* of the hip, knee or ankle joint.

The model establishes ground contact with the foot which, in this work, is represented by a rigid triangular segment spanned by the three contact points *Heel*, *Hallux* and *Meta5*.

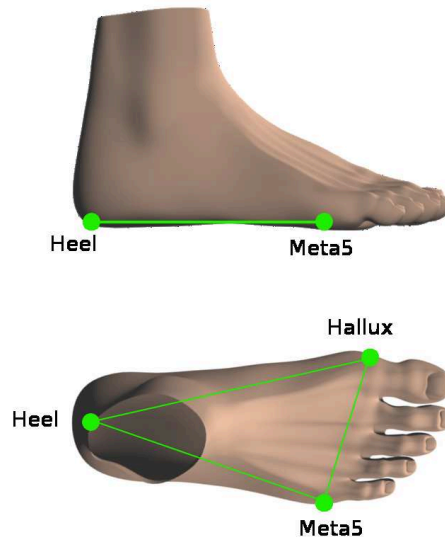


Figure 2.4: Foot model with the three contact points *Heel*, *Hallux* and *Meta5*.

2.4. Dynamic Model Parameters for Adults and Elderly Humans

The inertial parameters, center of mass positions, and body segment lengths of the multibody models representing young adult humans are determined using the regression equations provided by de Leva [29]. Adjustments are made to the reference points of the parameters for the upper body segments as they are chosen in a more practical way in the context of creating a multibody model in a tree structure with the pelvis representing the most proximal segment. The relative and absolute values for the adjusted parameters of young adult humans are summarized in the Tables A.1 - A.3 in Appendix A.

These regression equations are further adjusted to reflect the changes in proportion of the body parts of male and female humans due to aging. The relative and absolute values for the adjusted parameters of elderly humans can be found in the Tables 2.4 - 2.6.

The purpose of this part of the thesis is to compute the segment lengths, segment masses, radii of inertia, and the center of mass (COM) position for each major body segment of an elderly human (above 65 years) based on regression equations and knowledge of the full-body height and weight of the person. The distances, lengths, radii, and masses are provided as fractions of the full-body height and mass, respectively.

Due to age-related pathologies the human body parts are decreasing in length and altering the overall proportions of the body. Joint wear in the human vertebral column consisting of 24 articulating vertebrae causes the upper body to shorten by a higher amount than the lower body where only the hip, knee, and ankle joints are significantly exposed to joint degeneration. Since the arms, in contrast to the legs, do not mainly support body weight during the span of a human life-time only negligible wear and, thus, no changes in length of the joints is expected.

We derive the changes in body proportions due to aging effects from the ergonomic tables provided in [123]. In order to adapt the regression equations from [29] to the change in body proportions, the coefficients α_s are introduced enabling the separate linear scaling of the length of each body segment s . The coefficients for the length decrease in the upper body α_{up} and the lower body α_{lo} can be estimated from the tables in [123] as the ratio of the values for elderly humans and younger adults. For the length of the arms we assume $\alpha_{arm} = 1$.

Additionally, based on the tables provided in [71] we adjust the changes in mass distribution to the body segments which are caused by muscle degeneration and changes in tissue composition using the coefficients β_s . The ratio of the relative body segment masses of elderly humans [71] and younger adults [29] provides the changes in the relative mass of each segment s with respect to the full body mass. The coefficients for changes in both segment lengths and relative masses are summarized in Table 2.1.

2.4.1. Coordinate systems

The local coordinate system $x'y'z'$ of each segment is located at the joint which connects the segment with its next proximal neighbor with the *Pelvis* being the most proximal segment. The local coordinate system of the *Pelvis* originates from the middle of the connecting line between the left and right *Hip Joint Centers*. Except for the foot, the local coordinate systems of all segments are oriented such that the z' -axes are aligned with each segment's longitudinal axis and point towards the distal joint of each segment. The x' -axes point into the ventral direction and the y' -axes into the lateral direction. The length of the foot segment, however, is specified along the x' -axis and the foot height along the z' -axis.

Table 2.1: Shortening coefficients for upper and lower body α_p and mass distribution coefficients β_s for female and male subjects. These coefficients were used to derive the values in the Tables 2.4, 2.5 and 2.6.

	Symbol	Female	Male
Shortening coefficients α_p			
Upper body	α_{up}	0.9488	0.9614
Lower body	α_{lo}	0.9923	0.9793
Arm	α_{arm}	1.0000	1.0000
Mass distribution coefficients β_s			
Head	β_{head}	1.1063	0.9996
UPT	β_{upt}	1.0081	0.9079
MPT	β_{mpt}	1.1297	1.3463
Pelvis	β_{pelvis}	1.1297	1.3463
Upper arm	$\beta_{upperarm}$	1.2717	1.1872
Forearm	$\beta_{forearm}$	0.8134	1.0861
Hand	β_{hand}	0.8909	1.0713
Thigh	β_{thigh}	0.8629	0.6692
Shank	β_{shank}	0.9043	0.9868
Foot	β_{foot}	1.2207	1.0278

Table 2.2 summarizes the proximal and distal endpoints of the body segments. The proximal endpoints represent the origins of the segment-specific local coordinate systems. Figure 2.5 shows the major body segments of the human body as well as the location and orientation of the local coordinate systems of the segments *Pelvis*, *Upper Arm* and *Thigh*.

2.4.2. Regression equations

The regression equations are formulated such that the anthropometric parameters can be computed in relation to the whole-body height and mass. Furthermore, adjustment coefficients are introduced to consider for the changes in length and mass related body proportions due to age.

Segment lengths and masses

In a first step, the de Leva-tables are re-formulated as functions of the whole-body length and mass. The relative length $\lambda_{s,dL}$ of the segment s with respect to the whole-body height $l_{tot,dL}$ provided by [29] is obtained by

$$\lambda_{s,dL} = \frac{l_{s,dL}}{l_{tot,dL}} \quad (2.33)$$

In order to relate the measured body dimensions of an elderly person to the tables provided by [29], the total adult body height \tilde{l}_{tot} can be determined from the measured body height l_{tot}

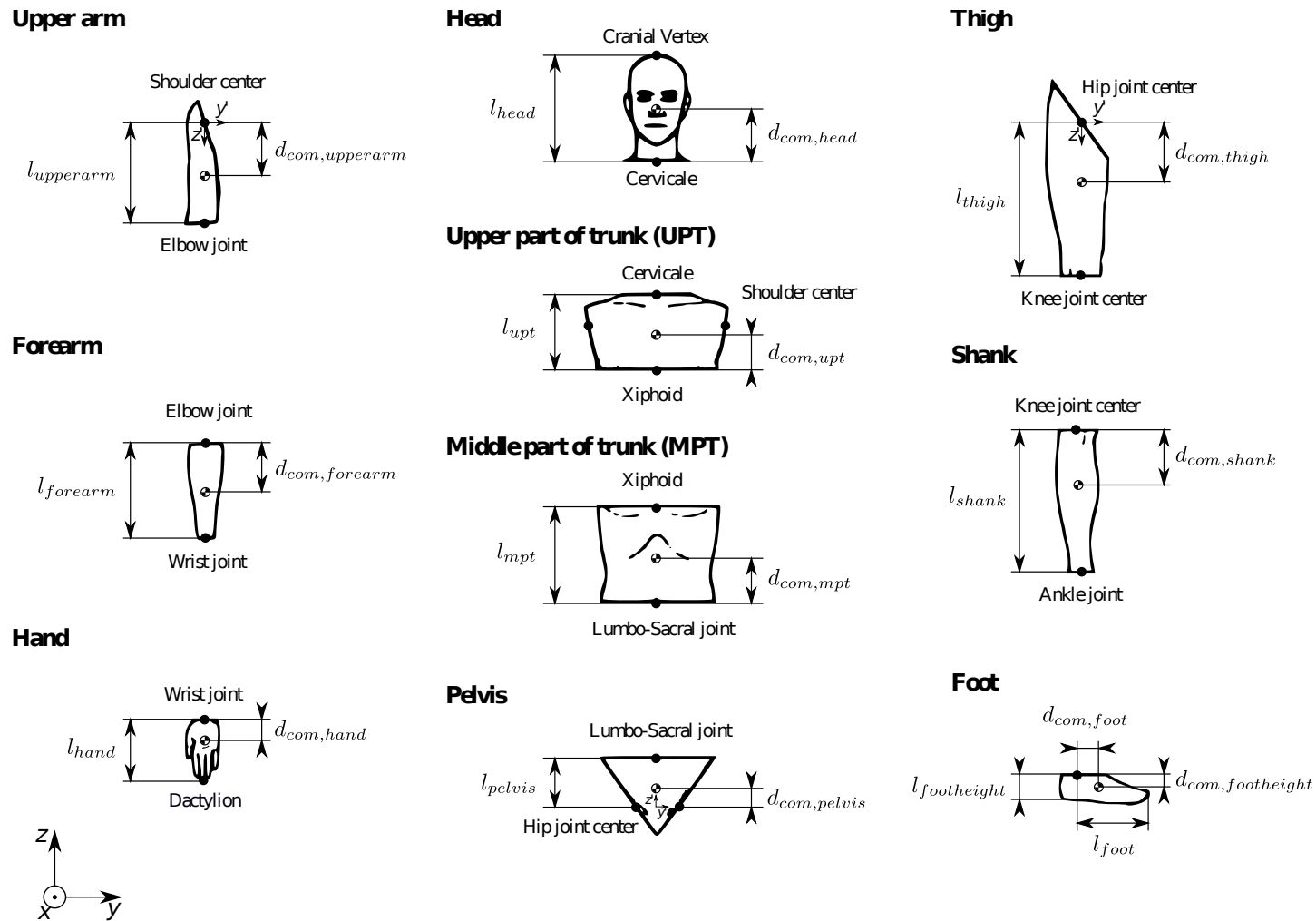


Figure 2.5: The major body segments of the human body are shown with the segment lengths l_s of each segment s as well as the center of mass locations $d_{com,s}$ assigned with respect to the origin of the segments' local coordinate systems $x'y'z'$. As shown e. g. for the Upper arm and the Thigh, the origin of the local coordinate systems are located at the joints which connect the segments with their next proximal neighbor with the Pelvis being the most proximal segment. The local coordinate system of the Pelvis originates from the middle of the connecting line between the left and right Hip Joint Centers. The local coordinate systems are oriented such that z' is aligned with the segment's longitudinal axis and y' points into the lateral direction.

Table 2.2: Proximal and distal endpoints of the body segments. The proximal endpoints are also the origins of the segments' local coordinate systems. UPT and MPT stand for Upper part of trunk and Middle part of trunk, respectively.

	Proximal endpoint	Distal endpoint
Head	Cervicale	Cranial Vertex
UPT	Xiphoid	Cervicale
MPT	Lumbo-Sacrum	Xiphoid
Pelvis	Mid-point between hip joint centers	Lumbo-Sacrum
Upper arm	Shoulder	Elbow
Forearm	Elbow	Wrist
Hand	Wrist	Dactylion
Thigh	Hip	Knee
Shank	Knee	Ankle
Foot	Ankle	Plantar surface

of the elderly subject and the segment-specific length adjustment coefficients α_s by

$$\hat{\lambda}_s = \alpha_s \cdot \lambda_{s,dL} \quad (2.34)$$

$$\tilde{l}_{tot} = \frac{l_{tot}}{\hat{\lambda}_{head} + \hat{\lambda}_{torso} + \hat{\lambda}_{pelv} + \hat{\lambda}_{leg}} \quad (2.35)$$

while only those body parts are considered that actually contribute to the full-body-height, i.e. $s \in \{Head, UPT, MPT, Pelvis, Thigh, Shank, Foot\}$.

Similarly, the adult mass \tilde{m}_{tot} of the subject can be computed from the subject's measured body mass m_{tot} and the length adjustment coefficients α_s . Additionally, the mass adjustment coefficients β_s are introduced to account for changes in mass proportions due to loss of muscle mass or changes in tissue composition

$$\hat{\mu}_s = \alpha_s \cdot \beta_s \cdot \mu_{s,dL} \quad (2.36)$$

$$\tilde{m}_{tot} = \frac{m_{tot}}{\hat{\mu}_{head} + \hat{\mu}_{torso} + \hat{\mu}_{pelv} + 2(\hat{\mu}_{leg} + \hat{\mu}_{arm})} \quad (2.37)$$

considering all body segments

$s \in \{Head, UPT, MPT, Pelvis, Upper Arm, Forearm, Hand, Thigh, Shank, Foot\}$.

The fraction of the segment masses with respect to the full body mass $\mu_{s,dL}$ are directly provided by [29]. The measured height l_{tot} and mass m_{tot} of the average of 116 elderly female subjects (F; body mass = 65.26 kg, body height = 158.6 cm) and 31 elderly male subjects (M; body mass = 74.97 kg, body height = 170.59 cm) participating at a clinical study [57] as well as the reconstructed height \tilde{l}_{tot} and mass \tilde{m}_{tot} of the subjects as younger adults are contained in Table 2.3.

The absolute values of the elderly human's actual segment lengths l_s and masses m_s are then determined by

$$l_s = \hat{\lambda}_s \cdot \tilde{l}_{tot} \quad (2.38)$$

$$m_s = \hat{\mu}_s \cdot \tilde{m}_{tot} \quad (2.39)$$

Table 2.3: Measured body height and mass of elderly female and male subjects [57] as well as the calculated adult body height and mass reconstructed using the regression equations in this paper (Section 2.4.2). These parameters were used to derive the values in the Tables 2.4, 2.5, and 2.6.

	Female	Male
no. of subjects n	116	31
Measured elderly height l_{tot} [cm]	158.60	170.59
Measured elderly mass m_{tot} [kg]	65.26	74.97
Calculated adult height \tilde{l}_{tot} [cm]	163.83	175.76
Calculated adult mass \tilde{m}_{tot} [kg]	69.49	77.51

and, eventually, the relative values λ_s and μ_s defined as

$$\lambda_s = \frac{l_s}{l_{\text{tot}}} \quad (2.40)$$

$$\mu_s = \frac{m_s}{m_{\text{tot}}} \quad (2.41)$$

These absolute and relative values are provided in the Tables 2.4 and 2.5.

Center of mass location

In [29], the relative center of mass (COM) positions $\tilde{\delta}_s$ for the upper body parts are specified with respect to their distal reference points. For the sake of consistency, we convert the COM positions $\tilde{\delta}_{\text{upperbody}}$ from the original de Leva value $\delta_{\text{upperbody,dL}}$ for each upper body segment $s \in \{\text{Head}, \text{UPT}, \text{MPT}, \text{Upper Arm}, \text{Forearm}, \text{Hand}\}$ to be specified with respect to their proximal reference points using

$$\tilde{\delta}_{\text{upperbody}} = 1 - \delta_{\text{upperbody,dL}} \quad (2.42)$$

The locations of the COM of each segment are assumed to be aligned with the principal longitudinal axes of the rigid bodies and scale linearly with the segment lengths. They are computed for the segment s as the distance from the proximal endpoint of the segment to the segment's COM as absolute values (2.43) and relative values (2.44)

$$d_{\text{com},s} = \tilde{\delta}_s \cdot l_s \quad (2.43)$$

$$\delta_s = \frac{d_{\text{com},s}}{l_{\text{tot}}} \quad (2.44)$$

where $\tilde{\delta}_s$ is taken from [29] for lower body segments and derived by (2.42) for upper body segments.

The absolute and relative values for the COM location of each segment are summarized in the Tables A.1 and A.2 in Appendix A for young adult humans and in the Tables 2.4 and 2.5 for elderly humans. For every segment s the COM is specified with respect to the origin of the segment's local coordinate system which is located at the joint that connects the segment

with its next proximal neighbor with the *Pelvis* being the most proximal one. The *Pelvis* COM is specified with respect to the middle point between the left and right hip centers.

Radii of gyration and moments of inertia

The moments of inertia with respect to the principal axes x, y and z of each segment s are given by

$$\Theta_s = \begin{pmatrix} \theta_{s,x} & 0 & 0 \\ 0 & \theta_{s,y} & 0 \\ 0 & 0 & \theta_{s,z} \end{pmatrix} \quad (2.45)$$

where each principal moment of inertia $\theta_{s,p}$, $p \in [x, y, z]$ can be expressed by its radius of gyration $r_{\text{gyr},s,p}$ as

$$\theta_{s,p} = r_{\text{gyr},s,p}^2 \cdot m_s \quad (2.46)$$

and the absolute (2.47) and relative (2.48) values for the radii of gyration can be determined by

$$r_{\text{gyr},s,p} = \varrho_{s,p,\text{dL}} \cdot l_s \quad (2.47)$$

$$\varrho_{s,p} = \frac{r_{\text{gyr},s,p}}{l_{\text{tot}}} \quad (2.48)$$

where $\varrho_{s,p,\text{dL}}$ is the de Leva value for the relative radius of gyration of the segment s with respect to the axis p . The radii of gyration $r_{\text{gyr},s,p}$ are parallel to the axes of the segments' local coordinate systems as described in Section 2.4.1 and specified with respect to each segment's COM. The radii are linearly proportional to the segment lengths l_s and according to (2.40) also to the whole-body height l_{tot} .

Equations (2.41) and (2.48) in (2.46) lead to the moments of inertia with respect to a subject's full body length l_{tot} and mass m_{tot} and, thus, (2.45) can be expressed as

$$\Theta_s = \mu_s m_{\text{tot}} l_{\text{tot}}^2 \begin{pmatrix} \varrho_{s,x}^2 & 0 & 0 \\ 0 & \varrho_{s,y}^2 & 0 \\ 0 & 0 & \varrho_{s,z}^2 \end{pmatrix} \quad (2.49)$$

Again, the values for $r_{\text{gyr},s,p}$, $\varrho_{s,p}$, and $\theta_{s,p}$ can be found in the Tables 2.4 and 2.5 and Table 2.6, respectively.

Table 2.4: Adjusted absolute values for the longitudinal lengths, masses, longitudinal center of mass (COM) position as well as the radii of inertia of the body segments of an average elderly female (F; body mass = 65.26 kg, body height = 158.6 cm, $\alpha_{up} = 0.0386$, $\alpha_{lo} = 0.0207$) and male (M; body mass = 74.97 kg, body height = 170.59 cm, $\alpha_{up} = 0.0567$, $\alpha_{lo} = 0.0077$) subject. The relative values are specified with respect to the full body height and mass, respectively. The segment lengths and COM positions are given with respect to the origin of the appropriate segment's coordinate system as described in Section 2.4.1 and displayed in Figure 2.5. The radii of inertia are specified parallel to the axes of the segments' local coordinate system and with respect to each segment's COM.

Segment	Longitudinal length l_s [mm]		Mass m_s [kg]		COM position $d_{com,s}$ [mm]		Radii of Gyration					
	F	M	F	M	F	M	Sagittal $r_{gyr,s,x}$ [mm]		Transversal $r_{gyr,s,y}$ [mm]		Longitudinal $r_{gyr,s,z}$ [mm]	
							F	M	F	M	F	M
Head	217.7	235.8	4.8	5.2	112.3	117.8	59.0	71.4	64.2	74.3	56.8	61.5
UPT	203.7	235.0	10.2	10.9	100.8	115.9	94.9	118.7	64.0	75.2	91.5	109.3
MPT	183.4	209.2	10.8	16.5	100.7	115.0	79.4	100.8	64.9	80.1	76.1	97.9
Pelvis	162.2	141.4	9.2	11.3	82.4	54.9	70.2	87.0	65.2	77.9	72.0	83.0
Upper arm	259.1	284.4	2.1	2.4	110.0	120.2	72.0	81.1	67.4	76.5	38.3	44.9
Forearm	248.9	271.5	0.7	1.3	135.4	147.3	65.0	74.9	64.0	71.9	23.4	32.9
Hand	73.5	87.0	0.3	0.5	18.6	18.3	39.2	54.7	33.4	44.6	24.6	34.9
Thigh	344.3	417.4	8.3	7.1	124.4	170.9	127.1	137.3	125.3	137.3	55.8	62.2
Shank	403.9	429.1	2.8	3.2	178.4	191.3	109.5	109.4	107.9	106.8	37.6	44.2
Foot	215.0	260.6	1.0	1.1	86.3	115.0	64.3	67.0	60.0	63.8	29.9	32.3
Foot height	70.7	38.2	-	-	35.4	19.08	-	-	-	-	-	-

Table 2.5: Adjusted relative values for the longitudinal lengths, masses, longitudinal center of mass (COM) position as well as the radii of inertia of the body segments of an average elderly female (F; body mass = 65.26 kg, body height = 158.6 cm, $\alpha_{up} = 0.0386$, $\alpha_{lo} = 0.0207$) and male (M; body mass = 74.97 kg, body height = 170.59 cm, $\alpha_{up} = 0.0567$, $\alpha_{lo} = 0.0077$) subject. The relative values are specified with respect to the full body height and mass, respectively. The segment lengths and COM positions are given with respect to the origin of the appropriate segment's coordinate system as described in Section 2.4.1 and displayed in Figure 2.5. The radii of inertia are specified parallel to the axes of the segments' local coordinate system and with respect to each segment's COM.

Segment	Longitudinal length λ_s [%]		Mass μ_s [%]		COM position δ_s [%]		Radii of Gyration					
							Sagittal $\varrho_{s,x}$ [%]		Transversal $\varrho_{s,y}$ [%]		Longitudinal $\varrho_{s,z}$ [%]	
	F	M	F	M	F	M	F	M	F	M	F	M
Head	217.7	235.8	4.8	5.2	112.3	117.8	59.0	71.4	64.2	74.3	56.8	61.5
UPT	203.7	235.0	10.2	10.9	100.8	115.9	94.9	118.7	64.0	75.2	91.5	109.3
MPT	183.4	209.2	10.8	16.5	100.7	115.0	79.4	100.8	64.9	80.1	76.1	97.9
Pelvis	162.2	141.4	9.2	11.3	82.4	54.9	70.2	87.0	65.2	77.9	72.0	83.0
Upper arm	259.1	284.4	2.1	2.4	110.0	120.2	72.0	81.1	67.4	76.5	38.3	44.9
Forearm	248.9	271.5	0.7	1.3	135.4	147.3	65.0	74.9	64.0	71.9	23.4	32.9
Hand	73.5	87.0	0.3	0.5	18.6	18.3	39.2	54.7	33.4	44.6	24.6	34.9
Thigh	344.3	417.4	8.3	7.1	124.4	170.9	127.1	137.3	125.3	137.3	55.8	62.2
Shank	403.9	429.1	2.8	3.2	178.4	191.3	109.5	109.4	107.9	106.8	37.6	44.2
Foot	215.0	260.6	1.0	1.1	86.3	115.0	64.3	67.0	60.0	63.8	29.9	32.3
Foot height	4.5	2.2	-	-	2.2	1.1	-	-	-	-	-	-

Table 2.6: Adjusted absolute values for the segments' moments of inertia of an average elderly female (F; body mass = 65.26 kg, body height = 158.6 cm) and male (M; body mass = 74.97 kg, body height = 170.59 cm) subject using the segment masses and radii of gyration from Table 2.4. The moments of inertia are specified in the local coordinate system and with respect to the COM of each segment.

Segment	Gender	Moments of Inertia [$\text{kg} \cdot \text{m}^2$]		
		θ_x	θ_y	θ_z
Head	F	0.0168	0.0199	0.0156
	M	0.0265	0.0287	0.0197
UPT	F	0.0916	0.0416	0.0850
	M	0.1530	0.0614	0.1297
MPT	F	0.0681	0.0455	0.0626
	M	0.1675	0.1058	0.1579
Pelvis	F	0.0453	0.0391	0.0477
	M	0.0853	0.0684	0.0777
Upper arm	F	0.0110	0.0096	0.0031
	M	0.0158	0.0141	0.0049
Forearm	F	0.0031	0.0030	0.0004
	M	0.0074	0.0068	0.0014
Hand	F	0.0005	0.0004	0.0002
	M	0.0015	0.0010	0.0006
Thigh	F	0.1344	0.1307	0.0259
	M	0.1340	0.1340	0.0275
Shank	F	0.0340	0.0330	0.0040
	M	0.0383	0.0366	0.0063
Foot	F	0.0042	0.0037	0.0009
	M	0.0047	0.0043	0.0011

3. OPTIMAL CONTROL FOR HUMAN MOTIONS

In the previous chapter, we described methods to model the human body in terms of a multi-body system. These models are used in this thesis in the context of optimal control computations in order to *reconstruct* and to *predict* human motions. Using the same methods, models of mobility assistive devices are established to compute *optimal mechanical design parameters*. This chapter presents the general expressions for the optimal control problems (OCPs) formulated within the scope of this thesis to solve these optimization problems considering multiple model phases (Section 3.1) and multiple-shooting discretization (Section 3.2). Application specific expressions of the OCP will be further elaborated in each relevant section in Part II.

3.1. Multi-Phase Optimal Control Problems

Due to the hybrid-dynamic, redundant and nonlinear nature of human motions multi-phase optimal control problems using the *direct multiple-shooting method* as well as the *Sequential Quadratic Programming (SQP) method* are suitable tools to solve the optimization problems in this thesis. Human gait can be decomposed into a sequence of finite disjoint phases. Each phase is characterized by a different set of ground contacts and, thus, a different set of external forces acting on the system. In addition, discontinuities might occur at phase transitions due to contact collisions. In the model formulation, external contacts are imposed on the system as model constraints (Section 2.2) and a separate constraint set is defined for each of the n_{ph} phases. During each phase, the dynamics of the model can then be expressed with the *ordinary differential equations (ODE)* described in Section 2.2:

$$\dot{\mathbf{x}} = \mathbf{f}_i(\mathbf{x}(t), \mathbf{u}(t)) \quad (3.1)$$

where $\mathbf{u}(t) \in \mathbb{R}^{n_u}$ and $i \in n_{\text{ph}}, n_{\text{ph}} \in \mathbb{N}$ is the index of the current model phase and

$$\mathbf{x}(t) = (\mathbf{q}(t), \dot{\mathbf{q}}(t))^T \in \mathbb{R}^{n_x} \quad (3.2)$$

is the differential state with the generalized states $\mathbf{q}(t) \in \mathbb{R}^{n_{\text{dof}}}$ and velocities $\dot{\mathbf{q}}(t) \in \mathbb{R}^{n_{\text{dof}}}$. For a given sequence of phases, we define a *multi-phase optimal control problem with discontinuities* as an OCP with n_{ph} phases. The time horizon $\mathcal{T} := [t_0, T] \subset \mathbb{R}$ is divided into the subintervals $\mathcal{T}_j := [\tau_{j-1}, \tau_j]$ where $j \in \mathcal{J} := \{1, \dots, n_{\text{ph}}\}$, $\tau_0 = 0$ and $\tau_{n_{\text{ph}}} = T$. This defines a constrained infinite-dimensional optimization problem

$$\min_{\mathbf{x}, \mathbf{u}, \mathbf{p}, t_1, \dots, t_{n_{\text{ph}}}} \Phi(\mathbf{x}, \mathbf{u}, \mathbf{p}) \quad (3.3a)$$

subject to:

$$\dot{\mathbf{x}}(t) = \mathbf{f}_j(\mathbf{x}(t), \mathbf{u}(t), \mathbf{p}), \quad t \in \mathcal{T}_j, \quad (3.3b)$$

$$\mathbf{x}(t_j^+) = \mathbf{h}_j(\mathbf{x}(t_j^-)), \quad j \in \mathcal{J}, \quad (3.3c)$$

$$0 \leq \mathbf{g}_j(t, \mathbf{x}(t), \mathbf{u}(t), \mathbf{p}), \quad t \in \mathcal{T}_j, \quad (3.3d)$$

$$0 = \mathbf{r}^{\text{eq}}(\mathbf{x}(0), \dots, \mathbf{x}(T), \mathbf{u}(0), \dots, \mathbf{u}(T), \mathbf{p}) \quad (3.3e)$$

$$0 \leq \mathbf{r}^{\text{ineq}}(\mathbf{x}(0), \dots, \mathbf{x}(T), \mathbf{u}(0), \dots, \mathbf{u}(T), \mathbf{p}) \quad (3.3f)$$

where the *objective function* $\Phi : \mathcal{X} \times \mathcal{U} \times \mathbb{R}^{n_p} \rightarrow \mathbb{R}$ with the set of all *dynamics trajectories* $\mathcal{X} : \mathcal{T} \rightarrow \mathbb{R}^{n_x}$ as well as the set of all *control trajectories* $\mathcal{U} : \mathcal{T} \rightarrow \mathbb{R}^{n_u}$ is minimized by determining a *piecewise continuous dynamic process* $\mathbf{x}(t) : \mathcal{T} \rightarrow \mathbb{R}^{n_x}$, *controls* $\mathbf{u}(t) : \mathcal{T} \rightarrow \mathbb{R}^{n_u}$, the *time instances for the phase transitions* $t_a, \dots, t_{n_{\text{ph}}}$, and the finite dimensional vector including the *free parameters* $\mathbf{p} \in \mathbb{R}^{n_p}$ while satisfying the *path constraints* $\mathbf{g}_i : \mathbb{R}^{n_x} \times \mathbb{R}^{n_u} \times \mathbb{R}^{n_p} \rightarrow \mathbb{R}^{n_g}$, $j \in \mathcal{J}$ as well as the *equality point constraints* $\mathbf{r}^{\text{eq}} : \mathbb{R}^{n_x} \times \mathbb{R}^{n_u} \times \mathbb{R}^{n_p} \rightarrow \mathbb{R}^{n_{re}}$ and *inequality point constraints* $\mathbf{r}^{\text{ineq}} : \mathbb{R}^{n_x} \times \mathbb{R}^{n_u} \times \mathbb{R}^{n_p} \rightarrow \mathbb{R}^{n_{ri}}$. For each of the n_{ph} model stages the dynamics of the process are described by a set of *ordinary differential equations (ODEs)* with right hand sides $\mathbf{f}_j : \mathbb{R}^{n_x} \times \mathbb{R}^{n_u} \times \mathbb{R}^{n_p} \rightarrow \mathbb{R}^{n_x}$, $j \in \mathcal{J}$. Using the *phase transition functions* $\mathbf{h}_j : \mathbb{R}^{n_x} \times \mathbb{R}^{n_p} \rightarrow \mathbb{R}^{n_x}$ from the right-side limit t_j^- of \mathcal{T}_j to the left-side limit t_j^+ of \mathcal{T}_{i+1} allows the handling of the discontinuities of $\mathbf{x}(t)$ and $\mathbf{u}(t)$ at t_j .

The *Bolza-type* objective function (3.3a) of an optimal control problem is commonly defined as

$$\Phi(\mathbf{x}(t), \mathbf{u}(t), \mathbf{p}) = \sum_{j=1}^{n_{\text{ph}}} \left(\int_0^T \Phi_{Lj}(t, \mathbf{x}(t), \mathbf{u}(t), \mathbf{p}) dt + \Phi_{Mj}(t_j, \mathbf{x}(t_j), \mathbf{p}) \right) \quad (3.4)$$

and consists of *Lagrange terms* $\Phi_{Lj} : \mathcal{T}_j \times \mathbb{R}^{n_x} \times \mathbb{R}^{n_u} \times \mathbb{R}^p \rightarrow \mathbb{R}$ which are integrated over the entire subintervals \mathcal{T}_j as well as *Mayer terms* $\Phi_{Mj} : \{t_j\} \times \mathbb{R}^{n_x} \times \mathbb{R}^p \rightarrow \mathbb{R}$ which are evaluated at the end of phase j . Lagrange terms and Mayer terms can be considered equivalent since the Lagrange terms can always be reformulated into Mayer terms and vice-versa. However, certain optimization problems suggest themselves to be formulated as either a Lagrange-type or a Mayer-type objective function.

As explained in Section 2.2, the dynamics of a multibody system with contacts is described by a set of DAEs. However, the optimal control problem is formulated based on a set of ODEs (3.3b) equivalent to the reduced index 1 DAEs (2.20) with the corresponding constraints on the initial values. The algebraic variables are computed implicitly during the integration of the equivalent set of ODEs and evaluated as constraints of the optimization problem. The phase transition equations (3.3c) determine how the differential states change between the phases. They are used to model contact collisions as instantaneous discontinuities in the differential states, e.g. occurring when the foot touches the ground. Upper and lower bounds for differential states $\mathbf{x}(t)$ and controls $\mathbf{u}(t)$ and other general path constraints are expressed using (3.3d). In addition, nonlinear point constraints necessary to express constraints such as contact forces, periodicity or end effector positions are defined in (3.3e) and (3.3f).

3.2. Direct Multiple-Shooting Method

In order to solve the optimal control problems formulated within the scope of this thesis, we use the *Direct Multiple-Shooting method* which is implemented in the software package MUSCOD-II [89] along with sophisticated integrators and SQP solvers.

3.2.1. Discretization of the Continuous Optimal Control Problem

Formulated in terms of the continuous functions $\mathbf{x}(t)$ and $\mathbf{u}(t)$, the optimal control problem (3.3) is also known as the *continuous optimal control problem*. *Direct methods* distinguish themselves from indirect methods by following the "first discretize, then optimize" approach. Hence, the continuous OCP is discretized before it is solved.

Control Discretization

In order to discretize the controls $\mathbf{u}(t)$ we define a grid on the time horizon $\mathcal{T} = [t_0, T]$ with m nodes:

$$\begin{aligned} t_0 < t_1 < \dots < t_{m-1} < t_m, \\ \mathcal{T}_j &= [t_j, t_{j+1}], \text{ for } t_m = T \text{ and } j = 1, \dots, m. \end{aligned} \quad (3.5)$$

On each subinterval \mathcal{T}_j we formulate a finite dimensional representation of the controls using base functions φ and parameters \mathbf{c}_j as

$$\begin{aligned} \mathbf{u}(t) &\approx \mathbf{u}(t, \mathbf{c}_j) = \varphi_j(t, \mathbf{c}_j), \\ \mathbf{c}_j &\in \mathbb{R}^{k_u n_u}, \\ t &\in \mathcal{T}_j = [t_j, t_{j+1}], \text{ for } j = 1, \dots, m. \end{aligned} \quad (3.6)$$

In most cases φ_j are vectors of polynomials. Since φ_j is only defined on the subinterval \mathcal{T}_j , this results in piecewise polynomial representation of \mathbf{u} . The two simplest cases are the piecewise constant discretization, where $k_u = 1$ and $\varphi_j(t, \mathbf{c}_j) = \mathbf{c}_j$ and, as shown in Figure 3.1, the piecewise linear approximation with $k_u = 2$ and the basis function

$$\varphi_j(t, \mathbf{c}_j) = \mathbf{c}_j^1 + \frac{t - t_j}{t_{j+1} - t_j} (\mathbf{c}_j^2 - \mathbf{c}_j^1), \quad \mathbf{c}_j = \begin{pmatrix} \mathbf{c}_j^1 \\ \mathbf{c}_j^2 \end{pmatrix} \in \mathbb{R}^{2n_u}. \quad (3.7)$$

Continuous piecewise linear controls are ensured by constraining the discretized optimal control problem to $\mathbf{c}_j^2 - \mathbf{c}_{j+1}^1 = 0$, i.e. by demanding that the parameter \mathbf{c} at the end point of the subinterval \mathcal{T}_j has the same value as at the start point of the subinterval \mathcal{T}_{j+1} . The discretized controls are summarized in $\mathbf{u}(t, \mathbf{c})$, where $\mathbf{c} = (\mathbf{c}_0, \dots, \mathbf{c}_{m-1})^T$ is the vector of control parameters.

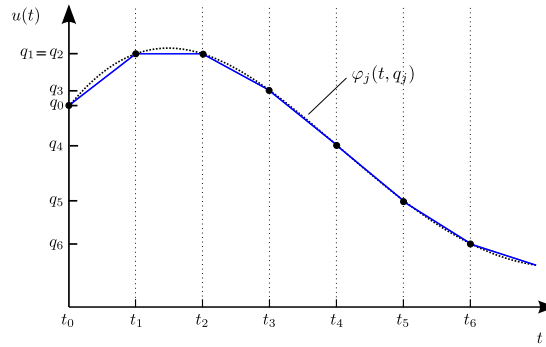


Figure 3.1: Piecewise linear control discretization of a scalar control function.

Differential State Discretization using Multiple-Shooting

The *direct multiple shooting method* is a numerical method for solving *boundary value problems (BVPs)*. Entire optimization intervals are solved by reducing them to the solution of *initial value problems (IVPs)* of several subintervals and imposing additional matching constraints between these subintervals. In contrast, the simpler *single shooting* method treats the entire integration interval of the BVP at once and varies the initial values of the integration until a trajectory is found that has the desired boundary values. However, compared to the multiple shooting

method, with the single shooting method it is difficult - if not impossible - to find a solution if the IVP solution is very sensitive to variations of the initial values.

Multiple shooting exploits the fact that the impact of the sensitivity is reduced with smaller integration intervals. The OCP is subdivided into m *multiple-shooting intervals* delimited by the $m + 1$ *multiple shooting nodes* t_0, t_1, \dots, t_m . At each node $\mathbf{s}_j \in \mathbb{R}^{n_x}$ specifies the differential states and can be used to initialize the problem according to prior knowledge about the optimal process.

In combination with (3.7), IVPs can be formulated for each of the m multiple-shooting intervals

$$\dot{\mathbf{x}} = \mathbf{f}(t, \mathbf{x}(t), \boldsymbol{\varphi}(t, \mathbf{c}_{j-1})), \text{ for } j = 1, \dots, m \text{ and } t \in \mathcal{T}_j \quad (3.8a)$$

$$\mathbf{x}(t_{j-1}) = \mathbf{s}_{j-1} \quad (3.8b)$$

The solution of the initial value problem starting at t_{j-1} with the initial value \mathbf{s}_{j-1} and discretized controls $\boldsymbol{\varphi}(t, \mathbf{c}_{j-1})$ evaluated at t can be summarized in $\boldsymbol{\xi}(t; t_{j-1}, \mathbf{s}_{j-1}, \mathbf{c}_{j-1})$. Since the values of $\boldsymbol{\xi}$ at the end point of each multiple-shooting interval do not necessarily coincide with the value of the start point of the next interval the resulting trajectories are generally not continuous (Figure 3.2). Continuity can be ensured, however, by introducing additional *continuity conditions*

$$\boldsymbol{\xi}(t_j; t_{j-1}, \mathbf{s}_{j-1}, \mathbf{c}_{j-1}) - \mathbf{s}_j = \mathbf{0} \text{ for } j = 1, \dots, m \text{ and } t \in \mathcal{T}_j \quad (3.9)$$

Summarizing the *state parameters* into $\mathbf{s} = (\mathbf{s}_0, \dots, \mathbf{s}_m)$, the continuous solution is then described by the solution of the nonlinear problem

$$\mathbf{h}(\mathbf{s}, \mathbf{c}) = \begin{pmatrix} \boldsymbol{\xi}(t_1; t_0, \mathbf{s}_0, \mathbf{c}_0) - \mathbf{s}_1 \\ \vdots \\ \boldsymbol{\xi}(t_{m-1}; t_{m-2}, \mathbf{s}_{m-2}, \mathbf{c}_{m-2}) - \mathbf{s}_{m-1} \\ \boldsymbol{\xi}(t_m; t_{m-1}, \mathbf{s}_{m-1}, \mathbf{c}_{m-1}) - \mathbf{s}_m \end{pmatrix} = \mathbf{0}. \quad (3.10)$$

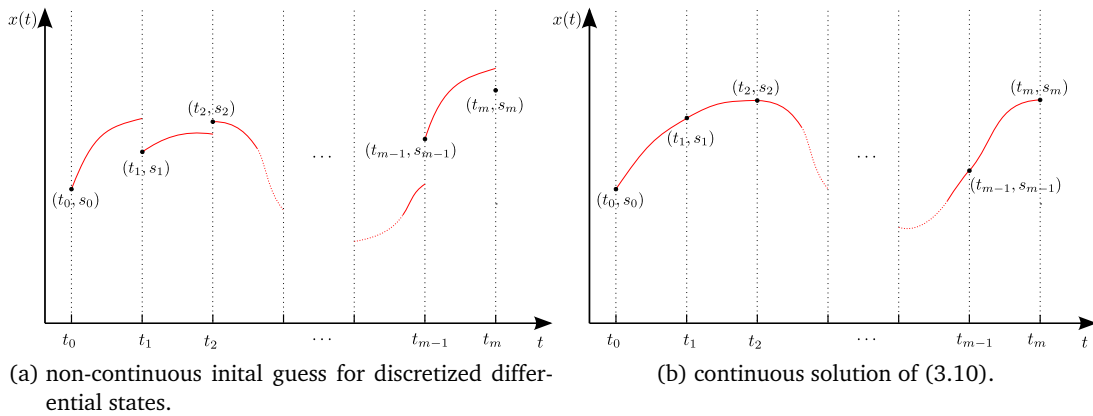


Figure 3.2: State discretization according to the multiple-shooting method.

Although it is not necessary to choose the same grid for the discretization of both the controls and the differential states, for this thesis, the same number of nodes within the subintervals is used for the discretization of states and controls for the sake of simplicity.

Constraint Discretization

In case small violations of the *path constraints* (3.3d) can be neglected, a straight-forward approach to discretize them exists in evaluating them directly on the multiple-shooting nodes while ignoring their behavior between the nodes:

$$\mathbf{g}(\mathbf{s}_j, \mathbf{c}_j) \geq \mathbf{0} \text{ for } j = 1, \dots, (m-1) \quad (3.11)$$

More precise methods which also ensure that the constraints are satisfied between the nodes are introduced in [131].

The *point constraints* (3.3e) are defined on a time grid. If the multiple-shooting grid is chosen such that the point constraint grid is a subset of it

$$\mathbf{r}(\mathbf{x}(\hat{t}_0), \dots, \mathbf{x}(\hat{t}_k)) \geq \mathbf{0}, \hat{t}_0, \dots, \hat{t}_k \in [t_0, T] \quad (3.12)$$

where

$$\{\hat{t}_0, \dots, \hat{t}_k\} \subseteq \{t_0, \dots, t_m\} \quad (3.13)$$

satisfying the point constraints can then be ensured by adjusting the state parameters $\mathbf{s}_j, j = 1, \dots, m$.

Free Parameters

In addition to the states $\mathbf{x}(t)$ and the controls $\mathbf{u}(t)$, problem specific *free parameters* $\mathbf{p} \in \mathbb{R}^{n_p}$ can be included into the optimization problem. Such parameters can consist e.g. of a desired step length, spring coefficients, geometric properties of the model or other optimizable values that remain constant for the whole time horizon. The free parameter vector \mathbf{p} is included into the optimization problem as an argument both in the objective and the constraint function.

Multiple Phases, Discontinuities and Free Phase Durations

As mentioned earlier in this chapter, some problems, such as human walking, can be divided into a fixed sequence of phases. In the context of an optimal control problem, each of these phases are formulated using a different right hand side in (3.3b).

With a total number of $m_{n_{ph}}$ multiple-shooting intervals, the first $m_j, 0 < m_j < m_{n_{ph}}, j = 1, \dots, (m-1)$ intervals are assigned to the j -th phase, the intervals $(m_j + 1), \dots, m_{j+1}, m_j < m_{j+1} < m_{n_{ph}}$ to the $(j+1)$ -th phase, and so on, until the intervals $m_{n_{ph-1}}, \dots, m_{n_{ph}}, m_{n_{ph-1}} < m_{n_{ph}}$ are assigned to phase $m_{n_{ph}}$.

To ensure continuity of the states between the phases, the continuity conditions formulated in (3.9) can be used. However, in case discontinuities between the phases are desired, e.g. to model the contact collision at touchdown of the foot, the transition between the phases is described in a dedicated infinitesimal model stage by the *phase transition function* $\sigma_j : \mathbb{R}^{n_x} \rightarrow \mathbb{R}^{n_x}$

$$\sigma_j(\xi(t_{m_j}; t_{m_{j-1}}, \mathbf{s}_{m_{j-1}}, \mathbf{c}_{m_{j-1}})) - \mathbf{s}_{m_j}, t \in [t_{m_{j-1}}, t_{m_j}], j = 1, \dots, (j-1) \quad (3.14)$$

which replaces the continuity condition (3.9).

The optimal control problem (3.3) is defined on the fixed time horizon $\mathcal{T} := [t_0, T] \subset \mathbb{R}$. However, (3.3) can also be re-formulated such that it includes *free phase durations* which are then part of the optimized variables. By introducing the duration $d = T - t_0, d \in \mathbb{R}$ and the time transformation

$$t(\tau) := t_0 + d\tau \quad (3.15)$$

the optimal control problem (3.3) can be re-written (for the sake of simplicity in a more general way) as

$$\min_{\mathbf{x}(t), \mathbf{u}(t), d} \Phi(\mathbf{x}(t(1))) \quad (3.16a)$$

subject to:

$$\dot{\mathbf{x}}(\tau) = \mathbf{f}(\mathbf{x}(t(\tau)), \mathbf{u}(t(\tau))), \quad \tau \in [0, 1], \quad (3.16b)$$

$$0 \leq \mathbf{g}(\mathbf{x}(t(\tau)), \mathbf{u}(t(\tau))), \quad t \in [0, 1], \quad (3.16c)$$

$$0 \leq \mathbf{r}^{\text{ineq}}(\mathbf{x}(t(\hat{\tau}_0)), \dots, \mathbf{x}(t(\hat{\tau}_k))), \quad \hat{\tau}_0, \dots, \hat{\tau}_k \in [0, 1]. \quad (3.16d)$$

3.2.2. Discretized Optimal Control Problem

The multiple-shooting discretization (3.10) and phase discontinuities (3.14) provide the discretized variables \mathbf{c} and \mathbf{s} , the free parameters \mathbf{p} , as well as the durations $d_1, \dots, d_{n_{\text{ph}}}$ of the n_{ph} phases which can be combined in the vector

$$\mathbf{y} = (\mathbf{s}_0, \mathbf{c}_0, \dots, \mathbf{s}_{m-1}, \mathbf{c}_{m-1}, \mathbf{s}_m, \mathbf{p}, d_1, \dots, d_{n_{\text{ph}}}). \quad (3.17)$$

Also using the discretized path constraints (3.11), the discretized optimal control problem can be written as a nonlinear program:

$$\min_{\mathbf{y}} F(\mathbf{y}) \quad (3.18a)$$

subject to:

$$\mathbf{h}(\mathbf{y}) = 0 \quad (3.18b)$$

$$\mathbf{g}(\mathbf{y}) \geq 0 \quad (3.18c)$$

with the total number of variables [88]

$$n_y = n_x(m+1) + n_u k_u m + n_p + n_{\text{ph}} \quad (3.19)$$

where $k_u \in \mathbb{N}$ depends on the chosen type of control discretization.

3.2.3. Sequential Quadratic Programming

Due to the redundant and highly nonlinear structure of the problems within this work, *Sequential Quadratic Programming (SQP)* methods are suitable to solve the discretized optimal control problems stated in (3.18). SQP arises from the application of the Newton method on the *Karush-Kuhn-Tucker (KKT) conditions* - the first-order necessary conditions for optimality of nonlinear constrained optimization problems. A detailed discussion of SQP methods can be found in [43, 114].

At first, the values of the cost function and the constraint functions as well as their gradients are evaluated for a feasible initial point. The search direction $\delta \mathbf{y}_k$ is estimated by an additional minimization of a quadratic approximation of the *Lagrangian* by a *second-order Taylor-series*

$$\min_{d \in \Omega_k} \nabla F(\mathbf{y}_k)^T \delta \mathbf{y}_k + \frac{1}{2} \delta \mathbf{y}_k^T \mathbf{H}_k \delta \mathbf{y}_k \quad (3.20)$$

subject to:

$$\mathbf{h}(\mathbf{y}_k) + \nabla \mathbf{h}(\mathbf{y}_k)^T \delta \mathbf{y}_k = 0 \quad (3.21)$$

$$\mathbf{g}(\mathbf{y}_k) + \nabla \mathbf{g}(\mathbf{y}_k)^T \delta \mathbf{y}_k \geq 0 \quad (3.22)$$

where \mathbf{H}_k is the *Hessian* of the *Lagrangian* which is initiated as the identity matrix. Using an appropriate *line search* method and considering the constraint functions the step length $\alpha_k > 0 \in \mathbb{R}$ can be estimated which, together with the step direction $\delta \mathbf{y}_k$, provides the subsequent iteration

$$\mathbf{y}_{k+1} = \mathbf{y}_k + \alpha \delta \mathbf{y}_k. \quad (3.23)$$

This procedure is iterated until a termination criterion is satisfied or the cost function has been sufficiently minimized. As long as the termination criterion has not been met, \mathbf{H}_k is updated according to its increasing convergence towards the true Hessian using so-called *Quasi-Newton methods* before the search direction is estimated in the next iteration. For the optimal control problems discussed in this thesis the *Broyden-Fletcher-Goldfarb-Shanno (BFGS)* algorithm has been used to update \mathbf{H}_k .

Due to the direct multiple-shooting approach, the approximate Hessians \mathbf{H}_k and the Jacobians $\nabla \mathbf{h}(\mathbf{y}_k)$ and $\nabla \mathbf{g}(\mathbf{y}_k)$ are sparse and highly structured. These structures can be exploited to remove the sparsities caused by the additional variables introduced by multiple-shooting and transform the quadratic problem into a dense one with a greatly reduced size using *Condensing* algorithms [17]. Standard QP solvers such as QPOPT [44] can be used to solve the condensed quadratic problem.

4. STABILITY CRITERIA FOR HUMAN LOCOMOTION

One of the main motivations of this thesis is to describe human movement related to balance and stability in both healthy and pathological walking. Walking on two legs in an erect pose enables for fast, efficient and versatile locomotion. However, walking is a highly complex, well-coordinated and, yet, instable motion which is prone to failure in case of unexpected events. Tripping over an object lying in the way of a walker, placing the foot at a wrong position or touching the ground out of time can lead to fall even at very low walking speeds. It seems that a certain amount of insecurity is risked in favor of a rapid and energy efficient progression.

In order to understand the walking motion of humans, i.e. where and when the swing foot is placed at the next step, it helps to make use of an analogy which compares walking with a recurring well-controlled falling motion followed by a well-timed and well-placed capture motion performed by the swing foot. Both the research community working on humanoid robots as well as the human movement sciences have been facing the problems of *fall detection* and *push recovery* for a long time and have already developed intuitive and straight-forward measures for stability and balance behavior of legged walking systems in occurrence of a sudden perturbation [45, 69, 132, 154]. Some effort has been conducted to establish criteria that describe gait stability as generalized as possible to enable legged robots to walk over uneven ground [33, 157, 160]. Eventually, predicting the stability and balance behavior in human walking motions enables advances in the fields of *fall prevention*, *gait classification* and *movement therapy* for elderly people.

The Chapters 2 and 3 provided the frameworks required to perform physiologically consistent simulation of human motions considering the dynamics of the system throughout the entire time horizon. We simulate human walking and analyze the motion for potential strategies to maintain stability while walking smoothly. In this Chapter we define basic definitions for stability (Section 4.1) and introduce stability of dynamic systems in the sense of *Lyapunov* (Section 4.2). We present ground reference points commonly used in the context of bipedal gait (Section 4.3) with a particular focus on the *Capture Point* (Section 4.3.4). Finally, we elaborate on the implications of these criteria on human motions in general and on human walking in particular (Section 4.4).

4.1. Basic Definitions for Stability Analysis

Describing *stability* in human walking involves the evaluation of a subject's motion. Definitions for *fall* and *stability* are provided in this chapter to enable a consistent discussion within the scope of this thesis.

Definition 1 (Fall)

Consider a legged locomotion system in a standing position or during walking. This system has fallen if its velocity equals zero and it is in contact with the ground with a set of points which is not a subset of the foot contact points.

Definition 2 (Stability)

Consider a legged locomotion system in a standing position or during walking subject to a set of initial conditions. This system is stable if it is able to maintain its intended motion over a finite time period without falling also after small external perturbations.

The meaning of the term *stability* in more general terms also considering the concepts of *robustness*, *constancy*, and *resilience* is discussed in [56].

The discussion on stability of legged-systems strongly relies on the description of the behavior of reference points into which certain whole body properties are united. A widely used reference is given by the *full body center of mass (full body COM)* which can be computed as the weighted sum of the *segment centers of masses (segment COM)*. Since, for the relevant research questions, one mainly talks about full body phenomena, the full body COM is simply expressed as the *center of mass (COM)*.

As described in Section 1.2, human walking is a balanced motion in which the limbs are swung in an antiphased manner. Due to that behavior, for natural human motions performed in an erect pose, the effective COM does not change significantly and can be assumed to maintain its position close to the pelvis center. However, the COM does significantly move away from the pelvis center in non-erect poses such as sitting, crouching, etc. and can be computed as the sum of the n segment COMs weighted by the segment masses $m_{\text{seg},i}$

$$\mathbf{r}_{\text{com}} = \frac{\sum_{i=1}^n m_{\text{seg},i} \mathbf{r}_{\text{scom},i}}{\sum_{i=1}^n m_{\text{seg},i}} \quad (4.1)$$

where the position $\mathbf{r}_{\text{scom},i}$ of the segment COM of the i -th segment can be estimated using the methods described in Section 2.4. A comparison of different popular COM approximation methods for simulating humanoid walking is included in Appendix 5.3.3.

The area of pressure forces applied by the foot in contact with the ground can be summarized in one resultant force vector which emanates from the point where the resultant moment vanishes, the *Center of Pressure (CoP)* [135]. Considering the normal vector \mathbf{n} of the contact surface and assuming the strictly unilateral contact forces \mathbf{f}_c and moments $\boldsymbol{\tau}_c$ are known, the CoP can be computed as

$$\mathbf{r}_{\text{cop}} = \frac{\mathbf{n} \times \boldsymbol{\tau}_c}{\mathbf{f}_c \mathbf{n}} \quad (4.2)$$

Stability criteria are mainly formulated based on the behavior of a reference point with respect to the *Base of Support (BoS)* which is defined as the convex hull spanned by all ground contact points. In the single stance phase, the BoS corresponds to the actual footprint of the stance foot. During double stance or other contact scenarios the BoS is the convex hull of the two or more discrete contact areas.

4.2. Stability of Dynamic Systems

In the sense of Lyapunov, a solution $\mathbf{x}_0(t)$ of a n -dimensional system of non-autonomous differential equations

$$\dot{\mathbf{x}} = f(t, \mathbf{x}(t)) \quad (4.3)$$

- (i) is stable, if for each $\epsilon > 0 \exists \delta > 0$ such that all solutions $\mathbf{x}_1(t)$ with $|\mathbf{x}_1(t_0) - \mathbf{x}_0(t_0)| < \delta$ satisfy $|\mathbf{x}_1(t) - \mathbf{x}_0(t)| < \epsilon \forall t \geq t_0$

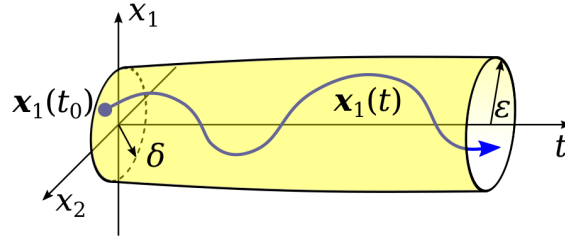


Figure 4.1: Stability in the sense of Lyapunov.

(ii) is asymptotically stable, if it satisfies (i) and additionally

$$\lim_{t \rightarrow \infty} |x_1(t) - x_0(t)| = 0$$

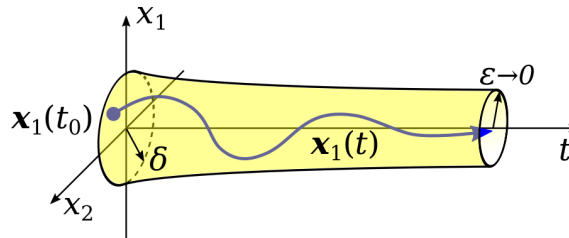


Figure 4.2: Asymptotic stability in the sense of Lyapunov.

Considering the repetitive motions during locomotion including both continuous and discontinuous dynamics, a walking legged system can be regarded as a hybrid dynamical nonlinear system performing periodic motions. In this context, stable bipedal gait can be expressed mathematically in terms of Lyapunov's first method as a periodic limit cycle of the system [65, 101] and the following theorem can be applied to describe the *stability of periodic solutions of non-autonomous systems* [101]:

Theorem 1 (Stability of periodic solutions of non-autonomous systems)

Given a non-autonomous T -periodic nonlinear system $\dot{x} = f(t, x(t))$ with $f(t + T, \cdot) = f(t, \cdot)$ and $f \in C^2$. In case the periodic solution $x_p(t) = x_p(t + T)$, $T \neq 0$ exists, its variational equation relative to $x_p(t)$ is given by

$$\Delta \dot{x} = \frac{\partial f}{\partial x}(t, x_p) \Delta x + h(t, \Delta x) \quad (4.4)$$

where it is assumed that

$$\lim_{\|\Delta x\| \rightarrow 0} \frac{\|h(t, \Delta x)\|}{\|\Delta x\|} = 0 \quad (4.5)$$

The periodic solution $x_p(t)$ is asymptotically stable if $|\lambda_i| < 1$ for all eigenvalues λ_i of the monodromy matrix

$$M(t, t + T) = \frac{\partial x(t + T)}{\partial x(t)}. \quad (4.6)$$

The Lyapunov criterion provides an elegant formulation for the stability analysis of dynamic systems. In fact, several solutions have been found for self-stabilizing open-loop motions like

hopping and running based on simple models [102, 106]. It has been used to design bipedal walking systems such as passive-dynamic walkers [27, 28, 51, 52]. However, due to several reasons it does not qualify as a suitable method for the stability analysis of individual humans conducted in the present thesis. First of all, a dynamic model (4.3) that adequately represents the full body kinematics during human motions would require equations that describe at least the most significant feedback loops which enable changes in human behavior due to perturbations and other unforeseen events. To this date, such equations are unknown [20]. Secondly, the methods proposed within the scope of this thesis to assess the human walking motion are supposed to provide reliable predictions with minimal computational effort in order to persist in a clinical routine. Unfortunately, the Lyapunov criteria are too complex in both modeling and computation to meet this requirement. Lastly, as will be shown in Section 5.3, the class of human motions analyzed in this thesis cannot be considered periodic which, however, is a condition in Theorem 1.

4.3. Ground reference points in bipedal locomotion

Ground reference points provide a clear and intuitive description of motion characteristics and control behavior in two-legged locomotion. The locations, directions of progression and velocities of the reference points with respect to each other can be interpreted in terms of whole-body movement and exploited as measures for the stability and balance state of the whole system. Various of such reference points have been proposed within both the biomechanics as well as the humanoid robotics research community. This thesis summarizes some of the most important reference points.

4.3.1. Center of Mass Projection

The balance state of entirely static poses and quasi-static motions in which neither any velocity nor any acceleration is involved at all or only to a negligible extent can be described by the vertical projection of the Center of Mass to the ground (*gCOM*) and its location with respect to the *Base of Support (BoS)*. Assuming neither external forces nor any accelerations due to movement, the Newton-Euler equations of the inverted pendulum model with respect to an arbitrary reference point \mathbf{O} can be expressed as

$$\mathbf{f}_{\text{cop}} - m\mathbf{g} = 0 \quad (4.7)$$

$$\mathbf{r}_{\text{com}} \times m\mathbf{g} - \mathbf{r}_{\text{cop}} \times \mathbf{f}_{\text{cop}} = 0 \quad (4.8)$$

The balance of forces (4.7) shows that, in case of static balance, the reaction forces are entirely vertical, since $m\mathbf{g}$ has no vertical component and $\mathbf{f}_{\text{cop}} = m\mathbf{g}$. Since $\mathbf{r}_{\text{com}} \neq \mathbf{r}_{\text{cop}}$, the balance of moments (4.8) can only be fulfilled if \mathbf{f}_{cop} and $m\mathbf{g}$ are collinear. Hence, in the static balance scenario, the CoP is the projection of the COM on the ground. By definition, the CoP exists only within or on the border of the BoS. Therefore, static balance exists as long as the *gCOM* is within or on the border of the BoS.

The balance condition related to the *gCOM* is intuitive and easy to validate. However, it is insufficient to characterize dynamic motions where balance can still be maintained with the *gCOM* outside the BoS. Approaches to quantify balance and stability in dynamic motions also account for the velocity of the COM and/or the whole-body angular momentum about the COM.

4.3.2. Zero Moment Point

The *Zero Moment Point (ZMP)* is defined as the point on the ground where the component of the inertia-gravitational moment tangential to the support surface vanishes [135]. The ZMP has been widely used in balancing biped robots and controlling their behavior such as foot placement etc. [45, 154]. The ZMP is located at the intersection of the axis of application of the inertia-gravitational moment τ^{ig} and the ground for which the axis is parallel to the surface normal. Also considering the dynamic case, i.e. acceleration of the COM and angular momentum about the COM, the ZMP can be written as

$$\tau_{\text{zmp}}^{\text{ig}} = (\mathbf{r}_{\text{com}} - \mathbf{r}_{\text{zmp}}) \times m\mathbf{g} - (\mathbf{r}_{\text{com}} - \mathbf{r}_{\text{zmp}}) \times m\mathbf{a}_{\text{com}} - \dot{\mathbf{H}}_{\text{com}} \quad (4.9a)$$

$$\tau_{\text{zmp}}^{\text{ig}} \times \mathbf{n} = 0 \quad (4.9b)$$

and its location on level ground computed as

$$\mathbf{r}_{\text{zmp}} = \frac{m\mathbf{g}\mathbf{z} \times \mathbf{r}_{\text{com}} \times \mathbf{z} + \mathbf{z} \times \dot{\mathbf{H}}}{m\mathbf{g} + m\mathbf{a}_{\text{com}} \cdot \mathbf{z}} \quad (4.10)$$

It has also been shown in [135] that the CoP and ZMP coincide where the CoP is associated with contact forces and the ZMP with inertia-gravitational forces. A dynamic legged locomotion system is considered in balance if the ZMP is inside the BoS.

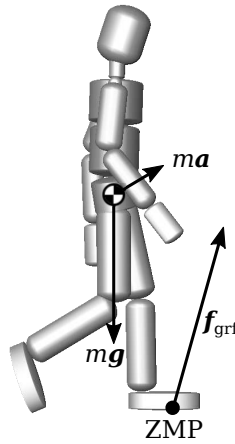


Figure 4.3: Location of Zero Moment Point.

4.3.3. Centroidal Moment Pivot, Foot Rotation Indicator, Zero Rate of Angular Momentum

Other ground reference points have been proposed to enable discussion about different phenomena in human walking also considering dynamic behavior and non-zero moments [129].

The *Centroidal Moment Pivot (CMP)* has been proposed around the same time by [46] and [128] to quantify the whole-body rotational dynamics around both horizontal axes. It can be constructed by a parallel translation of the action line of the ground reaction force \mathbf{f}_{grf} such that

it passes through the COM. The intersection point of this translated line and the ground is defined as the CMP

$$(\mathbf{r}_{\text{cmp}} - \mathbf{r}_{\text{com}}) \times \mathbf{f}_{\text{grf}} = 0 \quad (4.11a)$$

$$r_{\text{cmp},z} = 0 \quad (4.11b)$$

The location of the CMP can then be computed by expanding the cross product

$$r_{\text{cmp},x} = r_{\text{com},x} - \frac{f_{\text{grf},x}}{f_{\text{grf},z}} r_{\text{com},z} \quad (4.12a)$$

$$r_{\text{cmp},y} = r_{\text{com},y} - \frac{f_{\text{grf},y}}{f_{\text{grf},z}} r_{\text{com},z} \quad (4.12b)$$

or in terms of the ZMP location using (4.10)

$$r_{\text{cmp},x} = r_{\text{zmp},x} + \frac{\tau_{\text{com},y}}{f_{\text{grf},z}} \quad (4.13a)$$

$$r_{\text{cmp},y} = r_{\text{zmp},y} - \frac{\tau_{\text{com},x}}{f_{\text{grf},z}} \quad (4.13b)$$

One can see by (4.13) that if the CMP and ZMP coincide the line of application of \mathbf{f}_{grf} passes right through the COM indicating rotational equilibrium of the body. In contrast, it indicates an increasing non-zero whole-body angular momentum the further it moves away from the ZMP, refer also to Figure 4.4.

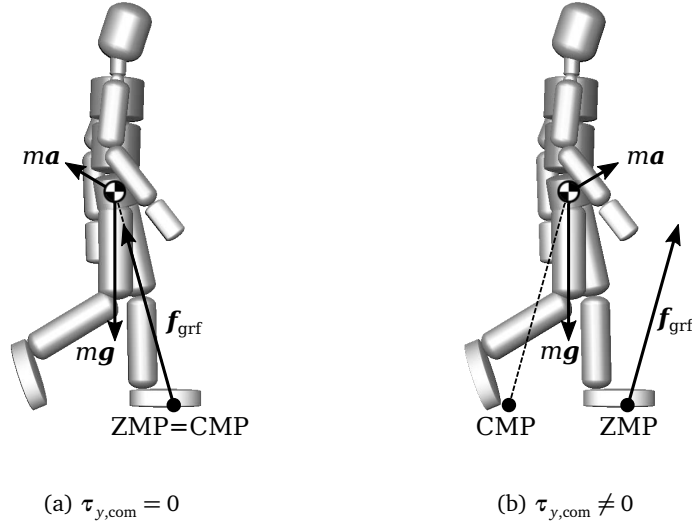


Figure 4.4: Centroidal Moment Pivot in case of (a) $\tau_{y,\text{com}} = 0$ and in case of (b) $\dot{\tau}_{y,\text{com}} \neq 0$.

4.3.4. Capture Point

Further approaches towards the quantification and control of balance and stability are motivated by the presence of unexpected loss of balance, e.g. when a sudden perturbation occurs. The so-called *push recovery* problem led to the introduction of the *Extrapolated Center of Mass (xCoM)* [69] as well as, at the same time, of the *Capturability* concept and the herein proposed *Capture Point (CaP)* [132]. Both rely on the inverted pendulum model and the linear inverted pendulum model, respectively, to represent whole-body dynamics of the legged system. The xCoM and the CaP describe the same quantity.

Inverted Pendulum Model

Meaningful knowledge about the full body dynamics of a legged locomotion system can often be obtained based on strongly simplified models of the system. Considering human walking and in particular the balance and stability behavior the *Inverted Pendulum Model* [74] has been widely used in the past [33, 69, 83, 132].

In the single support phase, when one foot maintains ground contact and the opposite leg swings forward, the dynamics of the human walker supported by the stance leg can be approximated by a single inverted pendulum composed of a mass point representing the full body center of mass of the human and a massless telescopic link with constant length. The pivot point of the inverted pendulum represents the ankle joint of the stance leg. In an even more abstract manner, the link length of the *Linear Inverted Pendulum Model* changes such that the vertical position of the mass point stays constant. Refer to Figure 4.5 for a comparison of both models.

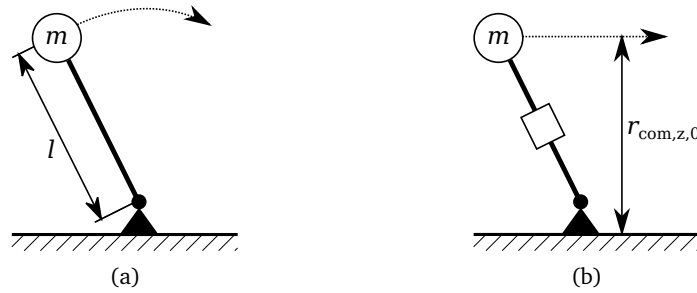


Figure 4.5: Representation of (a) an Inverted Pendulum Model (IPM) with the pendulum length l and (b) a Linear Inverted Pendulum Model (LIPM) with the mass point height $r_{\text{com},z,0} = \text{const.}$

The dynamics of an inverted pendulum can be expressed by *Euler's equation*

$$\sum \tau = I\alpha \quad (4.14)$$

With the inertia of the inverted pendulum

$$I = ml^2 \quad (4.15)$$

for the pendulum length l and the point mass m as well as the gCOM-position \mathbf{r}_{gcom} , its motion parallel to the xy -plane $\mathbf{r}_{\text{gcom},xy}$ as well as the CoP-position \mathbf{r}_{cop} we receive for small tilt

angles α [160]

$$(\mathbf{r}_{\text{cop}} - \mathbf{r}_{\text{gcom}})mg = I\alpha \approx -ml^2 \frac{\ddot{\mathbf{r}}_{\text{gcom},xy}}{l} \quad (4.16)$$

Introducing the *angular eigenfrequency* of a simple-pendulum $\omega_0 = \sqrt{g/l}$, (4.16) can be simplified to

$$(\mathbf{r}_{\text{cop}} - \mathbf{r}_{\text{gcom}}) = -\frac{\ddot{\mathbf{r}}_{\text{gcom}}}{\omega_0^2} \quad (4.17)$$

or as the dynamics of the gCOM location

$$\ddot{\mathbf{r}}_{\text{gcom}} = \omega_0^2(\mathbf{r}_{\text{gcom}} - \mathbf{r}_{\text{cop}}). \quad (4.18)$$

The gCOM accelerates backward if it is located behind the CoP and forward if its position is in front of the CoP. It will remain in balance if it coincides with the CoP, which is also in accordance with the definition of the static balance provided in section 4.3.1.

Introducing the initial COM position $\mathbf{r}_{\text{com},0}$ as well as its initial velocity $\mathbf{v}_{\text{com},0}$ and assuming a constant \mathbf{r}_{cop} solving (4.18) provides [149]

$$\mathbf{r}_{\text{com}}(t) = (\mathbf{r}_{\text{com},0} - \mathbf{r}_{\text{cop}}) \cosh(\omega_0 t) + \frac{\mathbf{v}_{\text{com},0}}{\omega_0} \sinh(\omega_0 t) \quad (4.19)$$

Referring to the interpretation of (4.18) and considering the initial velocity $\mathbf{v}_{\text{com},0}$, stability can be maintained, i.e. balance re-gained after perturbations, if $\mathbf{r}_{\text{com},0} \leq \mathbf{r}_{\text{cop}}$ at all time instances or with (4.19)

$$\mathbf{r}_{\text{cop}} - \mathbf{r}_{\text{com},0} \geq \frac{\mathbf{v}_{\text{com},0}}{\omega_0} \tanh(\omega_0 t) \quad (4.20)$$

and since $-1 < \tanh(\omega_0 t) < 1 \forall t$

$$\mathbf{r}_{\text{com},0} + \frac{\mathbf{v}_{\text{com},0}}{\omega_0} \leq \mathbf{r}_{\text{cop}} \quad (4.21)$$

where [69]

$$\mathbf{r}_{\text{xcom}} = \mathbf{r}_{\text{com}} + \frac{\mathbf{v}_{\text{com}}}{\omega_0} \quad (4.22)$$

Since the CoP is only defined within the BoS (see section 4.3.1), the condition (4.21) can be formulated as

Definition 3 (Extrapolated Center of Mass Stability)

Consider a legged locomotion system in a standing position and an initial velocity \mathbf{v}_0 acting on the center of mass. Stability can be maintained if the Extrapolated Center of Mass does not exceed the base of support at any considered time instance.

Theoretically, this can only be achieved if $\mathbf{v}_{\text{com},0}$ is sufficiently small. In case $\mathbf{v}_{\text{com},0}$ is too large to fulfill (4.21), balance maintaining actions need to be applied such as the ankle strategy which shifts the CoP in front of the xCoM fast enough by applying positive torque on the ankle. If the ankle torque is not sufficient to capture the xCoM in time, it will travel beyond the BoS and balance is lost.

The xCoM concept also provides an intuitive measure for dynamical stability [69]. The *margin of stability* can be defined as the Euclidean distance between the xCoM and the border of the BoS in the direction of travel of the xCoM

$$b = |\mathbf{r}_{\text{cop,max}} - \mathbf{r}_{\text{xcom}}| \quad (4.23)$$

Alternatively, the *maximum impulse allowed to maintain stability* $m\Delta\mathbf{v}$ has been proposed which evaluates the additional velocity $\Delta\mathbf{v} = \omega_0 b$ allowed to capture the xCoM right at the border of the BoS.

Equation (4.18) has been derived assuming small tilt angles α . This assumption is valid in case of standing where the COM of the legged system does not translate far distances. However, the same assumption is not *per se* valid for larger displacements which occur during walking or recovering from a push using multiple steps. In human walking motions, the vertical displacement of the COM is typically rather small compared to the horizontal displacement.

Linear Inverted Pendulum Model

This motivates the introduction of the *Linear Inverted Pendulum Model (LIPM)* [72, 74] illustrated in Figure 4.6, which further restricts the motion of the inverted pendulum's point mass to a constant vertical component $z_{\text{com},0}$ realized by an actuated telescopic pendulum leg and an actuation force \mathbf{f}_{lipm} which keeps the motion of the point mass in that constant plane parallel to the xy -plane. This assumption facilitates the computation of the dynamics because of its linear dynamic equations.

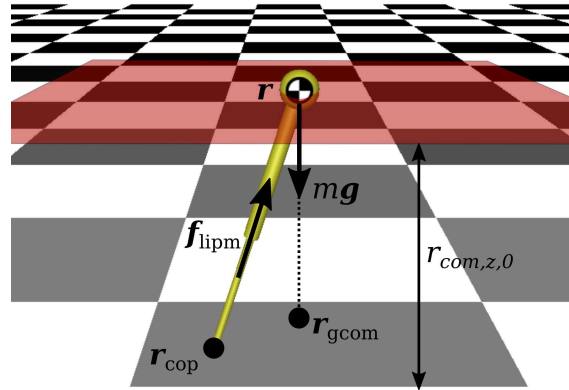


Figure 4.6: Three-dimensional Linear Inverted Pendulum Model with mass point m and linear force \mathbf{f}_{lipm} which keeps the mass point on the constant height $z_{\text{com},0}$. The position of the ankle is denoted with \mathbf{r}_{cop} . The projection of the mass point's position \mathbf{r} on the ground provides \mathbf{r}_{gcom} .

Considering this assumption, the LIPM possesses the same dynamical properties as the Inverted Pendulum model for small tilt angles from (4.18), refer to [74].

$$\ddot{\mathbf{r}}_{\text{com}} = \omega_0^2(\mathbf{r}_{\text{gcom}} - \mathbf{r}_{\text{cop}}) \quad (4.24)$$

with the only difference that, due to the variable leg length l , the eigenfrequency of the pen-

dulum is defined by means of $r_{\text{com},z,0}$

$$\omega_0 = \sqrt{\frac{g}{r_{\text{com},z,0}}} \quad (4.25)$$

The same quantity as the xCoM has been proposed and named the *(Instantaneous) Capture Point (ICaP)* [83]. However, the *Capturability* concept goes beyond the scope of the xCoM [69] and also addresses the case when the xCoM, or in this case, the (Instantaneous) Capture Point exceeds the BoS [132]. Capturability expresses the ability of a legged system to recover from a sudden push and to come to a complete stop after an appropriate foot placement considering the legged system's dynamics and actuation limits. The concept has also been extended to cover *N-Step Capturability* where the Capture Point moves away so fast that it cannot be reached with one step anymore but only after N steps.

A captured state of a legged system is defined as a state where it is in balance and its kinetic energy equals zero after an internal or external perturbation. Accordingly, Capturability is provided if the same legged system subject to a non-zero initial velocity \mathbf{v}_0 is able to reach a captured state without falling.

Definition 4 (Instantaneous Capture Point)

Given a legged system with the initial velocity \mathbf{v}_0 , the Instantaneous Capture Point (ICaP) is the ground reference point where the legged system could instantaneously place its Center of Pressure (CoP) upon to achieve a captured state.

The Instantaneous Capture Point neglects the physiological limits of the legged system and since it is derived from only the position and velocity of the COM it has a continuous trajectory. In reality, however, the ICaP cannot always be reached. In the time instances right after a step has been taken, the swing foot requires some time to be located towards the ICaP. On the other hand, the swing foot might have been brought forward too slowly and the ICaP has moved too far to be reached by a single step. Considering the minimum step duration as well as the maximum step length, there is only a finite time horizon in which the ICaP can be reached by the legged-system. It is only in these time instances in which the actual Capture Point exists. During its existence its location equals the ICaP location.

Definition 5 (Capture Point)

The Capture Point corresponds to the ICaP at time instances equal or greater than the time to place the CoP on the ICaP and at distances that are less or equal the maximum step length.

The computation of the (Instantaneous) Capture Point assumes on the *Orbital Energy* of the Linear Inverted Pendulum Model [73, 83, 133]. The three-dimensional orbital energy of the system is a conserved quantity which can be derived by interpreting the horizontal components of (4.24) as two decoupled mass-spring systems with unit mass. Also assuming zero torque at the ankle, we obtain the orbital energy E_{lip} of the legged-system by integrating (4.24)

$$E_{\text{lip},x} = \frac{1}{2}\dot{r}_{\text{com},x}^2 - \frac{1}{2}(r_{\text{com},x} - r_{\text{cop},x})^2\omega_0^2 \quad (4.26a)$$

$$E_{\text{lip},y} = \frac{1}{2}\dot{r}_{\text{com},y}^2 - \frac{1}{2}(r_{\text{com},y} - r_{\text{cop},y})^2\omega_0^2 \quad (4.26b)$$

where the term on the right resembles the potential energy of a spring with a stiffness of $c = -\omega_0^2$. Physically, the spring stiffness has to be negative in order to maintain the COM

at a constant height. Since the vertical component of the force $f_{lipm,z}$ generated by the leg is constant, the horizontal components $f_{lipm,x}$ and $f_{lipm,y}$ must be greater the greater the leg angle with respect to the vertical.

The sign of the orbital energy determines three fundamental cases of the behavior of the linear inverted pendulum. When the point mass moves towards the pendulum's pivot point in x -direction:

1. $E_{lip,x} > 0$: The point mass position $r_{com,x}$ approaches the pivot point position $r_{cop,x}$, passes over it and accelerates away from it in the same direction.
2. $E_{lip,x} < 0$: The point mass position $r_{com,x}$ approaches the pivot point position $r_{cop,x}$, does not reach it and returns in the opposite direction.
3. $E_{lip,x} = 0$: The point mass position $r_{com,x}$ approaches the pivot point position $r_{cop,x}$ and comes to a rest right above it.

The dynamical system (4.26a) has two eigenvectors defined by the equilibrium state $E_{lip,x} = 0$:

$$\dot{r}_{com,x,equi,1,2} = \pm r_{com,x} \omega_0 \quad (4.27)$$

which represent a saddle point with one stable ($r_{com,x}$ approaches $r_{cop,x}$) and one unstable ($r_{com,x}$ diverges from $r_{cop,x}$) eigenvector. Choosing the stable eigenvector and including the location of the pendulum's pivot point r_{cop} , we obtain the location of the Instantaneous Capture Point in the global coordinate system

$$r_{icp} = r_{cop} + \frac{\dot{r}_{com}}{\omega_0} \quad (4.28)$$

which is exactly the same quantity as (4.22). In further evolutions, the Capturability concept has also been enhanced by a finite size foot instead of a point foot, to determine Capturability considering the modulation of the CoP by actively applying ankle torques as well as a reaction mass wheel instead of the mass point to account for angular momentum applied by upper body actuation [83].

4.3.5. 3D Foot Placement Estimator

Modeling human motions based on the linear inverted pendulum model is connected to strict model assumptions which might not be suitable to describe a broad variety of natural motions. While the assumption that the center of mass maintains a constant height $r_{com,z,0}$ and that the impact at heel strike as well as the upper-body angular momentum can be neglected might be appropriate for walking and standing, the same assumptions fail to realistically describe running and jumping.

To overcome these limitations the *3D Foot Placement Estimator (3DFPE)* [99] is based on the planar foot placement estimator [158] and the *Euler pendulum* which connects the inverted pendulum with a circular foot model perpendicular to the leg. It is assumed that the foot-ground contact occurs along the circular line including rolling resistance and spin friction to ensure asymptotic stability by means of Lyapunov (Section 4.2).

A legged system placing a step in order to maintain balance can be modeled as a state change in the Euler pendulum to transit from an unstable to a statically stable state. An analysis

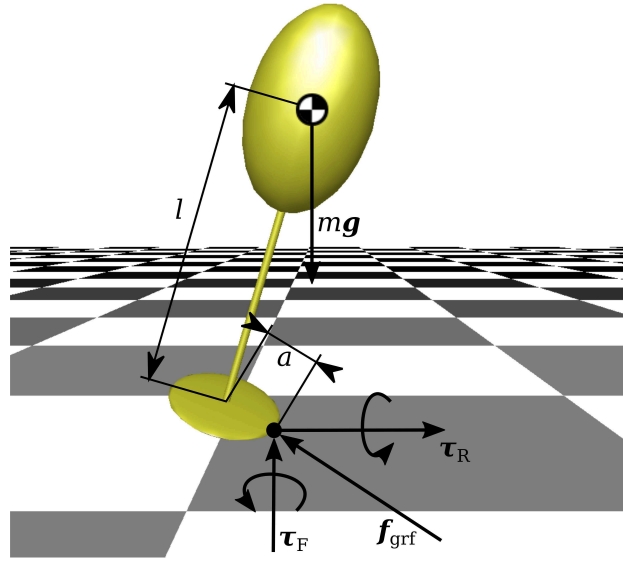


Figure 4.7: Euler pendulum with reaction mass m connected to a circular foot with radius a by a massless rod with the length l . The outer circumference of the disc always touches the ground. The ground reaction force f_{grf} is caused by contact and friction forces, τ_R by rolling resistance and τ_F by spin friction.

of the phase portrait of the threedimensional Euler pendulum reveals three different stability regions which can be distinguished by the family of initial conditions for the state vector $(\beta, \alpha, \theta, \dot{\beta}, \dot{\alpha}, \dot{\theta})$ which lead the pendulum to its equilibrium point $(\alpha, \beta, \dot{\alpha}, \dot{\theta}) = 0$.

- *Stable Region 1:* With smaller absolute values for the initial conditions the pendulum's system energy U_0 is less than the maximum potential energy

$$\underbrace{T_0 + V_0}_{U_0} \leq mgr_{com,z,max} \quad (4.29)$$

with T_0 and V_0 being the potential and kinetic energy, respectively, at ground contact. In this case, the energy well created by the foot cannot be escaped by the system energy.

- *Stable Region 2:* Considering that energy dissipates when impacts occur at and after ground contact, Stable Region 1 can be enlarged allowing for a higher system energy U_+ after ground contact.

$$\underbrace{T_+ + V_+}_{U_+} \leq mgr_{com,z,max} \quad (4.30)$$

- *Stable Region 3:* Taking into account that energy also dissipates when the system rotates around its contact point, the pendulum is able to transit into stable regions 1 and 2 even coming from an unstable state. In this case the system energy U_+ after ground contact has to be larger than the maximum potential energy to transit into stable regions and energy is assumed to be dissipated right after it enters a stable region

$$\underbrace{T_+ + V_+}_{U_+} \geq mgr_{com,z,max} \quad (4.31)$$

Neglecting the cases for which the pendulum's motion is not restricted to a vertical plane, the location of the 3DFPE can be obtained by

$$\mathbf{r}_{\text{fpe}} = \mathbf{r}_{\text{com},z,-} \tan \varphi_- \mathbf{u} \quad (4.32)$$

where, right before ground contact, the pendulum's point mass travels in a direction parallel to \mathbf{u} and has the vertical position $r_{\text{com},z,-}$ and the leg angle φ_- .

Experimental validation [99] has shown that foot placement in human walking and gait termination can be predicted equally well using the 3DFPE and the CaP. Since the stiffness of a human leg is supposed to be somewhere in between a very compliant leg represented by the linear inverted pendulum and a perfectly stiff leg represented by the Euler pendulum, a precise ground reference point to place the CoP on in order to come to a stop would be located somewhere between these two points. In jumping, however, the FPE clearly outperforms the CaP which shows that the limitation of a constant COM height of the linear inverted pendulum is not suitable for this particular task.

4.4. Implications for Human Motions

Although the stability measures summarized in this chapter are based on very simple representations of the complex structure of the human body such as a single mass-point, an inverted pendulum and a linear inverted pendulum, respectively, much of human-like behavior in locomotion can be explained using these tools.

While standing, depending on the magnitude of an external perturbation a human would apply the so-called *ankle*, *hip*, *arm*, or *suspensory strategy* to recover balance or even take a well-placed step in case this is necessary [112], as illustrated in Figure 4.8.

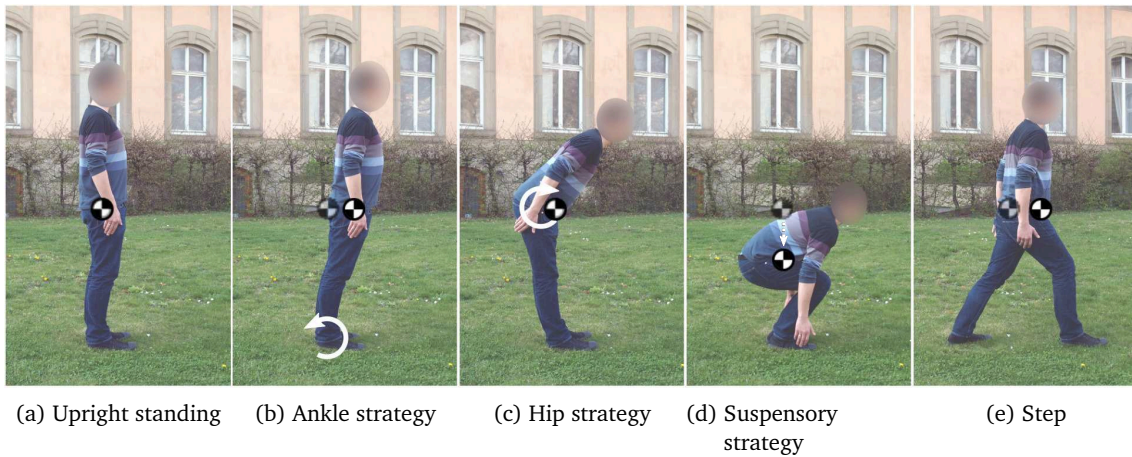


Figure 4.8: Recovering strategies to react on perturbations while standing.

The ankle strategy describes actively applying torque to the ankle joint in order to modulate the CoP within the boundaries of the BoS such that it is vertically aligned with the COM (according to the gCOM criterion) or to shift the inverted pendulum's pivot point into a position in which the COM comes to a stop above the BoS (according to the xCoM and Capturability concept).

In case the velocity of the COM, possibly induced by a stronger perturbation, is too large to be covered by only the ankle strategy humans would need to apply a more effective strategy

to maintain balance. Actively applying torque to the hips causes the whole-body COM to shift and the underlying inverted pendulum to change its shape. This way, the COM can be shifted back to come to a stop above the BoS.

In addition, due to the large inertia of the upper body, the hip strategy can be used to apply angular momentum on the system and bring the ZMP back into the BoS. Additional angular momentum can also be applied by swinging the arms. Another method to alter the shape of the underlying inverted pendulum is provided by the suspensory strategy where the COM is lowered by progressing into the squatting position.

If all these strategies fail due to very large magnitudes of perturbations balance might still be recovered by placing a step on the Capture Point, i.e. enlarging the BoS towards a position where the COM would come to a stop over the CoP defined by where the swing foot has been placed after the step.

4.4.1. Capturability applied to walking motion

A popular analogy describes the two-legged walking motion as a well-controlled sequence of intended falls followed by well-timed capture. The Capturability concept provides the suitable tools to describe human walking and establishes a foundation to develop an intuitive measure to assess the quality of two-legged walking.

However, in order to achieve an energy-efficient locomotion task, humans do not intend to come to a complete stop after each step and, hence, to not place the CoP right on the Capture Point. Rather than that, a residual orbital energy is maintained by stepping right before the Capture Point in order to exploit the progression in walking direction and fall into the next step. Hence, a certain risk of fall is accepted for the sake of energy efficiency.

Equation (4.28) quantifies this behavior and can be used as a tool to measure and compare *risk of fall* between different bipedal walking systems or human subjects. Similarly, (4.28) can be solved for a foot location to result in desired orbital energies and, consequently, in a desired COM velocity. In Chapter 5 the Capture Point location is compared vs. the actual foot placement for healthy and prosthetic walkers.

In order to enable a discussion about the foot location with respect to the Capture Point and establish a measure for the non-zero COM-CoP distance at the event of foot placement the two quantities *Residual Orbital Energy* and *Instantaneous Orbital Energy* are introduced here:

Definition 6 (Residual Orbital Energy)

The Residual Orbital Energy $E_{res, lip}$ of the LIPM is defined as a non-zero value of the orbital energy expressed in equations (4.26) which results from a foot location unequal to the Capture Point ($\mathbf{r}_{cap} \neq \mathbf{r}_{cop}$). It provides a generalized expression for the distance between the foot location and the actual Capture Point.

Definition 7 (Instantaneous Orbital Energy)

Since the COM does not necessarily maintain a constant height during human walking we extend the expression of the orbital energy E_{lip} in (4.26) towards the Instantaneous Orbital Energy E_{inst} which expresses the orbital energy at a given time step taking into account the current COM height. It is further assumed that the velocity vector is directed horizontally. According to Definition 6 we can also formulate the quantity of Residual Instantaneous Orbital Energy $E_{res, inst}$.

Part II

Application and Results

5. MODEL-BASED OPTIMIZATION OF HUMAN WALKING

The dynamics of the walking motion of three subjects, one of them walking with transfemoral prostheses, has been reconstructed from recorded motion capture data using individualized multibody models of the subjects and optimal control methods. The states of the subject-specific multibody models are fitted to the recorded motion in a least squares sense. This way, the individual patterns of the walking motion are preserved for the analysis of the subject-specific walking motion. Based on the reconstructed dynamics, general gait parameters are computed and compared between the subjects. Rather than assessing traditional gait parameters, the analysis conducted in this part of the thesis is focused on the behavior of the *Instantaneous Capture Point (ICaP)* during the different subject-specific modes of walking. In particular, we are interested in the characteristics of each subject's foot placement with respect to the ICaP right after the swing phase.

We describe the dynamic human model used to reconstruct the walking motions in Section 5.1. The least-squares optimal control problem formulation to fit the motion of the models to the recorded motion capture data is included in Section 5.2. The results obtained from the reconstructed walking motions are presented in Section 5.3 and discussed in Section 5.4.

5.1. Dynamic Human Model for Gait Reconstruction

Optimization is used to reconstruct the gait of two unimpaired adults and a young adult walking with two different transfemoral prostheses. The human body is modeled as a 34 degrees of freedom (DoFs) multibody system according to methods described in Section 2.3. The dynamic body segment parameters are computed using the regression equations for adults introduced in Section 2.4 and listed in Table A.2 in Appendix A. In case of prosthetic walking, the geometric and inertial parameters of the prosthetic legs have been experimentally determined and used instead of the values of the left unimpaired leg. In order to avoid additional distraction of the subject, arm motion has not been included into the recordings involving the prostheses. Hence, the joints *Elbow*, *Shoulder* and *Neck* have been modeled as rigid joints reducing the model for prosthetic gait to 25 DoFs. The models used for both the optimization of prosthetic and unimpaired walking are illustrated in Figure 5.1.

5.2. Least-Squares Reconstruction of Human Walking Motions

In this part of the thesis, unimpaired and prosthetic human walking motions are reconstructed by fitting the motions of subject-specific dynamic models to motion capture data by formulating and solving least-squares (LSQ) optimization problems. In addition, in order to minimize the dimension of the optimal control problem it is a reasonable choice to perform the motion fitting along the generalized coordinates of the model instead of the Cartesian coordinates. Due to skin artifacts and measurement errors the markers attached to a segment do not keep a fixed distance but move with respect to each other causing the marker configuration to be distorted from its reference configuration. Also the fact that a multibody model is an abstract representation of the human body which assumes rigid bodies and ideal joints stands in contrast to the complex kinematic behavior of the body segments in reality and causes a mismatch of the measured marker positions and their ideal positions on the model.

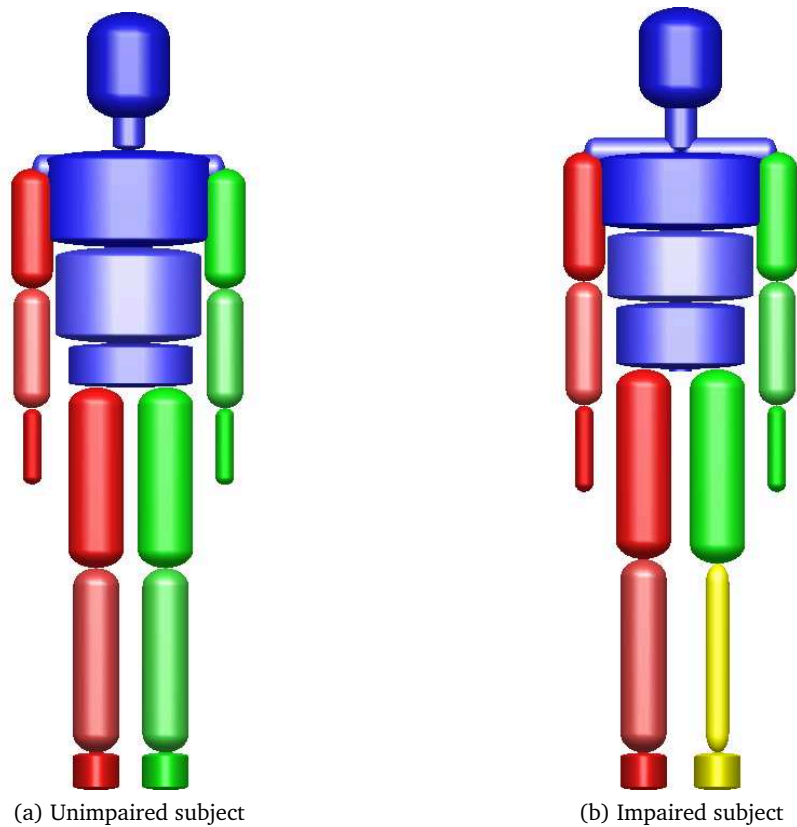


Figure 5.1: Different multibody models are used to model the gait of (a) unimpaired humans (34 DoFs) and (b) the humans walking with a prosthesis (25 DoFs). The prosthetic leg is indicated in yellow. Note that for model (b) the arms are assumed to be fixed with respect to the upper part of the trunk. The DoFs of both models are listed in Appendix B.

The reference motions for the optimal control problems are created by converting the measured motion capture data from marker trajectories into trajectories in joint angle space. This can be performed by using Inverse Kinematics (IK) to approximate the motion of a subject-specific multibody model such that the distance between virtual markers defined on the model and the appropriate measured marker positions are minimized for each time frame considered. The Inverse Kinematics fit is performed in a least-squares sense and considers the entire kinematic chain of the multibody model. Both steps, creating a subject specific model as well as converting the reference motion in its generalized coordinates are performed using the software tool PUPPETEER [38] which implements the Sugihara algorithm based on the Levenberg-Marquardt method [36, 147].

The walking motion has been reconstructed for three different subjects in four scenarios: *Unimpaired male*, *unimpaired female*, *Transfemoral Prosthesis Generation 1 (TransFem Gen 1)*, and *Transfemoral Prosthesis Generation 2 (TransFem Gen 2)*. Further details about the scenarios are discussed in Section 5.3. The LSQ fitting errors for each marker resulting from the inverse kinematics fit are listed in the Table 5.1 for the upper body and in Table 5.2 for the lower body. Table 5.1 also contains the average over the errors of all markers as well as their standard deviation. The largest deviations occurred on lower body markers likely due to the great skin movement caused by the high oscillations of the legs during walking (highlighted in bold in Table 5.2).

Table 5.1: Inverse Kinematics fitting errors in average and standard deviation over all markers. Absolute deviations are listed for the upper body markers in the scenarios *Unimpaired male*, *unimpaired female*, *Female walking with the Transfemoral Prosthesis Generation 1 (Female w/ TransFem Gen 1)*, and *Female walking with the Transfemoral Prosthesis Generation 2 (Female w/ TransFem Gen 2)*. The error is provided in centimeters [cm]. Arm motion was not measured in the case of prosthetic walking.

		Unimpaired male	Unimpaired female	Female w/ TransFem Gen 1	Female w/ TransFem Gen 2
Average		2.0±1.3	2.0±1.1	1.6±0.8	0.8±0.4
STRN	Sternum	1.3	1.4	-	-
T10	10 th Thoracic Vertebrae	1.1	1.6	-	-
C7	7 th Cervical Vertebrae	2.8	2.8	2.0	0.4
CLAV	Clavicula	2.9	3.1	2.5	0.9
LSHO	Left Shoulder	3.6	3.0	2.1	1.6
RSHO	Right Shoulder	2.6	2.9	2.2	0.9
RELB	Right Elbow 0	3.0	2.8	-	-
RELBW	Right Elbow 1	3.1	2.9	-	-
RHUMS	Right Humerus	2.8	2.4	-	-
RRAD	Right Radius	2.9	1.1	-	-
RULN	Right Ulna	2.8	1.5	-	-
LELB	Left Elbow 0	2.3	3.8	-	-
LELBW	Left Elbow 1	2.2	3.0	-	-
LHUMS	Left Humerus	1.8	2.5	-	-
LRAD	Left Radius	1.1	2.1	-	-
LULN	Left Ulna	1.6	1.0	-	-
HEAD	Forehead	0.5	1.5	-	-
LMAS	Left Mastoid	0.8	1.2	-	-
RMAS	Right Mastoid	0.7	1.0	-	-

Table 5.2: Inverse Kinematics fitting errors for the lower body markers in the scenarios *Unimpaired male*, *unimpaired female*, *Female walking with the Transfemoral Prosthesis Generation 1 (Female w/ TransFem Gen 1)*, and *Female walking with the Transfemoral Prosthesis Generation 2 (Female w/ TransFem Gen 2)*. The error is provided in centimeters [cm]. The largest fitting errors per scenario are highlighted as bold numbers.

		Unimpaired male	Unimpaired female	Female w/ TransFem Gen 1	Female w/ TransFem Gen 2
LASI	Left Anterior Superior Iliac Spine	1.7	2.0	1.1	0.8
RASI	Right Anterior Superior Iliac Spine	1.6	2.6	2.2	0.8
SACR	Sacrum	2.1	1.5	0.9	1.1
RKNE	Right Knee Lateral Epicondyles	1.7	1.6	2.7	0.8
RMEP	Right Knee Medial Epicondyles	2.8	2.5	2.4	1.8
RTHI	Right Thigh	2.2	1.9	3.5	1.0
RTIB	Right Tibialis	3.1	3.3	2.6	1.5
RANK	Right Ankle	1.6	1.5	1.0	0.7
RD2T	Right Hallux	1.0	0.8	0.5	0.4
RHEE	Right Heel	1.8	1.7	1.3	1.1
RMMAL	Right Medial Malleolus	1.7	1.1	0.7	0.6
RTOE	Right Toes	0.8	0.6	0.6	0.5
LKNE	Left Knee Lateral Epicondyles	1.4	1.5	2.0	0.5
LMEP	Left Knee Medial Epicondyles	2.7	4.0	1.3	1.3
LTHI	Left Thigh	2.2	1.4	1.3	0.9
LTIB	Left Tibialis	8.9	7.1	2.0	0.6
LANK	Left Ankle	1.5	2.0	1.0	0.3
LD2T	Left Hallux	0.8	0.9	0.9	0.2
LHEE	Left Heel	1.9	2.1	0.7	0.4
LMMAL	Left Medial Malleolus	1.8	1.6	1.4	0.4
LTOE	Left Toes	0.7	1.2	0.8	0.2

5.2.1. Optimal Control Problem for Human Motion Reconstruction

The least-squares optimal control problem approximates the motion of a subject-specific dynamic model to recorded reference data of a whole stride starting with the lift off of the left foot and ending with the same event two steps later (Figure 1.2).

The reference data can be summarized in a set of time discrete postures expressed in terms of the generalized coordinates $\mathbf{q}_j^{\text{ik}} \in \mathbb{R}^{n_{\text{dof}}}$, $j = 0, \dots, m$ at the time instances $t_0, \dots, t_m \in \mathbb{R}$. The least-squares problem is then described for the $n_{\text{ph}} = 12$ model stages by

$$\min_{\mathbf{x}(\cdot), \mathbf{u}(\cdot)} \sum_{j=1}^m \frac{1}{2} \|\mathbf{q}_j^{\text{ik}} - \mathbf{q}(t_j)\|_2^2 dt \quad (5.1a)$$

subject to:

$$\dot{\mathbf{x}}(t) = \mathbf{f}_i(\mathbf{x}(t), \mathbf{u}(t)), \quad (5.1b)$$

$$\mathbf{x}(t_i^+) = \mathbf{h}_i(\mathbf{x}(t_i^-)), \quad (5.1c)$$

$$0 \leq \mathbf{g}_i(t, \mathbf{x}(t), \mathbf{u}(t)), \quad (5.1d)$$

$$0 \leq \mathbf{r}^{\text{ineq}}(\mathbf{x}(0), \dots, \mathbf{x}(T), \mathbf{u}(0), \dots, \mathbf{u}(T)), \quad (5.1e)$$

$$\text{for } t \in [\tau_{i-1}, \tau_i], i = 1, \dots, 12, \tau_0 = 0, \tau_{12} = T$$

with the differential states

$$\mathbf{x}(t) = \begin{pmatrix} \mathbf{q}(t) \\ \dot{\mathbf{q}}(t) \end{pmatrix} \in \mathbb{R}^{2n_{\text{dof}}} \quad (5.1f)$$

and the model's generalized coordinates $\mathbf{q}(t) \in \mathbb{R}^{n_{\text{dof}}}$, generalized velocities $\dot{\mathbf{q}}(t) \in \mathbb{R}^{n_{\text{dof}}}$ and the controls $\mathbf{u}(t) \in \mathbb{R}^{n_{\text{act}}}$ which are modeled as torques that act directly on the model's joints.

The objective function (5.1a) minimizes the sum of squared differences between the model joint angles $\mathbf{q}(t)_j$ and the joint angles \mathbf{q}_j^{ik} from the inverse-kinematics analysis of the motion capture recordings. The ODEs (5.1b) describe the model dynamics in each phase where the right hand sides $\mathbf{f}_i : \mathbb{R}^{n_x} \times \mathbb{R}^{n_u} \times \mathbb{R}^{n_x}$ are characterized by the different constraint properties as explained later in this chapter. Discontinuities in the generalized velocities $\dot{\mathbf{q}}(t)$ that occur due to the model specific perfectly rigid impact at ground collision in case of touch-down events are handled using the phase transition functions (5.1c). Upper and lower bounds for the differential states $\mathbf{x}(t)$ as well as the controls $\mathbf{u}(t)$ are covered by the path constraints (5.1d). The path constraints for the generalized coordinates $\mathbf{x}(t)$ are chosen to reflect the ranges for the typical walking motions. The generalized velocities and the controls are constraint to values of realistic magnitude [125] by path constraints which are summarized in Appendix B. Additional constraints that, e.g., ensure physical feasibility such as unilateral ground contacts are contained in the interior point constraints (5.1e). These constraints distinguish the several gait phases from each other and will be further explained in Section 5.2.2.

5.2.2. Phase Descriptions

The gait phases can be distinguished by the different contact configurations between the human and the environment which also change the dynamics of the system. Accordingly, these contact properties are expressed in the model as nonlinear point constraints which define the

several phases of the optimal control problem. In reality the complex anatomical structure of a foot allows for a smooth rocking motion throughout the stance phase of a leg. Due to the model formulations in this thesis which assume rigid flat feet a rocking motion is not possible and an additional event is required in the OCP which reflects the ground collision impact of the forefoot. We will call this model-specific additional event the *toe strike*.

The point constraints are formulated as equality or inequality constraints on the position $r_a^{s,p}(\mathbf{x}(t))$, the velocity $\dot{r}_a^{s,p}(\mathbf{x}(t))$, and the ground reaction force $f_a^{s,p}$, respectively, acting at the point $p \in \{\text{Heel, Hallux, Meta5}\}$ on the $s \in \{\text{left, right}\}$ foot in the direction of the axis $a \in \{x, y, z\}$ in the global coordinate system (Section 2.3). Constraints are defined for the beginning of each of the n phases, at time step $t_i, i = 1 \dots n$, for time steps $t \in \mathcal{T}_i$ within the phases as well as for the very last time step $t_{n,\text{end}}$ of the gait cycle.

The physiological sequence of gait phases in human walking, as illustrated for a whole stride in Figure 1.2, is translated into the optimal control problem as a fixed sequence of 12 model stages (Figure 5.2). This includes four transition phases with a duration $\Delta t = 0$ to model the discontinuities occurring on the velocities at the inelastic touch-down of the heels and the toes, respectively.

- **Phase 1: Flat Right Foot Contact**

The beginning of the gait cycle is defined by position constraints on the contact points of the entire right foot and the left Hallux, constraints to impose zero initial velocity at the contacts as well as force constraints to ensure that unilateral contact forces. Within the first phase, only the direction of the contact forces is constraint.

$$\begin{array}{llll}
 r_z^{\text{right, heel}}(\mathbf{x}(t_0)) & = 0 & f_z^{\text{right, heel}}(\mathbf{x}(t_0), \mathbf{u}(t_0)) & \geq 0 \\
 r_z^{\text{right, hallux}}(\mathbf{x}(t_0)) & = 0 & f_z^{\text{right, hallux}}(\mathbf{x}(t_0), \mathbf{u}(t_0)) & \geq 0 \\
 r_z^{\text{right, meta5}}(\mathbf{x}(t_0)) & = 0 & f_z^{\text{right, meta5}}(\mathbf{x}(t_0), \mathbf{u}(t_0)) & \geq 0 \\
 r_z^{\text{left, hallux}}(\mathbf{x}(t_0)) & = 0 & f_z^{\text{right, heel}}(\mathbf{x}(t), \mathbf{u}(t)) & \geq 0, t \in \mathcal{T}_1 \\
 \dot{r}_x^{\text{right, heel}}(\mathbf{x}(t_0)) & = 0 & f_z^{\text{right, hallux}}(\mathbf{x}(t), \mathbf{u}(t)) & \geq 0, t \in \mathcal{T}_1 \\
 \dot{r}_y^{\text{right, heel}}(\mathbf{x}(t_0)) & = 0 & f_z^{\text{right, meta5}}(\mathbf{x}(t), \mathbf{u}(t)) & \geq 0, t \in \mathcal{T}_1 \\
 \dot{r}_z^{\text{right, heel}}(\mathbf{x}(t_0)) & = 0 & & \\
 \dot{r}_y^{\text{right, hallux}}(\mathbf{x}(t_0)) & = 0 & & \\
 \dot{r}_z^{\text{right, hallux}}(\mathbf{x}(t_0)) & = 0 & & \\
 \dot{r}_z^{\text{right, meta5}}(\mathbf{x}(t_0)) & = 0 & &
 \end{array}$$

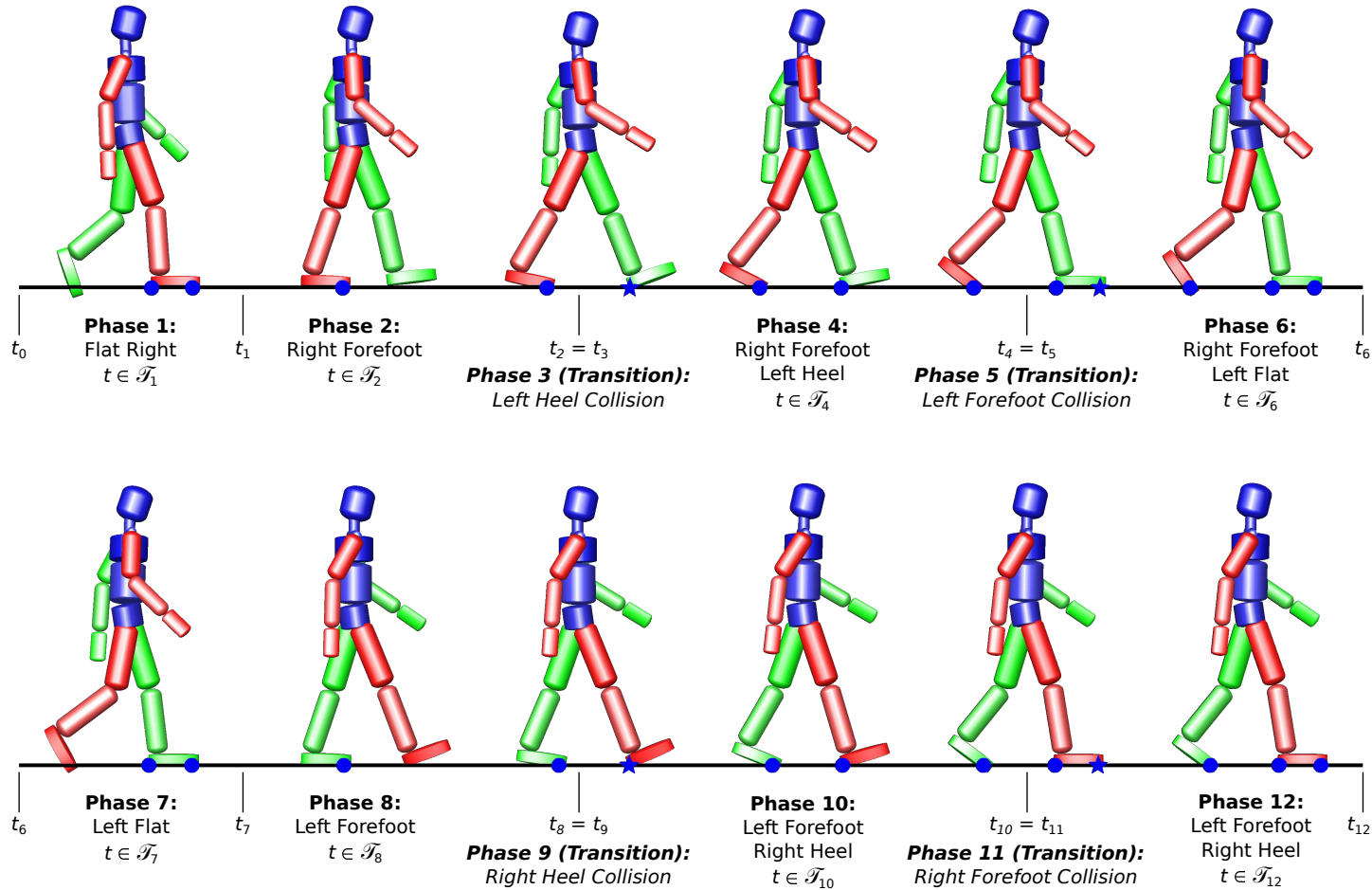


Figure 5.2: Model stages implemented in the optimal control problem according to the physiological gait sequence described in Section 1.2. The upper part shows the left swing phase, the lower part the right swing phase. The model stages are distinguished by the different number of constraints determined by the changing contact configurations with the ground. Transition stages have a duration of $\Delta t = 0$ and are required to handle the discontinuities caused by the ground collision impacts occurring when a contact is newly established. For each stage, the existing contact points are illustrated as blue dots, ground collision impacts are shown as blue stars.

- **Phase 2: Right Forefoot Contact**

The second phase is initiated when the heel contact to the ground is removed and the heel contact force vanishes. During the second phase, constraints are formulated to ensure that the points not in contact with the ground are maintained above ground-level and that the forces at the contact points remain positive.

$$\begin{aligned}
 f_z^{\text{right, heel}}(\mathbf{x}(t_1), \mathbf{u}(t_1)) &= 0 & f_z^{\text{right, hallux}}(\mathbf{x}(t_1), \mathbf{u}(t_1)) &\geq 0 \\
 & & f_z^{\text{right, meta5}}(\mathbf{x}(t_1), \mathbf{u}(t_1)) &\geq 0 \\
 & & r_z^{\text{left, heel}}(\mathbf{x}(t_1)) &\geq 0 \\
 & & r_z^{\text{left, hallux}}(\mathbf{x}(t_1)) &\geq 0 \\
 & & r_z^{\text{left, heel}}(\mathbf{x}(t)) &\geq 0, t \in \mathcal{T}_2 \\
 & & r_z^{\text{left, hallux}}(\mathbf{x}(t)) &\geq 0, t \in \mathcal{T}_2 \\
 & & r_z^{\text{right, heel}}(\mathbf{x}(t)) &\geq 0, t \in \mathcal{T}_2 \\
 & & f_z^{\text{right, hallux}}(\mathbf{x}(t), \mathbf{u}(t)) &\geq 0, t \in \mathcal{T}_2 \\
 & & f_z^{\text{right, meta5}}(\mathbf{x}(t), \mathbf{u}(t)) &\geq 0, t \in \mathcal{T}_2
 \end{aligned}$$

- **Phase 3 (Transition): Left Heel Collision**

The touch-down occurring at heel strike of the left foot marks the first discontinuity in the gait cycle. Both constraints on the left heel are formulated to ensure that the heel touches the ground and maintains its position.

$$\begin{aligned}
 r_z^{\text{left, heel}}(\mathbf{x}(t_2)) &= 0 & \dot{r}_z^{\text{left, heel}}(\mathbf{x}(t_2)) &\leq 0 \\
 & & r_z^{\text{left, meta5}}(\mathbf{x}(t_2)) &\geq 0 \\
 & & r_z^{\text{left, hallux}}(\mathbf{x}(t_2)) &\geq 0 \\
 & & r_z^{\text{right, heel}}(\mathbf{x}(t_2)) &\geq 0
 \end{aligned}$$

- **Phase 4: Right Forefoot and Left Heel Contact**

At the beginning and during the fourth model phase, it is ensured that the points not explicitly in contact with the ground remain above ground-level and that the forces at the contact points are positive.

$$\begin{aligned}
 r_z^{\text{left, hallux}}(\mathbf{x}(t_3)) &\geq 0 \\
 r_z^{\text{right, heel}}(\mathbf{x}(t_3)) &\geq 0 \\
 f_z^{\text{right, hallux}}(\mathbf{x}(t_3), \mathbf{u}(t_3)) &\geq 0 \\
 f_z^{\text{right, meta5}}(\mathbf{x}(t_3), \mathbf{u}(t_3)) &\geq 0 \\
 f_z^{\text{left, heel}}(\mathbf{x}(t_3), \mathbf{u}(t_3)) &\geq 0 \\
 r_z^{\text{left, hallux}}(\mathbf{x}(t)) &\geq 0, t \in \mathcal{T}_4 \\
 r_z^{\text{right, heel}}(\mathbf{x}(t)) &\geq 0, t \in \mathcal{T}_4 \\
 f_z^{\text{right, hallux}}(\mathbf{x}(t), \mathbf{u}(t)) &\geq 0, t \in \mathcal{T}_4 \\
 f_z^{\text{right, meta5}}(\mathbf{x}(t), \mathbf{u}(t)) &\geq 0, t \in \mathcal{T}_4 \\
 f_z^{\text{left, heel}}(\mathbf{x}(t), \mathbf{u}(t)) &\geq 0, t \in \mathcal{T}_4
 \end{aligned}$$

- **Phase 5 (Transition): Left Forefoot Collision**

The touch-down of the left forefoot indicates the second discontinuity in the gait cycle. Again, the constraints on the sign of the velocity of the colliding points are formulated to ensure that the touch-down is directed in the intended direction.

$$\begin{array}{llll}
 r_z^{\text{left, hallux}}(\mathbf{x}(t_4)) & = 0 & \dot{r}_z^{\text{left, hallux}}(\mathbf{x}(t_4)) & \leq 0 \\
 r_z^{\text{left, meta5}}(\mathbf{x}(t_4)) & = 0 & \dot{r}_z^{\text{right, meta5}}(\mathbf{x}(t_4)) & \leq 0 \\
 & & r_z^{\text{right, heel}}(\mathbf{x}(t_4)) & \geq 0 \\
 & & f_z^{\text{right, hallux}}(\mathbf{x}(t_4), \mathbf{u}(t_4)) & \geq 0 \\
 & & f_z^{\text{right, meta5}}(\mathbf{x}(t_4), \mathbf{u}(t_4)) & \geq 0 \\
 & & f_z^{\text{left, heel}}(\mathbf{x}(t_4), \mathbf{u}(t_4)) & \geq 0
 \end{array}$$

- **Phase 6: Right Forefoot and Left Flat Foot Contact**

At the beginning and during the sixth model phase, it is again ensured that the points not explicitly in contact with the ground remain above ground-level and that the forces at the contact points are positive.

$$\begin{array}{ll}
 r_z^{\text{right, heel}}(\mathbf{x}(t_5)) & \geq 0 \\
 f_z^{\text{right, hallux}}(\mathbf{x}(t_5), \mathbf{u}(t_5)) & \geq 0 \\
 f_z^{\text{right, meta5}}(\mathbf{x}(t_5), \mathbf{u}(t_5)) & \geq 0 \\
 f_z^{\text{left, hallux}}(\mathbf{x}(t_5), \mathbf{u}(t_5)) & \geq 0 \\
 f_z^{\text{left, meta5}}(\mathbf{x}(t_5), \mathbf{u}(t_5)) & \geq 0 \\
 f_z^{\text{left, heel}}(\mathbf{x}(t_5), \mathbf{u}(t_5)) & \geq 0 \\
 r_z^{\text{left, hallux}}(\mathbf{x}(t)) & \geq 0, t \in \mathcal{T}_6 \\
 f_z^{\text{right, hallux}}(\mathbf{x}(t), \mathbf{u}(t)) & \geq 0, t \in \mathcal{T}_6 \\
 f_z^{\text{right, meta5}}(\mathbf{x}(t), \mathbf{u}(t)) & \geq 0, t \in \mathcal{T}_6 \\
 f_z^{\text{left, hallux}}(\mathbf{x}(t), \mathbf{u}(t)) & \geq 0, t \in \mathcal{T}_6 \\
 f_z^{\text{left, meta5}}(\mathbf{x}(t), \mathbf{u}(t)) & \geq 0, t \in \mathcal{T}_6 \\
 f_z^{\text{left, heel}}(\mathbf{x}(t), \mathbf{u}(t)) & \geq 0, t \in \mathcal{T}_6
 \end{array}$$

- **Phases 7-12**

Due to the symmetry of a gait cycle, the model phases 7 to 12 are sequenced according to the phases 1 to 6, however with the right and left sides interchanged. Additionally, end constraints are formulated at the last time step t_{12} of the 12th model phase to conclude the entire gait cycle.

$$\begin{array}{llll}
 f_z^{\text{left, hallux}}(\mathbf{x}(t_{12}), \mathbf{u}(t_{12})) & = 0 & r_z^{\text{left, heel}}(\mathbf{x}(t_{12})) & \geq 0 \\
 f_z^{\text{left, meta5}}(\mathbf{x}(t_{12}), \mathbf{u}(t_{12})) & = 0 & f_z^{\text{right, heel}}(\mathbf{x}(t_{12}), \mathbf{u}(t_{12})) & \geq 0 \\
 & & f_z^{\text{right, hallux}}(\mathbf{x}(t_{12}), \mathbf{u}(t_{12})) & \geq 0 \\
 & & f_z^{\text{right, meta5}}(\mathbf{x}(t_{12}), \mathbf{u}(t_{12})) & \geq 0
 \end{array}$$

5.3. Numerical Results for Reconstructed Human Walking Motion

The characteristics of the human walking motion are described based on experimental data gathered during camera-based motion capture recordings in a gait lab as shown in Section 1.3. Two unimpaired subjects and one transfemoral amputee subject walking with two different prosthetic legs participated in the trials. The recorded motion is reconstructed using individual multibody models of the subjects and optimal control methods. This way, it could be ensured that the resulting motion is physiologically consistent and that the dynamics of the system is satisfied throughout the entire motion.

5.3.1. Unimpaired Walking Motion

The analysis of gait patterns, and in particular the foot placement strategy with respect to the Instantaneous Capture Point, in unimpaired walking is based on motion capture recordings of the walking motion of two unimpaired subjects walking at self-selected speeds (Figure 5.3). Both subjects exercise on a regular basis. The gait of the male subject (41 yrs., 1.88 m, 89 kg) could be described as strong and forward-driven the gait of the female subject (30 yrs., 1.68 m, 54.1 kg) appears quick and casual. The appearance of both gait motions would be considered healthy without any physical limitations. While no asymmetric patterns can be observed for the unimpaired male subject's gait on visual inspection, it can be noticed that the unimpaired female subject has an asymmetric arm swing pattern. The right arm has a significantly smaller range of motion than the left arm. The dynamic model parameters for all subjects were obtained using the regression equations provided by [29] for adults and summarized in Table A.1 in Appendix A.

5.3.2. Unilateral Amputee Walking with Transfemoral Prostheses

The characteristics of human walking after unilateral transfemoral amputation, and replacement of the leg by state of the art transfemoral prostheses, is analyzed using motion capture recordings of a young female subject (12 yrs., 1.67 m, 51.9 kg). The subject was individually fitted with two different prosthetic knees which also includes a customized socket and appropriately selected prosthetic components (Figure 5.4). The subject's walking motion is smooth with a slightly excessive lateral swing of the upper body and an asymmetric leaning towards the unimpaired side during the swing phase of the prosthetic side. However, the gait involved no significant arm swing. For the sake of simplicity and in order to avoid additional distraction of the subject, no markers were placed on the arms and their motion not included into the recordings. For the simulation, the arms of the subject were assumed to remain static with respect to the upper part of the trunk.

Both prosthetic legs, the Otto Bock C-Leg [118] and its successor the Otto Bock Genium [119] are micro-processor controlled and able to adapt their swing phase behavior to the current gait situation. Compared to the C-Leg, the Genium leg features improved control algorithms and additional functionalities which a prosthetic walker can apply to maintain a slightly flexed knee during the stance phase. This provides the subject the possibility to exploit a softer damping during load and a more physiological gait. Based on these advancements we refer to the C-Leg as the *Transfemoral Prosthesis Generation 1 (TransFem Gen 1)* and to the Genium leg as the *Transfemoral Prosthesis Generation 2 (TransFem Gen 2)* throughout this thesis. Both prosthetic legs are combined with an Otto Bock 1C60 [117] carbon spring foot.

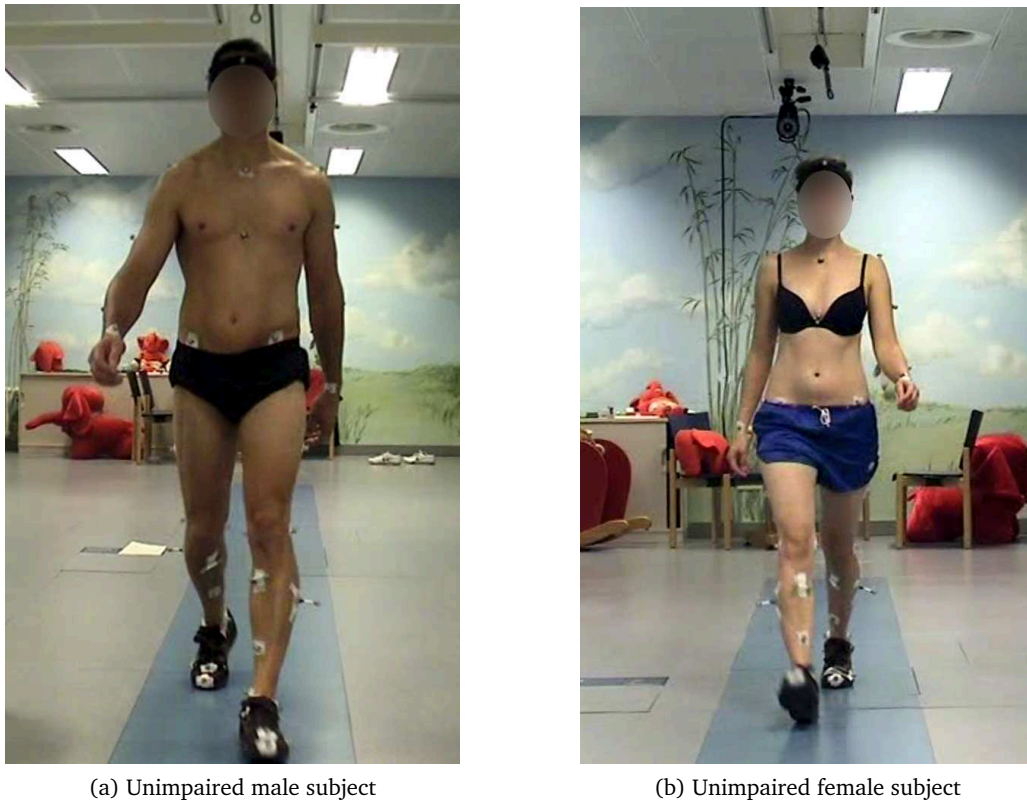


Figure 5.3: The unimpaired (a) male subject (41 yrs., 1.88 m, 89 kg) and (b) female subject (30 yrs., 1.68 m, 54.1 kg) participating in motion capture recordings in the gait lab.

The recordings of both prostheses were performed within a time span of four weeks to ensure a comparable physical constitution of the subject. While the subject had already been using the TransFem Gen 1 for several years, the TransFem Gen 2 had been tested by her in everyday life for two weeks prior to the experiments. Therefore, it can be assumed that the subject was sufficiently accustomed to the prostheses. Subjectively, the test person reported that she felt slightly insecure walking with the TransFem Gen 1 and more confident using the TransFem Gen 2. The dynamic model parameters for the prosthesis were obtained by simple experiments involving scaling, balancing and oscillating the two prosthetic legs similar to the procedure described in [66] and used in the model instead of the parameters of an unimpaired left leg. The dynamic model parameters for the two prosthetic devices are summarized in Table 5.3.

Table 5.3: Experimentally obtained dynamic model parameters of the TransFem Gen 1 and 2.

Parameter	Axis	Symbol	Unit	TransFem Gen 1	TransFem Gen 2
Length	longitudinal	l_s	[cm]	41.0	41.0
COM position	longitudinal	$d_{\text{com},s}$	[cm]	11.5	11.5
Mass	-	m_s	[kg]	1.36	1.52
Radii of Gyration	sagittal	$r_{\text{gyr},s,x}$	[cm]	1.8	2.1
	transversal	$r_{\text{gyr},s,y}$	[cm]	3.0	3.4
	longitudinal	$r_{\text{gyr},s,z}$	[cm]	1.3	1.4

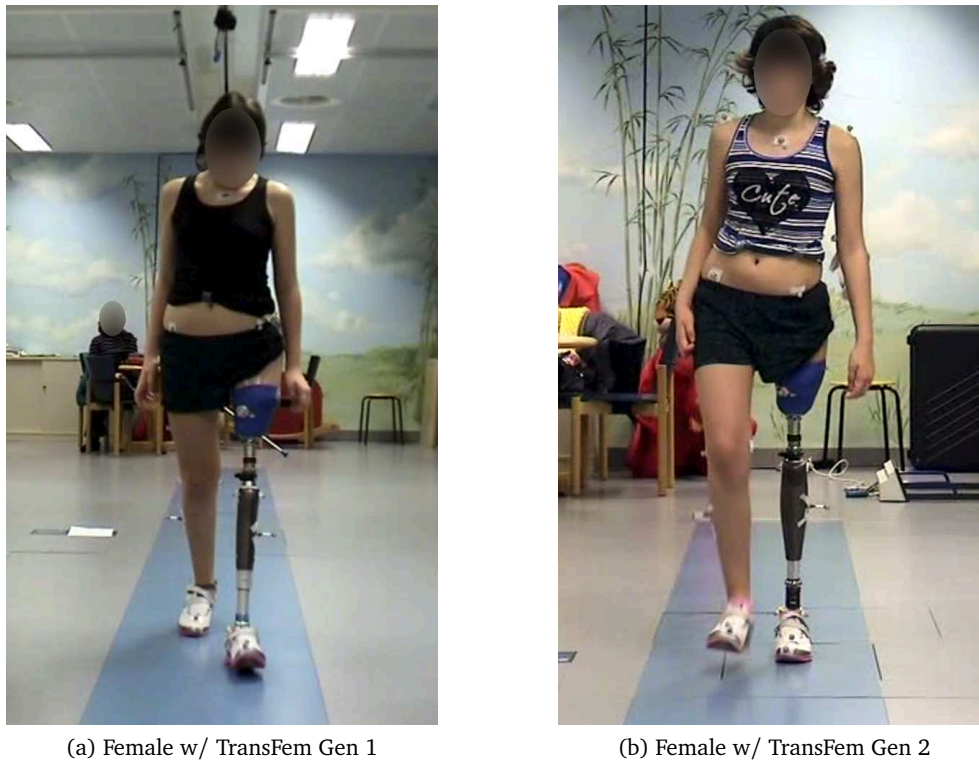


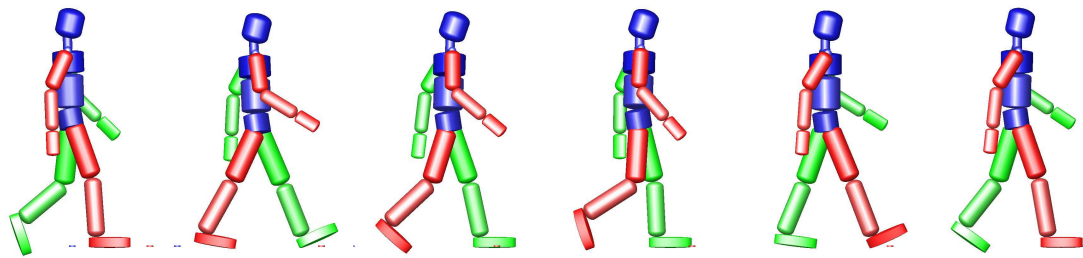
Figure 5.4: The young female subject (12 yrs., 1.67 m, 51.9 kg) performing motion capture recordings in the gait lab with (a) the TransFem Gen 1 and (b) the TransFem Gen 2. No reflective markers were placed on the arms of the subject.

Reconstructed Walking Motion

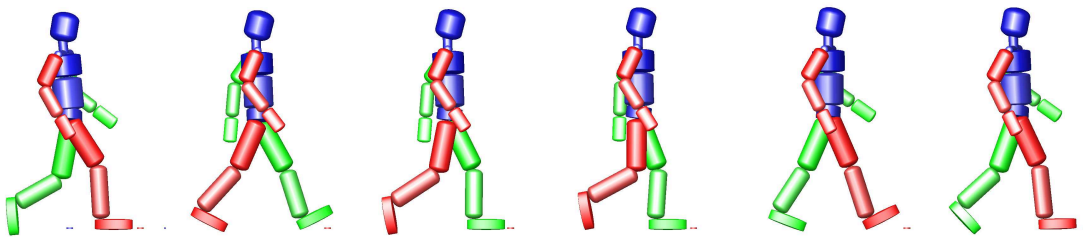
Using the optimal control approach to reconstruct the walking motions ensures that the dynamics of the body are satisfied throughout the motion. The motions which resulted from the optimal control problems described in this chapter are illustrated in Figure 5.5 for the sagittal plane and in Figure 5.6 for the frontal plane. The resulting generalized positions, generalized velocities and torques are shown in the Figures 5.7 - 5.10, for the upper and the lower body segments, respectively.

It is noticeable from the flexion of the right knee ($rKnee\ rotY$) that the swing phase of the unimpaired side in prosthetic walking begins later in the gait cycle and lasts for only half of the cycle. The unimpaired male and female walking show an physiological pattern with the swing phase lasting for approximately 60% of the gait cycle. In contrast to that, the knee flexion of the affected side ($lKnee\ rotY$) of the prosthetic gait shows a pattern that is more in accordance with the unimpaired subjects. The asymmetric arm swing pattern applied by the unimpaired female subject (see Section 5.3.1) can be observed by comparing the shoulder motion shown in $rShoulder\ rotY$ and $lShoulder\ rotY$. The upper body of the gait involving the prostheses shows an asymmetric rotation around the x -axis towards the prosthetic side during the swing phase of the unimpaired side. According to clinical evaluation¹, this pattern is adapted in order to compensate for the reduced muscular strength in the residual limb. By applying upper body momentum the pelvis is leaned towards the weaker side to reduce the hip abduction moment required to prevent the pelvis from collapsing during the swing phase of the stronger side.

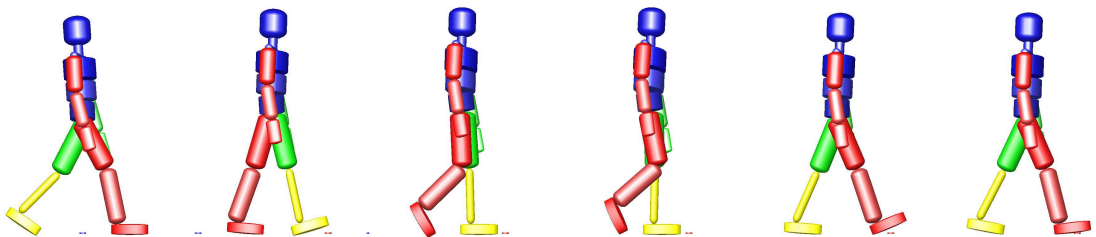
¹provided by our partners at the Heidelberg MotionLab, www.heidel-motionlab.de



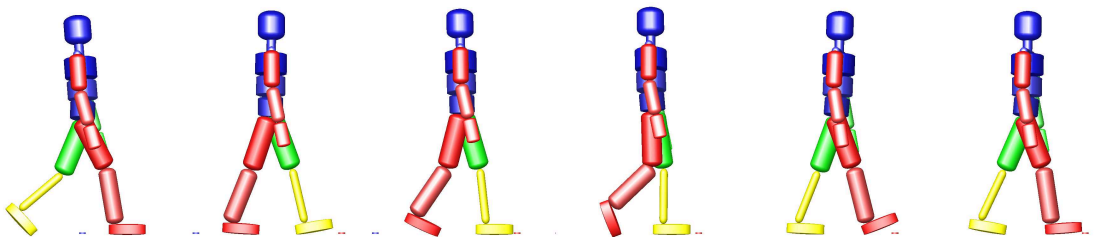
(a) Unimpaired male subject



(b) Unimpaired female subject

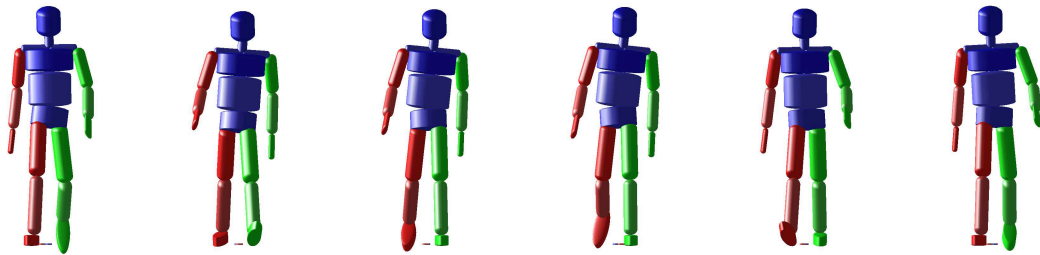


(c) Female w/ TransFem Gen 1

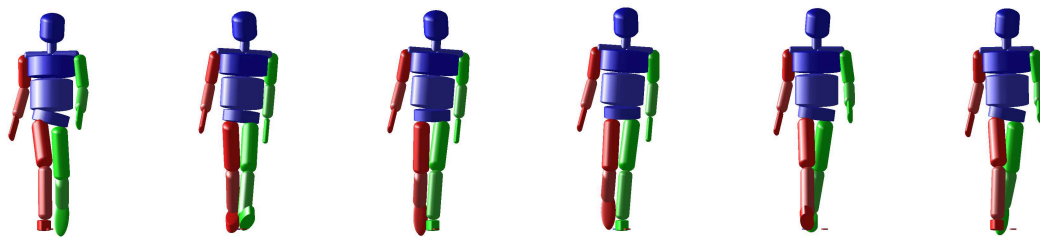


(d) Female w/ TransFem Gen 2

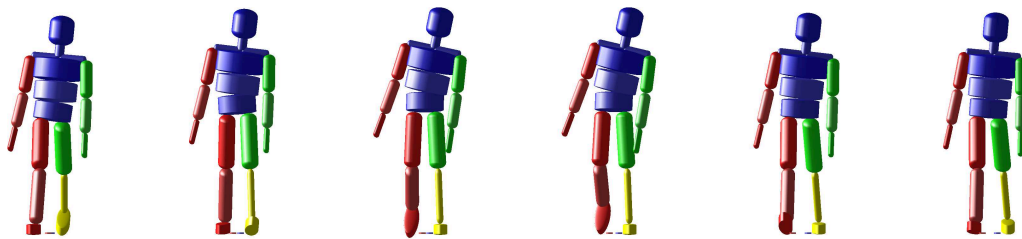
Figure 5.5: The simulated walking motion of the unimpaired (a) male and (b) female subject as well as the young female subject walking with (c) the TransFem Gen 1 and (d) the TransFem Gen 2 in the gait events *left toe off*, *left heel strike*, *left toe strike*, *right toe off*, *right heel strike*, and *right toe strike* in the sagittal plane. The prosthetic legs are indicated in yellow.



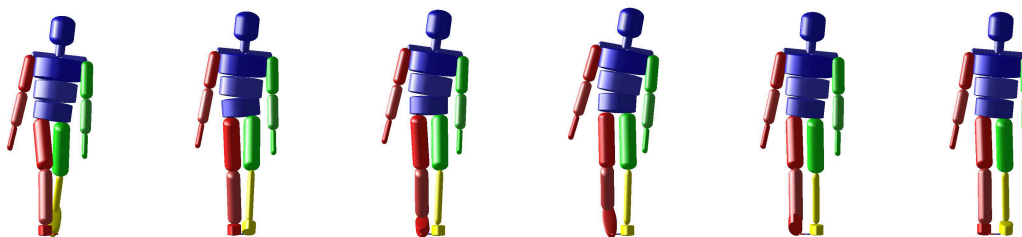
(a) Unimpaired male



(b) Unimpaired female



(c) Female w/ TransFem Gen 1



(d) Female w/ TransFem Gen 2

Figure 5.6: Sequence of motion for a full step for (a) unimpaired male and (b) unimpaired female walking as well as the female subject walking with (c) TransFem Gen 1, and (d) TransFem Gen 2, respectively, in front view. Again, the prosthetic legs are indicated in yellow.

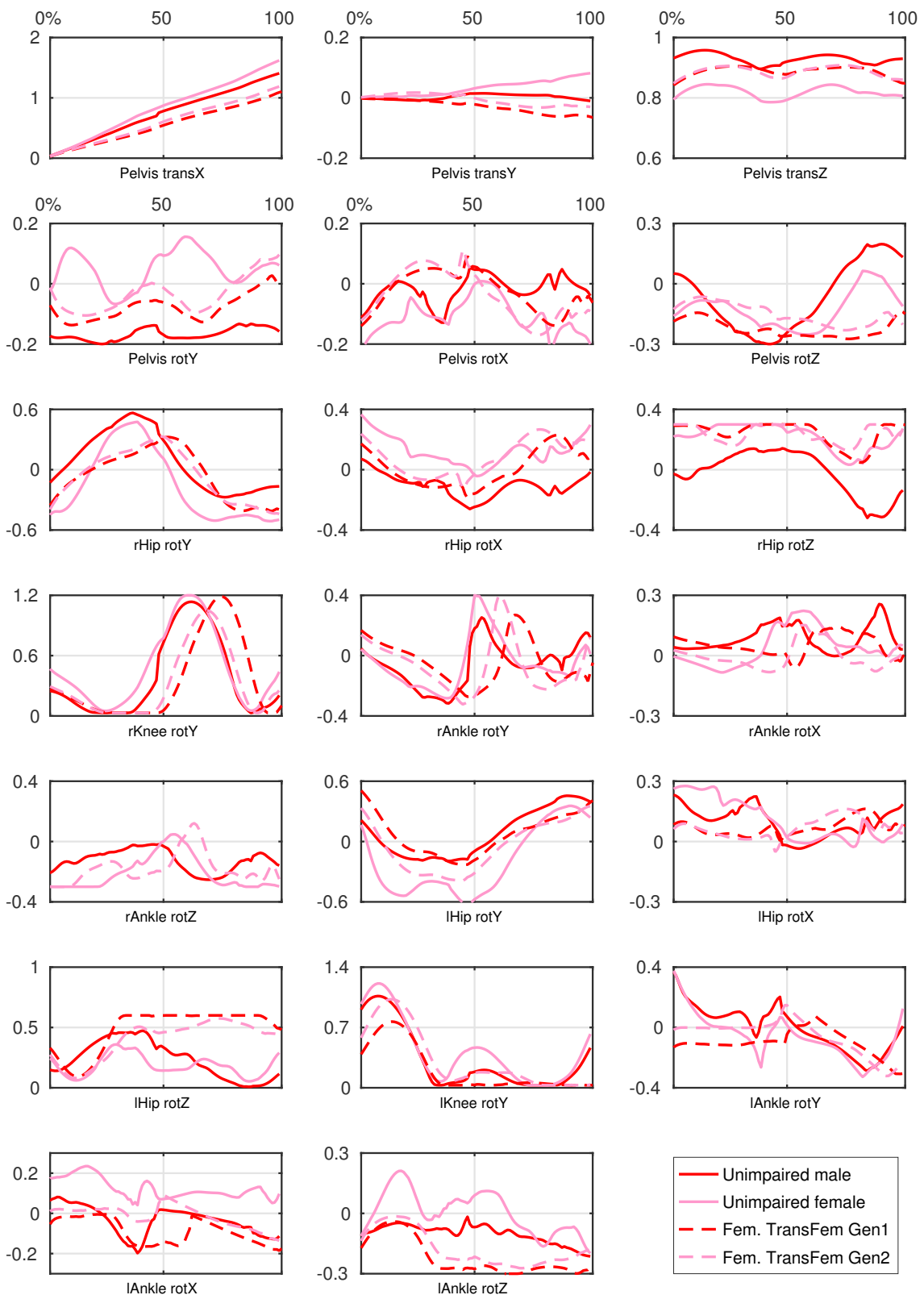


Figure 5.7: Generalized positions for the lower body resulting from the gait optimization. The first row shows the absolute translation of the pelvis [m]. The remaining plots contain rotations given in [rad].

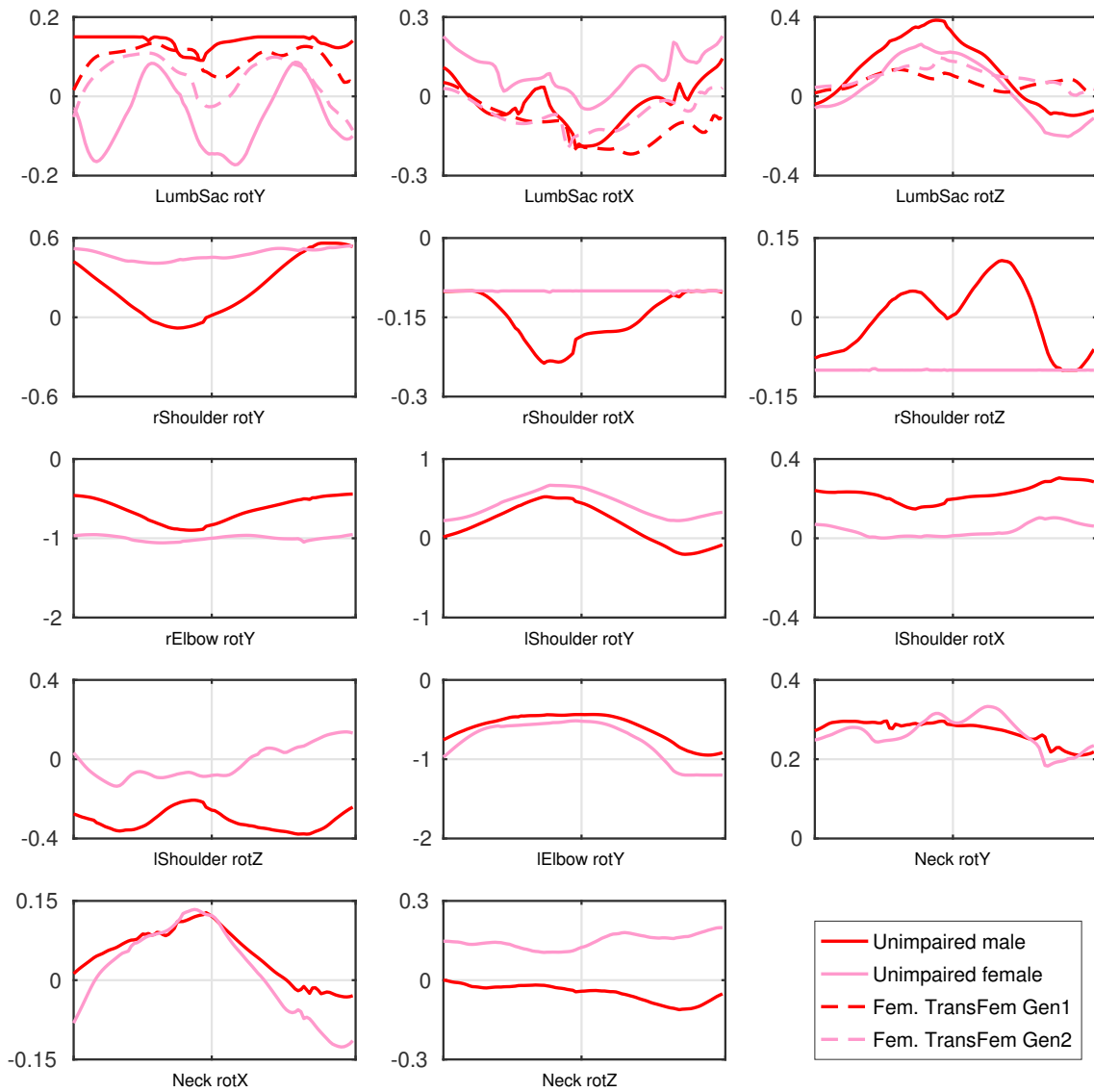


Figure 5.8: Generalized positions [rad] for the upper body resulting from the gait optimization. Arm motion has not been recorded for the female subject walking with transfemoral prostheses.

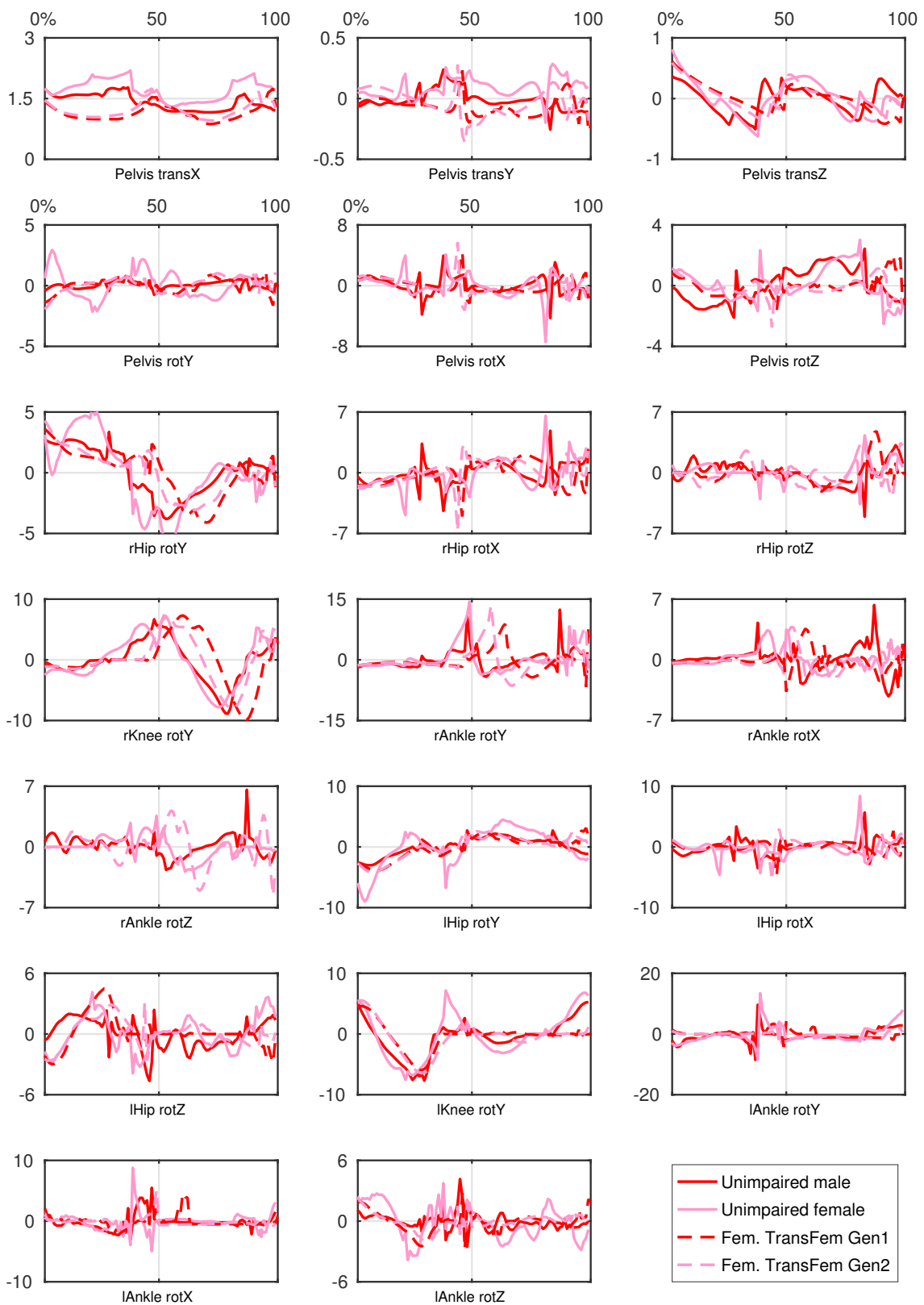


Figure 5.9: Generalized velocities for the lower body resulting from the gait optimization. The first row contains translational velocities [m/s]. The remaining plots show rotational velocities [rad/s].

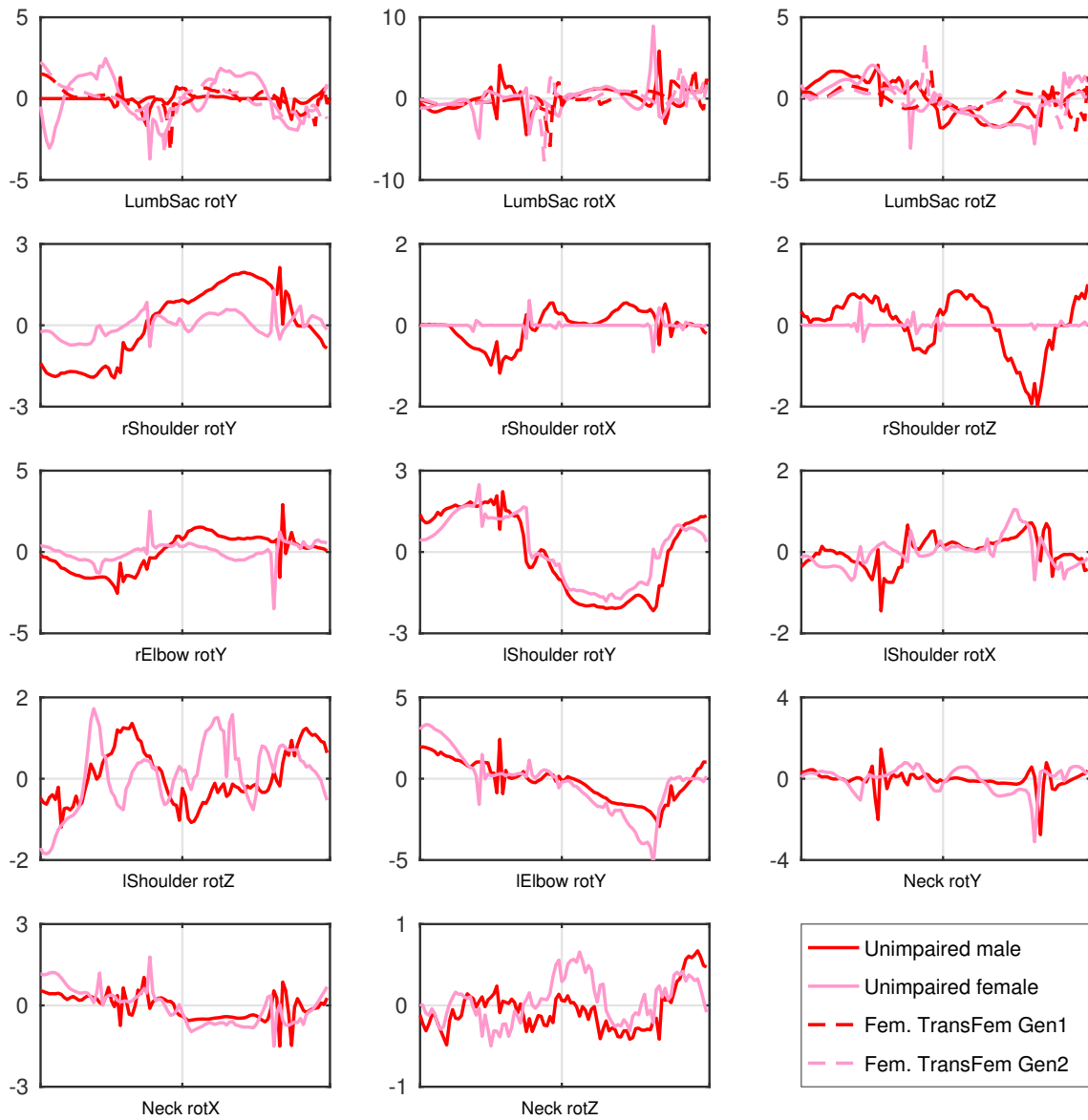


Figure 5.10: Generalized velocities [rad/s] for the upper body resulting from the gait optimization.

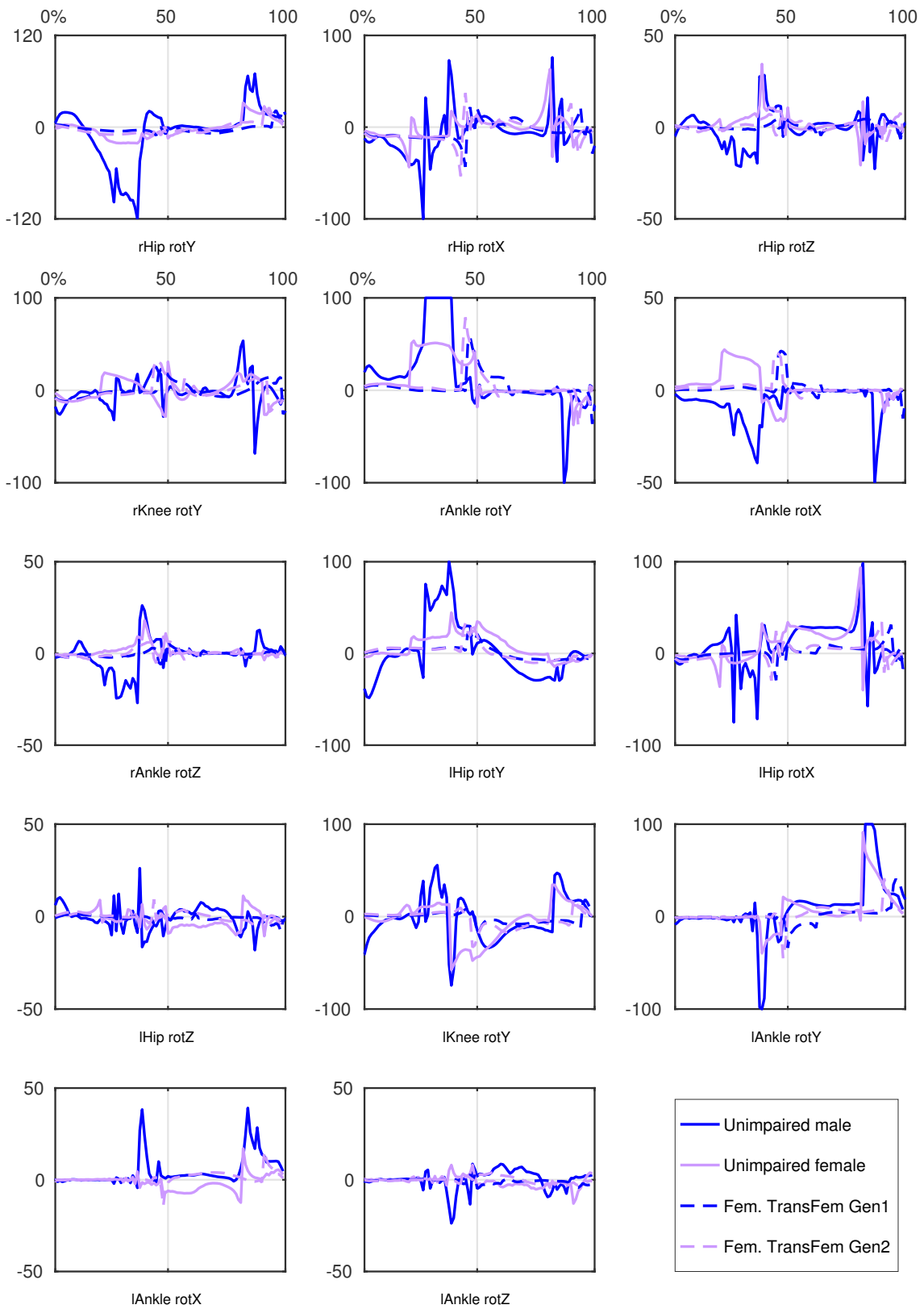


Figure 5.11: Generalized torques [Nm] for the lower body resulting from the gait optimization.

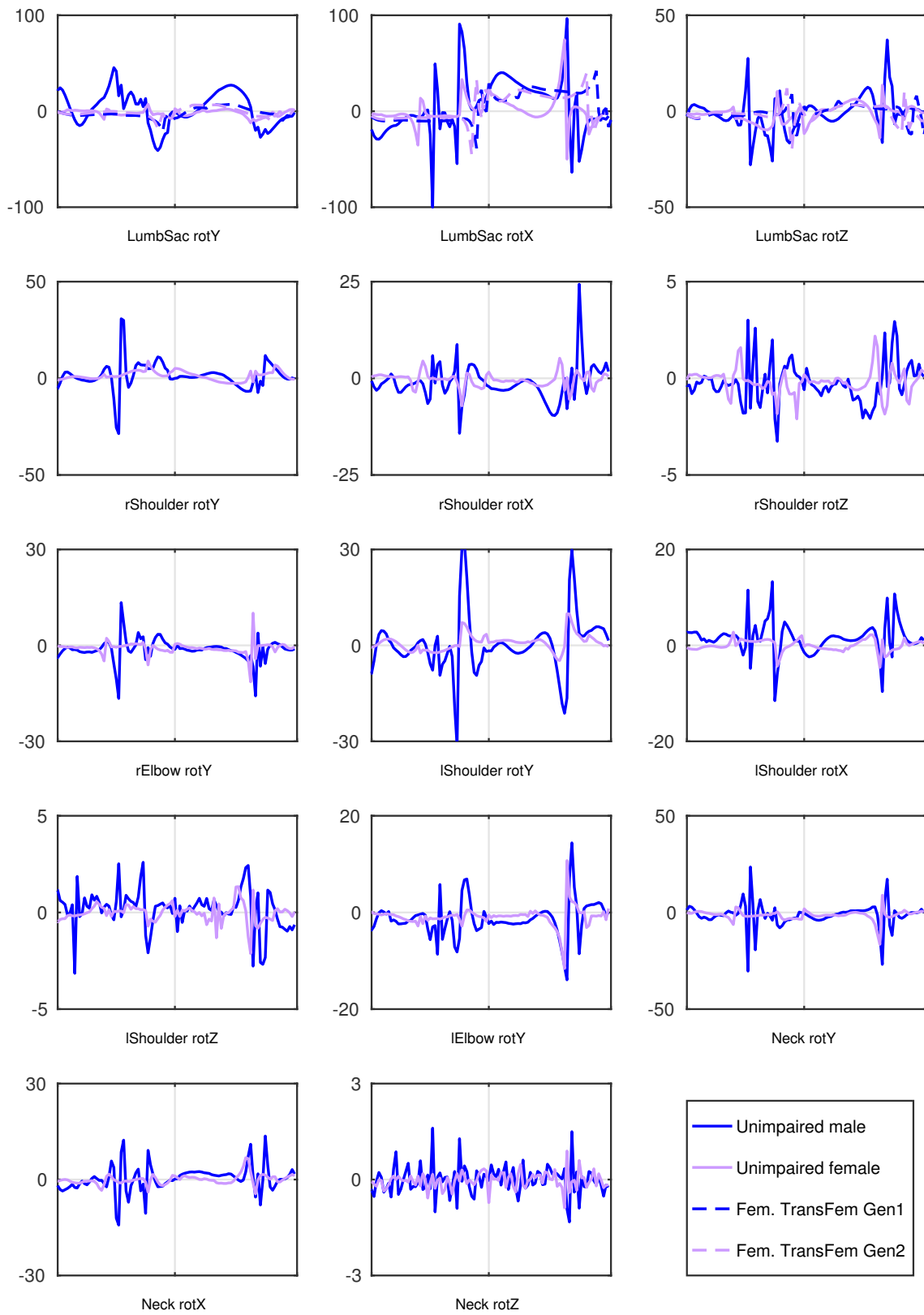


Figure 5.12: Generalized torques [Nm] for the upper body resulting from the gait optimization.

5.3.3. Comparison of Methods Used to Approximate the COM Location During Human Walking

Walking is a highly balanced motion characterized by anti-phased motions of the limbs maintaining the full body COM close to the body center. Depending on the desired complexity of the model in simulation tasks of human motions the full body COM of a human is often approximated by

- the center of mass of the pelvis $\mathbf{r}_{\text{com,pelv}}$,
- the weighted sum of the segment COMs $\mathbf{r}_{\text{com,real}}$ as described in (4.1).

These two COM approximation have been implemented in the computations for human walking and plotted in the Figures 5.13 - 5.14 for the sagittal and the horizontal plane, respectively. The deviations of both methods in the x , y , and z -directions are listed in Table 5.4.

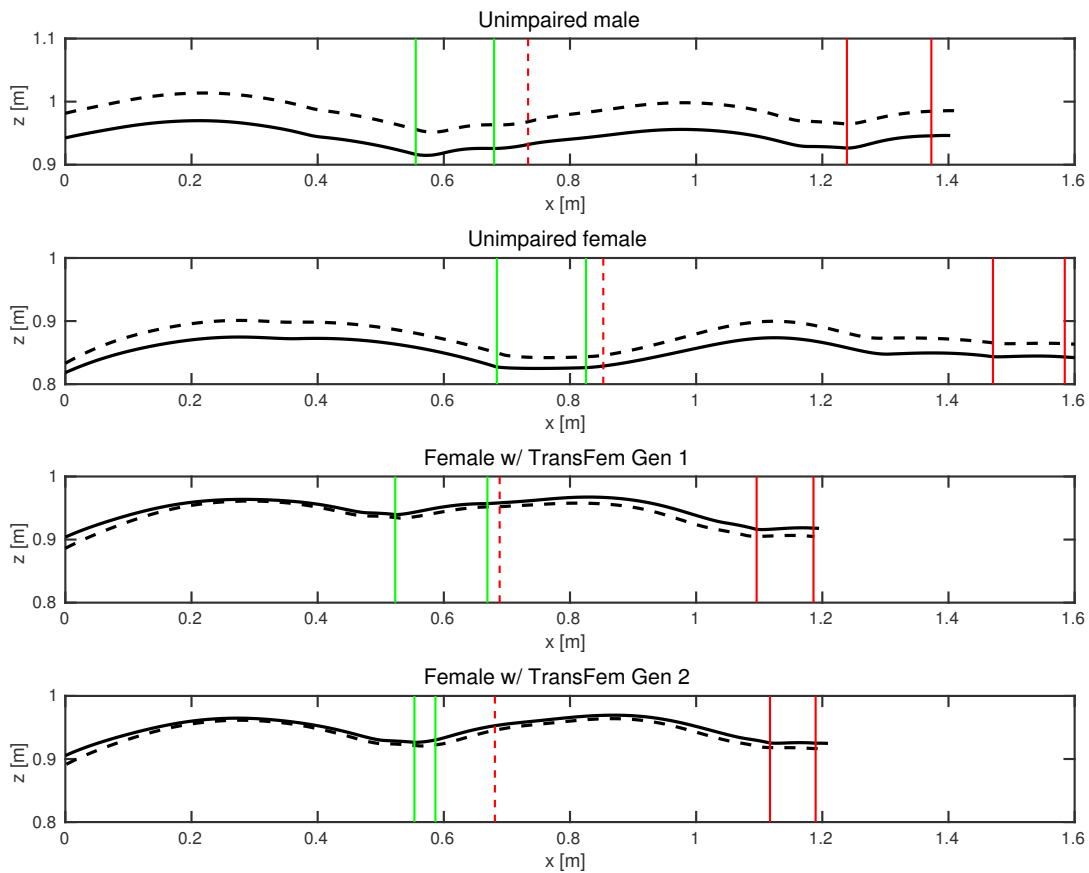


Figure 5.13: Trajectories of the Center of Mass (COM) of the subjects in sagittal plane estimated using the weighted sum of segment COMs (solid) and the pelvis COM (dashed).

In all considered scenarios, the vertical COM positions based on the two different approximation methods follow very similar trajectories only with a vertical offset of a few centimeters. While in the case of unimpaired humans $\mathbf{r}_{\text{com,real}}$ is located a few centimeters below $\mathbf{r}_{\text{com,pelv}}$, a much smaller deviation can be observed in case of the prosthetic walker. Since the mass of the prostheses is only about half of the mass of an unimpaired shank $\mathbf{r}_{\text{com,real}}$ is shifted closer towards $\mathbf{r}_{\text{com,pelv}}$.

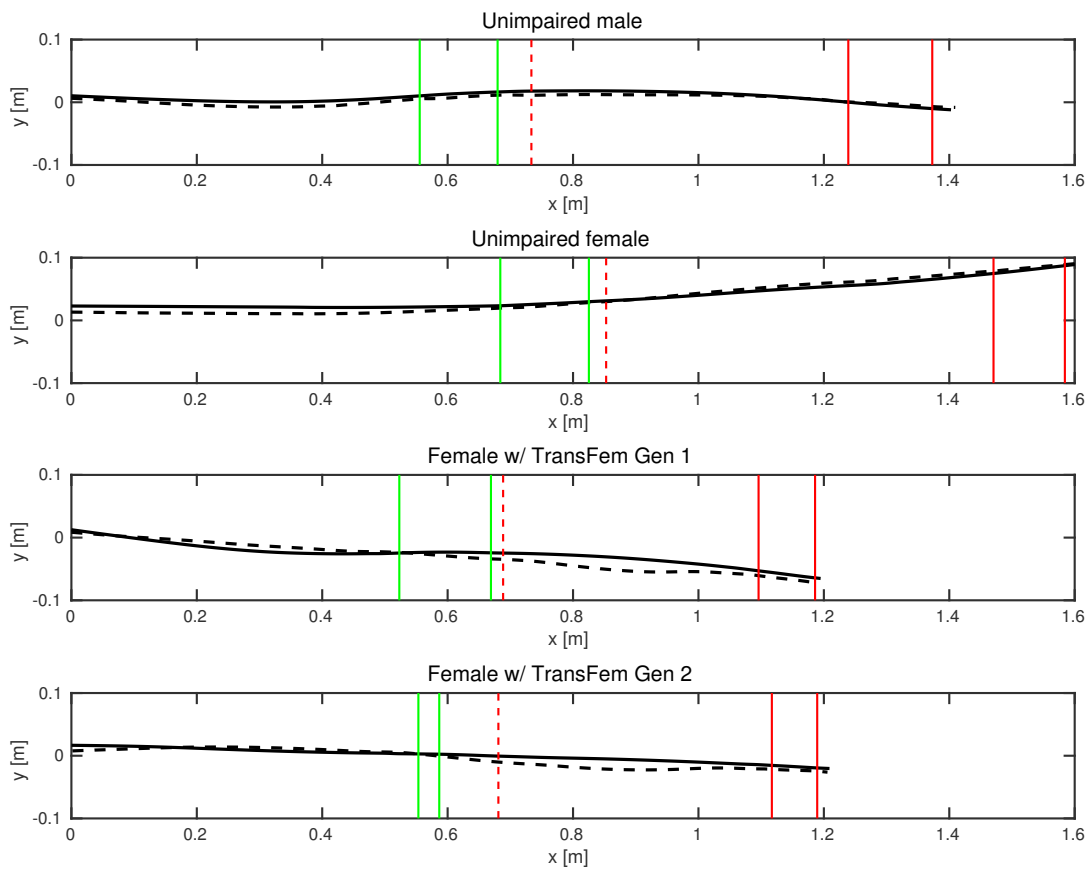


Figure 5.14: Trajectories of the Center of Mass (COM) of the subjects in horizontal plane estimated using the weighted sum of segment COMs (solid) and the pelvis COM (dashed).

Table 5.4: Deviations between the full body COMs in x , y and z -direction approximated by the pelvis COM and the weighted sum of the segment COMs. The deviations are provided as average, standard, minimum and maximum values in centimeters [cm].

Direction	Deviation	Unimpaired male	Unimpaired female	Female w/ TransFem Gen 1	Female w/ TransFem Gen 2
x	ave	-0.3 ± 0.5	-0.1 ± 0.8	0.4 ± 1.1	0.4 ± 0.9
	min	-1.3	-1.4	-1.6	-1.5
	max	0.7	1.5	2.3	1.9
y	ave	0.4 ± 0.3	0.2 ± 0.6	0.4 ± 0.9	0.5 ± 0.7
	min	-0.4	-0.5	-0.9	-0.5
	max	0.8	1.1	1.9	1.6
z	ave	-4.1 ± 0.2	-2.3 ± 0.3	0.7 ± 0.3	0.5 ± 0.2
	min	-4.4	-2.7	-0.2	-0.2
	max	-3.7	-1.7	1.7	1.4

Although the two approximation methods lead to very similar trajectories in the horizontal plane for the unimpaired male and female subjects, a larger deviation can be observed for the later part of the walking motion involving the prosthetic legs. As described earlier in this chapter, the upper body of the prosthetic walker leans towards the prosthetic side of the body during the right swing phase. Obviously, this lateral shift of the upper body COM, which represents almost 50% of the full body weight (Table 2.5) cannot be reflected by approximating the full body COM only by the pelvis COM. In case of asymmetric and other irregular motions approximating the full body COM by the weighted sum of the segment COMs should be favored. The computations performed in this thesis are based on this method for COM approximation.

5.3.4. Foot Placement Considering Instantaneous Capture Point

The walking motion recorded for the four scenarios *unimpaired male*, *unimpaired female*, *Female w/TransFem Gen 1*, and *Female w/TransFem Gen 2* have been described using the location of the Instantaneous Capture Point (ICaP) and the touch-down location of the foot with respect to it. Based on the gait characteristics elaborated in this part of the work, we consider the gait patterns of the unimpaired male subject as regular and aiming at a well-adjusted relation between energy-efficiency and safety. On the other hand, we consider the unimpaired female subject's gait patterns irregular based on the asymmetry as well as less consistent choices regarding safety and energy-efficiency. We analyze the prosthetic gait patterns and put them into context with the unimpaired ones.

For all four scenarios, Figure 5.15 visualizes the footprints as well as the trajectories of the ICaP and the gCOM for one stride with the gait directed into the positive x -direction. The location of the ICaP and the gCOM are highlighted for the time instances around the event of heel strike of the right and left foot, respectively. Significant gait parameters according to the definitions from Section 1.2.1 are summarized in Table 5.5.

General Gait Patterns

The gait pattern of the unimpaired male subject shown in Figure 5.15a appears symmetric and well-balanced due to the trajectories of the ICaP and the gCOM which both have a symmetric shape and lie well in between the right and left footprints. The step width is relatively wide but remains very similar for both sides (Table 5.5). Although both the step length and the step width are very consistent for the unimpaired male subject, the durations of the left and right step deviate by almost 50%. The ratio of the stance phase to the swing phase conforms to physiological patterns [125].

Despite the perfectly regular appearance, the unimpaired female's ICaP and gCOM trajectories reveal a tendency into the left direction, refer to Figure 5.15b. The gait parameters in Table 5.5 show a stronger deviation in step lengths between the right and left step, respectively, compared to the unimpaired male subject's gait as well as a very narrow step width. The large relative deviation in the unimpaired female's step width can be explained by the effect of moderate absolute deviations on small absolute values. The step durations deviate by more than 30%. Similar to the unimpaired male subject, the stance-swing phase ratio is according to physiological behavior.

The asymmetric behavior of the unimpaired female subject's ICaP and gCOM can be traced back to the subject's full body motion patterns. Observing the shoulder motion in sagittal

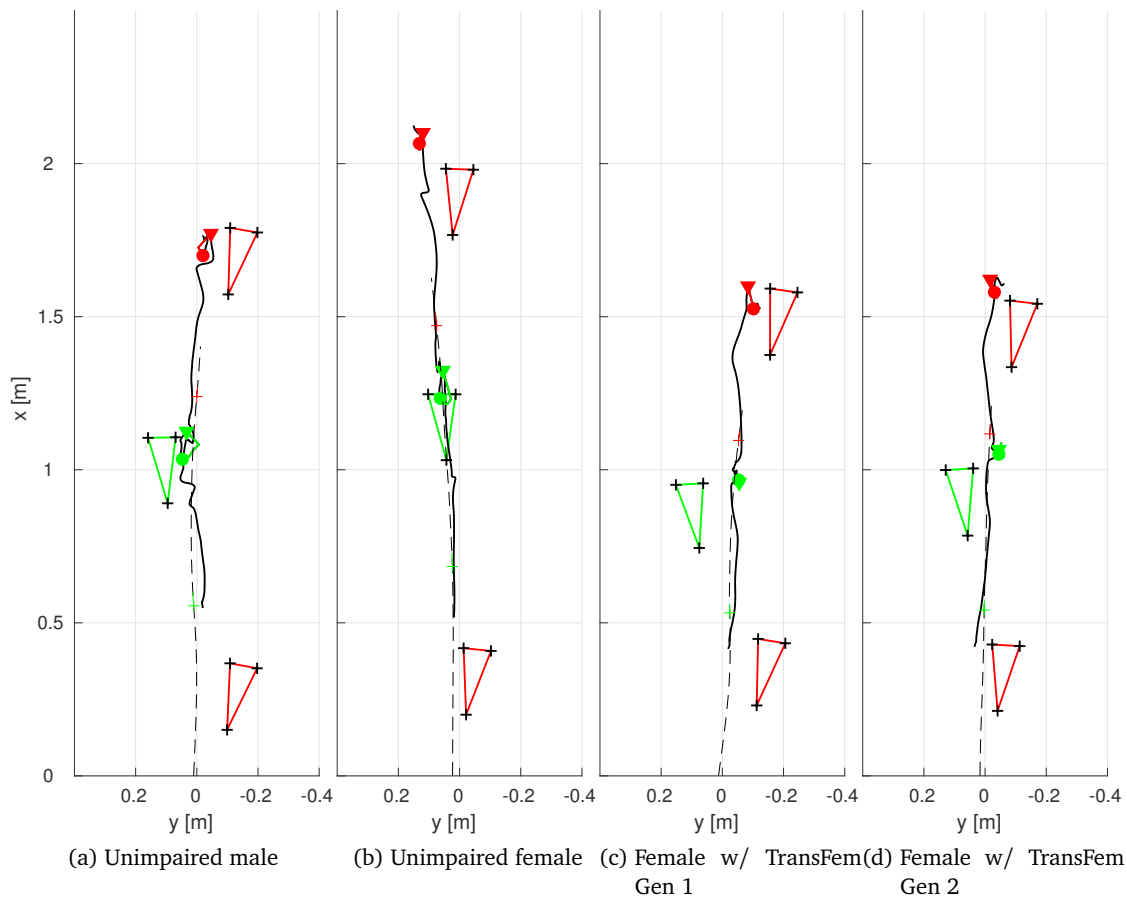


Figure 5.15: Footprints of left (green) and right (left) feet in relation with the trajectories of Instantaneous Capture Point (ICaP, solid) and ground Center of Mass (gCOM, dashed) of (a) unimpaired male, (b) unimpaired female subjects as well as of the female subject walking with the unilateral transfemoral prosthetic (c) TransFem Gen 1 and the (d) TransFem Gen 2 replacing the left leg of the subject. The figure also includes the position of the ICaP right before (Δ) and after (\circ) ground contact of the left and right foot, respectively, as well as the position of the gCOM right at ground contact (+). The gait direction is in positive x -direction.

plane shows that the unimpaired female subject (Figure 5.5b) has a dominant swing in the right arm while the left arm remains almost static. Oppositely, the unimpaired male subject has an elaborative and almost symmetric arm swing behavior (Figure 5.5a).

The gait of the subject walking with prosthetic legs is slower than the unimpaired gait adjusted by both, shorter steps and longer step durations, refer to Table 5.5. In case of the TransFem Gen 1, both the step lengths and step durations are highly symmetric. The step width is rather wide and deviates by more than 20% which gives the gait motion a slightly unsteady appearance. While walking with the TransFem Gen 2 results in quite consistent step durations and rather narrow step widths, the step lengths deviate by 18%. The stance-swing phase ratio deviates significantly from the physiological pattern and indicates a shorter noticeably shorter stance duration on the prosthetic leg.

The front view of the walking motions shown in Figure 5.6 confirms the wide step width for the unimpaired male (a) and the rather narrow steps and irregular appearance for the unimpaired female subject. The subject walking with both the TransFem Gen 1 (c) and the TransFem Gen 2

Table 5.5: Gait parameters from the scenarios *unimpaired male*, *unimpaired female*, *Female w/ TransFem Gen 1*, and *Female w/ TransFem Gen 2*. Step lengths and widths are evaluated as the distance in x and y -direction, respectively, between the heel positions of the consecutive steps. Furthermore, the durations of the single support (SS) and double support (DS) phases as well as the ratio of the swing phase to the stance phase are listed for the left and the right step, respectively. The front foot outreach (FFO) and the rear foot outreach (RFO) are fundamental segments of the step length and have been introduced in Section 1.2.

Gait parameter	Unit	Unimpaired male	Unimpaired female	Female w/ TransFem Gen 1	Female w/ TransFem Gen 2	
Gait velocity	[m/s]	1.42	1.72	1.22	1.15	
Left	Step length	[cm]	74.0	83.2	51.5	57.6
	Step width	[cm]	19.4	6.4	18.8	9.7
	SS duration	[s]	0.35	0.37	0.47	0.46
	DS duration	[s]	0.15	0.11	0.15	0.12
	Stance/swing	[s/s]	0.65/0.35	0.61/0.39	0.55/0.45	0.53/0.47
	FFO/RFO	[cm/cm]	33.5/40.5	34.7/48.5	22.2/29.3	23.5/34.1
Right	Step length	[cm]	68.2	73.6	63.0	54.7
	Step width	[cm]	19.8	2.1	23.1	14.3
	SS duration	[s]	0.37	0.39	0.33	0.33
	DS duration	[s]	0.13	0.09	0.08	0.07
	Stance/swing	[s/s]	0.59/0.41	0.68/0.32	0.46/0.54	0.50/0.50
	FFO/RFO	[cm/cm]	33.4/34.8	29.7/43.9	27.9/35.1	21.8/32.9

(d) tends to lean strongly towards the prosthetic side during the swing phase of the unimpaired side. As explained earlier in this chapter this pattern is adapted to compensate for a lack of muscular strength in the residual limb of the impaired leg.

Instantaneous Capture Point Patterns

Figure 5.15 shows that during human walking step locations are chosen such that the ICaP is approximately reached by the toes of the anterior foot in sagittal direction. Due to the loss in kinetic energy during the touch-down impact and the corresponding loss in gait velocity (see Figure 5.16), the ICaP moves back closer to the mid foot. Generally, well-balanced gait maintains the ICaP between both feet in lateral direction simplifying the lateral oscillation from one stance leg to the other.

Capturability in Human Walking

In case of the unimpaired male subject (Figure 5.15a) both feet are consistently placed such that the ICaP is reached by the forefoot and the touch-down impact is scaled such that the ICaP moves under the mid foot. This behavior enables the subject to quickly navigate the CoP onto the ICaP only by applying ankle torque in case a sudden stop should be desired. Although

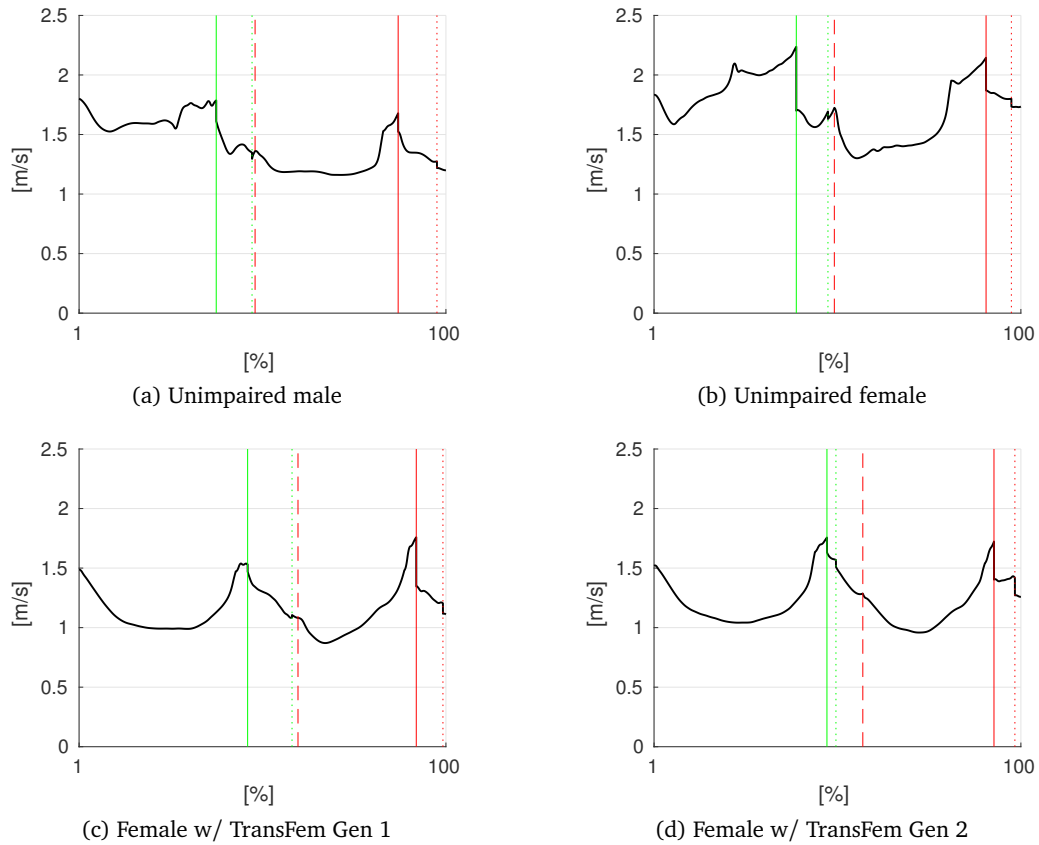


Figure 5.16: Step-by-step gait velocity in sagittal plane. The gait phases heel strike (solid), toe strike (dotted) and toe off (dashed) are indicated for the left (green) and right (red) foot, respectively.

the average gait velocity differs slightly between the two steps, the velocity loss at heel strike is consistent for both feet with $\Delta v_x \approx 0.17$ m/s, refer to Figure 5.16a.

The asymmetric gait patterns of the unimpaired female subject is also reflected in the ICaP behavior (Figure 5.15b). While the left foot touches the ground with a rather great impact and the ICaP is brought right under the forefoot in both sagittal and lateral direction, the right foot is placed much further from the respective ICaP location and the lower impact at ground-contact fails to bring the ICaP significantly closer to the foot. In case of a sudden perturbation, the unimpaired female subject would have to apply additional strategies other than the ankle strategy in order to come to a complete stop.

The prosthetic gait patterns seem well-balanced with both the ICaP and gCOM trajectories running almost symmetrically between the footsteps. Walking with the TransFem Gen 1 results in more conservative gait patterns with the ICaP being reached with the forefoot in sagittal plane. TransFem Gen 2 gait patterns show a more dynamic behavior since the ICaP is located further from the heel and barely reached by the toes. For both prosthetic devices, the *pre-impact* locations of the ICaP are symmetric for the right and left leg.

For walking with both prosthetic devices, the velocity loss at touch-down of the unimpaired leg matches the values for the unimpaired subjects bringing the ICaP closer to the mid foot. However, the velocity loss becomes much smaller when the prosthetic leg touches the ground and, in consequence, the ICaP does not significantly move towards the mid foot.

The ICaP allows for further analysis of the gait behavior in terms of the Orbital Energy E_{lip} of the Linear Inverted Pendulum Model (LIPM) representing the human body during gait. As defined in Definition 7 in Section 4.4.1, we extend the orbital energy E_{lip} towards the *Instantaneous Orbital Energy* E_{inst} which expresses the Orbital Energy of the LIPM at a given time instance taking into account the current COM height and assuming that the velocity vector is horizontal.

In order to assess the gait quality of a subject, we analyze the *foot placement strategy* which includes the *location* where the subject chooses to place the swing foot, the *step duration* after which the swing foot is placed as well as the self-selected *impact* occurring at heel strike. We put our particular interest upon the value of the Instantaneous Orbital Energy in the instances right before and after the heel strike. Figure 5.15 confirms the hypothesis formulated in Section 4.4.1: Human walking is performed in a such manner that the ICaP is not directly reached by the CoP. Rather than that, a positive residual amount of the orbital energy is maintained in order to progress into the next step.

Based on that notion, we introduce the expression *Residual Instantaneous Orbital Energy* $E_{res,inst}$, the non-zero amount of E_{inst} at heel strike, to provide a measure for the foot placement strategy during walking. Furthermore, we differ between

- (i) $E_{res,inst,-}$: the Residual Instantaneous Orbital Energy **right before** the impact,
- (ii) $E_{res,inst,+}$: the Residual Instantaneous Orbital Energy **right after** the impact and
- (iii) $\Delta E_{res,inst} = E_{res,inst,-} - E_{res,inst,+}$: the loss in Residual Instantaneous Orbital Energy due to the impact.

In particular, the value of $E_{res,inst,-}$ allows for an evaluation of the temporal-spatial gait parameters step length and step duration adjusted by the subject based on the parameters gait velocity, gCOM-CoP distance and COM height right at heel strike (Equation (4.26)). The value of $\Delta E_{res,inst}$ is determined by the loss of kinetic energy and, thus, gait velocity due to the ground collision impact at heel strike. Eventually, $E_{res,inst,+}$ can be interpreted as the actual Residual Instantaneous Orbital Energy which characterizes the specific gait behavior of the subject established by the self-selected combination of the temporal-spatial gait parameters mentioned above and the magnitude of the heel strike impact.

Figure 5.17 shows E_{inst} during *Left Swing/Right Support* (green) and *Right Swing/Left Support* (red), respectively. The Residual Instantaneous Orbital Energy $E_{res,inst}$ are highlighted right before ($E_{res,inst,-}$, Δ) and after ($E_{res,inst,+}$, \circ) heel strike. The transition from the green to the red curve, and vice-versa, is not necessarily continuous since a new LIPM configuration is set up at each heel strike. With each step, the new LIPM is based on a continuous COM trajectory, however, also using a discrete CoP position when the pendulum's base is switched from the CoP position $\mathbf{r}_{cop,rear}$ of the rear foot in terminal stance to the CoP position $\mathbf{r}_{cop,front}$ of the front foot just about to touch the ground, refer also the illustration in Figure 5.18. In fact, according to (4.26), the discontinuity at the heel strike event (t_{hs}) in

$$E_{inst,hs} = \begin{cases} E_{inst,rear} & \text{for } t < t_{hs} \\ E_{inst,front} & \text{for } t \geq t_{hs} \end{cases} \quad (5.2)$$

is caused by the loss in gait velocity $\Delta \dot{\mathbf{x}}^2$ (Figure 5.16) and the difference between the *rear foot outreach (RFO)* and the *front foot outreach (FFO)* $\Delta(\mathbf{r}_{com,x} - \mathbf{r}_{cop,x})^2$ such that

$$\Delta E_{inst,hs} \sim \Delta \dot{\mathbf{x}}^2 - \frac{\Delta(\mathbf{r}_{com,x} - \mathbf{r}_{cop,x})^2}{\omega_0^2}. \quad (5.3)$$

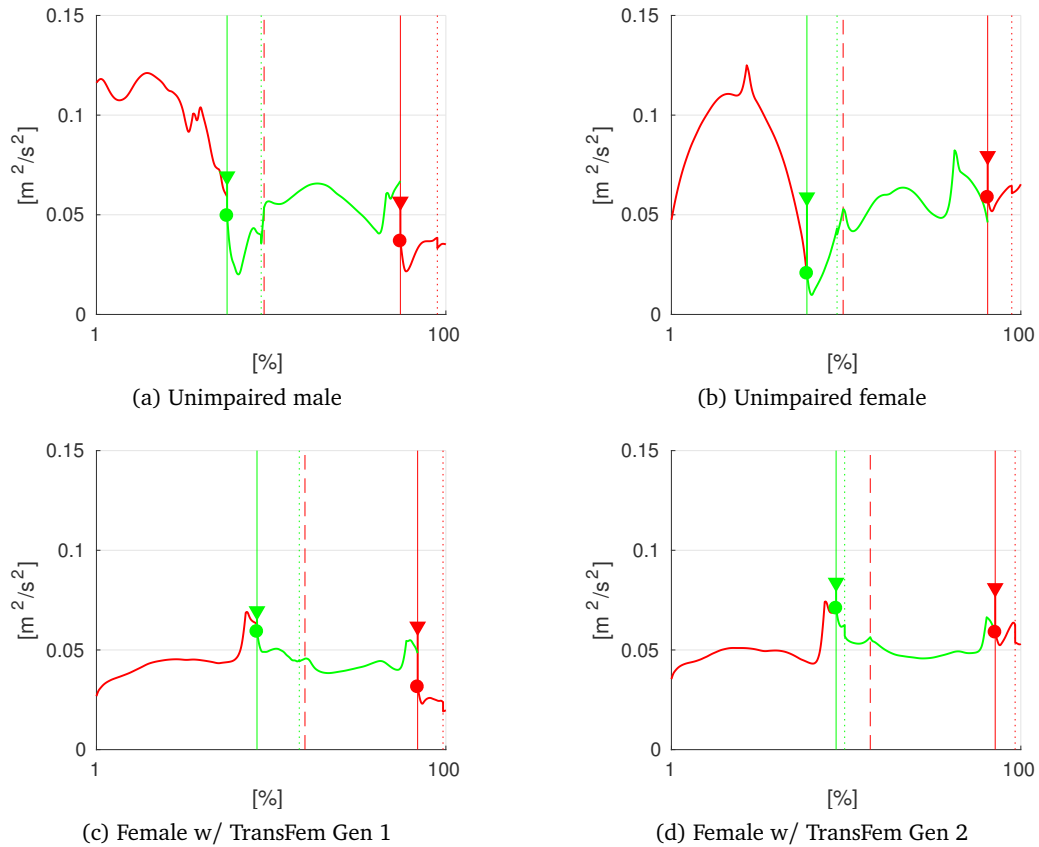


Figure 5.17: Step-by-step Instantaneous Orbital Energy $E_{inst,x}$ in sagittal plane. The curve is divided into parts corresponding to the Orbital Energy of the LIPM during *Left Swing/Right Support* (red) and a part for the *Right Swing/Left Support* (green), respectively. The Residual Instantaneous Orbital Energy $E_{res,inst,x}$ is indicated for the left (green) and the right (red) heel strike right before (Δ) and after (\circ) the respective impact.

The unimpaired subjects show a strongly asymmetric orbital energy behavior which is mostly caused by the inconsistent step-by-step gait velocity, compare to Figure 5.16. A noticeable symmetric behavior can be observed in the orbital energy losses $\Delta E_{res,inst}$ between the right and left heel strike of the unimpaired male subject reflecting a well-controlled ground impact behavior and, thus, a consistent balancing strategy in moving the ICaP close to the mid-foot area in sagittal plane after each heel strike.

In contrast to that, the asymmetric gait patterns of the unimpaired female subject lead to a very large $E_{res,inst,-}$ before the left heel strike caused by the step location chosen very far from the ICaP and to a even larger value before the right heel strike. A noticeably large impact after this subject's left heel strike causes a great loss in orbital energy. The combination of a great loss of energy due to the large impact and a great CoP-ICaP distance implies a walking motion that is possibly neither aimed at being energy efficient nor particularly secure.

The prosthetic gait patterns resemble the assumption of an energy conserving LIPM closer than the unimpaired gait patterns, since over most of the swing phases of each leg the Instantaneous Orbital Energy varies less than in unimpaired gait. For both feet a symmetric combination of gait velocity, step length and step timing at the respective heel strikes leads to almost symmetrical values for $E_{res,inst,-}$. However, the losses $\Delta E_{res,inst}$ occurring at the heel strike impacts of the prosthetic legs are remarkably low compared to the unimpaired legs. This behavior indi-

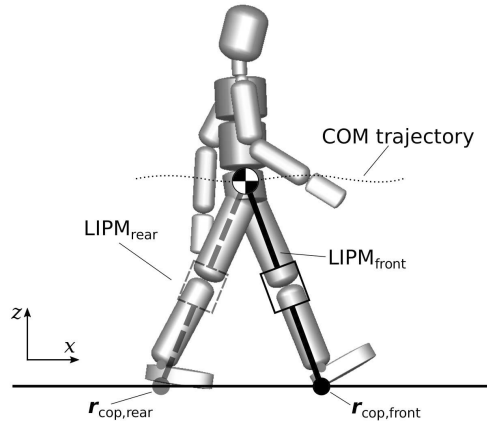


Figure 5.18: With each heel strike the linear inverted pendulum underlying the just ending single support phase $LIPM_{rear}$ is replaced by the newly established $LIPM_{front}$ representing the subsequent single support phase. The distance between $r_{cop,rear}$ and $r_{com,x}$ indicates the *rear foot outreach (RFO)*. The adjacent double support phase is not further regarded here.

cates that the subject avoids greater impacts at the prosthetic leg to prevent pain and injuries in the socket-stump interface, i.e. the region where the prosthetic device is attached to the subject. Because of this, the ICaP remains out of reach for the prosthetic foot and since joint torques cannot be actively applied in the prosthetic leg, the subject must fully rely on more extensive compensation strategies other than the ankle strategy to come to a stop in case of an unexpected perturbation. Enhancing the prosthetic design such that a greater amount of energy is dissipated and the gait velocity is further reduced at heel strike would cause the ICaP to move closer towards the CoP and provide better security in terms of Capturability.

Table 5.6: Residual Instantaneous Orbital Energy $E_{res,inst}$ [m^2/s^2] for left and right heel strike in *unimpaired male, unimpaired female, Female w/ TransFem Gen 1, and Female w/ TransFem Gen 2* gait before ($E_{res,inst,-}$) and after ($E_{res,inst,+}$) the impact at heel strike. $\Delta E_{res,inst}$ refers to the loss of orbital energy due to the impact.

Event		Unimpaired male	Unimpaired female	Female w/ Trans Fem Gen1	Female w/ Trans Fem Gen2
Left HS	$E_{res,inst,-}$	0.0693	0.0588	0.0695	0.0838
	$E_{res,inst,+}$	0.0495	0.0206	0.0592	0.0709
	$\Delta E_{res,inst}$	-0.0198	-0.0382	-0.0103	-0.0129
Right HS	$E_{res,inst,-}$	0.0566	0.0795	0.0618	0.0811
	$E_{res,inst,+}$	0.0367	0.0587	0.0314	0.0588
	$\Delta E_{res,inst}$	-0.0199	-0.0208	-0.0304	-0.0223

Based on the interpretation of the ICaP and the orbital energy and considering the gait patterns analyzed in this section, we formulate following statements which indicate the trade-off between energy-efficiency and security in well-adjusted gait:

- The farther a step is placed behind the ICaP the greater amount of Residual Instantaneous Orbital Energy can be exploited to propel into the next step leading to a more energy efficient gait.
- The closer a step is placed to the ICaP the quicker the CoP can be aligned with the ICaP to come to a complete stop leading to a more *capturable* gait.
- Well-adjusted gait is oriented towards a trade-off between these two strategies by placing the foot such that the ICaP is aligned with the forefoot right before heel strike
- The amplitude of the ground collision impact force is adjusted such that the ICaP is aligned with the mid foot right after heel strike.

In consequence, greater values for $E_{res,inst}$, refer to the definition in equation (4.26), come along with a greater CoP-ICaP distance and indicate that the steps are inappropriately short for the selected gait velocity in terms of Capturability, however, lead to a more energy-efficient gait. Based on these criteria, the prosthetic gait analyzed in this thesis can be regarded as energy-efficient and well-adjusted. In case of walking with the TransFem Gen 1, the gait patterns are more conservative and capturable with wider steps and the ICaP kept underneath the forefoot. The gait patterns using the TransFem Gen 2 resembles slightly more dynamic gait with narrower step widths and the ICaP a little further out of reach. Considering the whole body motion, the asymmetric appearance and temporal-spatial gait patterns of the prosthetic gait compensate for a lack of muscular strength in the residual limb and for asymmetric dynamic body segment properties. Their application leads to a symmetric and well-adjusted foot placement strategy in terms of Capturability.

5.4. Discussion

It has been shown in this chapter that, during walking, foot placement represented by the CoP position is correlated to the ICaP location. However, humans do not align the CoP with the ICaP but place it on a further lateral-posterior location such that the ICaP lies just medial to the forefoot. This way they are able to maintain energy efficient locomotion, however, sacrifice a small amount of security in terms of being unable to come to a stop without any additional effort. In fact, a foot position is chosen which enables the human to progress in forward direction while exploiting a positive residual orbital energy. Ground contact collision occurs at the event of heel strike and causes a loss in kinetic energy and, thus, a reduction of the gait velocity. Due to the collision impulse, the ICaP is brought closer back to the CoP and its magnitude is adjusted such that the ICaP moves right underneath the mid foot. This way, propelling Residual Orbital Energy is maintained while, in case of an unexpected perturbation, it is still possible for the human walker to come to a stop in one step by applying a quick and appropriate torque on the ankle.

A similar pattern could be observed in the cases of prosthetic walking analyzed in this thesis. Asymmetry in terms of step length, upper body motion, and impact force at right and left heel strike, respectively, as well as a combination of a slower gait velocity during swing of the prosthetic leg and a shorter step enables the prosthetic walker to maintain a symmetric step duration as well as a symmetric CoP-ICaP distance right before both the unimpaired and prosthetic heel strike.

Prosthetic gait is associated with hard impacts which should be avoided in order to prevent pain in the interface region between the residual limb and the prosthetic socket [80, 127].

However, due to the the lack of a significant ground collision impact at heel strike of the prosthetic leg the subject fails to move the ICaP towards the mid foot area. Since no active ankle torque can be applied on the prosthetic foot, in case of an unexpected emergency the subject would have to place an additional step or apply extensive upper body momentum to come to a stop on the prosthetic leg. A possible measure to ensure a more conservative ICaP position right after heel strike of the prosthetic side, and to maintain a higher level of security, could be to enhance the design of the prosthetic leg such that it dissipates energy at ground collision impact to an amount similar to the unimpaired side.

A major drawback in this part of the thesis is the lack of recorded arm motion for the subject walking with prostheses. Placing markers on the arms of the subject has been omitted during the preparation for the experiments in order to avoid additional distraction of the subject. Although the subject's arm motion has been observed to be minimal on video recordings of the experiments, we cannot entirely excluded any influence on the upper body dynamics.

Capturability has not yet been considered in traditional movement analysis. Based on these findings, we propose Capturability, evaluated on walking motions reconstructed using optimal control, as a complementary criterion to the traditional clinical stability assessment methods. Due to the novel perspective in the interpretation of human walking stability it might lead to a further progress in target-oriented clinical diagnostics. However, in order to be able to deliver reliable clinical results it is crucial to gain more experience in clinical experiments.

6. OPTIMAL SIT-TO-STAND MOTIONS

In the field of motion analysis a particular interest lies in optimizing the motion transfer from sitting to standing, commonly called the *sit-to-stand (STS)* motion. Large torques are applied on the joints of the lower body in order to lift the better part of the body mass into an erect pose. This way, the STS transfer can be considered one of the most physically demanding everyday tasks in a human life, especially for elderly people.

In Chapter 5, human walking motions are reconstructed from recorded motion data using optimal control methods and subject-specific multibody models. This approach allows for analysis of individual gait patterns based on physiologically consistent motions considering the entire dynamics of the system.

In this part of the thesis, however, model-based optimal control methods are applied to *predict* the STS motion. We consider models representing elderly humans in three different cases reflecting different levels of mobility capabilities: *high-dynamic*, *unimpaired* and *severely impaired*, respectively. In contrast to the *unimpaired* STS motion, the *high-dynamic* case is an example to study motion sequences which would arise if a greater amount of the full body dynamics would be exploited by unimpaired humans. *Severely impaired* describes geriatric subjects with a stroke history or suffering from Parkinson's disease, dementia or other diseases that affect mobility and cognitive functions. Due to their high level of immobility, the group of impaired subjects is not able to perform the STS transfer without assistance. Consequently, the STS optimization for the geriatric subjects includes assistive forces applied at suitable body parts. The terms for the cost function of the optimal control problem have been heuristically determined in consultation with clinical experts.

In Section 6.1, we establish the model for the STS simulation including external support forces which are supposed to assist the unimpaired subject. The optimal control problem for the STS motion generation is described in Section 6.2. The Sections 6.3 and 6.3 present the simulation results for the unassisted STS and the assisted STS motion, respectively.

6.1. Modeling of Sit-to-Stand Motions

For the optimization of the STS motion the human body is modeled according to the procedure described in Section 2.3. However, since STS transfers can be assumed to be symmetric with respect to the sagittal plane, the model can be reduced to an 2-dimensional 8-segmented multibody system where the right and left arm and leg segments are merged into combined segments, respectively. Since in this STS problem, the feet are not supposed to move with relative to the global coordinate system, they are chosen as the root segment of the multibody model exploiting their constant position and orientation to define the absolute position and orientation of the whole model. This way, the model consists only of rotary DoFs and their number can be reduced to 8 (Figure 6.1).

The model is actuated by 8 torques acting on the joints *ankle*, *knee*, *hip*, *Lumbo-Sacral joint*, *Xiphoid*, *Cervicale*, *shoulder* and *elbows*. In order to realistically reflect motions of elderly humans, dynamic model parameters are implemented in the models which are specifically adjusted to the body proportions of elderly people using the regression equations from Section 2.4.2. The resulting parameters can be found in Table 2.4.

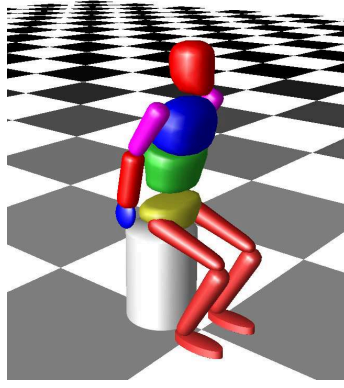


Figure 6.1: The multibody model based on the model described in Section 2.3. Since the STS motion is assumed to be symmetric, the model can be reduced to the sagittal plane. Since also the feet are chosen as the root segment, the model can further be reduced to 8 rotary DoF.

The STS motion of the geriatric subjects is assumed to be supported by external forces. Hence, the equations of motion introduced in Section 2.2 are enhanced by a term for external forces

$$\begin{pmatrix} \mathbf{H} & \mathbf{G}^T \\ \mathbf{G} & \mathbf{0} \end{pmatrix} \begin{pmatrix} \ddot{\mathbf{q}} \\ -\boldsymbol{\lambda} \end{pmatrix} = \begin{pmatrix} \mathbf{C} + \boldsymbol{\tau} + \boldsymbol{\tau}_{\text{ext}} \\ \boldsymbol{\gamma} \end{pmatrix} \quad (6.1)$$

where \mathbf{H} is the inertia matrix in joint space, \mathbf{G} the point Jacobians of the contact points, $\ddot{\mathbf{q}}$ the joint accelerations, and $\boldsymbol{\lambda}$ the contact forces. \mathbf{C} is the vector of generalized nonlinear effects that contains the Coriolis, centrifugal and gravitational forces, $\boldsymbol{\gamma}$ the part of the contact point accelerations which are independent from the generalized accelerations, and $\boldsymbol{\tau}$ the joint torques. External forces \mathbf{f}_{ext} are included into the equations of motion (6.1) in state space as the product of the forces and the translated *Jacobian* $\mathbf{G}_{\text{ext}}^T$ of their application points $\boldsymbol{\tau}_{\text{ext}} = \mathbf{G}_{\text{ext}}^T \mathbf{f}_{\text{ext}}$. For the unassisted STS motions $\boldsymbol{\tau}_{\text{ext}}$ remains zero since no assistive force is applied.

6.2. Optimal Control Problem for Sit-to-Stand Motions

The multi-phase optimal control problem for the STS motion can be formulated as

$$\min_{\mathbf{x}(\cdot), \mathbf{u}(\cdot), \boldsymbol{\tau}} \sum_{i=1}^2 \int_{\tau_{i-1}}^{\tau_i} \left(\sum_{j=1}^{n_{\text{act}}} (\alpha \mathbf{u}_j^2 + \beta |\mathbf{u}_j \dot{\mathbf{q}}_j|) + \gamma \dot{\mathbf{q}}_{\text{head}}^2 + \delta \sum_{k=1}^{n_{\text{ext}}} \mathbf{u}_{\text{ext},k}^2 \right) dt \quad (6.2a)$$

subject to:

$$\dot{\mathbf{x}}(t) = \mathbf{f}_i(t, \mathbf{x}(t), \mathbf{u}(t), \mathbf{p}) \quad (6.2b)$$

$$0 \leq \mathbf{g}_i(t, \mathbf{x}(t), \mathbf{u}(t), \mathbf{p}) \quad (6.2c)$$

$$0 = \mathbf{r}^{\text{eq}}(\mathbf{x}(0), \dots, \mathbf{x}(T), \mathbf{p}) \quad (6.2d)$$

$$0 \leq \mathbf{r}^{\text{ineq}}(\mathbf{x}(0), \dots, \mathbf{x}(T), \mathbf{p}) \quad (6.2e)$$

$$\text{for } t \in [\tau_{i-1}, \tau_i], i = 1, 2, \tau_0 = 0, \tau_2 = T$$

The objective function (6.2a) is a weighted combination of four cost terms which have been heuristically determined in consultation with clinical experts¹ to underlie human motion. In

these cost terms following quantities are minimized:

- (i) joint torques u_j
- (ii) mechanical power $u_j \dot{q}_j$
- (iii) angular velocity of the head \dot{q}_{head}
- (iv) external support forces $u_{\text{ext},k}$ to smoothen the support force profiles

The weighting factors for these terms are listed in Table 6.1 and are chosen such that joint power is stronger penalized the higher the impairment level. Furthermore, the optimal control problem is defined by the equations of motion (6.2b), path constraints (6.2c), equality constraints (6.2d), and inequality constraints (6.2e), respectively. In order to include the external forces into the optimization, the controls \mathbf{u} (Appendix B) are enhanced by $\mathbf{u}_{\text{ext}} = \mathbf{f}_{\text{ext}}$.

Table 6.1: Weighting factors for the cost terms in the objective function (6.2a) for the three mobility levels *high-dynamic*, *unimpaired* and *severely impaired*.

Mobility level	α	β	γ	δ
High-dynamic	0.4	5.0	15.0	-
unimpaired	0.4	10.0	15.0	-
Severely Impaired	0.4	15.0	15.0	0.05

6.2.1. Phase Descriptions

The STS motion is divided into two phases distinguished by the lift-off which occurs in the instance when the contact to the chair is lost (Figure 6.2).

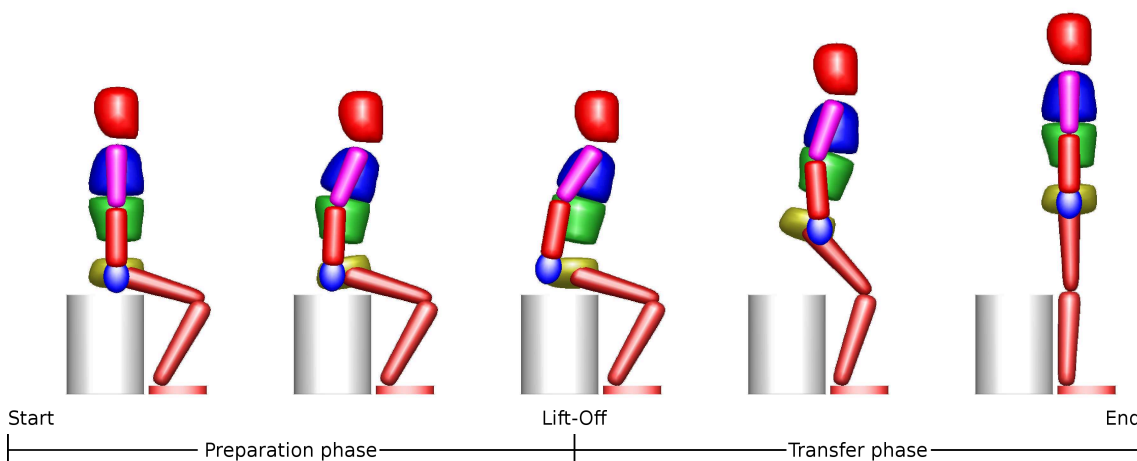


Figure 6.2: 8-segmented multibody model of human performing sit-to-stand (STS) motion divided in preparation and transfer phase. The STS motion is assumed to be symmetric with respect to the sagittal plane.

¹Agaplesion Bethanien Hospital Heidelberg, www.bethanien-heidelberg.de

- **Phase 1: Preparation Phase**

During the first phase the subject maintains contact with the chair and performs preparatory actions for the actual STS transfer, such as building up momentum. The preparation phase is initiated with a straight sitting pose and zero velocities.

$$\begin{aligned}
 r_x^{\text{pelvis}}(\mathbf{x}(t_0)) &= 0 \\
 r_z^{\text{pelvis}}(\mathbf{x}(t_0)) &= 0 \\
 q^{\text{ankles}}(t_0) + q^{\text{knees}}(t_0) + q^{\text{hips}}(t_0) &= 0 \\
 q^{\text{LumbSac}}(t_0) &= 0 \\
 q^{\text{Xiphoid}}(t_0) &= 0 \\
 q^{\text{Cervicale}}(t_0) &= 0 \\
 q^{\text{shoulders}}(t_0) &= 0 \\
 q^{\text{elbow}}(t_0) &= 0 \\
 \dot{\mathbf{q}}(t_0) &= \mathbf{0}
 \end{aligned}$$

- **Phase 2: Transfer Phase**

The second phase begins as soon as the contact force between the subject and the chair vanishes and terminates in the upright standing pose.

$$\begin{aligned}
 \mathbf{q}(t_1) &= \mathbf{0} \\
 \dot{\mathbf{q}}(t_1) &= \mathbf{0}
 \end{aligned}$$

Switching from the first into the second phase occurs as soon as the vertical contact force at the chair vanishes according to the switching function (see also (2.22))

$$f_z^{\text{chair}}(\mathbf{x}(t_1), \mathbf{u}(t_1)) = 0$$

6.3. Optimal Unassisted Sit-to-Stand Motions

The optimal unassisted STS motions have been computed for a 50th body height percentile elderly male subject (≥ 65 yrs., 1.705 m, 75.3 kg). The resulting motions are shown in Figure 6.3.

With the weaker weight on minimizing the mechanical power in the joints (see Table 6.1) the solution for the high-dynamic subject is more dynamic and faster than for the unimpaired subject (Table 6.2). Allowing for higher mechanical power and, thus, for higher angular velocities in the joints results in motions with a higher range as shown in Figure 6.6. Furthermore, a greater amount of angular momentum is built up in the arms to facilitate the load in the legs during the STS transfer. In fact, Figure 6.7 shows that while the joint torques in the upper extremities increase the torques in the lower extremities are reduced. The results from the high-dynamic case imply that the load applied on the lower body during the STS motion could be reduced by exploiting the dynamics of the upper body to a greater extent. In contrast, since with increasing age and diseases like arthritis and rheumatism humans lose their ability to move the joints with high velocities joint-friendly motion patterns are adopted, however, greater leg muscle forces have to be applied.

6.4.1. Optimal Assisted Sit-to-Stand Motion for Severely Impaired Humans

The assisted STS motion of severely impaired subjects has also been optimized for a 50th body height percentile elderly male subject (1.705 m, 75.3 kg). Three kinds of support actions are provided to the severely impaired human during the STS-transition at three locations of the subject's body as shown in Figure 6.4.

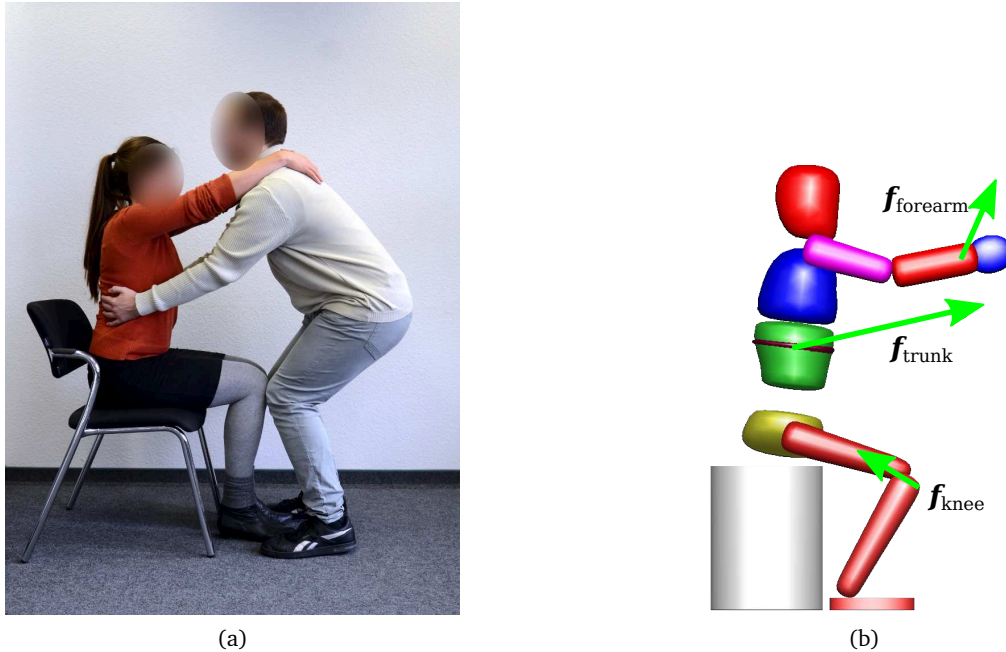


Figure 6.4: (a) STS assistance as practiced in clinical environments. (b) Support actions applied by a generic assistive device acting on the model as external forces.

These actions are chosen to resemble the support provided by a nurse or caregiver in rehabilitation hospital:

- Drag force acting at mid-trunk:
rather than a vertical force simply pulling the subject upwards, the support action applied to the mid-trunk is supposed to resemble a nurse's flat hand placed on the back of the subject and drags the trunk horizontally. The drag force acting at the origin of the mid-trunk segment is the main contributing force for the STS-assistance. The vertical force component of the drag force is constrained to not exceed 50% of the patient's body weight since a certain amount of self-effort is desired to be allocated to the subject during the STS-transition for therapeutic reasons such as prevention of muscle loss.
- Pushing force acting at the knee:
a caregiver places his knees against the subject's knees to prevent him from slipping from the chair. The support force points into the posterior direction and is constrained to $f_{\max, \text{knee}, x} = -50 \text{ N}$ in horizontal direction and to $f_{\max, \text{knee}, z} = \pm 5 \text{ N}$ in vertical direction. In the natural initial pose of the STS-motion, the knees are located right above the toes. During the STS-transition it follows a curve to eventually reach its final location right above the ankle.
- Arm support applied to the forearm:
the subject places his arms on the nurse's shoulders to enhance the lateral stability in the

upper body. The force application point is located with a distance of $l_{f,\text{forearm}} = 0.2\text{ m}$ from the elbow towards the wrist. The forearm is kept in anterior direction within an angle between $12^\circ - 15^\circ$ with respect to the horizontal. At any time, the upper arm maintains a slight angle in forward direction while the wrist is kept lower than the shoulder. The support forces of the forearm support are limited to $f_{\text{max,forearm},z} \leq 100\text{ N}$ in order to avoid the subject to exploit the forearm support to push himself upwards. However, resting the full weight of his arms as well as a small amount of leaning his upper body weight against the support is tolerated.

All three kinds of support can be regarded as external forces acting on the corresponding body parts and are included into the problem formulation (6.2) as \mathbf{u}_{ext} considering appropriate constraints.

The resulting STS motion sequence with the duration listed in Table 6.2 is shown in Figure 6.5. The strong weight on the mechanical joint power ($\beta = 15.0$) causes rather small ranges of motion (Figure 6.6). The upper extremities can not be used to build up a significant angular momentum to facilitate the STS transfer. Hence, the preparation phase remains short.

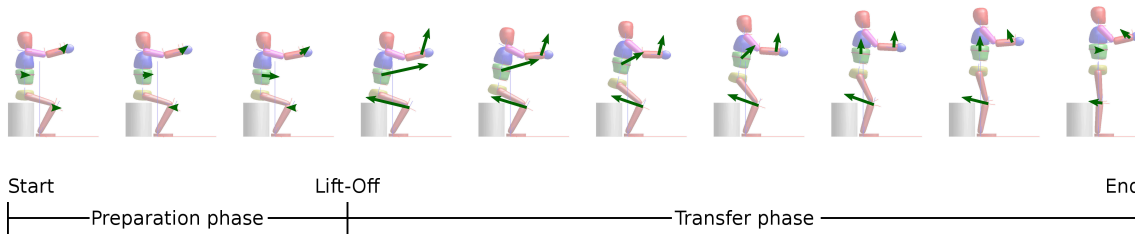


Figure 6.5: Motion sequence of the optimal STS motion for the severely impaired subject. The arrows show the support force vectors originating from the three support force application points chosen to provide *nurse-type* assistance.

Table 6.2: Resulting durations of the STS motion comprised of the preparation phase and the transfer phase for high-dynamic, unimpaired and severely impaired subjects.

STS Phase	High-dynamic	Unimpaired	Severely impaired
Preparation phase [s]	0.91	1.09	0.22
Transfer phase [s]	0.67	0.78	0.74
Sum [s]	1.58	1.87	0.96

Although the STS motion of the severely impaired subjects is less dynamic than the unassisted STS motions in Section 6.3 and no significant amount of upper body momentum contributes to the transfer, the joint torques shown in Figure 6.7 are slightly lower than in the high-dynamic case. However, since the support action is limited to 50% of the subject's body weight, a significant part of the joint load remains to be applied by the subject.

With regard to optimizing the design of a STS assistance device to support severely impaired persons performing the STS transfer the optimal assisted STS motion has been computed for six different models of the human body representing the dynamic and geometrical body parameters for male and female subjects of the 20th, 50th, and 80th body height percentile. The total height l_{tot} and total weight m_{tot} listed in Table 6.3 have been derived from ergonomic tables [123] and the dynamic body parameters are obtained using the regression equations

from Section 2.4.2. For these six scenarios Figure 6.8 shows the resulting support forces along with the trajectories of their application points. Table 6.4 summarizes the corresponding phase durations.

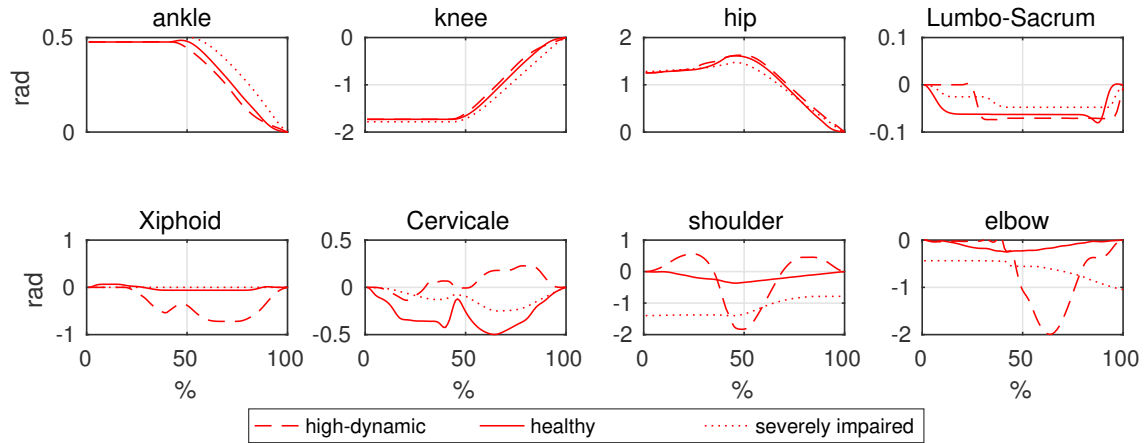


Figure 6.6: Joint angles for the high-dynamic, unimpaired and severely impaired subjects performing the STS motion.

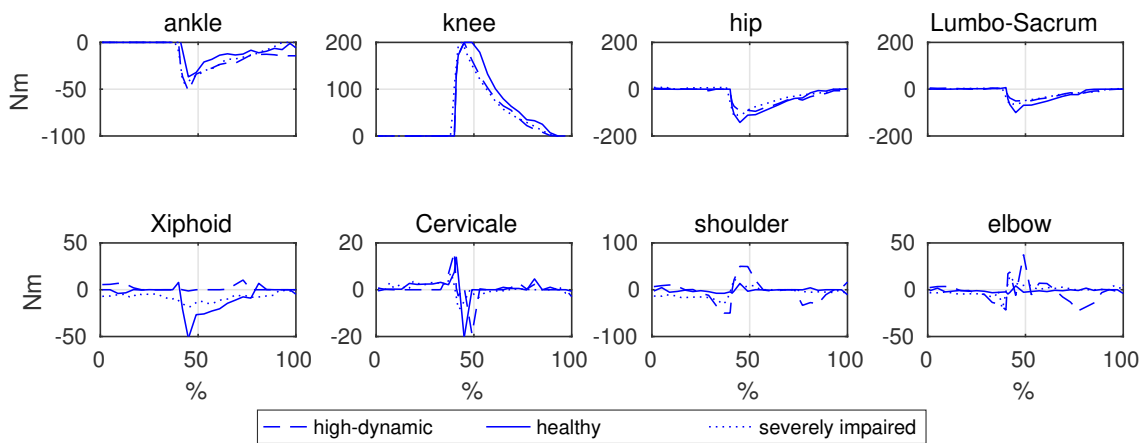


Figure 6.7: Joint torques required for the high-dynamic, unimpaired and severely impaired subjects to perform the STS motion.

Table 6.3: Total height l_{tot} and total weight m_{tot} of elderly subjects, 20th, 50th, and 80th percentile.

	Percentile	l_{tot} [m]	m_{tot} [kg]
Female	20	1.530	53.0
	50	1.585	64.3
	80	1.630	75.3
Male	20	1.640	68.2
	50	1.705	75.3
	80	1.756	82.0

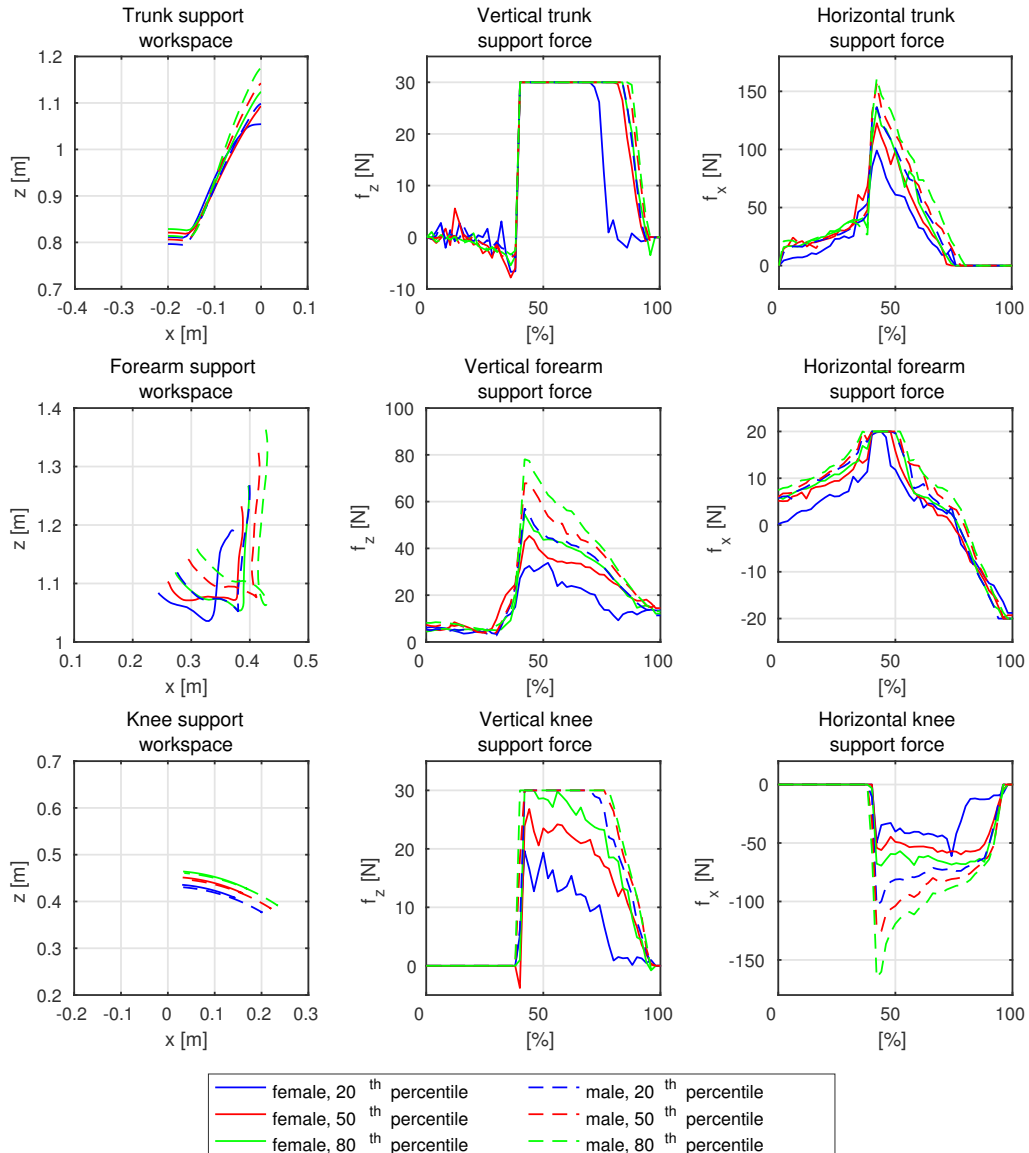


Figure 6.8: Support forces and the trajectories of their application points for 20th, 50th, 80th body height percentile of severely impaired female and male subjects during the assisted STS.

Table 6.4: Durations of the *preparation* and *transfer* phases, respectively, for the simulation of the sit-to-stand motion of severely impaired elderly subjects, 20th, 50th, and 80th percentile.

	Percentile	Preparation Phase [s]	Transfer Phase [s]	Total [s]
Female	20	0.20	0.90	1.10
	50	0.21	0.71	0.92
	80	0.23	0.72	0.95
Male	20	0.22	0.71	0.93
	50	0.23	0.73	0.96
	80	0.25	0.76	1.10

6.5. Discussion

In this part of the thesis, the sit-to-stand (STS) motion has been simulated based on realistic two-dimensional models of the adult and geriatric human body. The adult STS transfer has been simulated for *unimpaired* humans. The resulting motion sequence has a natural appearance without any exaggerating patterns and is subject to realistic joint torques. The *high-dynamic* case exploits the full amount of full-body dynamics which can be applied by a healthy human body. Motion in the arms is strongly increased in order to apply a significant amount of momentum and to facilitate the lower-body torques required to lift the body up. Due to the constraints induced by the hypothetical assistive device, the assisted STS motion of the *severely impaired* subject has a rather static appearance. The torques required to perform the STS motion are reduced by the STS support forces, albeit not to a great amount, since the support has been limited to 50% of the subject's weight to allocate some effort to the subject.

For the mobility levels defined in this thesis, the optimization computations predict different patterns which include significant arm motion in both phases. Therefore, the results support our approach to choose a full body representation of the human as well as to consider two stages in the optimal control problem.

7. OPTIMAL DESIGN OF SIT-TO-STAND ASSISTANCE DEVICES

Elderly people with moderate to severe mobility impairments are often able to independently perform basic everyday tasks provided a suitable form of mobility assistance and a minimal amount of self-effort. Standing up from the sitting position and navigating through familiar surroundings are such tasks which observably benefit from the support of assistive devices. Typically, STS assistance tasks are adopted by nurses and caregivers in home or clinical environments with the suitable expertise and physical abilities. However, this demanding task can be facilitated by the support of robotic devices which are specifically designed to provide appropriate STS assistance considering the individual physiological conditions of the subject.

Based on the results from Chapter 6, this part of the thesis proposes model-based optimal control methods to compute optimal design parameters for two different kinds of STS assistance devices, the *nurse-type* device to support *severely impaired* subjects (Sections 7.1-7.2) and the *rollator-type* device to provide assistance for *moderately impaired* subjects (Sections 7.3-7.4).

7.1. Human-Centered Approach for Severely Impaired Subjects

In this part of the work, we apply the optimal assistance trajectories and forces from the previous section as desired trajectories and external forces, respectively, on an initial model of an assistive device. Optimal control methods are used to compute the states and controls as well as the set of mechanical design parameters that enables the device to provide optimal STS-assistance. Since the purpose of the assistive device is to provide STS support based on the techniques of a human nurse or caregiver in a clinical environment, in the remainder of this thesis, it is referred to as the *nurse-type* device.

7.1.1. Multibody Model of Assistance Device for Severely Impaired Subjects

A three-dimensional rigid-body model of the device has been established to be included into an optimal control problem (Figure 7.1a). We assume the STS-transfer to be a symmetrical motion occurring mainly in the sagittal plane in which both arms and both legs perform the same motions. Using this assumption it can be simplified to a two-dimensional problem. Although a drivable platform is considered to prepare the device to provide a walking support functionality, during the STS-support, the position of the device is assumed to be fixed. Furthermore, the model also includes the location and mass properties of a control unit consisting of a *base* consisting of two PCs and batteries.

The three-dimensional model of the device consists of 19 rigid bodies where the *control unit* and four *wheels* belong to the *base* and the *STS-mechanism* is represented by the *levers 1-6* and the *knee support* (Figure 7.1a). The rigid bodies of the STS-mechanism are connected by the rotary joints *AS1-2*, *MTS1-3* and *KS1*, which, on each side, allow for three degrees of freedom in the sagittal plane at each of the supports for the *arms*, *trunks* and *knees*. No degrees of freedom have been allowed between the Control Unit and the Wheels as well as for the Wheels with respect to the ground, constraining the device to stay at its place. Since the STS-transfer is reduced to a two-dimensional problem assuming symmetric behavior with

¹ACCREA Engineering, www.accrea.com

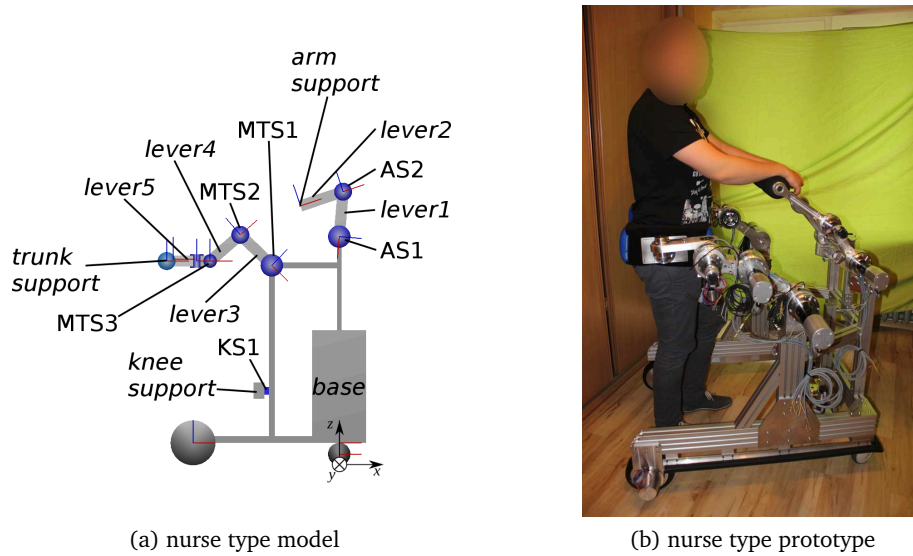


Figure 7.1: In the multibody model (a) of the *nurse-type* device the position of the actuators (in capitals) and the lengths of the levers (lowercase) are optimized model parameters. The local coordinate systems of each lever are located in each lever's origin and their x' -axes (red) aligned with the longitudinal axes of the levers. A prototype (b) has been built by ACCREA Engineering¹ based on the optimized design which resulted from this thesis.

the left and right levers of the STS-mechanism performing the same motion, in the model, they can be combined into virtual levers with double mass and inertia. The joint torques and actuator forces determined by the computations based on this model will then have to be split in half in order to determine the necessary torques and forces on each lever and actuator of the real device. The local coordinate systems of the STS-mechanism segments are located in the joint that connects one segment with its next proximal neighbor with the base being the most proximal segment. The axes of the local coordinate system in each segment are oriented such that the local x' -axis points away from the segment and is aligned with its longitudinal axis. The local y' -axis points into the same direction as the global y -axis. The segments lever5 which provide the trunk support are required to be aligned parallel to the xy -plane at all times. This turns the joint angle of MTS3 to a function of the angles MTS1 and MTS2 and introduces the explicit constraint on the joint angles φ_i of MTS $\{i\}$, $i = 1, \dots, 3$

$$\sum_{i=1}^3 \varphi_i = 0 \tag{7.1}$$

Equations of Motion

Considering the external support forces acting at the support points, the equations of motion for the model of the nurse type device are formulated in terms of the *generalized coordinates*, which in this case are the absolute position of the device's base with respect to the global coordinate system as well as the joint angles of the model's rotational degrees of freedom. The external forces $\mathbf{f}_{\text{ext,opt}}$ are included into the equations of motion (6.1) as generalized forces $\boldsymbol{\tau}_{\text{ext,opt}} = \mathbf{G}_{\text{ext,opt}}^T \mathbf{f}_{\text{ext,opt}}$.

$$\begin{pmatrix} \mathbf{H} & \mathbf{G}^T \\ \mathbf{G} & \mathbf{0} \end{pmatrix} \begin{pmatrix} \ddot{\mathbf{q}} \\ -\lambda \end{pmatrix} = \begin{pmatrix} \mathbf{C} + \boldsymbol{\tau} + \boldsymbol{\tau}_{\text{ext,opt}} \\ \boldsymbol{\gamma} \end{pmatrix} \quad (7.2)$$

where $\mathbf{f}_{\text{ext,opt}}$ are the optimized assistive forces obtained by the optimization of assisted STS motions described in Section 6.4 and $\mathbf{G}_{\text{ext,opt}}$ is the Jacobian of the support force application points. In order to induce $\mathbf{f}_{\text{ext,opt}}$ onto the model during the optimization the appropriate values are fixed on every discretization node of the multiple shooting process.

Model Parameters

To include the mechanical design as part of the optimization problem, model parameters p are introduced to represent the lengths l_j of lever $\{j\}$, $j = 1, \dots, 5$ as well as the location of the actuators AS1, MTS1 and KS1. The locations of AS2 and MTS2-3 are then implicitly determined by the lengths of the levers.

7.1.2. Optimization of Support Action and Design Parameters

Computations are performed for the optimal trajectories and forces computed in Section 6.4, see Figure 6.8. The optimization computations in this part of the work are aimed towards a single set of mechanical design parameters p for an assistive device that equally serves all subjects from all six scenarios considered. To achieve this, all six scenarios are combined into a single optimal control problem which will result in a common set of parameters for all sub-problems. A large-scale optimal control problem with 17 stages is formulated where the six sub-problems with each two stages are put in consecutive order while five transition stages are formulated to allow for discontinuities between the sub-problems in both the states and controls (Figure 7.2). Since the velocities are required to be zero at the beginning and the end of each sub-problem, no discontinuities need to be regarded on velocity level. Phase durations for these computations are fixed to the values determined for the human motions in Section 6.4. A similar approach would be to arrange the sub-problems in parallel order. However, this requires that all sub-problems have the same stage durations which is not the case here.

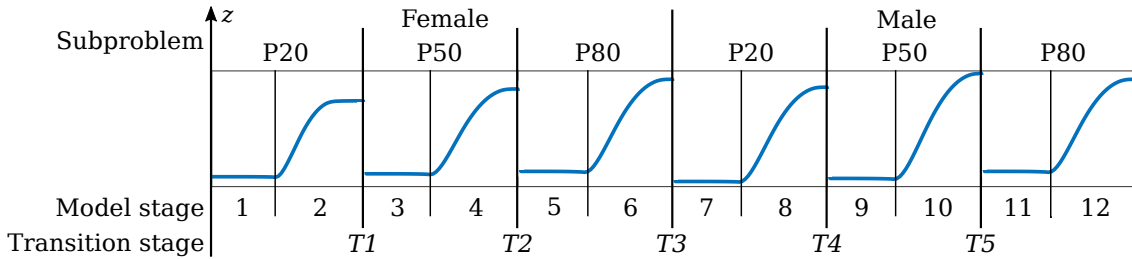


Figure 7.2: The six scenarios (female/male, 20th/50th/80th body height percentile) are arranged subsequently to a single large-scale optimal control problem in order to obtain a single set of model parameters for all considered scenarios. In this figure, the subproblems are illustrated by the z -coordinate of the support force application point at the trunk over time. Each subproblem consists of the two model stages (i) Preparation and (ii) Transfer phase altogether leading to 12 model stages and 5 transition stages to deal with the discontinuities between the subproblems.

The model states $\mathbf{x}(t)$ contain the degrees of freedom $\mathbf{q}(t)$ of the model as well as their velocities $\dot{\mathbf{q}}(t)$. The controls $\mathbf{u}(t)$ are represented by the torques $\tau_j(t)$, $j = 1, \dots, 5$ in the joints yielding in 10 states and five controls. The objective function (7.3a) minimizes the square of the controls \mathbf{u} .

Considering also the model parameters p , the nonlinear optimal control problem can be formulated as

$$\min_{\mathbf{x}(t), \mathbf{u}(t), p} \sum_{i=1}^{17} \int_{\tau_{i-1}}^{\tau_i} \mathbf{u}^2(t) dt \quad (7.3a)$$

subject to:

$$\dot{\mathbf{x}}(t) = \mathbf{f}_i(t, \mathbf{x}(t), \mathbf{u}(t), p) \quad (7.3b)$$

$$\mathbf{x}(\hat{t}_i^+) = \mathbf{h}(\mathbf{x}(\hat{t}_i^-)), \quad (7.3c)$$

$$0 \leq \mathbf{g}_i(t, \mathbf{x}(t), \mathbf{u}(t), p) \quad (7.3d)$$

$$0 = \mathbf{r}^{eq}(\mathbf{x}(0), \dots, \mathbf{x}(T), p) \quad (7.3e)$$

$$0 \leq \mathbf{r}^{ineq}(\mathbf{x}(0), \dots, \mathbf{x}(T), p) \quad (7.3f)$$

$$\text{for } t \in [\tau_{i-1}, \tau_i], i = 1, \dots, 17, \tau_0 = 0, \tau_{17} = T$$

where the objective function is minimized by modifying $\mathbf{x}(t)$, $\mathbf{u}(t)$ and p . The right hand side of the equations of motion (7.3b) is formulated separately for each of the $n_{ph} = 17$ model stages. Equation (7.3c) treats the discontinuities of the positions and controls between the scenarios.

Phase Descriptions

Each of the six subproblems consists of two stages which have the same number of multiple shooting nodes as well as the same stage durations as the corresponding problem from Section 6.4. According to the optimal STS motions, the two stages of each subproblem are denoted the *Phase 1: Preparation Phase* and the *Phase 2: Transfer Phase* and are defined by a specific set of constraints.

The equality constraints (7.3e) contain the conditions that the handle maintains a horizontal position (7.1) and $\dot{\mathbf{q}}(t) = \mathbf{0}$ at the beginning and the end of each sub-problem. The difference between the optimal support point positions $\mathbf{r}_{opt,m}(t)$ and the desired support point positions $\mathbf{r}_{des,m}(t)$ from Section 6.3 is constrained to be equal zero at every discretization node m

$$\mathbf{r}_{des,m}(t) - \mathbf{r}_{opt,m}(t) = 0. \quad (7.4)$$

The inequality constraints (7.3f) contain the condition for unilaterality of the ground reaction forces.

Specific Parameters for the Optimal Control Problem

Within each scenario, the states and controls are continuous between the preparation phase and the STS-transfer phase. However, combined to a single large-scale optimal control problem, the generalized positions and controls are discontinuous at the transitions between the subproblems. Since there is no physical connection between the end of one scenario and the be-

ginning of the next scenario, sudden transitions must be allowed at these points. Such discontinuities on the generalized positions and controls can be handled using transition phases (7.3c).

Solution of the Optimal Control Problem

Due to the complexity and nonlinearity of the problem, we choose to discretize the optimal control problem using the *direct multiple-shooting method* applying a piecewise linear control discretization and solve the discretized problem using SQP methods. The methods are described in further details in Section 3.2.

7.2. Optimal Design Parameters for Nurse-Type Device

The optimal control problem (7.3) results in segment lengths and joint positions which enable the device to follow the desired trajectories of all scenarios considered and, at the same time, minimize the torque in the joints of the STS-mechanism. Table 7.1 summarizes the resulting optimal values for the model parameters from the optimal control computations. The resulting motion sequence for the assisted STS motion of severely impaired subjects is shown in Figure 7.3 for the combination of both subject and device.

Following the desired trajectories shown in the left most column of Figure 6.8 with the support points at the arms, trunk, and knees, respectively, has been included into the optimal control problem as an equality constraint. Since the mechanical design parameters of the STS-mechanism are also optimized variables a unique set of parameters \mathbf{p} can always be found which enables the fulfillment of (7.4).

The resulting optimal joint angles are shown in Figure 7.4a. The angle of MTS3 is a function of the angles in MTS1 and MTS2 as constrained by (7.1). The joint angle velocities are shown in Figure 7.4b and the joint torques in Figure 7.4c. The resulting joint torques and angular velocities can be directly interpreted as the required actuator torques and speeds to apply the desired STS support forces on the subject.

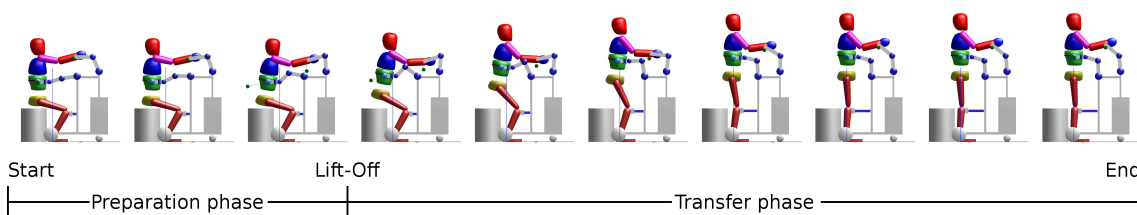


Figure 7.3: Motion sequence of the optimal STS motion for the severely impaired subject assisted by the design optimized *nurse-type* STS assistance device.

7.3. Human-Centered Approach for Moderately Impaired Subjects

Moderately impaired subjects are assumed to have enough strength to support themselves with their arms and to securely grasp a handle with their hands. While STS assistance to a reduced amount might still be necessary, the most effective way to transfer support actions from the hands to the body is through stretched arms oriented along the direction of the effective support force vector. The support motion profiles as well as the mechanical design

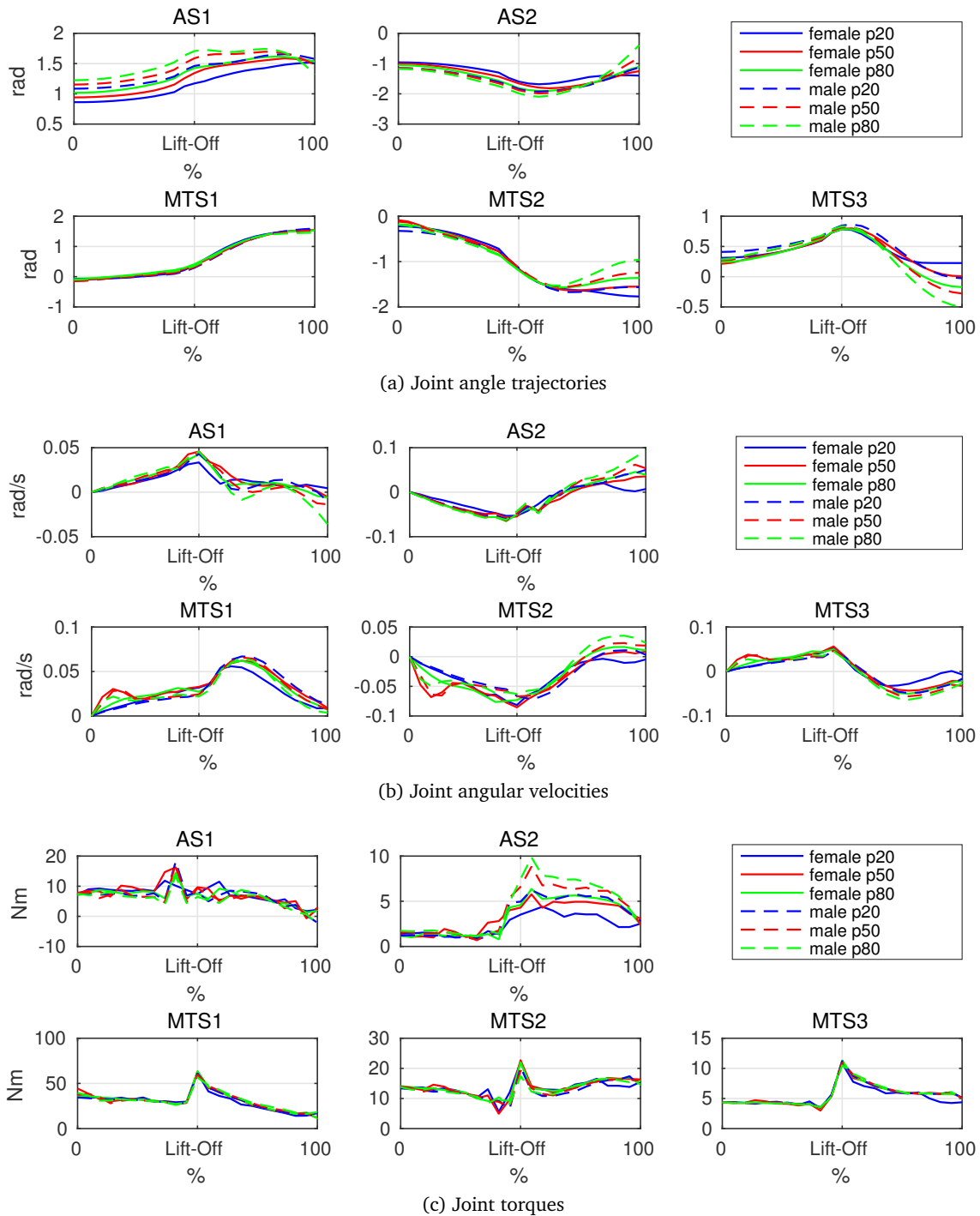


Figure 7.4: Resulting optimal states and controls for the actuators AS1-2 and MTS1-3.

parameters of an STS-assistance device for *moderately impaired subjects* have been optimized with the same methods as described in Section 6.4.

In order to identify the best possible way to provide such kind of STS-assistance by any kind of external assistance, an optimal control problem has been formulated similar to (6.2) including dynamic models as described in Section 6.1 reflecting the 20th, 50th and 80th body height percentile of female and male subjects. These computations have been performed in the scope of related work [103]. The support force profiles as well as their application points resulting

Table 7.1: Resulting model parameters of the optimal model.

Symbol	Description	Value [m]
$AS1_x$	Horizontal coordinate of actuator AS1	-0.0010
$AS1_z$	Vertical coordinate of actuator AS1	0.9498
$MTS1_x$	Horizontal coordinate of actuator MTS1	-0.2979
$MTS1_z$	Vertical coordinate of actuator MTS1	0.8837
l_{lever1}	Lever 1 length	0.2095
l_{lever2}	Lever 2 length	0.2524
l_{lever3}	Lever 3 length	0.2096
l_{lever4}	Lever 4 length	0.1741
l_{lever5}	Lever 5 length	0.1602

from that work are used in this part to compute the optimal states and controls as well as optimal design parameters of an STS assistance device. Due to resemblance of such a device with a rollator we refer to it as the *rollator-type* STS assistance device.

7.3.1. Multibody Model of Assistance Device for Moderately Impaired Subjects

A three-dimensional rigid-body model of the rollator-type device has been reduced to a two-dimensional problem due to the symmetry underlying the STS motion and included into the optimal control computations (Figure 7.5a). In addition to the STS-mechanism, a drivable platform was considered to enable possible walking support functionality. Furthermore, the model also includes the location and mass properties of a control unit.

The model of the rollator-type device consists of 13 rigid bodies where the *base* includes the *control unit* and four *wheels*. The *STS-mechanism* comprises the *STS frame*, *Segment 1*, *Segment 2* and *Handle* (Figure 7.5a). The rigid bodies of the STS-mechanism are connected by the rotary joints *Joint 1*, *2* and *3* creating three degrees of freedom in the sagittal plane on each side. The STS frame, the control unit and the wheels are not allowed to move with respect to each other. Similarly, there is no degree of freedom of the wheels with respect to the ground. Due to the symmetry of the STS-problem, both arms of the model can be combined into one virtual arm with double mass and inertia. The joint torques and actuator forces resulting from the computations based on this model will then have to be split in half in order to determine the torques and forces on each arm and actuator of the real device.

The local coordinate systems of the STS-mechanism segments are located in the joint that connects one segment with its next proximal neighbor with the STS frame being the most proximal segment. The axes of the local coordinate system in each segment are oriented such that the local x' -axis points away from the segment and is aligned with its longitudinal axis. The local y' -axis points into the same direction as the global y -axis.

²ACCREA Engineering, www.accrea.com

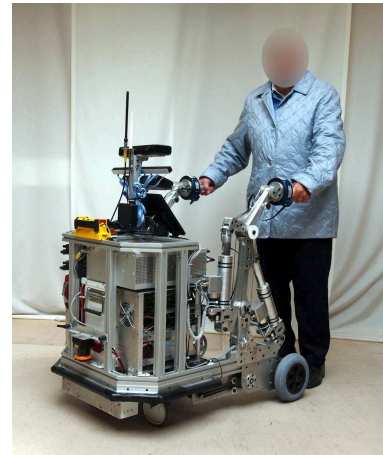
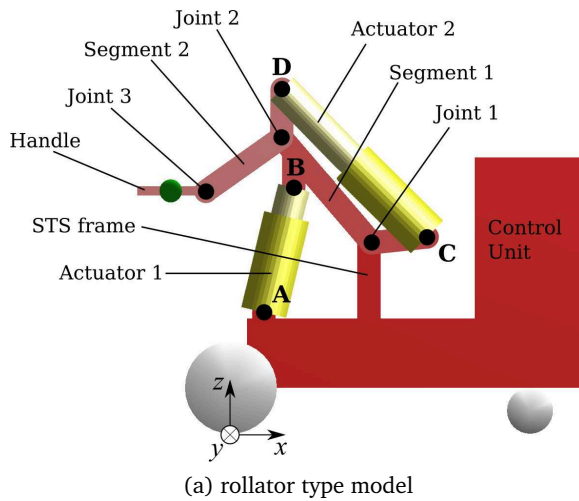


Figure 7.5: (a) Rigid body model of the *rollator-type* STS assistance device for moderately impaired subjects consisting of 13 segments. The external support force is modeled to be applied at mid-handle (green dot). (b) Elderly subject operating a prototype of the device manufactured by ACCREA Engineering² based on the results presented in this thesis.

Linear Actuators

In the final device, the joint torques will be applied to the *Joints 1* and *2* by linear actuators (compare Figure 7.5). We include the location of the connecting points of the actuators with the appropriate segments as well as the lengths of the linear actuators into the optimal control problem as model parameters. During optimization, the locations of the connecting points are computed to minimize the lever arms that map the linear actuator force into the joint torques. Minimizing the lever arms results in minimizing the linear actuator velocities and maximizing the actuator forces. The lengths $l_{act,i}$ of the *Actuators* $\{i\}$, $i \in [1, 2]$ are determined by their stroke $s_{act,i}$ and a constant length for the housing of the actuator control unit, i. e. $s_{act,i} + 0.170 \leq l_{act,i} \leq 2 \cdot s_{act,i} + 0.170$. The linear forces of the actuators are constrained to $f_{act} = 550$ N. No constraint has been formulated for the velocity of the linear actuators.

Equations of Motion

The equations of motion for the model of the assistive device are formulated according to (7.2) in terms of generalized coordinates, i.e. the absolute position of the device's base with respect to the global coordinate system as well as the joint angles of the model's rotational degrees of freedom.

Optimal support trajectories and forces (Figures 7.6) as well as phase durations (Table 7.2) have been computed in previous work [103] for six scenarios reflecting the 20th, 50th and 80th percentile of the body heights and weights of female and male subjects. The optimal support forces f_{ext} applied to the subject's hands during the assisted STS-transfer are imposed as external forces $f_{ext,opt}$ to the middle of the handles of the STS mechanism, i.e. $f_{ext,opt}$ is multiplied by the translated Jacobian $G_{ext,opt}^T$ of the mid-handle location and added as $\tau_{ext,opt}$ to the right hand side of the equations of motion in (7.2).

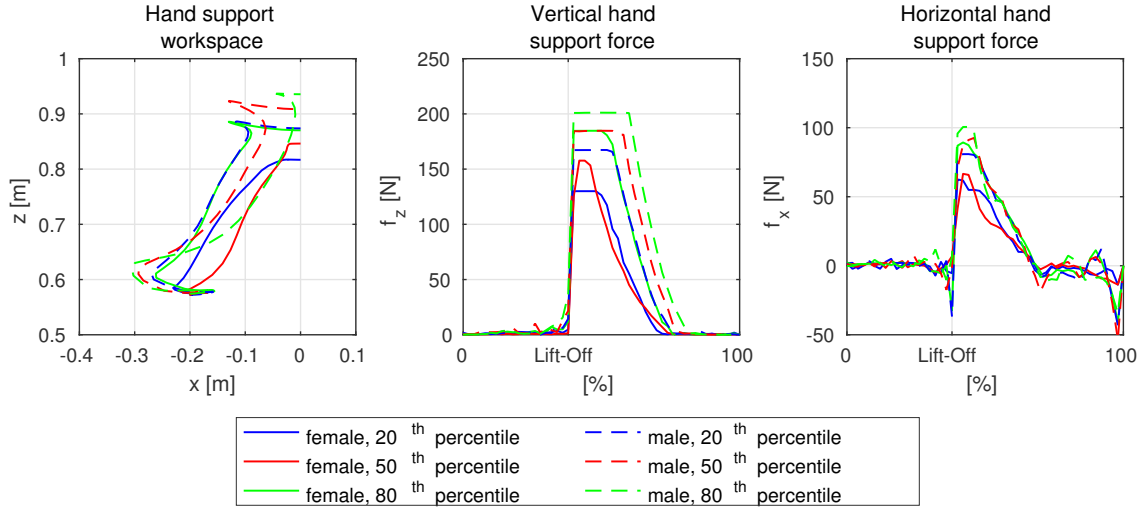


Figure 7.6: Desired STS support action from [103] for the six scenarios $F20$, $F50$, $F80$, $M20$, $M50$, and $M80$. Left plot: Desired handle trajectories in the sagittal plane. For all scenarios, the trajectories are shown in the global frame which is located on ground level right below the ankle of the human model. They all start in the lower left and end in the upper right corner of the plot. Middle and right plot: Support forces applied as external forces on the mid-handle of the device in horizontal (x) and vertical (z) direction, respectively.

Table 7.2: Durations of the *preparation* and *transfer* phases, respectively, for the simulation of the sit-to-stand motion of moderately impaired elderly subjects, 20th, 50th, and 80th percentile.

	Percentile	Preparation Phase [s]	Transfer Phase [s]	Total [s]
Female	20	1.16	1.10	2.26
	50	1.23	1.04	2.27
	80	1.35	1.09	2.44
Male	20	1.29	1.08	2.37
	50	1.35	1.05	2.40
	80	1.40	1.04	2.44

Model Parameters

To include the mechanical design into the optimization problem, model parameters \mathbf{p} are introduced to represent the lengths l_j of the *Segments* $\{j\}$ and $j = 1, 2$ as well as the location of *Joint 1*. The locations of *Joint 2* and *Joint 3* are then implicitly determined by the lengths of the segments, as can be seen in Figure 7.5. Furthermore, the connecting points of the linear actuators to the segments A , B , C and D as well as the actuator strokes s_{act} are included as parameters. Table 7.3 lists the initial values for the free parameters of the model. These values correspond to the geometrical properties of the prototype shown in Figure 7.5b which were not sufficient to cover the range of desired trajectories (Figure 7.6).

7.3.2. Optimization of Support Action and Design Parameters

Computations are performed for the optimal trajectories and forces in the six scenarios investigated in [103], see Figure 7.6. In each scenario, the optimal control problem is divided into

two stages to distinguish the preparation phase in which the subject prepares for standing up from the phase in which the subject performs the actual STS-transfer. The six scenarios are related to different percentiles of patients with respect to their dynamic data: male and female, 20th, 50th and 80th percentile of the population older than 65 years. In the optimization study in this paper, however, the goal is not to provide a different optimal design for each of these classes, but to give one that equally serves all considered patients.

We therefore aim to find a single set of model parameters \mathbf{p} that minimizes the objective function and satisfies the constraints of all scenarios at the same time and combine all six scenarios into a single large-scale optimal control problem similar to the procedure illustrated in Figure 7.2. The phase durations for these computations are fixed to the values determined for the human motions in [103].

Objective Function

The model states $\mathbf{x}(t)$ contain the degrees of freedom $\mathbf{q}(t)$ of the model as well as their velocities $\dot{\mathbf{q}}(t)$. The controls $\mathbf{u}(t)$ are represented by the torques $\tau_j(t)$ in the *Joints* $\{j\}$, $j = 1, \dots, 3$, yielding six states and three controls. The objective function (7.5a) contains the square of the controls \mathbf{u} as well as the square of the lever arms \mathbf{r}_{act} which are established by the connecting points of the linear actuators with the segments, while the weighting factors α and β is used to adjust the influence of these different terms.

Considering also the model parameters \mathbf{p} , the nonlinear optimal control problem can be formulated as

$$\min_{\mathbf{x}(t), \mathbf{u}(t), \mathbf{p}} \sum_{i=1}^{17} \int_{\tau_{i-1}}^{\tau_i} \alpha \mathbf{u}^2(t) + \beta \mathbf{r}_{\text{act}}^2 dt \quad (7.5a)$$

subject to:

$$\dot{\mathbf{x}}(t) = \mathbf{f}_i(t, \mathbf{x}(t), \mathbf{u}(t), \mathbf{p}) \quad (7.5b)$$

$$\mathbf{x}(\hat{t}_i^+) = \mathbf{h}(\mathbf{x}(\hat{t}_i^-)), \quad (7.5c)$$

$$0 \leq \mathbf{g}_i(t, \mathbf{x}(t), \mathbf{u}(t)), \quad (7.5d)$$

$$0 = \mathbf{r}^{\text{eq}}(\mathbf{x}(0), \dots, \mathbf{x}(T), \mathbf{p}), \quad (7.5e)$$

$$0 \leq \mathbf{r}^{\text{ineq}}(\mathbf{x}(0), \dots, \mathbf{x}(T), \mathbf{p}), \quad (7.5f)$$

$$\text{for } t \in [\tau_{i-1}, \tau_i], i = 1, \dots, 17, \tau_0 = 0, \tau_{17} = T$$

where $\mathbf{x}(t)$, $\mathbf{u}(t)$ and \mathbf{p} are modified to minimize the objective function (7.5a). The right hand side of the equations of motion (7.5b) is formulated separately for each of the $n_{\text{ph}} = 17$ model stages. Equation (7.5c) allows the handling of the discontinuities of the positions and controls between the scenarios.

7.3.3. Phase Descriptions

The path constraints (7.5d) define general limits to the states such as maximum joint angles and velocities. The equality constraints (7.5e) contain the condition that the handle maintains a horizontal position and the optimized handle trajectory $\mathbf{r}_{\text{opt},m}(t)$ follows the desired

trajectories $\mathbf{r}_{\text{des},m}(t)$ at all m discretization nodes (7.6)

$$\mathbf{r}_{\text{des},m}(t) - \mathbf{r}_{\text{opt},m}(t) = 0. \quad (7.6)$$

The inequality constraints (7.5f) contain the condition for unilateral ground reaction forces, the ratio between the minimal and maximum lengths of the linear actuators, as well as the maximum value for the linear force of the actuators.

Specific Parameters for the Optimization Problem

Within each scenario, the generalized positions and controls are continuous between the preparation phase and the transfer phase. However, combined to a single optimal control problem, the positions and controls are discontinuous between the scenarios. Since there is no physical connection between the end of one scenario and the beginning of the next scenario, sudden transitions must be allowed at these points. These discontinuities can be handled using transition phases (7.5c).

7.4. Optimal Design Parameters for Rollator-Type Device

The segment lengths and joint positions which result from the optimal control problem (7.5) enable the device to follow the desired trajectories of all scenarios and simultaneously minimize the torque in the joints of the STS-mechanism. Locations for the connecting points of the linear actuators to the segments are computed for which the linear actuator force is maximized while minimizing the linear actuator velocity. The desired trajectories (7.6) could be approximated by the force application point without any deviation.

The resulting optimal joint angles are shown in Figure 7.7a. In order to remain horizontal at all times the angle of *Joint 3* is a function of the *Joints 1* and *2*. The joint angle velocities are shown in Figure 7.7b and the joint torques in Figure 7.7c. The joint torques show a steep increase right in the instance in which the subject loses contact from the chair.

Optimal Design Parameters

Table 7.3 summarizes the resulting optimal value for the design parameters of the model from the optimal control computations along with their initial values. The segment lengths $l_{1,2}$ are greater than their initial values since, initially, the segments were too short to cover the whole range of desired trajectories from all six scenarios. The optimal location of *Joint 1* as well as of the *Joints 2* and *3* changed due to the first part of the objective function (7.5a) in which the joint torques τ are minimized. As expected, the connecting points *A*, *B*, *C* and *D* of the *Actuators 1* and *2* changed due to the second part of (7.5a) where the lever arms are optimized to minimize the linear velocity of the actuators. The difference in the design of the rollator-type assistive device due to the optimal control computations are illustrated in Figure 7.8.

Optimal Linear Forces and Velocities

In order to gain knowledge about the specifications of the linear actuators, which are supposed to create the joint torques in the final device, we compute the optimal forces and velocities of

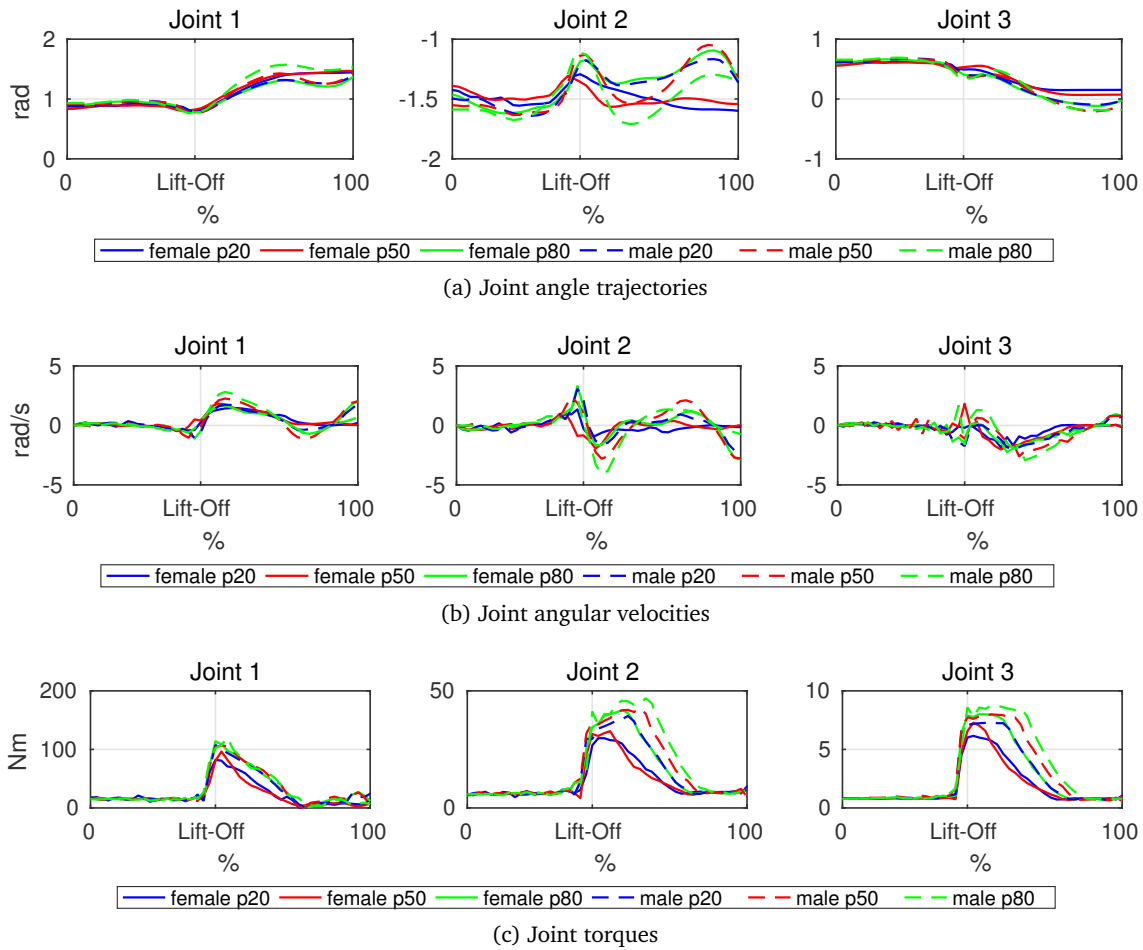


Figure 7.7: Resulting optimal states and controls for the *Joints 1, 2 and 3*.

the linear actuators from the optimal joint torques and angular velocities. The linear forces of the actuators can be computed using the lever arms which result from the optimal locations of connecting points *A*, *B*, *C* and *D* of the actuators to the segments. The linear velocities of the actuators are determined by computing the difference of the global velocities of these connecting points. The results for the optimal actuator forces and velocities are shown in the Figures 7.9a and 7.9b, respectively.

7.5. Discussion

Based on the results obtained from the computations for the severely impaired subject as well as for a mildly impaired subject published in [103] optimal support force profiles and the trajectories of their application points have been used as requirements for the design optimization of two different kinds of STS assistance devices. Using optimal control methods, sets of design parameters for the devices have been computed which enable the devices to provide STS support with minimal effort and to cover the workspace required to provide support for subjects ranging from the 20th up to the 80th body height percentile of both male and female elderly subjects. Prototypes of the STS assistance devices have been manufactured based on the results presented in this thesis. However, a rigorous validation of the devices to prove their applicability and user acceptance is still to be undertaken.

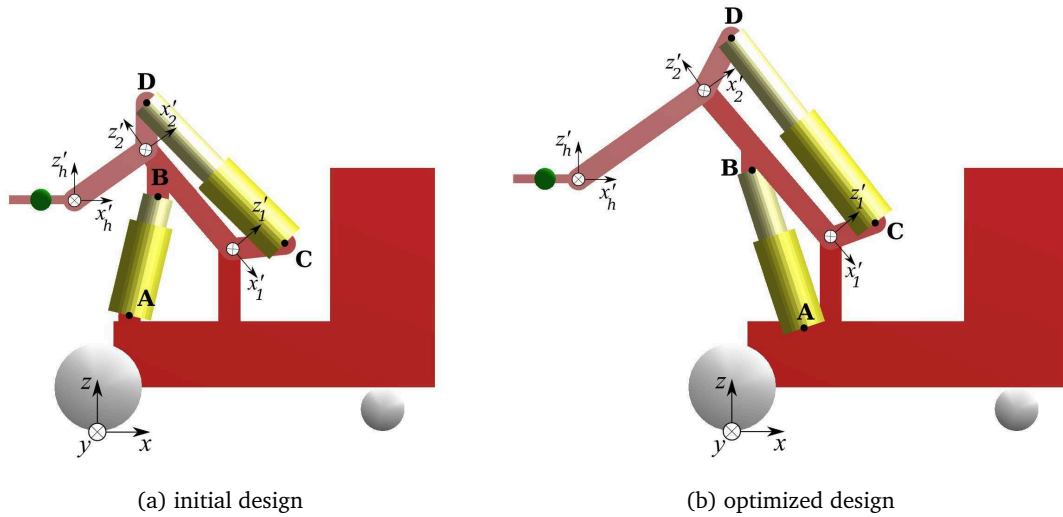


Figure 7.8: (a) initial design and (b) optimized design of the assistive device with the location and orientation of the global and local coordinate systems. The geometrical properties are summarized in the Table 7.3.

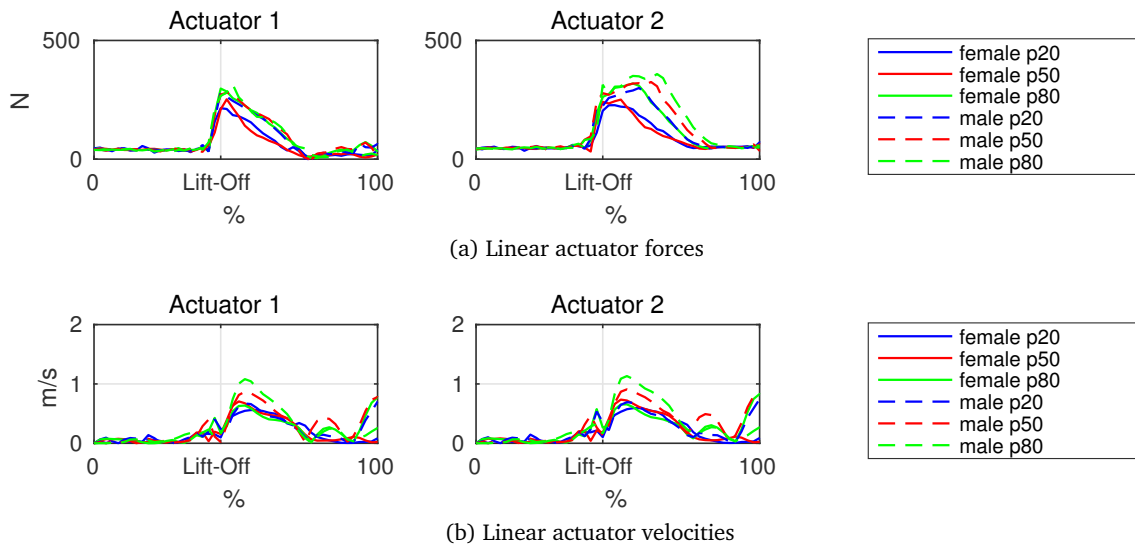


Figure 7.9: (a) Resulting linear actuator forces and (b) velocities for the *Actuators 1* and *2*.

Table 7.3: Initial and optimized values for the model parameters of the optimal model. The coordinates are specified in the global frame (*), in the *Joint 1* frame (#), and in the *Joint 2* frame (†).

Symbol	Description	initial values [cm]	optimized values [cm]
$Joint1_x$	Horizontal coordinate of Joint 1*	30.5	22.5
$Joint1_z$	Vertical coordinate of Joint 1*	41.5	43.9
$l_{segment1}$	Segment 1 length	30.0	44.5
$l_{segment2}$	Segment 2 length	20.0	35.0
A_x	Horizontal coordinate of A*	7.5	16.5
A_z	Vertical coordinate of A*	26.5	23.5
B_x	Horizontal coordinate of B#	-20.0	-23.6
B_z	Vertical coordinate of B#	-5.0	-3.5
C_x	Horizontal coordinate of C#	7.0	12.0
C_z	Vertical coordinate of C#	10.0	6.2
D_x	Horizontal coordinate of D†	6.0	3.9
D_z	Vertical coordinate of D†	8.6	10.0
s_{act1}	Actuator 1 stroke	12.6	13.4
s_{act2}	Actuator 2 stroke	14.7	20.7

Part III

Conclusion and Outlook

CONCLUSION

In this thesis, optimal control methods are applied to combine approaches from scientific computing and human motion analysis seeking to provoke progress in these both fields and, additionally, in the fields of mechanical engineering and physical rehabilitation. We approach challenging clinical questions from three different perspectives: *motion reconstruction*, *motion prediction*, as well as *design optimization*. Using optimal control methods ensures that the dynamics are satisfied for the entire motion.

The human walking motion has been recorded in a motion capture laboratory with unimpaired subjects and subjects walking with transfemoral prostheses. The recorded motions have been *reconstructed* based on individualized threedimensional multibody models of the subjects which have been included into a multi-stage optimal control problem. Furthermore, optimal sit-to-stand motions have been *generated* for several levels of mobility among the elderly population. Finally, *optimal mechanical design parameters* for a novel approach to mobility assistance devices have been obtained for the group of elderly humans with mobility disabilities. In summary, dynamic modeling and numerical optimization prove to be appropriate tools to realistically simulate challenging human motions. As shown in this thesis, such physiologically consistent simulation results can be exploited to describe fundamental patterns of human motions.

Dynamic Model Parameters for Elderly Humans

Regression equations which provide the dynamic model parameters for elderly humans are derived by combining existing sources for dynamic parameters of unimpaired adults with other sources for the age-related changes in body proportions. The resulting parameters are related to the full body mass and length, respectively, facilitating the creation of parameterized multibody models. Using the equations and values presented in this thesis generic models of the body of an elderly human can be established with realistic dynamic parameters which are difficult to obtain on living humans.

Foot Placement in Human Walking

Realistic, i.e. non-periodic and asymmetric, unimpaired and prosthetic human walking motions have been reconstructed for a whole stride from motion capture data recorded in a gait laboratory by formulating multi-stage nonlinear optimal control problems and least-squares objective functions as well as applying multiple-shooting discretization and Sequential Quadratic Programming methods. Physiologically consistent simulation results are ensured by formulating appropriate constraints on the ground contacts as well as on the ranges of joint angles, angular velocities and torques. It has been shown that the upper-body dynamics have a strong influence on the lower-body dynamics. On one hand, gait patterns originating from a lower-body with symmetric properties can be strongly asymmetric due to asymmetric upper-body motions. On the other hand, upper-body asymmetry can be intentionally applied to compensate for asymmetric lower-body properties and result in symmetric gait patterns. Foot placement during human walking has been shown to correlate with the Capture Point while, apparently, the subjects aim at trading off between effortless progression and quick response to perturbations.

The amplitude of the ground contact collision force has been found to play a major role in the strategy to maintain step-by-step stability. In fact, a loss in Capturability due to the reduced ground collision impact force at the prosthetic leg of the subject walking with prostheses can possibly be counteracted with prosthetic components which dissipates more energy at heel strike. These findings encourage us to propose Capturability, evaluated on walking motions reconstructed by optimal control, as a complementary criterion to the already existing clinical stability assessment methods. Since it presents a novel interpretation of stability in human walking, it might lead to a further progress in goal-oriented clinical diagnostics.

Optimal Assisted and Unassisted Sit-to-Stand Motions

Three different cases of sit-to-stand motions have been synthesized based on two-dimensional multibody models of adult and elderly humans and assumptions on their levels of mobility. The *unimpaired* sit-to-stand simulation leads to a natural and conservative motion with healthy appearance based on increased weights on the mechanical work term in the objective function. The *high-dynamic* sit-to-stand simulation results in exaggerating arm motions due to the fact that a greater, however, still realistic amount of body dynamics is assumed to be available to the model to perform the sit-to-stand task. For the *severely impaired* sit-to-stand simulation additional external assistive forces are included into the model acting at predefined force insertion points to represent the support provided by a caregiver to an elderly human. The resulting sit-to-stand motion along with the resulting assistive force profiles as well as the trajectories of their insertion points can be used as requirements for the optimization of the mechanical design parameters for an assistance device providing *nurse-type* sit-to-stand support. In addition, the differences between the predicted motions show that it is crucial for analyzing the sit-to-stand motion to consider a full body model of the human and that the preparatory motions performed right before the actual lift-off significantly contribute to the entire sit-to-stand transfer.

Optimal Design Parameters for a Sit-to-Stand Assistance Device

The resulting optimal support force profiles and the trajectories of their application points obtained from the sit-to-stand simulations for the severely impaired subject as well as for a mildly impaired subject published in [103] have been used as requirements for the design optimization of two different kinds of sit-to-stand assistance devices: the *rollator-type* device to assist the sit-to-stand motion of the mildly impaired as well as the *nurse-type* device to assist the sit-to-stand motion of the severely impaired subjects. Formulating multiple-stage nonlinear optimal control problems, design parameters for the devices have been computed which cover the workspace required to provide support for subjects ranging from the 20th to the 80th body height percentile of both male and female elderly subjects and, at the same time, enable the devices to provide sit-to-stand support with minimal effort. Prototypes of the sit-to-stand assistance devices have been manufactured based on the results presented in this thesis.

OUTLOOK

The results presented in this thesis promote the use of model-based numerical optimization to approach clinical questions related to human motions. Novel findings have been gained towards the step-by-step stability strategies in human walking as well as the assisted and unassisted sit-to-stand motions which encourage a further elaboration of the topics into the following directions:

Distinguishing Individual from Stereotypical Gait Patterns

The findings about foot placement during human walking presented in this thesis are based on the reconstruction of a whole stride from recorded motion data of three subjects in four different walking scenarios. In order to gain a high threshold of statistical confidence for the observations made with regard to both individual as well as stereotypical gait patterns it is necessary to analyze the gait of significantly greater number of subjects. It is also of particular interest to what extent a subject maintains a certain behavior over a sequence of several strides.

Foot Placement in Other Types of Locomotion

Human walking has been shown to aim at trading off between effortless propulsion and prompt responsiveness to perturbations. Other types of locomotion, such as long-distance running or sprinting with transtibial prostheses serve different purposes. Foot placement with respect to the Capture Point should, therefore, also reflect the objectives of these types of gait and enable motion recommendations, e.g. in sport sciences, from a different perspective.

Motion Synthesis for Humanoid Robots

Just as in human walking, energy-efficiency and safety are both amongst the primary, however, conflicting goals in synthesizing gait for humanoid robots. While the different morphologies of the many existing humanoid robots results in a great variety of accomplishable motions, foot placement with respect to the Capture Point might serve well as a motion primitive used in the objective function of an optimal control problem to generate walking motions which are energy-efficient, natural and dynamic and, at the same time, enable fast response to perturbations.

Multi-Contact Capturability

Human locomotion is rarely restricted to flat and regular surfaces. Many situations require humans to walk on stairs, slopes and through rough environment. In certain circumstances, humans increase their maneuverability by additionally establishing contact to the environment with their hands, e.g. by holding to a handrail or leaning against a wall. Generalizing the Capturability concept towards multiple contacts subject to arbitrary contact surface normals and surface-specific friction properties allows for understanding a significantly wider range of types of locomotion.

Asymmetric Sit-to-Stand Motions

The sit-to-stand motion has been synthesized in this thesis using a two-dimensional model of a human assuming perfectly symmetric behavior. However, subjects requiring mobility assistance are often unilaterally affected. Future studies might consider the sit-to-stand motions of elderly people using threedimensional models possibly including muscle models and asymmetric constraints on the ranges of joint angles, angular velocities and joint torques.

Optimization of Future Sit-to-Stand Assistance Devices

Sit-to-stand assistance is assumed in this thesis to be provided by a mobile rollator-type device through the hands and a mobile nurse-type device through the trunk, the forearms and the knees. The recent technological development towards smaller and more efficient electronic components, batteries and actuators enable the design of inconspicuous assistive devices such as wearable exoskeletons or suits made of actuated fabrics. The design of such can be optimized by a profound knowledge of the human anatomy and the methods proposed in this thesis.

Part IV

Appendices

A. ANTHROPOMETRIC PARAMETERS FOR THE HUMAN BODY

Table A.1: Adjusted absolute values for the longitudinal lengths, masses, longitudinal center of mass (COM) position as well as the radii of inertia of the body segments of an average young adult female (F; body mass = 61.9 kg, body height = 173.5 cm) and male (M; body mass = 73.0 kg, body height = 174.1 cm) subject. The segment lengths and COM positions are given with respect to the origin of the appropriate segment's coordinate system as described in Section 2.4.1 and displayed in Figure 2.5. The radii of inertia are specified parallel to the axes of the segments' local coordinate system and with respect to each segment's COM.

Segment	Longitudinal length l_s [mm]		Mass m_s [kg]		COM position $d_{\text{com},s}$ [mm]		Radii of Gyration					
	F	M	F	M	F	M	Sagittal $r_{\text{gyr},s,x}$ [mm]		Transversal $r_{\text{gyr},s,y}$ [mm]		Longitudinal $r_{\text{gyr},s,z}$ [mm]	
							F	M	F	M	F	M
Head	243.7	242.9	4.1	5.1	125.7	121.4	66.0	73.6	71.9	76.5	63.6	63.4
UPT	228.0	242.1	9.6	11.7	112.9	119.5	106.3	122.3	71.5	77.5	102.4	112.6
MPT	205.3	215.5	9.1	11.9	112.7	118.5	88.9	103.9	72.7	82.5	85.2	100.8
Pelvis	181.5	145.7	7.7	8.2	92.2	56.6	78.6	89.6	73.0	80.3	80.6	85.5
Upper arm	275.1	281.7	1.6	2.0	116.8	119.1	76.5	80.3	71.5	75.8	40.7	44.5
Forearm	264.3	268.9	0.9	1.2	143.8	145.9	70.0	74.2	67.9	71.3	24.8	32.5
Hand	78.0	86.2	0.4	0.5	19.7	18.1	41.7	54.1	35.4	44.2	26.1	34.6
Thigh	368.5	422.2	9.2	10.3	133.1	172.9	136.0	138.9	134.1	138.9	59.7	62.9
Shank	432.3	434.0	3.0	3.2	190.9	193.5	117.2	110.7	115.4	108.1	40.2	44.7
Foot	228.3	258.1	0.8	1.0	91.6	114.0	68.3	66.3	63.7	63.2	31.7	32.0
Foot height	75.7	38.6	-	-	37.9	19.3	-	-	-	-	-	-

Table A.2: Adjusted relative values for the longitudinal lengths, masses, longitudinal center of mass (COM) position as well as the radii of inertia of the body segments of an average young adult female (F; body mass = 61.9 kg, body height = 173.5 cm) and male (M; body mass = 73.0 kg, body height = 174.1 cm) subject. The relative values are specified with respect to the full body height and mass, respectively. The segment lengths and COM positions are given with respect to the origin of the appropriate segment's coordinate system as described in Section 2.4.1 and displayed in Figure 2.5. The radii of inertia are specified parallel to the axes of the segments' local coordinate system and with respect to each segment's COM.

Segment	Longitudinal length λ_s [%]		Mass μ_s [%]		COM position δ_s [%]		Radii of Gyration					
							Sagittal $\varrho_{s,x}$ [%]		Transversal $\varrho_{s,y}$ [%]		Longitudinal $\varrho_{s,z}$ [%]	
	F	M	F	M	F	M	F	M	F	M	F	M
Head	14.1	14.0	6.7	6.9	7.3	7.0	3.8	4.2	4.1	4.4	3.7	3.6
UPT	13.1	13.9	15.5	16.0	6.5	6.9	6.1	7.0	4.1	4.5	5.9	6.5
MPT	11.8	12.4	14.7	16.3	6.5	6.8	5.1	6.0	4.2	4.7	4.9	5.8
Pelvis	10.5	8.4	12.5	11.2	5.3	3.3	4.5	5.2	4.2	4.6	4.6	4.9
Upper arm	16.9	16.8	2.6	2.7	6.7	6.8	4.4	4.6	4.1	4.4	2.4	2.6
Forearm	16.1	16.1	1.4	1.6	8.3	8.4	4.0	4.3	3.9	4.1	1.4	1.9
Hand	5.2	5.2	0.6	0.6	1.1	1.0	2.4	3.1	2.0	2.5	1.5	2.0
Thigh	21.2	24.3	14.8	14.2	7.7	9.9	7.8	8.0	7.7	8.0	3.4	3.6
Shank	24.9	24.9	4.8	4.3	11.0	11.1	6.8	6.4	6.7	6.2	2.3	2.6
Foot	15.4	15.4	1.3	1.4	5.3	6.6	3.9	3.8	3.7	3.6	1.8	1.8
Foot height	4.4	2.2	-	-	2.2	1.1	-	-	-	-	-	-

Table A.3: Adjusted absolute values for the segments' moments of inertia of an average young adult female (F; body mass = 61.9 kg, body height = 173.5 cm) and male (M; body mass = 73.0 kg, body height = 174.1 cm) subject using the segment masses and radii of gyration from Table A.1. The moments of inertia are specified in the local coordinate system and with respect to the COM of each segment.

Segment	Gender	Moments of Inertia [$\text{kg} \cdot \text{m}^2$]		
		θ_x	θ_y	θ_z
Head	F	0.0180	0.0214	0.0167
	M	0.0274	0.0297	0.0204
UPT	F	0.1080	0.0490	0.1002
	M	0.1742	0.0699	0.1477
MPT	F	0.0717	0.0479	0.0658
	M	0.1286	0.0812	0.1213
Pelvis	F	0.0477	0.0411	0.0501
	M	0.0655	0.0526	0.0596
Upper arm	F	0.0092	0.0081	0.0026
	M	0.0128	0.0114	0.0039
Forearm	F	0.0041	0.0039	0.0005
	M	0.0065	0.0060	0.0013
Hand	F	0.0006	0.0004	0.0002
	M	0.0013	0.0009	0.0005
Thigh	F	0.1692	0.1646	0.0326
	M	0.1994	0.1994	0.0409
Shank	F	0.0409	0.0397	0.0048
	M	0.0387	0.0369	0.0063
Foot	F	0.0037	0.0032	0.0008
	M	0.0044	0.0040	0.0010

B. PATH CONSTRAINTS FOR HUMAN WALKING

Table B.1: Upper and lower bounds for the generalized positions \mathbf{x} in human walking reconstruction specified as translational (*trans*) and rotational (*rot*) degrees of freedom (DoF) along the X , Y , and Z -axis, respectively.

Joint	DoF	Description	Min	Max
Pelvis	<i>transX</i>	Pelvis translation in forward direction [m]	-2.0	2.0
	<i>transY</i>	Pelvis translation in lateral direction [m]	-0.2	0.2
	<i>transZ</i>	Pelvis translation in vertical direction [m]	0.7	1.0
	<i>rotY</i>	Pelvis tilt [rad]	-0.3	0.2
	<i>rotX</i>	Pelvis roll [rad]	-0.3	0.3
	<i>rotZ</i>	Pelvis yaw [rad]	-0.5	0.5
Hip right	<i>rotY</i>	Right hip flexion/extension [rad]	-0.8	0.6
	<i>rotX</i>	Right hip abduction/adduction [rad]	-0.7	0.4
	<i>rotZ</i>	Right hip outer/inner rotation [rad]	-0.6	0.3
Hip left	<i>rotY</i>	Left hip flexion/extension [rad]	-0.8	0.6
	<i>rotX</i>	Left hip adduction/abduction [rad]	-0.4	0.7
	<i>rotZ</i>	Left hip inner/outer rotation [rad]	-0.3	0.6
Knee right	<i>rotY</i>	Right knee extension/flexion [rad]	0.03	1.2
Knee left	<i>rotY</i>	Left knee extension/flexion [rad]	0.03	1.2
Ankle right	<i>rotY</i>	Right ankle dorsal/plantar flexion [rad]	-0.4	0.4
	<i>rotX</i>	Right ankle valgus/varus [rad]	-0.3	0.3
	<i>rotZ</i>	Right ankle outer/inner rotation [rad]	-0.3	0.3
Ankle left	<i>rotY</i>	Left ankle dorsal/plantar flexion [rad]	-0.4	0.4
	<i>rotX</i>	Left ankle varus/valgus [rad]	-0.3	0.3
	<i>rotZ</i>	Left ankle inner/outer rotation [rad]	-0.3	0.3
Middle trunk	<i>rotY</i>	Middle trunk tilt [rad]	-0.3	0.15
	<i>rotX</i>	Middle trunk roll [rad]	-0.25	0.25
	<i>rotZ</i>	Middle trunk yaw [rad]	-0.7	0.7
Shoulder right	<i>rotY</i>	Right shoulder flexion/extension [rad]	-0.5	0.8
	<i>rotX</i>	Right shoulder abduction/adduction [rad]	-0.7	-0.1
	<i>rotZ</i>	Right shoulder horizontal ext./flex. [rad]	-0.1	0.8
Shoulder left	<i>rotY</i>	Left shoulder flexion/extension [rad]	-0.5	0.8
	<i>rotX</i>	Left shoulder adduction/abduction [rad]	0.1	0.7
	<i>rotZ</i>	Left shoulder horizontal flex./ext. [rad]	-0.8	0.1
Elbow right	<i>rotY</i>	Right elbow flexion/extension [rad]	-1.2	-0.2
Elbow left	<i>rotY</i>	Left elbow flexion/extension [rad]	-1.2	-0.2
Head	<i>rotY</i>	Head tilt [rad]	-0.8	0.8
	<i>rotX</i>	Head roll [rad]	-0.8	0.8
	<i>rotZ</i>	Head yaw [rad]	-0.8	0.8

Table B.2: Upper and lower bounds for the generalized velocities \dot{x} in human walking reconstruction specified according to the translational (*trans*) and rotational (*rot*) degrees of freedom (DoF) along the *X*, *Y*, and *Z*-axis, respectively.

Joint	DoF	Description	Min	Max
Pelvis	<i>transX</i>	Pelvis translation in forward direction [m/s]	-10.0	10.0
	<i>transY</i>	Pelvis translation in lateral direction [m/s]	-10.0	10.0
	<i>transZ</i>	Pelvis translation in vertical direction [m/s]	-10.0	10.0
	<i>rotY</i>	Pelvis tilt [rad/s]	-10.0	10.0
	<i>rotX</i>	Pelvis roll [rad/s]	-10.0	10.0
	<i>rotZ</i>	Pelvis yaw [rad/s]	-10.0	10.0
Hip right	<i>rotY</i>	Right hip flexion/extension [rad/s]	-10.0	10.0
	<i>rotX</i>	Right hip abduction/adduction [rad/s]	-10.0	10.0
	<i>rotZ</i>	Right hip outer/inner rotation [rad/s]	-10.0	10.0
Hip left	<i>rotY</i>	Left hip flexion/extension [rad/s]	-10.0	10.0
	<i>rotX</i>	Left hip adduction/abduction [rad/s]	-10.0	10.0
	<i>rotZ</i>	Left hip inner/outer rotation [rad/s]	-10.0	10.0
Knee right	<i>rotY</i>	Right knee extension/flexion [rad/s]	-10.0	10.0
Knee left	<i>rotY</i>	Left knee extension/flexion [rad/s]	-10.0	10.0
Ankle right	<i>rotY</i>	Right ankle dorsal/plantar flexion [rad/s]	-10.0	10.0
	<i>rotX</i>	Right ankle valgus/varus [rad/s]	-10.0	10.0
	<i>rotZ</i>	Right ankle outer/inner rotation [rad/s]	-10.0	10.0
Ankle left	<i>rotY</i>	Left ankle dorsal/plantar flexion [rad/s]	-10.0	10.0
	<i>rotX</i>	Left ankle varus/valgus [rad/s]	-10.0	10.0
	<i>rotZ</i>	Left ankle inner/outer rotation [rad/s]	-10.0	10.0
Middle trunk	<i>rotY</i>	Middle trunk tilt [rad/s]	-10.0	10.0
	<i>rotX</i>	Middle trunk roll [rad/s]	-10.0	10.0
	<i>rotZ</i>	Middle trunk yaw [rad/s]	-10.0	10.0
Shoulder right	<i>rotY</i>	Right shoulder flexion/extension [rad/s]	-10.0	10.0
	<i>rotX</i>	Right shoulder abduction/adduction [rad/s]	-10.0	10.0
	<i>rotZ</i>	Right shoulder horizontal ext./flex. [rad/s]	-10.0	10.0
Shoulder left	<i>rotY</i>	Left shoulder flexion/extension [rad/s]	-10.0	10.0
	<i>rotX</i>	Left shoulder adduction/abduction [rad/s]	-10.0	10.0
	<i>rotZ</i>	Left shoulder horizontal flex./ext. [rad/s]	-10.0	10.0
Elbow right	<i>rotY</i>	Right elbow flexion/extension [rad/s]	-10.0	10.0
Elbow left	<i>rotY</i>	Left shoulder flexion/extension [rad/s]	-10.0	10.0
Head	<i>rotY</i>	Head tilt [rad/s]	-10.0	10.0
	<i>rotX</i>	Head roll [rad/s]	-10.0	10.0
	<i>rotZ</i>	Head yaw [rad/s]	-10.0	10.0

Table B.3: Upper and lower bounds for the controls \mathbf{u} in human walking reconstruction which act as torques directly on the rotational degrees of freedom (DoF) with respect to the X, Y , and Z -axis, respectively.

Joint	DoF	Description	Min	Max
Hip right	<i>rotY</i>	Right hip flexion/extension [Nm]	-50.0	50.0
	<i>rotX</i>	Right hip abduction/adduction [Nm]	-50.0	50.0
	<i>rotZ</i>	Right hip outer/inner rotation [Nm]	-50.0	50.0
Hip left	<i>rotY</i>	Left hip flexion/extension [Nm]	-50.0	50.0
	<i>rotX</i>	Left hip adduction/abduction [Nm]	-50.0	50.0
	<i>rotZ</i>	Left hip inner/outer rotation [Nm]	-50.0	50.0
Knee right	<i>rotY</i>	Right knee extension/flexion [Nm]	-50.0	50.0
Knee left	<i>rotY</i>	Left knee extension/flexion [Nm]	-50.0	50.0
Ankle right	<i>rotY</i>	Right ankle dorsal/plantar flexion [Nm]	-50.0	50.0
	<i>rotX</i>	Right ankle valgus/varus [Nm]	-50.0	50.0
	<i>rotZ</i>	Right ankle outer/inner rotation [Nm]	-50.0	50.0
Ankle left	<i>rotY</i>	Left ankle dorsal/plantar flexion [Nm]	-50.0	50.0
	<i>rotX</i>	Left ankle varus/valgus [Nm]	-50.0	50.0
	<i>rotZ</i>	Left ankle inner/outer rotation [Nm]	-50.0	50.0
Middle trunk	<i>rotY</i>	Middle trunk tilt [Nm]	-50.0	50.0
	<i>rotX</i>	Middle trunk roll [Nm]	-50.0	50.0
	<i>rotZ</i>	Middle trunk yaw [Nm]	-50.0	50.0
Shoulder right	<i>rotY</i>	Right shoulder flexion/extension [Nm]	-50.0	50.0
	<i>rotX</i>	Right shoulder abduction/adduction [Nm]	-50.0	50.0
	<i>rotZ</i>	Right shoulder horizontal ext./flex. [Nm]	-50.0	50.0
Shoulder left	<i>rotY</i>	Left shoulder flexion/extension [Nm]	-50.0	50.0
	<i>rotX</i>	Left shoulder adduction/abduction [Nm]	-50.0	50.0
	<i>rotZ</i>	Left shoulder horizontal flex./ext. [Nm]	-50.0	50.0
Elbow right	<i>rotY</i>	Right elbow flexion/extension [Nm]	-50.0	50.0
Elbow left	<i>rotY</i>	Left shoulder flexion/extension [Nm]	-50.0	50.0
Head	<i>rotY</i>	Head tilt [Nm]	-50.0	50.0
	<i>rotX</i>	Head roll [Nm]	-50.0	50.0
	<i>rotZ</i>	Head yaw [Nm]	-50.0	50.0

BIBLIOGRAPHY

- [1] G. Abellan van Kan, Y. Rolland, S. Andrieu, J. Bauer, O. Beauchet, M. Bonnefoy, M. Cesari, L. Donini, S. Gillette Guyonnet, M. Inzitari, F. Nourhashemi, G. Onder, P. Ritz, A. Salva, M. Visser, and B. Vellas. Gait speed at usual pace as a predictor of adverse outcomes in community-dwelling older people an international academy on nutrition and aging (IANA) task force. *Journal of Nutrition, Health and Aging*, 13(10):881 – 889, December 2009.
- [2] M. Ackermann. *Dynamics and energetics of walking with prostheses*. PhD thesis, University of Stuttgart, 2007.
- [3] M. Ackermann and W. Schiehlen. Dynamic analysis of human gait disorder and metabolic cost estimation. *Archive of Applied Mechanics*, 75:569–594, 2006. URL www.elib.uni-stuttgart.de/opus/volltexte/2007/2939.
- [4] M. Ackermann and W. Schiehlen. *Physiological Methods to Solve the Force-Sharing Problem in Biomechanics*, pages 1–23. Springer Netherlands, Dordrecht, 2009. ISBN 978-1-4020-8829-2. doi: 10.1007/978-1-4020-8829-2_1.
- [5] M. Ackermann and A. J. van den Bogert. Optimality principles for model-based prediction of human gait. *Journal of Biomechanics*, 43:1055–1060, 2010. URL [10.1016/j.jbiomech.2009.12.012](http://dx.doi.org/10.1016/j.jbiomech.2009.12.012).
- [6] Z. Aftab. *Simulation dynamique de perte d'équilibre : Application aux passagers debout de transport en commun*. Theses, Universite de Lyon, Nov. 2012.
- [7] R. Aissaoui and J. Dansereau. Biomechanical analysis and modelling of sit to stand task: a literature review. In *Systems, Man, and Cybernetics, 1999. IEEE SMC '99 Conference Proceedings. 1999 IEEE International Conference on*, volume 1, pages 141–146 vol.1, 1999. doi: 10.1109/ICSMC.1999.814072.
- [8] C. Alessandro, I. Delis, F. Nori, S. Panzeri, and B. Berret. Muscle synergies in neuroscience and robotics: from input-space to task-space perspectives. *Frontiers in Computational Neuroscience*, 7:43, 2013. ISSN 1662-5188. doi: 10.3389/fncom.2013.00043.
- [9] F. Anderson, J. Siegler, M. Pandy, and R. Whalen. Application of high-performance computing to numerical simulation of human movement. *Jorunal of Biomechanical Engineering*, 117:155–155, 1995.
- [10] F. C. Anderson and M. G. Pandy. Dynamic optimization of human walking. *Journal of biomechanical engineering*, 123(5):381–390, 2001.
- [11] U. M. Ascher, H. Chin, L. R. Petzold, and S. Reich. Stabilization of constrained mechanical systems with daes and invariant manifolds. *Mechanics of Structures and Machines*, 23(2):135–157, 1995. doi: 10.1080/08905459508905232.
- [12] C. E. Bauby and A. D. Kuo. Active control of lateral balance in human walking. *Journal of Biomechanics*, 33(11):1433 – 1440, 2000.

- [13] M. Bellmann, T. Schmalz, and S. Blumentritt. Comparative biomechanical analysis of current microprocessor-controlled prosthetic knee joints. *Archives of physical medicine and rehabilitation*, 91(4):644–652, 2010.
- [14] L. J. Bhargava, M. G. Pandy, and F. C. Anderson. A phenomenological model for estimating metabolic energy consumption in muscle contraction. *Journal of Biomechanics*, 37(1):81 – 88, 2004. ISSN 0021-9290. doi: 10.1016/S0021-9290(03)00239-2.
- [15] J. Block, S. Van Drongelen, D. W. W. Heitzmann, R. Müller, M. Grün, and S. I. Wolf. Sit to stand movement supported by an active orthosis. *Gait & Posture*, 38:S22–S23, 2017/04/26 2013. ISSN 0966-6362. doi: 10.1016/j.gaitpost.2013.07.049.
- [16] M. F. Bobbert, D. A. Kistemaker, M. A. Vaz, and M. Ackermann. Searching for strategies to reduce the mechanical demands of the sit-to-stand task with a muscle-actuated optimal control model. *Clinical Biomechanics*, 37:83 – 90, 2016. ISSN 0268-0033. doi: 10.1016/j.clinbiomech.2016.06.008.
- [17] H. Bock and K. Plitt. *A Multiple Shooting algorithm for direct solution of optimal control problems*. Sonderforschungsbereich 72, Approximation u. Optimierung, Universität Bonn, 1983.
- [18] J. Borenstein and I. Ulrich. The GuideCane - A Computerized Travel Aid for the Active Guidance of Blind Pedestrians. In *Proceedings of the IEEE International Conference on Robotics and Automation*, pages 1283–1288, Apr. 1997.
- [19] S. M. Bruijn, D. J. Bregman, O. G. Meijer, P. J. Beek, and J. H. van Dieën. Maximum lyapunov exponents as predictors of global gait stability: A modelling approach. *Medical Engineering & Physics*, 34(4):428 – 436, 2012. ISSN 1350-4533. doi: 10.1016/j.medengphy.2011.07.024.
- [20] S. M. Bruijn, O. G. Meijer, P. J. Beek, and J. H. van Dieën. Assessing the stability of human locomotion: a review of current measures. *Journal of The Royal Society Interface*, 11(90), 2013. ISSN 1742-5689. doi: 10.1098/rsif.2013.0900.
- [21] T. Buschmann, A. Ewald, A. von Twickel, and A. Büschges. Controlling legs for locomotion—insights from robotics and neurobiology. *Bioinspiration & Biomimetics*, 10(4): 041001, 2015. URL <http://stacks.iop.org/1748-3190/10/i=4/a=041001>.
- [22] A. Cappozzo. Gait analysis methodology. *Human Movement Science*, 3(1–2):27 – 50, 1984. ISSN 0167-9457. doi: 10.1016/0167-9457(84)90004-6.
- [23] A. Cappozzo, T. Leo, and A. Pedotti. A general computing method for the analysis of human locomotion. *Journal of Biomechanics*, 8(5):307 – 320, 1975. ISSN 0021-9290. doi: 10.1016/0021-9290(75)90083-4.
- [24] A. Cappozzo, U. D. Croce, A. Leardini, and L. Chiari. Human movement analysis using stereophotogrammetry: Part 1: theoretical background. *Gait & Posture*, 21(2):186 – 196, 2005. ISSN 0966-6362. doi: 10.1016/j.gaitpost.2004.01.010.
- [25] C. Chow and D. Jacobson. Studies of human locomotion via optimal programming. *Mathematical Biosciences*, 10(3):239 – 306, 1971. ISSN 0025-5564. doi: 10.1016/0025-5564(71)90062-9.

- [26] D. Chugo, T. Asawa, T. Kitamura, S. Jia, and K. Takase. A rehabilitation walker with standing and walking assistance. *IEEE/RSJ International Conference on Intelligent Robots and Systems, IROS*, pages 260–265, Sept 2008. doi: 10.1109/IROS.2008.4650845.
- [27] M. J. Coleman. *A Stability Study of a Three-Dimensional Passive-Dynamic Model of Human Gait*. PhD thesis, Cornell University, 1998.
- [28] S. Collins, A. Ruina, R. Tedrake, and M. Wisse. Efficient bipedal robots based on passive-dynamic walkers. *Science*, 307(5712):1082–1085, 2005. ISSN 0036-8075. doi: 10.1126/science.1107799.
- [29] P. de Leva. Adjustments to Zatsiorsky-Seluyanov’s segment inertia parameters. *Journal of Biomechanics*, 29 (9):1223–1230, 1996. doi: 10.1016/0021-9290(95)00178-6.
- [30] A. de Rugy, G. Loeb, and T. Carroll. Are muscle synergies useful for neural control? *Frontiers in Computational Neuroscience*, 7:19, 2013. ISSN 1662-5188. doi: 10.3389/fncom.2013.00019.
- [31] S. F. Donker and P. J. Beek. Interlimb coordination in prosthetic walking: effects of asymmetry and walking velocity. *Acta Psychologica*, 110(2–3):265 – 288, 2002. ISSN 0001-6918. doi: 10.1016/S0001-6918(02)00037-9.
- [32] R. Dumas, L. Cheze, and J.-P. Verriest. Adjustments to McConville et al. and Young et al. body segment inertial parameters. *Journal of Biomechanics*, 40(3):543 – 553, 2007. ISSN 0021-9290. doi: 10.1016/j.jbiomech.2006.02.013.
- [33] J. Engelsberger, C. Ott, and A. Albu-Schäffer. Three-dimensional bipedal walking control based on divergent component of motion. *IEEE Transactions on Robotics*, 31(2):355–368, 2015.
- [34] I. Fantoni and R. Lozano. *Non-Linear Control for Underactuated Mechanical Systems*. Springer-Verlag New York, Inc., Secaucus, NJ, USA, 2001. ISBN 1852334231.
- [35] R. Featherstone. *Rigid Body Dynamics Algorithms*. Springer-Verlag New York, Inc., Secaucus, NJ, USA, 2008. ISBN 0387743146.
- [36] M. L. Felis. *Modeling Emotional Aspects in Human Locomotion*. PhD thesis, Combined Faculty for the Natural Sciences and Mathematics of Heidelberg University, Germany, July 2015 2015.
- [37] M. L. Felis. RBDL: an efficient rigid-body dynamics library using recursive algorithms. *Autonomous Robots*, 41(2):495–511, 2017. ISSN 1573-7527. doi: 10.1007/s10514-016-9574-0.
- [38] M. L. Felis. Puppeteer - a motion capture mapping to convert marker movement to skeletal animations. Code repository, April 2017. URL <https://github.com/martinfelis/puppeteer>.
- [39] M. L. Felis, K. Mombaur, H. Kadone, and A. Berthoz. Modeling and identification of emotional aspects of locomotion. *J. Comput. Science*, 4(4):255–261, 2013. doi: 10.1016/j.jocs.2012.10.001.
- [40] Fraunhofer Institute for Manufacturing Engineering and Automation (IPA). Care-O-bot II. online, March 2017. URL <https://www.care-o-bot.de/en/care-o-bot-3/history/care-o-bot-ii.html>.

BIBLIOGRAPHY

- [41] H. Gage. Accelerographic analysis of human gait. In *Biomechanics Monograph, ASME Paper Number 64-WA/HUF-8*, pages 137–152, 1967.
- [42] J. Geursen, D. Altena, and C. Massen. of the standing wan for the description of his dynamic behaviour. *Agressologie*, 17(63-69), 1976.
- [43] P. E. Gill, W. Murray, and M. H. Wright. *Practical optimization*. Academic Press Inc. [Harcourt Brace Jovanovich Publishers], London, 1981. ISBN 0-12-283950-1.
- [44] P. E. Gill, W. Murray, and M. A. Saunders. User's guide for qpopt 1.0: A fortran package for quadratic programming. Technical report, Department of Mathematics, University of California, San Diego; Systems Optimization Laboratory, Department of Operations Research, Stanford University, Stanford, 1995.
- [45] A. Goswami. Postural stability of biped robots and the foot-rotation indicator (fri) point. *International Journal of Robotics Research*, 18(6):523–533, 1999.
- [46] A. Goswami and V. Kallem. Rate of change of angular momentum and balance maintenance of biped robots. *International Conference on Robotics and Automation*, pages 3785–3790, 2004. doi: 10.1109/ROBOT.2004.1308858.
- [47] A. Gouelle, F. Mégrot, A. Presedo, I. Husson, A. Yelnik, and G.-F. Penneçot. The gait variability index: A new way to quantify fluctuation magnitude of spatiotemporal parameters during gait. *Gait & Posture*, 38(3):461 – 465, 2013. ISSN 0966-6362. doi: 10.1016/j.gaitpost.2013.01.013.
- [48] B. Graf, M. Hans, and R. Schraft. Care-O-Bot II — development of a next generation robotic home assistant. *Autonomous Robots*, 16(2):193–205, 2004. ISSN 0929-5593. doi: 10.1023/B:AURO.0000016865.35796.e9.
- [49] B. Graf, C. Parlitz, and M. Hägele. *Robotic Home Assistant Care-O-bot® 3 Product Vision and Innovation Platform*, pages 312–320. Springer Berlin Heidelberg, Berlin, Heidelberg, 2009. ISBN 978-3-642-02577-8. doi: 10.1007/978-3-642-02577-8_34.
- [50] R. J. Griffin, T. Cobb, T. Craig, M. Daniel, N. van Dijk, J. Gines, K. Kramer, S. Shah, O. Siebinga, J. Smith, and P. D. Neuhaus. Design and approach of team IHMC in the 2016 cybathlon. *CoRR*, abs/1702.08656, 2017. URL <http://arxiv.org/abs/1702.08656>.
- [51] J. W. Grizzle, G. Abba, and F. Plestan. Asymptotically stable walking for biped robots: analysis via systems with impulse effects. *IEEE Trans. Automat. Contr.*, 46(1):51–64, 2001. doi: 10.1109/9.898695.
- [52] J. W. Grizzle, G. Abba, and F. Plestan. Correction to "asymptotically stable walking for biped robots: analysis via systems with impulse effects". *IEEE Trans. Automat. Contr.*, 46(3):513, 2001. doi: 10.1109/TAC.2001.911439.
- [53] L. Hak, H. Houdijk, P. J. Beek, and J. H. van Dieën. Steps to take to enhance gait stability: The effect of stride frequency, stride length, and walking speed on local dynamic stability and margins of stability. *PLoS ONE*, 8(12):e82842, 2013.
- [54] L. Hak, H. Houdijk, F. Steenbrink, A. Mert, P. van der Wurff, P. J. Beek, and J. H. van Dieën. Stepping strategies for regulating gait adaptability and stability. *Journal of Biomechanics*, 46(5):905 – 911, 2013. ISSN 0021-9290. doi: 10.1016/j.jbiomech.2012.12.017.

- [55] L. Hak, J. H. van Dieën, P. van der Wurff, and H. Houdijk. Stepping asymmetry among individuals with unilateral transtibial limb loss might be functional in terms of gait stability. *Physical Therapy*, 94(10):1480, 2014. doi: 10.2522/ptj.20130431.
- [56] S. O. Hansson and G. Helgesson. What is stability? *Synthese*, 136:219–235, 2003.
- [57] K. Hauer, M. Schwenk, T. Zieschang, M. Essig, C. Becker, and P. Oster. Physical training improves motor performance in people with dementia: A randomized controlled trial. *Journal of the American Geriatric Society*, 60(1):8–15, 2012. ISSN 1532-5415.
- [58] J. M. Hausdorff. Gait dynamics, fractals and falls: Finding meaning in the stride-to-stride fluctuations of human walking. *Human Movement Science*, 26(4):555 – 589, September 2007. ISSN 0167-9457. doi: 10.1016/j.humov.2007.05.003.
- [59] S. Hawking. My computer. online, April 2017. URL <http://www.hawking.org.uk/the-computer.html>.
- [60] D. W. W. Heitzmann, M. Alimusaj, J. Block, T. Dreher, F. Braatz, and S. I. Wolf. Gait strategies of transfemoral amputees descending slopes. *Gait & Posture*, 38:S26–S27, 2017/04/26 2013. ISSN 0966-6362. doi: 10.1016/j.gaitpost.2013.07.057.
- [61] H. Herr. Exoskeletons and orthoses: classification, design challenges and future directions. *Journal of NeuroEngineering and Rehabilitation*, 6(1):21, 2009. ISSN 1743-0003. doi: 10.1186/1743-0003-6-21.
- [62] H. Herr and G. P. Whiteley. *Cyborg Technology - Biomimetic Orthotic and Prosthetic Technology*, chapter Chapter 5:, pages 103–144. SPIE Press, 2004.
- [63] Y. Hirata, A. Hara, and K. Kosuge. Passive-type intelligent walking support system "RT Walker". In *2004 IEEE/RSJ International Conference on Intelligent Robots and Systems (IROS) (IEEE Cat. No.04CH37566)*, volume 4, pages 3871–3876, September 2004. doi: 10.1109/IROS.2004.1390018.
- [64] Y. Hirata, A. Hara, and K. Kosuge. Motion control of passive intelligent walker using servo brakes. *IEEE Transactions on Robotics*, 23(5):981–990, Oct 2007. ISSN 1552-3098. doi: 10.1109/TRO.2007.906252.
- [65] M. W. Hirsch, S. Smale, and R. L. Devaney. *Differential equations, dynamical systems, and an introduction to chaos*. Academic Press, Waltham (Mass.), 2013. ISBN 978-0-12-382010-5.
- [66] K.-L. Ho Hoang. Modellierung und Simulation von Oberschenkelprothesen. Diplomarbeit, Universität Stuttgart, March 2008.
- [67] K.-L. Ho Hoang and K. Mombaur. Optimal design of a physical assistive device to support sit-to-stand motions. *IEEE International Conference on Robotics and Automation (ICRA)*, pages 5891–5897, May 2015. doi: 10.1109/ICRA.2015.7140024.
- [68] K.-L. Ho Hoang, D. Corradi, S. Delbasteh, and K. Mombaur. Gait performance indicators for elderly humans interacting with robotic mobility assistance devices. *IEEE International Conference on Rehabilitation Robotics (ICORR)*, pages 758–763, Aug 2015. doi: 10.1109/ICORR.2015.7281293.
- [69] A. L. Hof, M. G. J. Gazendam, and W. E. Sinke. The condition for dynamic stability. *Journal of Biomechanics*, 38:1–8, 2005.

- [70] M. K. Holden and K. M. Gill. Clinical gait assessment in the neurologically impaired: reliability and meaningfulness. *Physical Therapy*, 64(1):35–40, 1984.
- [71] R. K. Jensen and P. Fletcher. Distribution of mass to the segments of elderly males and females. *Journal of Biomechanics*, 27(1):89 – 96, 1994. ISSN 0021-9290. doi: 10.1016/0021-9290(94)90035-3.
- [72] S. Kajita and K. Tani. Study of dynamic biped locomotion on rugged terrain-derivation and application of the linear inverted pendulum mode. In *Proceedings on IEEE International Conference on Robotics and Automation*, volume 2, pages 1405–1411, April 1991. doi: 10.1109/ROBOT.1991.131811.
- [73] S. Kajita, K. Tani, and A. Kobayashi. Dynamic walk control of a biped robot along the potential energy conserving orbit. In *Intelligent Robots and Systems '90. 'Towards a New Frontier of Applications', Proceedings. IROS '90. IEEE International Workshop on*, volume 2, pages 789–794, July 1990. doi: 10.1109/IROS.1990.262497.
- [74] S. Kajita, F. Kanehiro, K. Kaneko, K. Yokoi, and H. Hirukawa. The 3D linear inverted pendulum mode: a simple modeling for a biped walking pattern generation. *IEEE/RSJ International Conference on Intelligent Robots and Systems*, 1, 2001.
- [75] K. Kamiya. Development and evaluation of life support technology in nursing. In *Proc. of 7th RACE Symp., Research into Intelligent Artifacts for the Generalization of Engineering*, pages 116–121. The University of Tokyo, 2005.
- [76] M. L. Kaplan and J. H. Heegaard. Predictive algorithms for neuromuscular control of human locomotion. *Journal of Biomechanics*, 34(8):1077 – 1083, 2001. ISSN 0021-9290. doi: 10.1016/S0021-9290(01)00057-4.
- [77] K. Kaufman, J. Levine, R. Brey, B. Iverson, S. McCrady, D. Padgett, and M. Joyner. Gait and balance of transfemoral amputees using passive mechanical and microprocessor-controlled prosthetic knees. *Gait & Posture*, 26(4):489 – 493, 2007. ISSN 0966-6362. doi: 10.1016/j.gaitpost.2007.07.011.
- [78] Kistler Instrumente GmbH. company website, April 2017. URL <http://www.kistler.com>. Sindelfingen, Germany.
- [79] R. Kittmann, T. Fröhlich, J. Schäfer, U. Reiser, F. Weißhardt, and A. Haug. Let me introduce myself: I am Care-O-bot 4, a gentleman robot. In S. Diefenbach, N. Henze, and M. Pielot, editors, *Mensch und Computer 2015 – Proceedings*, pages 223–232, Berlin, 2015. De Gruyter Oldenbourg.
- [80] G. K. Klute, C. F. Kallfelz, and J. M. Czerniecki. Mechanical properties of prosthetic limbs: Adapting to the patient. *Journal of Rehabilitation Research & Development*, 38(3):299 – 307, 2001. ISSN 07487711.
- [81] K. H. Koch. *Using Model-based Optimal Control for Conceptual Motion Generation for the Humanoid Robot HRP-2 14 and Design Investigations for Exo-Skeleton*. PhD thesis, University Heidelberg, June 2015.
- [82] S. A. Kolakowsky-Hayner, J. Crew, S. Moran, and A. Shah. Safety and feasibility of using the eksotm bionic exoskeleton to aid ambulation after spinal cord injury. *Journal of Spine*, 2013. doi: 10.4172/2165-7939.S4-003.

- [83] T. Koolen, T. de Boer, J. Rebula, A. Goswami, and J. Pratt. Capturability-based analysis and control of legged locomotion, part 1: Theory and application to three simple gait models. *The International Journal of Robotics Research*, 31(9):1094–1113, 2012. doi: 10.1177/0278364912452673.
- [84] T. Koolen, J. Smith, G. Thomas, S. Bertrand, J. Carff, N. Mertins, D. Stephen, P. Abeles, J. Engelsberger, S. McCrory, J. van Egmond, M. Griffioen, M. Floyd, S. Kobus, N. Manor, S. Alsheikh, D. Duran, L. Bunch, E. Morphis, L. Colasanto, K.-L. Ho Hoang, B. Layton, P. Neuhaus, M. Johnson, and J. Pratt. Summary of team IHMC’s virtual robotics challenge entry. *13th IEEE-RAS International Conference on Humanoid Robots (Humanoids)*, pages 307–314, Oct 2013. ISSN 2164-0572. doi: 10.1109/HUMANOIDS.2013.7029992.
- [85] M. Krause, J. Engelsberger, P.-B. Wieber, and C. Ott. Stabilization of the capture point dynamics for bipedal walking based on model predictive control. *IFAC Proceedings Volumes*, 45(22):165 – 171, 2012. ISSN 1474-6670. doi: <http://dx.doi.org/10.3182/20120905-3-HR-2030.00165>.
- [86] D. Kulić, G. Venture, K. Yamane, E. Demircan, I. Mizuuchi, and K. Mombaur. Anthropomorphic movement analysis and synthesis: A survey of methods and applications. *IEEE Transactions on Robotics*, 32(4):776–795, Aug 2016. ISSN 1552-3098. doi: 10.1109/TRO.2016.2587744.
- [87] C. J. C. Lamoth, E. Ainsworth, W. Polomski, and H. Houdijk. Variability and stability analysis of walking of transfemoral amputees. *Medical Engineering and Physics*, 32(9):1009–1014, November 2010. ISSN 1350-4533. doi: 10.1016/j.medengphy.2010.07.001.
- [88] D. Leineweber. The theory of MUSCOD in a nutshell. Technical Report 96-19, Interdisciplinary Center for Scientific Computing (IWR), 1996.
- [89] D. Leineweber, I. Bauer, A. Schäfer, H. Bock, and J. Schlöder. An efficient multiple shooting based reduced SQP strategy for large-scale dynamic process optimization (Parts I and II). *Computers and Chemical Engineering*, 27:157–174, 2003.
- [90] E. A. Lewis. Fluid-controlled knee mechanisms clinical considerations. *Bulletin of Prosthetic Research*, 1965.
- [91] P. Manns, M. Sreenivasa, M. Millard, and K. Mombaur. Motion optimization and parameter identification for a human and lower-back exoskeleton model. *IEEE Robotics and Automation Letters*, 2017.
- [92] E.-J. Marey. *Le Mouvement*. G. Masson, 1894.
- [93] M. Mast, M. Burmester, B. Graf, F. Weisshardt, G. Arbeiter, M. Španěl, Z. Materna, P. Smrž, and G. Kronreif. *Design of the Human-Robot Interaction for a Semi-Autonomous Service Robot to Assist Elderly People*, pages 15–29. Springer International Publishing, Cham, 2015. ISBN 978-3-319-11866-6. doi: 10.1007/978-3-319-11866-6_2.
- [94] R. B. McGhee. *Computer Simulation of Human Movements*, pages 41–78. Springer Vienna, Vienna, 1980. ISBN 978-3-7091-4366-7. doi: 10.1007/978-3-7091-4366-7_2.
- [95] S. G. McLean, X. Huang, A. Su, and A. J. van den Bogert. Sagittal plane biomechanics cannot injure the {ACL} during sidestep cutting. *Clinical Biomechanics*, 19(8):828 – 838, 2004. ISSN 0268-0033. doi: 10.1016/j.clinbiomech.2004.06.006.

BIBLIOGRAPHY

- [96] P. Médéric, V. Pasqui, F. Plumet, P. Bidaud, and J. Guinot. Design of a walking-aid and sit-to-stand transfer assisting device for elderly people. *15th CISM-IFTToMM Symposium on Robot Design, Dynamics and Control, St Hubert, Canada, 2004*.
- [97] P. Médéric, V. Pasqui, F. Plumet, and P. Bidaud. *Sit to Stand Transfer Assisting by an Intelligent Walking-Aid*, pages 1127–1135. Springer Berlin Heidelberg, Berlin, Heidelberg, 2005. ISBN 978-3-540-29461-0. doi: 10.1007/3-540-29461-9_111.
- [98] P. Médéric, V. Pasqui, F. Plumet, and P. Bidaud. Elderly people sit to stand transfer experimental analysis. *Climbing and Walking Robots*, pages 953–960, 2006.
- [99] M. Millard, J. McPhee, and E. Kubica. Foot placement and balance in 3d. *ASME J. Comp. Non. Dyn.*, 7:1–14, 2012. doi: 10.1115/1.4005462.
- [100] MOBOT. Intelligent Active MObility Assistance RoBOT integrating Multimodal Sensory Processing Proactive Autonomy and Adaptive Interaction funded by the European Union within the FP7 program under grant agreement no. 600796, 2013 - 2016. URL www.mobot-project.eu.
- [101] K. Mombaur. *Stability Optimization of Open-loop Controlled Walking Robots*. PhD thesis, University of Heidelberg, 2001. ISBN 3-18-392208-8.
- [102] K. Mombaur. Using optimization to create self-stable human-like running. *Robotica*, 27: 321–330, May 2009. ISSN 0263-5747. doi: 10.1017/S0263574708004724.
- [103] K. Mombaur and K.-L. Ho Hoang. How to best support sit to stand transfers of geriatric patients: Motion optimization under external forces for the design of physical assistive devices. *Journal of Biomechanics*, 58:131 – 138, 2017. ISSN 0021-9290. doi: 10.1016/j.jbiomech.2017.04.037.
- [104] K. Mombaur, H. G. Bock, J. P. Schlöder, and R. W. Longman. Human-like actuated walking that is asymptotically stable without feedback. In *IEEE International Conference on Robotics and Automation (ICRA)*, 2001.
- [105] K. Mombaur, A. Truong, and J.-P. Laumond. From human to humanoid locomotion— an inverse optimal control approach. *Autonomous Robots*, 28(3):369–383, 2010. ISSN 1573-7527. doi: 10.1007/s10514-009-9170-7.
- [106] K. D. Mombaur, R. W. Longman, H. G. Bock, and J. P. Schlöder. Open-loop stable running. *Robotica*, 23(01):21–33, 2005. doi: 10.1017/S026357470400058X.
- [107] E. F. Murphy. The swing phase of walking with above-knee prostheses. *Bulletin of Prosthetic Research*, pages 5–39, 1964.
- [108] M. P. Murray, A. Seireg, and R. C. Scholz. Center of gravity, center of pressure, and supportive forces during human activities. *Journal of Applied Physiology*, 23(6):831–838, 1967. ISSN 8750-7587. URL <http://jap.physiology.org/content/23/6/831>.
- [109] E. Muybridge. *Muybridge’s Complete Human and Animal Locomotion: All 781 Plates from the 1887 Animal Locomotion*. Dover, 1979.
- [110] Y. Nakamura. *Advanced Robotics: Redundancy and Optimization*. Addison-Wesley Longman Publishing Co., Inc., Boston, MA, USA, 1st edition, 1990. ISBN 0201151987.

- [111] NASA. *Anthropometric source book. Volume 2: A handbook of anthropometric data*. NASA Reference Publication 1024, National Aeronautics and Space Administration, Scientific and Technical Information Office, 1978.
- [112] L. M. Nashner and G. McCollum. The organization of human postural movements: A formal basis and experimental synthesis. *Behavioral and Brain Sciences*, 8(1):135–150, 1985. doi: 10.1017/S0140525X00020008.
- [113] C. Nester, M. van der Linden, and P. Bowker. Effect of foot orthoses on the kinematics and kinetics of normal walking gait. *Gait & Posture*, 17(2):180 – 187, 2003. ISSN 0966-6362. doi: 10.1016/S0966-6362(02)00065-6.
- [114] J. Nocedal and S. J. Wright. *Numerical optimization*. Springer Series in Operations Research and Financial Engineering. Springer, Berlin, 2006. ISBN 978-0387-30303-1.
- [115] Össur hf. Power Knee. online, April 2017. URL www.ossur.com/prosthetic-solutions/products/dynamic-solutions/power-knee.
- [116] Össur hf. Rheo Knee 3. online, April 2017. URL www.ossur.com/prosthetic-solutions/products/dynamic-solutions/rheo-knee-3.
- [117] Otto Bock HealthCare Deutschland GmbH. Triton Prothesenfüße. online, March 2017. URL <http://www.ottobock.de/prothetik/produkte-a-bis-z/prothesenfuesse/triton-produktfamilie/>.
- [118] Otto Bock HealthCare Deutschland GmbH. C-Leg Beinprothese. online, March 2017. URL <http://www.ottobock.de/cleg.html>.
- [119] Otto Bock HealthCare Deutschland GmbH. Genium Beinprothese. online, March 2017. URL <http://www.ottobock.de/genium.html>.
- [120] P. Overstall, A. Exton-Smith, F. Imms, and A. Johnson. Falls in the elderly related to postural imbalance. *Br Med J*, 1(6056):261–264, 1977.
- [121] M. G. Pandy and N. Berme. A numerical method for simulating the dynamics of human walking. *Journal of Biomechanics*, 21(12):1043 – 1051, 1988. ISSN 0021-9290. doi: 10.1016/0021-9290(88)90250-3.
- [122] M. G. Pandy, B. A. Garner, and F. C. Anderson. Optimal control of non-ballistic muscular movements: A constraint-based performance criterion for rising from a chair. *Journal of Biomechanical Engineering*, 117(1):15–26, Feb 1995. ISSN 0148-0731. doi: 10.1115/1.2792265.
- [123] J. Panero and M. Zelnik. *Human dimension & interior space: a source book of design reference standards*. Whitney library of design. Whitney Library of Design, 1979. ISBN 9780823072712.
- [124] V. Pasqui, L. Saint-Bauzel, and O. Sigaud. *Characterization of a Least Effort User-Centered Trajectory for Sit-to-Stand Assistance*, pages 197–204. Springer Netherlands, Dordrecht, 2011. ISBN 978-94-007-1643-8. doi: 10.1007/978-94-007-1643-8_22.
- [125] J. Perry and J. M. Burnfield. *Gait Analysis, Normal and Pathological Function*. Slack Incorporated, 2nd edition, 2010.

BIBLIOGRAPHY

- [126] S. Pheasant and C. Haslegrave. *Bodyspace: Anthropometry, Ergonomics and the Design of Work, Third Edition*. Taylor & Francis, 2005. ISBN 9780415285209.
- [127] M. R. Pitkin. Effects of design variants in lower-limb prostheses on gait synergy. *Journal of Prosthetics and Orthotics*, 9(3):113–122, 1997.
- [128] M. Popovic, A. Hofmann, and H. Herr. Angular momentum regulation during human walking: biomechanics and control. *IEEE International Conference on Robotics and Automation*, 3:2405–2411, April 2004. ISSN 1050-4729. doi: 10.1109/ROBOT.2004.1307421.
- [129] M. B. Popovic, A. Goswami, and H. M. Herr. Ground reference points in legged locomotion: Definitions, biological trajectories and control implications. *The International Journal of Robotics Research*, 24(12):1013–1032, 2005.
- [130] Z. Popović and A. Witkin. Physically based motion transformation. *Proceedings of the 26th Annual Conference on Computer Graphics and Interactive Techniques*, pages 11–20, 1999. doi: 10.1145/311535.311536.
- [131] A. Potschka, H. G. Bock, and J. P. Schlöder. A minima tracking variant of semi-infinite programming for the treatment of path constraints within direct solution of optimal control problems. *Optimization Methods and Software*, 24(2):237–252, 2009. doi: 10.1080/10556780902753098.
- [132] J. Pratt, J. Carff, S. Drakunov, and A. Goswami. Capture point: A step toward humanoid push recovery. In *6th IEEE-RAS International Conference on Humanoid Robots*, pages 200–207, 2006.
- [133] J. E. Pratt and R. Tedrake. Velocity-based stability margins for fast bipedal walking. In M. Diehl and K. Mombaur, editors, *In Fast Motions in Biomechanics and Robotics*, volume 340, pages 299–324. Springer, 2006.
- [134] Qualisys AB. company website, 2017. URL <http://www.qualisys.com/>. Gothenburg, Sweden.
- [135] P. Sardain and G. Bessonnet. Forces acting on a biped robot. center of pressure - zero moment point. *IEEE Transactions on Systems, Man, and Cybernetics*, 34(5):630 – 637, September 2004.
- [136] D. M. Scarborough, C. A. McGibbon, and D. E. Krebs. Chair rise strategies in older adults with functional limitations. *Journal of rehabilitation research and development*, 44 1:33–42, 2007.
- [137] W. Schiehlen. Recent developments in multibody dynamics. *Journal of Mechanical Science and Technology*, 19(1):227–236, 2005. ISSN 1738-494X. doi: 10.1007/BF02916141.
- [138] W. Schiehlen and M. Ackermann. Estimation of metabolical costs for human locomotion. In *ASME 2005 International Design Engineering Technical Conferences and Computers and Information in Engineering Conference, Volume 6: 5th International Conference on Multibody Systems, Nonlinear Dynamics, and Control, Parts A, B, and C*, pages 299–315, Long Beach, CA, September 2005.
- [139] W. Schiehlen and P. Eberhard. *Technische Dynamik: Modelle für Regelung und Simulation*. Vieweg+Teubner, 4th edition, 2014. ISBN 978-3-658-06184-5.

- [140] R. Schraft, C. Schaeffer, and T. May. Care-O-bot™: the concept of a system for assisting elderly or disabled persons in home environments. In *Proceedings of the 24th Annual Conference of the IEEE Industrial Electronics Society, 1998. IECON '98*, volume 4, pages 2476–2481, August 1998. doi: 10.1109/IECON.1998.724115.
- [141] M. Schünke, E. Schulte, and U. Schumacher. *Prometheus: Allgemeine Anatomie und Bewegungssystem : LernAtlas der Anatomie*. Thieme, 2005. ISBN 978-3-131-39521-4.
- [142] B. Siciliano and O. Khatib, editors. *Springer Handbook of Robotics*. Springer, Heidelberg, Germany, second edition, 2016.
- [143] R. Soames and J. Atha. The validity of physique-based inverted pendulum models of postural sway behaviour. *Annals of Human Biology*, 7(2):145–153, 1980. doi: 10.1080/03014468000004171.
- [144] A. M. Spungen, P. K. Asselin, D. B. Fineberg, S. D. Kornfeld, and N. Y. Harel. Exoskeletal-assisted walking for persons with motor-complete paraplegia, force sustainment: Rehabilitation, regeneration and prosthetics for re-integration to duty. *Meeting Proceedings STO-MP-HFM-228, Paper 6. Neuilly-sur-Seine, France*, pages 6–1 – 6–14, April 2013.
- [145] H. W. Stoudt, A. Damon, R. McFarland, and J. Roberts. *Weight, Height, and Selected Body Dimensions of Adults, United States 1960-1962*. Public Health Service Publication 1000, Series 11, No. 8, 1965.
- [146] S. Studenski. Gait, mobility, and function: A review and proposed classification scheme. In J. M. Hausdorff and N. B. Alexander, editors, *Gait Disorders: Evaluation and Management*, pages 1 – 17. Taylor & Francis Group, 2005.
- [147] T. Sugihara. Solvability-unconcerned inverse kinematics by the Levenberg-Marquardt method. *IEEE Transactions on Robotics*, 27(5):984–991, Oct 2011. ISSN 1552-3098. doi: 10.1109/TRO.2011.2148230.
- [148] J. Thiele, B. Westebbe, M. Bellmann, and M. Kraft. Designs and performance of microprocessor-controlled knee joints. *Biomedizinische Technik. Biomedical engineering*, 59(1):65—77, February 2014. ISSN 0013-5585. doi: 10.1515/bmt-2013-0069.
- [149] M. A. Townsend. Biped gait stabilization via foot placement. *Journal of Biomechanics*, 18(1):21 – 38, 1985. ISSN 0021-9290. doi: 10.1016/0021-9290(85)90042-9.
- [150] M. C. Tresch and A. Jarc. The case for and against muscle synergies. *Current opinion in neurobiology*, 19(6):601–607, 2009.
- [151] B. R. Umberger, K. G. M. Gerritsen, and P. E. Martin. A model of human muscle energy expenditure. *Computer Methods in Biomechanics and Biomedical Engineering*, 6(2):99–111, 2003. doi: 10.1080/1025584031000091678. PMID: 12745424.
- [152] Vicon Motion Systems Limited. company website, 2017. URL <http://www.vicon.com>. Oxford, United Kingdom.
- [153] *PlugIn-Gait Product Guide - Foundation Notes, Version 2.0*. Vicon Motion Systems Ltd., March 2010. URL www.vicon.com.
- [154] M. Vukobratovic and B. Branislav. Zero moment point - thirty five years of its life. *International Journal of Humanoid Robotics*, 1(1):157–173, 2004.

BIBLIOGRAPHY

- [155] A. Wall, J. Borg, and S. Palmcrantz. Clinical application of the hybrid assistive limb (hal) for gait training—a systematic review. *Frontiers in Systems Neuroscience* 9, 9(48): 1–10, March 2015. doi: 10.3389/fnsys.2015.00048.
- [156] W. Weber and E. Weber. *Mechanik der menschlichen Gehwerkzeuge : eine anatomisch-physiologische Untersuchung*. Dietrich, 1836.
- [157] P.-B. Wieber. On the stability of walking systems. In *Proceedings of the International Workshop on Humanoid and Human Friendly Robotics*, Tsukuba, Japan, 2002.
- [158] D. L. Wight, E. G. Kubica, and D. W. Wang. Introduction of the foot placement estimator: A dynamic measure of balance for bipedal robotics. *Journal of Computational and Nonlinear Dynamics*, 3(1):1–10, Nov 2007.
- [159] M. Windrich, M. Grimmer, O. Christ, S. Rinderknecht, and P. Beckerle. Active lower limb prosthetics: a systematic review of design issues and solutions. *Biomedical Engineering Online*, 15(Suppl 3):140, Dec 2016. ISSN 1475-925X. doi: 10.1186/s12938-016-0284-9. 284[PII].
- [160] D. A. Winter. Human balance and posture control during standing and walking. *Gait and Posture*, 3(4):193–214, December 1995.
- [161] D. A. Winter. *Biomechanics and motor control of human movement*. A Wiley-Interscience publication. J. Wiley & Sons, New York, 2009. ISBN 0-471-50908-6.
- [162] D. A. Winter, R. K. Greenlaw, and D. A. Hobson. Television-computer analysis of kinematics of human gait. *Computers and Biomedical Research*, 5(5):498 – 504, 1972. ISSN 0010-4809. doi: [http://dx.doi.org/10.1016/0010-4809\(72\)90056-0](http://dx.doi.org/10.1016/0010-4809(72)90056-0).
- [163] S. I. Wolf, M. Alimusaj, L. Fradet, J. Siegel, and F. Braatz. Pressure characteristics at the stump/socket interface in transtibial amputees using an adaptive prosthetic foot. *Clinical Biomechanics*, 24(10):860 – 865, 2009. ISSN 0268-0033. doi: 10.1016/j.clinbiomech.2009.08.007.
- [164] F. E. Zajac, R. R. Neptune, and S. A. Kautz. Biomechanics and muscle coordination of human walking: Part ii: Lessons from dynamical simulations and clinical implications. *Gait & Posture*, 17(1):1 – 17, 2003. ISSN 0966-6362. doi: 10.1016/S0966-6362(02)00069-3.
- [165] V. Zatsiorsky. *Kinetics of human motion*. Human Kinetics, 2002.